First Application of CsI(Tl) Pulse Shape Discrimination at an e^+e^- Collider to Improve Particle Identification at the Belle II Experiment

by

Savino Longo
B.Eng., McMaster University, 2013
M.Sc., University of Victoria, 2015

A Dissertation Submitted in Partial Fulfillment of the
Requirements for the Degree of

DOCTOR OF PHILOSOPHY

in the Department of Physics and Astronomy

First Application of CsI(Tl) Pulse Shape Discrimination at an e^+e^- Collider to Improve Particle Identification at the Belle II Experiment

by

Savino Longo
B.Eng., McMaster University, 2013
M.Sc., University of Victoria, 2015

Supervisory Committee

Dr. John Michael Roney, Supervisor
(Department of Physics and Astronomy)

Dr. Robert Kowalewski, Departmental Member
(Department of Physics and Astronomy)

Dr. Michel Lefebvre, Departmental Member
(Department of Physics and Astronomy)

Dr. Alexandre Brolo, Outside Member
(Department of Chemistry)

Abstract

This dissertation investigates CsI(Tl) pulse shape discrimination (PSD) as a novel experimental technique to improve challenging areas of particle identification at high energy e^+e^- colliders using CsI(Tl) calorimeters. In this work CsI(Tl) PSD is implemented and studied at the Belle II experiment operating at the SuperKEKB e^+e^- collider, representing the first application of CsI(Tl) PSD at a B factory experiment.

Results are presented from Belle II as well as a testbeam completed at the TRIUMF proton and neutron irradiation facility. From the analysis of the testbeam data, energy deposits from highly ionizing particles are shown to produce a CsI(Tl) scintillation component with decay time of 630 ± 10 ns, referred to as the hadron scintillation component, and not present in energy deposits from electromagnetic showers or minimum ionizing particles. By measuring the fraction of hadron scintillation emission relative to the total scintillation emission, a new method for CsI(Tl) pulse shape characterization is developed and implemented at the Belle II experiment's electromagnetic calorimeter, constructed from 8736 CsI(Tl) crystals.

A theoretical model is formulated to allow for simulations of the particle dependent CsI(Tl) scintillation response. This model is incorporated into GEANT4 simulations of the testbeam apparatus and the Belle II detector, allowing for accurate simulations of the observed particle dependent scintillation response of CsI(Tl). With $e^\pm$, $\mu^\pm$, $\pi^\pm$, $K^\pm$ and $p/\bar{p}$ control samples selected from Belle II collision data the performance of this new simulation technique is evaluated. In addition the performance of hadronic interaction modelling by GEANT4 particle interactions in matter simulation libraries is studied and using PSD potential sources of data vs. simulation disagreement are identified.

A PSD-based multivariate classifier trained for K_L^0 vs. photon identification is also presented. With K_L^0 and photon control samples selected from Belle II collision data, pulse shape discrimination is shown to allow for high efficiency K_L^0 identification with low photon backgrounds as well as improved π^0 identification compared to shower-shape based methods.

Contents

Acknowledgements

I would like to thank:

Dr. J. Michael Roney for the guidance, support and encouragement he provided through my Masters and PhD at the University of Victoria. His wisdom and expertise was instrumental to the success of this project.

Dr. Robert Kowalewski for the continued guidance provided throughout my graduate studies at the University of Victoria and the interesting discussions throughout this work.

Dr. Alexei Sibidanov and The Belle II Calorimeter Group for their expertise and aiding in implementation of pulse shape discrimination at Belle II.

Dr. Paul Poffenberger for the advice both in and out of the lab.

Dr. Michel Lefebvre for the advice and encouragement throughout my studies.

My parents for their constant love and support.

Dedication

To mom and dad

Chapter 1

Introduction

Particle physics aims to search for the basic building blocks of nature and, under a unified framework, understand their interactions via the electromagnetic, strong, weak and gravitational forces. The investigation and understanding of the fundamental particles and forces has progressed over the past century with discoveries of quarks, leptons, gauge bosons, Charge-Parity violation and the Higgs boson, with our current best-understanding cumulating into the present day Standard Model of particle physics. The Standard Model is one of the most successful scientific theories to date, demonstrating the ability to describe, to our current level of experimental precision, all of the observed interactions of the known fundamental particles through the electromagnetic, weak and strong interactions [1, 2]. Despite the numerous successes of the Standard Model, it is however an incomplete theory. This is evident from its inability to describe gravitational interactions, and explain several astronomical and cosmological observations such as the nature of dark matter, dark energy and the origin of the observed matter-antimatter asymmetry of the universe. These are examples of open questions that modern high energy physics experiments seek to gain insight [1, 2].

The Belle II experiment, located at the SuperKEKB electron-positron collider in Tsukuba, Japan, is an upcoming B-Factory experiment that will search for new physical phenomenon through searches for processes that are forbidden by the Standard Model and by performing precision tests of Standard Model predictions. Over the lifetime of the Belle II experiment, the SuperKEKB collider will provide a dataset that will be $\sim 50\times$ larger than the individual datasets collected by previous e^+e^- Factories. The increase in statistical precision provided by this large dataset will allow Belle II to study unexplored areas of particle physics [3, 4].

To further push the boundaries set by past B-Factories, new experimental methods that can reduce systematic uncertainties and allow for new measurements, will also be crucial for Belle II. For this reason, Belle II includes several detector upgrades relative to past e^+e^- Factories that will improve performance in areas of precision vertexing, tracking and charged particle identification [3, 4]. Continuing in this direction, the work in this dissertation investigates and implements a novel method for calorimeter-based particle identification at Belle II, through the first application of thallium doped cesium iodide (CsI(Tl)) pulse shape discrimination (PSD) at a B-Factory experiment. The results in this dissertation show that using CsI(Tl) pulse shape discrimination, direct insight into the secondary particles produced in a CsI(Tl) crystal volume can be gained, allowing for the capabilities of the Belle II experiment to be extended by improving photon, K_L^0, neutron and π^0 identification, as well as, challenging areas of charged particle identification. These improvements will potentially allow Belle II to pursue new tests of the Standard Model and improve the experimental precisions of already planned searches.

The organization of this dissertation is outlined below.

- Chapter 2 presents an overview of the Standard Model with a focus on the types of particles and interactions that are studied by the Belle II experiment and discussed throughout this work. This chapter concludes by outlining some examples of measurements that are planned to be conducted by the Belle II experiment to test the Standard Model and also will directly benefit from the work in this dissertation.

- Chapter 3 outlines the theoretical background for how particles interact when entering dense materials such as the Belle II electromagnetic calorimeter, which is constructed from CsI(Tl) scintillator crystals. The premise for applying CsI(Tl) pulse shape discrimination to identify an electromagnetic vs. hadronic showers is outlined and the research objectives of the dissertation are defined.

- Chapter 4 outlines the technical details of the SuperKEKB collider and the Belle II detector.

- Chapter 5 studies neutron and proton testbeam data from a testbeam that was completed at the TRIUMF proton and neutron irradiation facility. The results of the analysis presented in this chapter establish a proof-of-concept that CsI(Tl)

pulse shape discrimination can be used to improve hadronic shower identification at high energy collider experiments. As a part of this study a new method for CsI(Tl) pulse shape characterization is developed and a theoretical model is formulated that allows the particle dependent CsI(Tl) scintillation response to be computed. This model is integrated with GEANT4 particle interaction in matter simulation libraries [5] allowing for simulations of the particle dependent scintillation response in CsI(Tl). This new simulation method is then validated with the testbeam data.

- Chapter 6 outlines the work completed to implement pulse shape discrimination at the Belle II Experiment by using the data analysis and simulation techniques developed in Chapter 5. In this chapter the Belle II CsI(Tl) pulse shape characterization methods, development of the calibration procedures, as well as integration of the CsI(Tl) scintillation response simulation methods into the Belle II simulation framework are described.

- Chapter 7 uses pulse shape discrimination to study the CsI(Tl) calorimeter interactions of $e^{\pm}$, $\mu^{\pm}$, $\pi^{\pm}$, $K^{\pm}$ and $p/\bar{p}$ control samples selected from Belle II collision data. This is the first analysis to apply pulse shape discrimination in this energy regime to further understand the interactions of these particles in CsI(Tl). Throughout this chapter comparisons with simulation are presented, allowing the simulation methods developed in Chapter 5 to be tested with Belle II data. In addition using the information provided by pulse shape discrimination, the models applied by GEANT4 to simulate hadronic interactions are evaluated and potential sources for improvement in data vs. simulation agreement are identified.

- Chapter 8 applies pulse shape discrimination to improve neutral particle identification at the Belle II experiment. This chapter begins with the training of a multivariate classifier, which uses pulse shape discrimination to identify hadronic vs. electromagnetic interactions in the Belle II calorimeter. With control samples of K_L^0, photons and π^0 selected form Belle II collision data, the performance of the pulse shape discrimination based classifier is evaluated and shown to achieve improved performance over existing methods for hadronic shower identification.

- Chapter 9 presents the conclusions of this work and comments on the poten-

tial for the application of scintillator pulse shape discrimination at future high energy physics experiments to improve calorimeter-based particle identification.

Chapter 2

Motivations for applying Pulse Shape Discrimination at the Belle II Experiment

This chapter begins with an overview of the Standard Model which is the theoretical framework that the Belle II experiment aims to test. This is followed by a brief description of the Belle II experiment and the types of particles whose properties the Belle II detector is designed to measure. The final section outlines examples of measurements that are planned to be conducted at Belle II where the application of PSD is predicted to improve the sensitivity of the measurement to potential signs of new physics.

2.1 The Standard Model

2.1.1 Fundamental Particles

The Standard Model theoretically describes the interactions of particles through the electromagnetic (EM), weak and strong forces [6, p.1]. In the Standard Model, each type of particle has an associated field, $\Phi(x,t)$, and the particles are defined as quantized excitations of their respective field [7, p.124-125]. Through the interactions between fields, a particles state can change, including the possibility of the particle transforming into other particles [7, 8].

The probability to observe a system of particles in a state with the set of properties $a, b, ...$, is computed using the wave function, $\psi_{a,b,...}(x,t) \equiv |a,b,...\rangle$, which describes

the state of the system [1]. All of the known fundamental particles are classified as fermions or bosons [1, p. 3]. In units of $\hbar$, fermions have intrinsic angular momentum, called spin, of $(1+n)1/2$ and bosons have intrinsic angular momentum of n where n is an integer that is greater or equal to zero [1, p.183]. For a system of two identical particles, the wave function is symmetric under the exchange of the particles if they are bosons and anti-symmetric if they are fermions [1, p.183].

Each fundamental force that is described in the Standard Model has a set of fundamental bosons, called gauge bosons, which are responsible for mediating the interactions between the particles via the specified force. The gauge bosons of the Standard Model are listed in Table 2.1 including their mass and associated interaction [1, 2, 7, 8].

Table 2.1: Gauge bosons of the Standard Model. Mass values are from Particle Data Group [2].

Gauge Boson	Mass (GeV/c^2)	Interaction Mediator
γ (photon)	0	Electromagnetic
$g_1, .., g_8$ (gluon's)	0	Strong
$W^{\pm}$	80.379 ± 0.012	Weak
Z	91.1876 ± 0.0021	Weak

Particles can interact through the exchange of gauge boson mediators only if the interacting particles have a charge coupling for the corresponding interaction. Electromagnetically interacting particles are electrically charged, strongly interacting particles are colour charged and weakly interacting particles have hypercharge/weak isospin charge [1, 7, 8].

Using the charge couplings, the fundamental fermions are categorized as leptons or quarks, where quarks have colour charge and leptons do not. Listed in Table 2.2 are the known leptons with some of their defining properties. Electrically charged leptons interact through the electromagnetic and weak force while neutrinos only interact through the weak interaction. In Table 2.2 the leptons are organized into three generations such that each generation contains one charged lepton and a neutrino partner. This organization relates to how the leptons interact through weak interactions and is discussed in Section 2.1.5 [1, 7, 8].

Table 2.2: List of the known leptons. Values for mass and lifetime are from Particle Data Group [2].

Generation	Label	Name	Mass (MeV/c^2)	Charge	Lifetime (s)
1	e	electron	0.5109	1	stable
	ν_e	electron neutrino	$< 2 \times 10^{-6}$	0	stable
2	μ	muon	105.65	1	2.19×10^{-6}
	ν_μ	muon neutrino	< 0.16	0	stable
3	τ	tau	1776.86 ± 0.12	1	2.90×10^{-13}
	ν_τ	tau neutrino	< 18.2	0	stable

There are six known quarks, which are listed in Table 2.3. As with leptons, quarks are organized into three generations that relate to their weak interactions. Quarks have colour charge in addition to electric and weak charges, allowing them to interact through electromagnetic, weak and strong forces [1, 7, 8].

Table 2.3: Quark properties. Values for mass are from Particle Data Group [2].

Generation	Label	Flavour	Mass (MeV/c^2)	Charge
1	u	up	$2.16^{+0.49}_{-0.26}$	2/3
	d	down	$4.67^{+0.48}_{-0.17}$	-1/3
2	c	charm	$(1.27\pm0.02) \times 10^3$	2/3
	s	strange	93^{+11}_{-5}	-1/3
3	t	top	$(172.9 \pm 0.4) \times 10^3$	2/3
	b	bottom	$(4.18^{+0.03}_{-0.02}) \times 10^3$	-1/3

The final fundamental particle described in the Standard Model is the Higgs boson. The Higgs boson has spin 0 and is electrically neutral [1, 2, 7, 8]. The Higgs boson is the particle associated with the Higgs field. The Higgs field is included in the Standard Model to provide a mechanism of mass generation for the fundamental particles [8, p.278]. A unique property of the Higgs boson is that it couples to other particles through their mass [8]. The Higgs boson was discovered in 2012 by the ATLAS and CMS experiments at CERN's Large Hadron Collider [2] and was the last Standard Model particle to be discovered. It is measured to have a mass of 125.10 ± 0.14 GeV/c^2 [2].

2.1.2 Particle Interactions

A fundamental principle of the Standard Model is that gauge bosons and particle interactions arise as a consequence of requiring the interactions to be invariant under local phase transformations of the particles field [1, p.361] [6, p.424] [8, p.28]. That is, given a field, $\Phi(x,t)$, with charge, $\boldsymbol{\beta}$, the phase transformation defined in equation 2.1 should leave the interactions unchanged, where $\boldsymbol{g(x,t)}$ is an arbitrary function [1] [6, p.420] [8].

$$\Phi(x,t) \rightarrow e^{i\boldsymbol{\beta}\cdot\boldsymbol{g(x,t)}}\Phi(x,t) \tag{2.1}$$

By obeying equation 2.1, each force is associated with a symmetry, such that the type of symmetry is defined by the nature of the force's charge, $\boldsymbol{\beta}$ [6, 8]. By Noether's theorem, this symmetry leads to the charge conservation laws for each force [8, p.28]. All interactions must obey the charge conservation law derived from this symmetry that defines the interactions [8]. In addition, by requiring local gauge invariance particles must acquire mass through the Higgs mechanism [8].

The two primary types of particle interactions studied at particle colliders are collisions and decays. A collision can be elastic where only the particles momentum is changed or inelastic where new particles are produced. When two particles interact, the likelihood for a collision to result in a final state ξ is characterized by the cross section, σ_ξ, which is typically expressed in units of barns where, 1 barn = 10^{-28} m^2 [1]. Using the cross section, the number of events expected for the final state ξ can be computed with equation 2.2 [1, p.203].

$$n_\xi = \mathcal{L}\sigma_\xi \tag{2.2}$$

In equation 2.2, $\mathcal{L}$ is the luminosity, defined as the number of collisions per second per unit area and n_ξ is the number of events per second produced in the state ξ.

Decays occur when a particle spontaneously transforms into a set of lighter particles. The probability for a particle to decay at a time t is described by the exponential distribution shown in equation 2.3 [1, p.203].

$$\Gamma_\xi e^{-t\Gamma_\xi} \tag{2.3}$$

In equation 2.3, Γ_ξ is the decay rate of the particle ξ [1, p.203]. In general, a particle can have many possible decay modes. For a particle with multiple decay modes, Γ_ξ

is computed by the sum over the decay rates for all potential decay modes. The lifetime of the particle, τ_ξ, is defined as $1/\Gamma_\xi$ [1, p.203]. When a particle decays, the probability for a particular decay mode to occur is given by the branching fraction of the decay mode [1].

In the Standard Model, cross sections and branching fractions are computed using perturbation theory [7]. Perturbation theory assumes the coupling strength of the interaction is much less than one[1] [6, p.13] [7]. This allows the calculation of the cross section or branching fraction to be expressed as an infinite series expanded around the coupling parameter such that the lower order terms in the series are the dominant contributions to the total value [6, p.13] [7]. Feynman diagrams are a tool used to visually represent the terms in these infinite series and provide an understanding for how the interaction could proceed [7]. Each fundamental force has a set of basic Feynman vertices which correspond to one order in the perturbative expansion [7]. Using the basic vertices, higher order diagrams, which represent the higher order terms in the series, can be constructed [7]. In the following sections, the basic Feynman vertices and the coupling strengths of the electromagnetic, strong and weak interactions are discussed.

2.1.3 Electromagnetic Interactions

The coupling strength of the electromagnetic interaction is given by the fine structure constant, $\alpha_{\mathrm{EM}} = e^2/4\pi \approx 1/137$ [6, p.11] [7, p.222]. For electromagnetic interactions, cross sections and branching fractions can be computed to high precision using only the lowest order terms of the interaction because $\alpha_{\mathrm{EM}} \ll 1$ [7, p.222]. The basic Feynman vertex for electromagnetic interactions, which corresponds to one order in α_{EM}, is illustrated in Figure 2.1 [1, 6, 7]. This diagram shows a pair of electrically charged particles ($a^{\pm}$) interacting with a photon. The basic electromagnetic interaction vertex shown in Figure 2.1 is a forbidden process on its own due to momentum and energy conservation, however by combining vertices allowed processes can be constructed [6, p.11].

[1] If the coupling strength is approaching unity, such as for strong interactions at energies near hadron mass scales, other methods such as Lattice Gauge Theory/Lattice Quantum Chromodynamics can be applied [6, p.196].

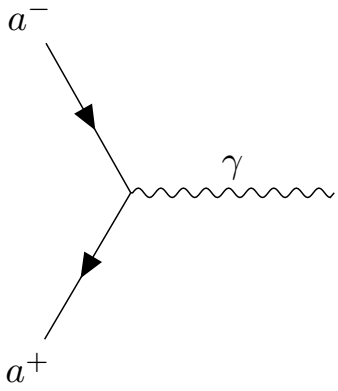

Figure 2.1: Basic Feynman vertex for the electromagnetic interaction [6, p.11].

An example of a lowest order Feynman diagram for the interaction $e^+e^- \to f^+f^-$, where f is a charged fermion, is shown in Figure 2.2. In this diagram time flows from left-to-right such that the Feynman diagram is depicting an electron and positron interacting to produce a charged fermion + anti-fermion pair through a photon mediator. At the SuperKEKB e^+e^- collider, this diagram illustrates the dominant method by which the e^+e^- collisions can produce a variety of final states. For the collisions at SuperKEKB, f can be any charged fermion in Tables 2.2 and 2.3, except for the top quark due to energy conservation, as the total centre-of-mass collision energy is 10.58 GeV.

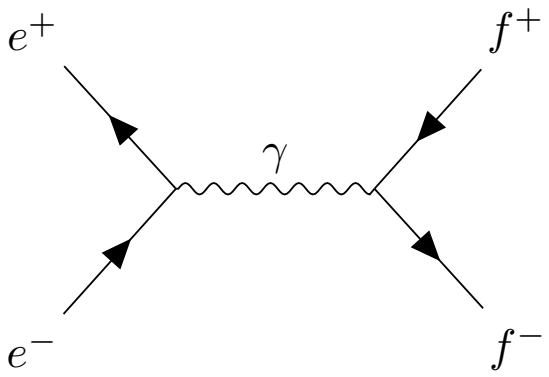

Figure 2.2: Lowest order Feynman diagrams for the interaction $e^+e^- \to f^+f^-$.

2.1.4 Strong Interactions

Particles with colour charge can interact through the strong force by the exchange of gluons. Colour charge, Q_c, has three types labelled red/anti-red ($r/\bar{r}$), green/anti-

green ($g/\bar{g}$) and blue/anti-blue ($b/\bar{b}$). The combinations rgb, $\bar{r}\bar{g}\bar{b}$, $r\bar{r}$, $g\bar{g}$ and $b\bar{b}$ are colour neutral [1]. Quarks carry r, g or b colour charge whereas anti-quarks carry $\bar{r}, \bar{g}$ or $\bar{b}$ colour charge and gluons carry pairs of colour charge.

The lowest order basic Feynman vertex for the strong interaction is shown in Figure 2.3. This figure illustrates two quarks with colour charge Q_c^i and Q_c^j interacting with a gluon of charge Q_c^{ij} [1].

The coupling strength of the strong interaction, α_s, changes with the energy scale of the interaction [6, p.198]. At the energy scale of the Z boson mass, $\alpha_s(m_Z) = 0.118 \pm 0.002$ [2] [6, p.198]. As the energy scale of the interaction increases, α_s decreases and as the energy scale decreases, α_s increases [6, p.198]. Due to α_s approaching unity at energy scales near hadron mass scales, strong interactions in this energy regime are not well described by perturbation theory and thus are challenging to compute [6, p.198].

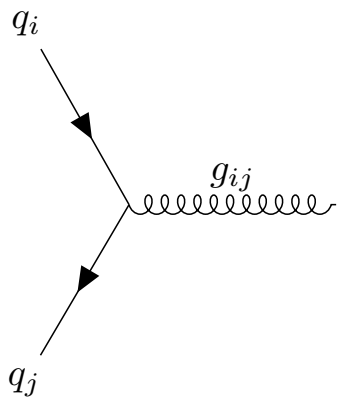

Figure 2.3: Lowest order basic Feynman vertex for the strong interaction [1].

An example of a strong interaction that frequently occurs at the Belle II experiment is shown in Figure 2.4. This figure illustrates one of the lowest order Feynman diagrams for the decays $\Upsilon(4S) \rightarrow B^0\bar{B}^0$ and $\Upsilon(4S) \rightarrow B^+B^-$. The left side of this diagram begins with a $b\bar{b}$ strongly bound state called an $\Upsilon(4S)$ meson. At SuperKEKB $\Upsilon(4S)$ can be produced through the electromagnetic interaction by the diagram shown previously in Figure 2.2, where the fermions $f^{\pm}$ correspond to a b and anti-b quark. Once produced, an $\Upsilon(4S)$ can decay into a $B^0\bar{B}^0$ or B^+B^- meson pair through the strong interaction by the diagrams shown in Figure 2.4. In these diagrams a gluon is radiated from one of the b quarks followed by the production of a $d\bar{d}$ or $u\bar{u}$ pair which then become bound to one of the b quarks, forming a pair of $B^0\bar{B}^0$ or B^+B^- mesons.

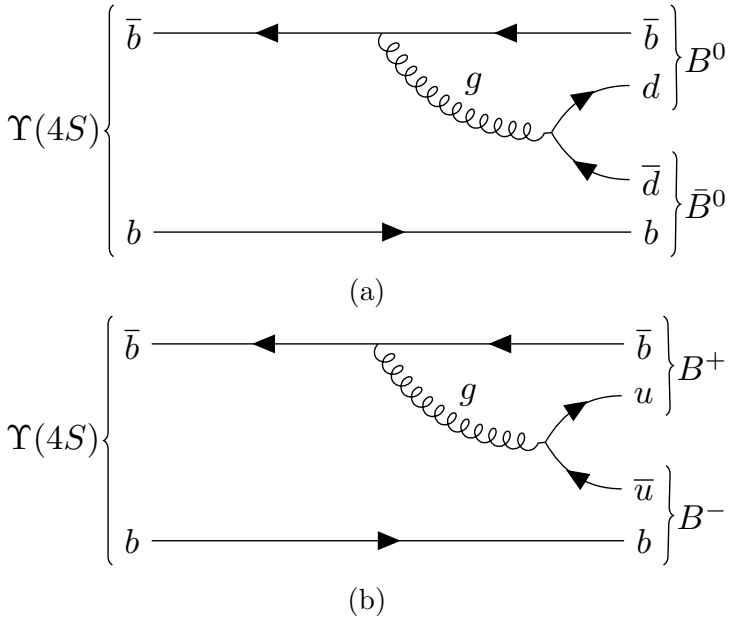

Figure 2.4: One of the first order Feynman diagrams for an Υ(4S) meson decaying to a) $B^0\bar{B}^0$ b) B^+B^-.

2.1.5 Weak Interactions

The weak interaction has three gauge boson mediators, the Z and $W^{\pm}$. The lowest order basic Feynman vertices for these mediators are shown in Figure 2.5 [1].

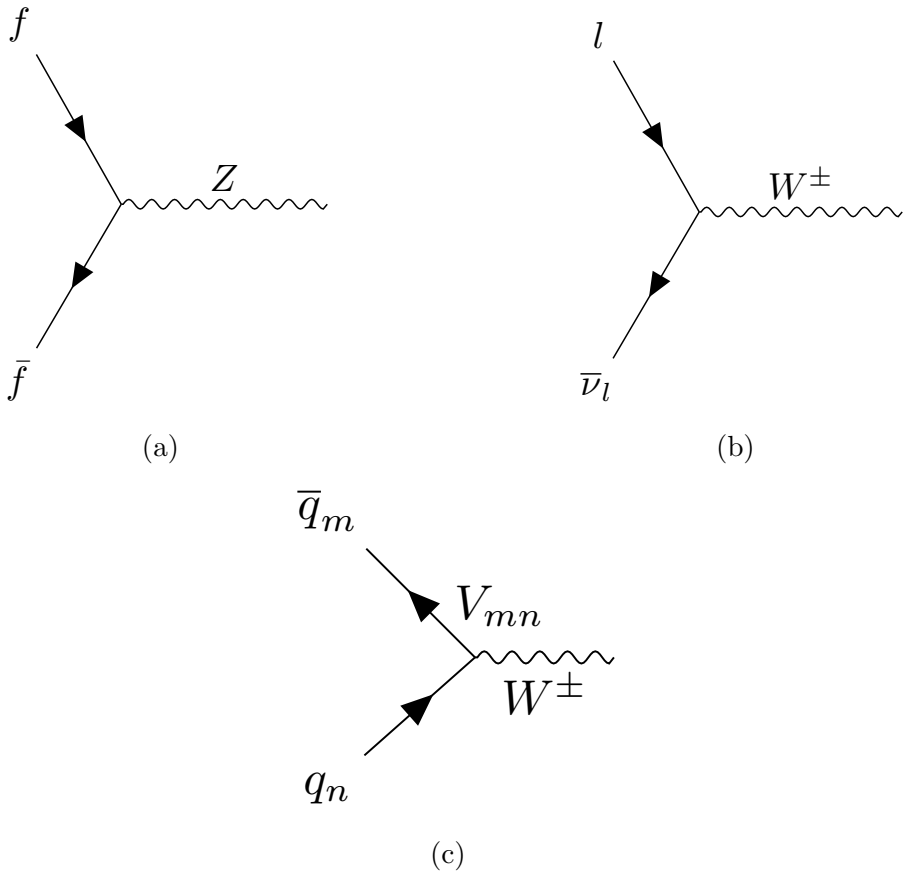

Figure 2.5: Lowest order basic Feynman vertices for the weak interaction [1].

The vertex in Figure 2.5a illustrates a fermion and anti-fermion interacting with a neutral Z boson. This diagram is similar to the basic Feynman vertex for the electromagnetic interaction shown previously in Figure 2.1, however unlike the basic electromagnetic vertex, the fermions in Figure 2.5 include neutrinos [1]. The vertex in Figure 2.5b shows how leptons interact with $W^{\pm}$ bosons. In Figure 2.5b $l = e, \mu$ or τ, demonstrating that leptons interacting with a $W^{\pm}$ boson will do so with their associated partner in their generation. Figure 2.5c shows how quarks interact with a $W^{\pm}$ boson. In this figure, $m = u, c$ or t, $n = d, s$ or b and V_{mn} is the corresponding element in the Cabibbo–Kobayashi–Maskawa matrix which will be discussed in the following section and suppresses flavour changing interactions [1]. The vertex in Figure 2.5c shows that through the weak interaction, quarks can change their flavour. This will be discussed further in Section 2.1.6.

The coupling strength of the weak interaction is $\alpha_{\text{weak}} = 0.0042 \pm 0.0002$ [6, p.254]. Despite α_{weak} being a similar scale to α_{EM}, the observed strength of weak interactions

is much lower than electromagnetic interactions, due to the masses of the $W^{\pm}$ and Z boson mediators. This is because an interaction that proceeds through a mediator with mass, m, will be suppressed by a factor of $1/(q^2 - m^2)$ where q is the momentum transfer of the interaction [1, p.308].

2.1.6 Cabibbo–Kobayashi–Maskawa Matrix

An interaction has parity symmetry if the interaction is unchanged under the parity transformation, P, which results in the spatial inversion of the particle's field as shown in equation 2.4 [1, p.139].

$$P\Phi(x, y, z) = \Phi(-x, -y, -z) \tag{2.4}$$

In addition, an interaction has Charge symmetry if the interaction is unchanged under the charge conjugation, C, which replaces particles with their anti-particles [1, p.142]. The electromagnetic and strong interactions both have charge and parity symmetry [1]. The weak interaction however violates both charge symmetry and parity symmetry [1]. Most weak interaction processes preserve the combination of C and P (CP), however, in some weak interaction processes CP symmetry is violated.

CP violation is measured to occur in quark flavour changing weak interactions. This is described theoretically by the Cabibbo–Kobayashi–Maskawa (CKM) matrix quark mixing model [8, p.319]. This model states that in weak interactions, the d, s and b quark fields interact as the linear combinations d', s' and b' defined in equation 2.5 [8, p.386].

$$\begin{pmatrix} d' \\ s' \\ b' \end{pmatrix} = \begin{pmatrix} V_{ud} & V_{us} & V_{ub} \\ V_{cd} & V_{cs} & V_{cb} \\ V_{td} & V_{ts} & V_{tb} \end{pmatrix} \begin{pmatrix} d \\ s \\ b \end{pmatrix} \tag{2.5}$$

In this equation the matrix V_{ij} is a unitary matrix called the CKM matrix as it was first proposed by M. Kobayashi and T. Maskawa to theoretically describe CP violation in flavour changing weak interactions [8, p.319]. This is achieved by a 3×3 unitary matrix because the matrix can be parametrized by three real angles and one complex phase. The three real angles describe quark mixing and the complex phase allows for CP violation [8, p.319].

The elements of the CKM matrix are not predicted in the Standard Model and thus must be measured [1]. Equation 2.6 shows the current status of the measured

values for the CKM matrix [2]. These values also illustrate that interactions where a quarks flavour is changed to a flavour outside its generation are suppressed.

$$|V_{ij}| = \begin{pmatrix} 0.97446 \pm 0.00010 & 0.22452 \pm 0.00044 & 0.00365 \pm 0.00012 \\ 0.22438 \pm 0.00044 & 0.97359^{+0.00010}_{-0.00011} & 0.4214 \pm 0.00076 \\ 0.00896^{+0.00024}_{-0.00023} & 0.04133 \pm 0.00074 & 0.999105 \pm 0.000032 \end{pmatrix} \tag{2.6}$$

As mentioned above, the CKM matrix is predicted to be a unitary matrix. From this requirement, constraints such as equation 2.7 can be derived [8, p.320].

$$1 + z_1 + z_2 = 0 \tag{2.7}$$

where

$$z_1 = \frac{V_{td}V_{tb}^*}{V_{cd}V_{cb}^*} \tag{2.8}$$

$$z_2 = \frac{V_{ud}V_{ub}^*}{V_{cd}V_{cb}^*} \tag{2.9}$$

Equation 2.7 defines a unitary triangle which can be visualized when it is plotted on the complex plane, forming a triangle of side lengths 1, z_1 and z_2 [8, p.320]. The interior angles of this triangle are given by equations 2.10, 2.11 and 2.12 [8, p.320][2, 4].

$$\alpha \equiv \phi_2 \equiv arg(-\frac{V_{td}V_{tb}^*}{V_{ud}V_{ub}^*}) = (84.5^{+5.9}_{-5.2})\,\text{deg} \tag{2.10}$$

$$\beta \equiv \phi_1 \equiv arg(-\frac{V_{cd}V_{cb}^*}{V_{td}V_{tb}^*}) = (22.5 \pm 0.9)\,\text{deg} \tag{2.11}$$

$$\gamma \equiv \phi_3 \equiv arg(-\frac{V_{ud}V_{ub}^*}{V_{cd}V_{cb}^*}) = (73.5^{+4.2}_{-5.1})\,\text{deg} \tag{2.12}$$

Experimental tests of the CKM quark mixing model are achieved by performing independent measurements of the elements of the CKM matrix, and/or combinations of elements, such as the angles defined in equations 2.10, 2.11 and 2.12. With these measurements the unitarity of the measured matrix is tested through constraints such as equation 2.7 and equation 2.13 [8, p.321].

$$\alpha + \beta + \gamma = \pi \tag{2.13}$$

Discussed in Section 2.2 of this chapter, the work completed in this dissertation to implement pulse shape discrimination at the Belle II Experiment is expected to improve the measurements of V_{ub} and β/ϕ_1 that are planned to be completed by Belle II.

2.1.7 Hadrons

Quarks are observed to only exist in colour singlet, strongly bound, composite states called hadrons. Hadrons are composed of valence quarks that are bound by gluons. The valence quarks determine the hadron's interactions, spin and charge [9, 10-3]. Hadrons also have sea quarks which are $q\bar{q}$ pairs that can spontaneously be produced by gluons and exist briefly in the hadron [9, p. 10-3].

From the six flavours of quarks, there are numerous colour neural combinations that can be constructed, resulting in many potential hadrons. Hadrons are classified as mesons if they are a quark anti-quark bound state or baryons if they are a three quark or three anti-quark bound state [9]. Hadrons can be characterized by their valence quark content, mass, lifetime and quantum numbers J^{PC} where J is the total angular momentum of the bound system, defined as the sum of the spin (S) and orbital angular momentum (L) contributions [9, p. 10-4]. P and C are the parity and charge conjugation quantum numbers that describe how the hadron transforms under the P and C transformations discussed in Section 2.1.6. Listed in Table 2.4 are some of the hadrons that are frequently discussed in this dissertation. Mass values and lifetimes to compute decay lengths in this table are from the Particle Data Group [2].

With the exception of the proton, all hadrons are unstable and decay into lighter hadrons and/or leptons [1, p. 79]. Depending on the interaction that the decay proceeds through, the lifetimes of hadrons can span a wide range. Hadrons that can decay electromagnetically or strongly, have lifetimes much shorter than hadrons that are restricted to only decaying through the weak interactions [1]. This is due to the suppression caused by the large mass of the Z and $W^{\pm}$ bosons that mediate weak interactions, as discussed in Section 2.1.5.

When produced at particle colliders, hadrons can have a speed ($\beta = v/c$) that is close to the speed of light, c, and due to time dilation, they can travel significant distances in the laboratory before decaying [1, p. 91]. This is illustrated in Table 2.4 which lists the decay length in the laboratory frame computed using equation 2.14,

Table 2.4: List of hadrons that are frequently studied in this dissertation. Mass values and lifetimes to compute decay lengths are from the Particle Data Group [2].

Particle	Valence quarks	J^P or J^{PC}	mass (MeV/c^2)	Decay length at 0.5 GeV/c (m)
π^+	$u\bar{d}$	0^-	139.57	28
π^0	$\frac{1}{\sqrt{2}}(u\bar{u} - d\bar{d})$	0^{-+}	134.97	9.4×10^{-8}
K^+	$u\bar{s}$	0^-	493.67	3.7
K^0	$d\bar{s}$	0^-	497.61	-
K^0_S	$\frac{1}{\sqrt{2}}(d\bar{s} + s\bar{d})$	0^-	-	2.7×10^{-2}
K^0_L	$\frac{1}{\sqrt{2}}(d\bar{s} - s\bar{d})$	0^-	-	15.4
ϕ	$s\bar{s}$	1^{--}	1019.46	2.28×10^{-14}
Υ(4S)	$b\bar{b}$	1^{--}	10579	4.55×10^{-16}
B^0	$d\bar{b}$	0^-	5279	4.31×10^{-5}
B^+	$u\bar{b}$	0^-	5279	4.65×10^{-5}
p	uud	$1/2^+$	938.27	stable
n	udd	$1/2^+$	939.56	$> 10^{11}$
Δ^{++}	uuu	$3/2^+$	1210	6.97×10^{-16}
Δ^+	uud	$3/2^+$	1210	6.97×10^{-16}
Δ^0	udd	$3/2^+$	1210	6.97×10^{-16}
Δ^-	ddd	$3/2^+$	1210	6.97×10^{-16}
Λ^0	uds	$1/2^+$	1115	3.5×10^{-2}
Σ^+	uus	$1/2^+$	1189	3.5×10^{-2}
Σ^0	uds	$1/2^+$	1192	9.31×10^{-12}
Σ^-	dds	$1/2^+$	1197	1.84×10^{-2}

for the listed hadron travelling with $\mathrm{p_{lab}} = 0.5$ GeV/c of momentum. The extended decay lengths of some hadrons mean that when they are produced at SuperKEKB, they will typically not decay in the Belle II detector volume, which extends only ~ 3.5 meters from the interaction point [3]. From the perspective of the Belle II detector, these particles can be treated as stable particles and the Belle II detector must function to detect and identify them [3].

$$l_{\mathrm{lab},i} = \tau_i c \frac{\mathrm{p_{lab},i}}{m_i} \tag{2.14}$$

2.1.8 Neutral Kaons

Included in Table 2.4, neutral kaons have a valence quark content of $K^0 = d\bar{s}$ and $\bar{K}^0 = \bar{d}s$. From the strange quark, the strangeness quantum number of the neutral kaons are defined to be $S_{K^0} = -1$ and $S_{\bar{K}^0} = 1$ [9, p.10-2]. The definite strange quark content of these states means they represent the strong interaction states for the neutral kaons [1, p.147]. Neutral kaons are the lightest hadrons with a strange quark and thus due to conservation of quark flavour by the strong and electromagnetic interactions, neutral kaons can only decay through flavour changing weak interactions [9, p. 19-1].

Prior to decaying, neutral kaons undergo a process called $K^0 - \bar{K}^0$ mixing. $K^0 - \bar{K}^0$ mixing is a weak interaction process by which a $K^0(\bar{K}^0)$ can transform into a $\bar{K}^0(K^0)$. This interaction is illustrated by the Feynman diagram shown in Figure 2.6 [8, p. 346]. Shown in this diagram, through two $W^{\pm}$ bosons a $\bar{K}^0$ can transform into a K^0 [8, p. 346]. A consequence of $K^0 - \bar{K}^0$ mixing is that once a K^0 or $\bar{K}^0$ is produced, it propagates as a linear combination of both a K^0 and $\bar{K}^0$. If the neutral kaon remains isolated from other particles, the probability that the neutral kaon is a K^0 or $\bar{K}^0$ will oscillate in time until it decays [8, p. 346].

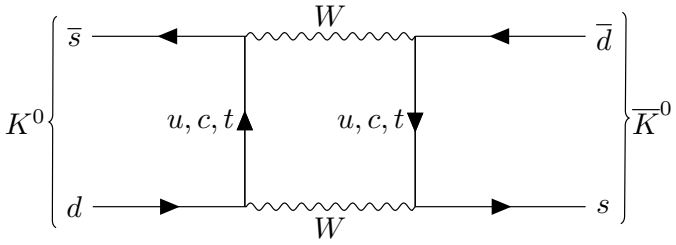

Figure 2.6: Sample Feynman diagram for $K^0 - \bar{K}^0$ mixing [8, p. 347].

There are two dominant classes of decay modes for neutral kaons which are of the form $K \to \pi l^{\pm} \nu_l$ and $K \to n\pi$ where $l = e$ or μ, $n = 2$ or 3 and $\pi = \pi^{\pm}$ or π^0 [9, p. 19-1]. The decays to $\pi l^{\pm} \nu_l$ final states are called semileptonic modes and the decays to $n\pi$ are called hadronic modes. Figure 2.7 shows one of the lowest order Feynman diagrams for the semileptonic decay, $\bar{K}^0 \to \pi^+ l^- \nu_l$, and the hadronic decay, $\bar{K}^0 \to \pi^+ \pi^-$.

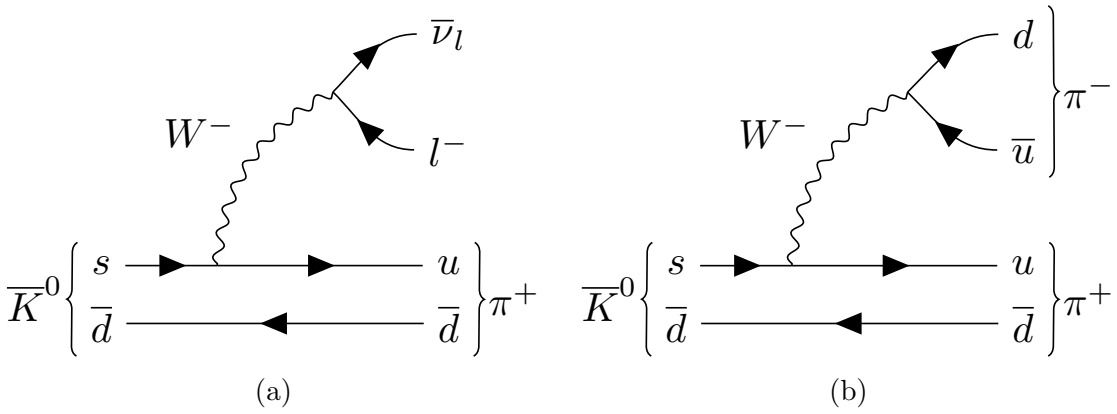

Figure 2.7: One of the lowest order Feynman diagrams for a) the semi-leptonic decay $\bar{K}^0 \to \pi^+ l^- \nu_l$ and b) the hadronic decay $\bar{K}^0 \to \pi^+ \pi^-$.

The Feynman diagrams shown in Figure 2.7 illustrate that in a semileptonic decay, the charge of the lepton in the final state can identify if the kaon was in a K^0 or $\bar{K}^0$ state at the time of the decay [9, p. 19-1]. For hadronic decays however, as shown in Figure 2.7, the same final states are possible for a K^0 and $\bar{K}^0$ and thus the final state alone cannot be used to immediately determine if the neutral kaon was a K^0 or $\bar{K}^0$ at the time of the decay [9, p. 19-1 - 19-3].

To understand the state of the neutral kaon in an hadronic decay, eigenstates of CP need to be constructed. This is because for the $n\pi$ final states, the CP transformation gives [1, p.146] [9, p.19-5]:

$$CP\,|\pi^0\pi^0\rangle = |\pi^0\pi^0\rangle \tag{2.15}$$

$$CP\,|\pi^0\pi^0\pi^0\rangle = -\,|\pi^0\pi^0\pi^0\rangle \tag{2.16}$$

Using the convention $CP\,|K^0\rangle = -\,|\bar{K}^0\rangle$, the states $|K_1\rangle$ and $|K_2\rangle$, defined in equations 2.17 and 2.18, can be constructed such that by definition: $CP\,|K_1\rangle = |K_1\rangle$ and $CP\,|K_2\rangle = -\,|K_2\rangle$ [1, p. 146].

$$|K_1\rangle = \frac{1}{\sqrt{2}}(|K^0\rangle - |\bar{K}^0\rangle) \tag{2.17}$$

$$|K_2\rangle = \frac{1}{\sqrt{2}}(|K^0\rangle + |\bar{K}^0\rangle) \tag{2.18}$$

If CP was a perfect symmetry of the weak interaction, the neutral kaons that decay

to 2π could be understood to originate from the $|K_1\rangle$ state and the 3π from the $|K_2\rangle$ state [1, p. 146]. Mentioned above, CP symmetry is violated by the weak interaction. This means that the weak interaction states of neutral kaons are given by the states K_S^0 and K_L^0, defined in equations 2.19 and 2.20, as a linear combination of the $|K_1\rangle$ and $|K_2\rangle$ states [1].

$$|K_L^0\rangle = \frac{1}{\sqrt{1+|\epsilon|^2}}(|K_2\rangle + \epsilon\,|K_1\rangle) \tag{2.19}$$

$$|K_S^0\rangle = \frac{1}{\sqrt{1+|\epsilon|^2}}(|K_1\rangle + \epsilon\,|K_2\rangle) \tag{2.20}$$

In equations 2.19 and 2.20, $|\epsilon|$ is experimentally measured to be $\epsilon = 2.24 \times 10^{-3}$ [1, p. 148] demonstrating the amount of CP violation is small and thus the K_L^0 (K_S^0) state is approximately equal to the K_2 (K_1) states. The difference in phase space available between the 2π and 3π final states results in the lifetime of the K_2 to the much longer than the K_1 [9, p. 19-5]. This results in the lifetime of the K_L^0 ($\tau_{\text{long}} \approx 5 \times 10^{-8}$ s), to be significantly longer than the lifetime of the K_S^0 ($\tau_{\text{short}} \approx 9 \times 10^{-11}$s) [1, p. 147][9, p. 19-5][2].

The detector signature for a neutral kaon produced at Belle II can now be discussed. In the SuperKEKB collisions, neutral kaons can be produced either directly by reactions such as $e^+e^- \to K^0\bar{K}^0$ or in decay chains of other particles, for example by $B^0 \to J/\psi\bar{K}^0$. After production, the neutral kaon immediately begins undergoing $K^0 - \bar{K}^0$ mixing as it propagates into the Belle II detector. If the kaon decays as a K_S^0, then although the lifetime is much shorter than the K_L^0, the decay length will typically be long enough to allow the majority of K_S^0's to decay in the tracking detectors in Belle II. Thus the detector signature for $K_S^0 \to \pi^+\pi^-$ candidates will be two tracks in the detector that form a vertex which is displaced a from the interaction point [4].

If the neutral kaon decays as a K_L^0, then the lifetime is long enough such the K_L^0 will most likely not decay before reaching the outer Belle II detectors such as the calorimeter and K_L^0 and Muon Detector. The calorimeter is one of the densest detectors in Belle II and when the K_L^0 enters the calorimeter about half of the time it will strongly interact with a proton or neutron in the detector material [2]. When this occurs, either the K^0 or $\bar{K}^0$ component of the K_L^0 will undergo the strong interaction with the proton or neutron [10].

2.1.9 Neutral Kaon Production from ϕ Decays

In Chapter 8, a sample of K_L^0 produced from the reaction $e^+e^- \rightarrow \phi\gamma_{\text{ISR}} \rightarrow K_S^0 K_L^0 \gamma_{\text{ISR}}$ are studied. In this equation γ_{ISR} is an Initial State Radiation (ISR) photon that is radiated by either the electron or position. Indicated in Table 2.4, the valence quarks of the ϕ are $s\bar{s}$. At SuperKEKB, a ϕ can be produced electromagnetically through Feynman diagrams such as the one shown earlier in Figure 2.2 where the fermions $f^{\pm}$ are a strange and anti-strange quark.

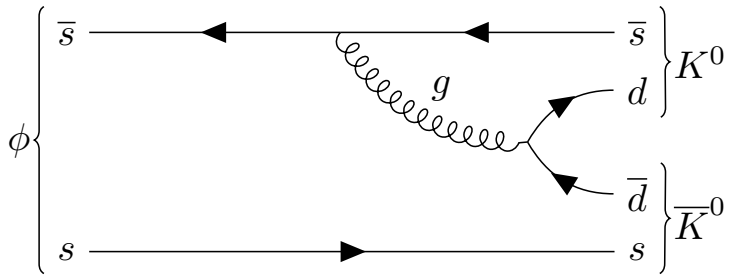

Figure 2.8: One of the first order Feynman diagrams for an ϕ meson decaying into a $K^0\bar{K}^0$ meson pair.

Once produced, the ϕ can decay through the strong interaction by $\phi \rightarrow K^0\bar{K}^0$ through the Feynman diagram shown in Figure 2.8. This decay can also be written as $\phi \rightarrow K_S^0 K_L^0$. This is because for this decay final states of two identical spin 0 bosons such as, $K_L^0 K_L^0$ or $K_S^0 K_S^0$, are forbidden [11]. This is can be seen from the angular momentum of the system. Before the decay, the ϕ has a total angular momentum of $J_\phi = S_\phi + L_\phi = 1$. The neutral kaons produced after the decay each have spin 0 ($S_{K0} = 0$) and thus together the $K^0\bar{K}^0$ system must have an orbital angular momentum of $L_{K^0\bar{K}^0} = 1$, to conserve angular momentum. This prevents final states of identical bosons, such as $K_L^0 K_L^0$ and $K_S^0 K_S^0$, because for an state with $L = 1$ with two identical particles, the wave function is anti-symmetric when the two particles are exchanged [11, p. 7][1, p. 161]. The $K_L^0 K_L^0$ and $K_S^0 K_S^0$ final states are thus forbidden by the spin-statistics theorem that states a system of two identical bosons must be symmetric under the exchange of the particles [1, p. 183].

2.2 A Sample of Belle II Measurements that will Benefit from Pulse Shape Discrimination

The Belle II experiment consists of the SuperKEKB asymmetric electron-positron collider and the Belle II detector. These primary components of the experiment are illustrated in Figure 2.9 [12]. The technical details of the SuperKEKB accelerator and the Belle II detector are discussed in Chapter 4. The primary objective of the Belle II experiment is to search for new physical processes that could potentially be produced in the electron-positron collisions, which occur in the centre of the Belle II detector. These searches occur though a variety of methods such as searches for processes that are predicted by the Standard Model to be rare or forbidden, and through precision measurements that can test the predictions made by the Standard Model [3, 4].

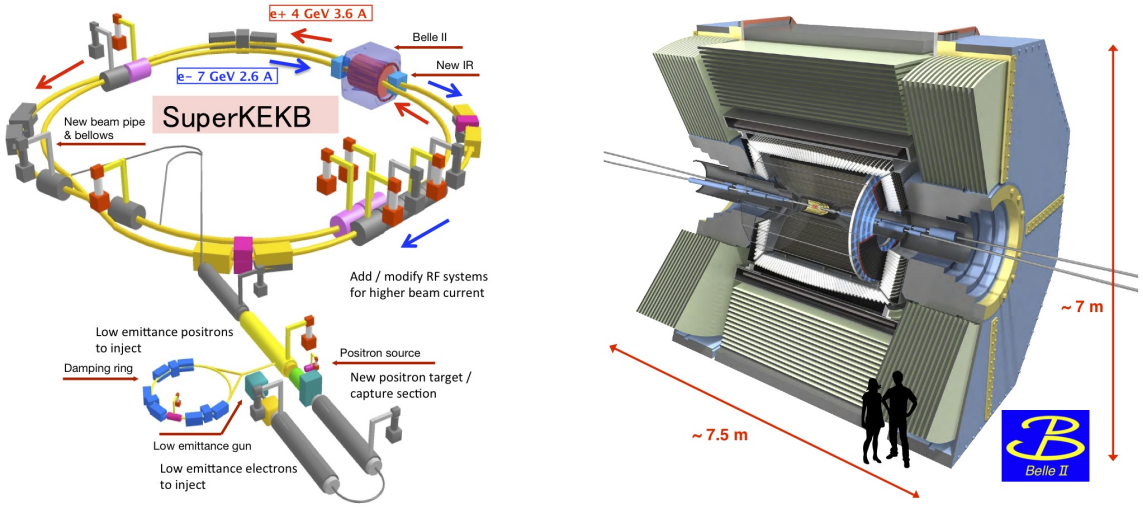

Figure 2.9: Illustration of the main components of the Belle II Experiment including the SuperKEKB accelerator and the Belle II detector. Image is from reference [12].

A collision event begins with the beams of electrons and positrons colliding in the centre of the Belle II detector. From the collision, Table 2.5 lists some of the possible final states that Belle II aims to study and their cross sections [4]. For most of these final states, the dominant contribution to the interaction cross section are from the Feynman diagram illustrated previously in Figure 2.2.

Table 2.5: List of commonly produced final states at SuperKEKB collisions and their corresponding cross section [4]. $e^-e^+(\gamma)$ cross sections corresponds to a scattering angle $10\,\text{deg} < \theta_e < 170\,\text{deg}$ and electron energy of $E_e > 0.15$ GeV [4].

Prompt Final State	Cross Section (nb)
$\Upsilon(4S)$	1.110
$u\bar{u}(\gamma)$	1.61
$d\bar{d}(\gamma)$	0.40
$s\bar{s}(\gamma)$	0.38
$c\bar{c}(\gamma)$	1.30
$e^-e^+(\gamma)$	300
$\mu^-\mu^+(\gamma)$	1.148
$\tau^-\tau^+(\gamma)$	0.919
$\gamma\gamma(\gamma)$	4.99

The purpose of the Belle II detector is to detect and identify, on a collision-by-collision basis, the prompt final state that was produced from the SuperKEKB collision. This is achieved by reconstructing the decay chains of the prompt particles that were produced. For example for the $q\bar{q}$ final states listed in Table 2.5, almost immediately after production the quarks will form hadrons through processes such as the strong interaction decay shown earlier in Figure 2.4. Typically the hadrons produced will have very short lifetimes and will decay before reaching the detector components of Belle II. This decay chain will proceed until the particles produced have a lifetime to allow them to reach the components of the Belle II detector, which begins at 14 mm from the interaction point and extends to ~ 3.5 m [3]. Thus although there are numerous potential particles that can be produced, only a limited subset of particles have a lifetime that is long enough to allow them to potentially reach the components of the Belle II detector.

The long-lived particles that are most frequently emitted from collisions at SuperKEKB are listed in Table 2.6. To detect these particles, the Belle II detector is constructed from four types of sub-detectors [3]. The tracking (PXD, VXD, CDC) and charged particle identification detectors (TOP, ARICH) detect charged particles and measure their momentum and mass. The calorimeter and Kaon-Long/Muon (KLM) detector are designed to detect charged and neutral particles and measure their energy. The components of the Belle II detector that the long-lived particles

are typically detected by are indicated in Table 2.6 [3].

Table 2.6: The long-lived particles that are most frequently emitted from collisions at SuperKEKB and how they are typically detected at Belle II [3].

Particle	PXD/SVD/CDC	TOP/ARICH	Calorimeter	KLM
$e^{\pm}$	✓	✓	✓	
$\mu^{\pm}$	✓	✓	✓	✓
$\pi^{\pm}$	✓	✓	✓	✓
$K^{\pm}$	✓	✓	✓	✓
$p/\bar{p}$	✓	✓	✓	✓
γ			✓	
$n/\bar{n}$			✓	✓
K_L^0			✓	✓
ν				

For the particles listed in Table 2.6, the Belle II detector is designed to:

- Detect the presence of the particle.
- Measure the momentum vector of the particle.
- Determine the identity of the particle.

By accomplishing these tasks, energy and momentum conservation allows the decay chains of the collisions to be reconstructed and the prompt final state of the collision to be determined.

A primary research objective of this dissertation concerns the implementation of a new method of particle identification at Belle II through the use of CsI(Tl) pulse shape discrimination with the Belle II calorimeter. PSD at Belle II is a new experimental technique that can allow for interactions in the Belle II calorimeter to be identified as a hadronic or electromagnetic showers. The introduction of this experimental technique at Belle II will improve photon vs K_L^0 identification as well as areas of charged particle identification, such as $e^{\pm}$ vs $\pi^{\pm}$ and $\mu^{\pm}$ vs $\pi^{\pm}$ separation. Any Belle II measurement that uses calorimeter information and/or relies on identification of photons, π^0's, K_L^0, or neutrons can potentially benefit from PSD. The sections below detail some measurements that are planned to be done at Belle II and will potentially be improved by PSD.

2.2.1 Measurements of $\sin 2\beta$ ($\sin 2\phi_1$)

One of the main objectives of the past B-Factory experiments Belle and BaBar was to test the CKM matrix model described in Section 2.1.6. This is done by measuring CP violation in the B meson system through measurements of $\sin 2\beta$ where β is the CKM matrix angle discussed in Section 2.1.6 [13–16]. Similar to $K^0 - \bar{K}^0$ mixing discussed in Section 2.1.8, $B^0\bar{B}^0$ pairs produced by an Υ(4S) decay are predicted to undergo $B^0 - \bar{B}^0$ mixing and the B mesons are predicted to have CP violating decays [15, 16]. CP violation in the neutral B meson system was first measured in 2001 by the BaBar and Belle experiments and provided the experimental evidence to solidify the CKM model and led to the 2008 Nobel Prize in Physics awarded to Kobayashi and Maskawa for developing this model [3]. The current value of β is computed from measurements made by the BaBar, Belle and LHCb experiments and is given as $\beta = 22.5 \pm 0.9\,\text{deg}$ [4]. At Belle II, precision measurements of $\sin 2\beta$ through measurements of neutral B meson CP violation will be a continued focus [4]. With the additional statistical precision the significant Belle II dataset will provide, reduction of systematic errors will be even more critical at Belle II. Improving this measurement allows for the unitarity of the CKM matrix to be tested. If the CKM matrix if found to be non-unitary this would be evidence of physics beyond the Standard Model [4].

To measure $\sin 2\beta$, $B^0\bar{B}^0$ events are selected such that the decay of one of the B's, labelled B_{tag}, allows the flavour to be identified [13–16]. This can be done for example in a semi-leptonic B decay as the lepton charge can be used to determine if B_{tag} was a B^0 or $\bar{B}^0$ state at the time of the decay. By identifying the flavour of B_{tag}, the flavour of the second B, labelled B_{CP}, is known at the time of the B_{tag} decay. This is because, similar to the $\phi \rightarrow K^0_S K^0_L$ system, in the decay $\Upsilon(4S) \rightarrow B^0\bar{B}^0$ the two B mesons must have different flavour due to the spin statistics theorem [8, p.335]. To measure $\sin 2\beta$, B_{CP} is required to decay to a CP eigenstate [13, 14]. In the measurements of $\sin 2\beta$ made by Belle and BaBar, the B_{CP} decay modes included $B \rightarrow J/\psi K^0_S$, $B \rightarrow J/\psi K^0_L$, $B \rightarrow \psi(2S)K^0_S$ and $B \rightarrow \chi_{c1}K^0_S$ [14–16]. Of these modes, $B \rightarrow J/\psi K^0_L$ is the only mode where B_{CP} has $CP = +1$ [4, 16].

The objective of the analysis is to measure the distance between the decay vertices of B_{CP} and B_{tag}, given by Δz [13, 14]. From Δz, the time between the B_{CP} and B_{tag} decay, Δt, can be computed using $\Delta t = \Delta z / \beta\gamma c$ where $\beta\gamma$ is the boost of the collider [14]. The time dependent CP-violation asymmetry, $A_{CP}(\Delta t)$, is then given by equation 2.21 [13].

$$A_{CP}(\Delta t) = \frac{f_+(\Delta t) - f_-(\Delta t)}{f_+(\Delta t) + f_-(\Delta t)} = -\eta_f \sin 2\beta \sin \Delta m_B \Delta t \tag{2.21}$$

In equation 2.21, $f_+(f_-)$ is the decay rate of B_{CP} corresponding to $B_{tag} = B^0(\bar{B}^0)$, $\eta_f = \pm 1$ is the CP of B_{CP}, and Δm_B is the mass difference between the heavy and light weak interaction states that arise from $B^0/\bar{B}^0$ mixing [8, 13].

In this measurement of $\sin 2\beta$, the identification of B_{CP} is a critical component. In Table 2.7 the measured purity of several B_{CP} samples used in the most recent $\sin 2\beta$ measurements done by Belle and BaBar are listed [15, 16]. Shown in this table, the purity of the $J/\psi K_L^0$ sample is much lower than the B_{CP} modes that have a K_S^0. This low purity arises from the difficultly to identify K_L^0 clusters in the calorimeter and distinguish them from photons for example from $B \to J/\psi K_S^0(K_S^0 \to \pi^0\pi^0)$[17]. In the Belle measurement [14], of the background events where the K_L^0 was mis-identified by the calorimeter, $\sim 58\%$ of the events did not have a true K_L^0 in the event [14]. From the work in this dissertation to implement PSD at Belle II, the improved K_L^0 vs photon separation achieved from pulse shape discrimination is expected to substantially improve the K_L^0 purity in this measurement when competed at Belle II, leading to improved measurements of $\sin 2\beta$.

Table 2.7: Measured purity for several B_{CP} samples used in the most recent $\sin 2\beta$ ($\sin 2\phi_1$) measurements completed by the BaBar [15] and Belle [16] experiments.

Measurement	B_{CP} Mode	# of B_{tag}	Purity (%)
BaBar [15]	$J/\psi K_S^0(\pi^+\pi^-)$	5426	96
	$J/\psi K_S^0(\pi^0\pi^0)$	1324	87
	$\psi(2S)K_S^0$	861	87
	$\chi_{c1}K_S^0$	385	88
	$J/\psi K_L^0$	5813	56
Belle [16]	$J/\psi K_S^0$	12649	97
	$\psi(2S)(l^+l^-)K_S^0$	904	92
	$\psi(2S)(J/\psi\pi^+\pi^-)K_S^0$	1067	90
	$\chi_{c1}K_S^0$	940	86
	$J/\psi K_L^0$	10040	63

2.2.2 Measurements of $|V_{ub}|$

Precision measurement of the CKM matrix element $|V_{ub}|$ is another area where improved K_L^0 identification is expected to have a significant impact at Belle II. Measurements of $|V_{ub}|$ are important to test the unitarity of the CKM matrix [2, 8].

At Belle and BaBar, one of the methods that was applied to measure $|V_{ub}|$ was through measuring the branching fraction of semi-leptonic B meson decays that have a $b \to u$ quark flavour transition [4]. These decays can occur through the Feynman diagram in Figure 2.10 where $l = e$ or μ and X_u is a hadron containing a u quark [4].

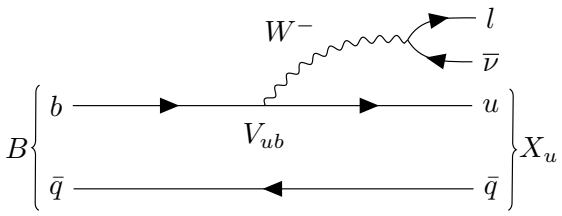

Figure 2.10: A lowest order Feynman diagram for a B meson decay involving a $b \to u$ quark flavour transition.

A challenge in measuring $|V_{ub}|$ with this method however is there is a large background from $B \to X_c l \nu_l$ decays where X_c is a hadron containing a charm quark [2, 4]. $B \to X_c l \nu_l$ decays proceed by a $b \to c$ transition which is CKM-favoured relative to $b \to u$ and thus occurs at much higher rates [2, 4]. Frequently the X_c will decay to a final state that includes a $K^{\pm}$, K_S^0 or K_L^0 [4]. In the case of a $K^{\pm}$ and K_S^0, tracking detectors can be used to apply vetos and reject the $B \to X_c l \nu$ background [4]. For K_L^0 however vetos were rarely applied in past analyses partly due to the difficulty of identifying the K_L^0 [4]. To mitigate K_L^0 backgrounds, past $|V_{ub}|$ were limited to kinematic ranges where $B \to X_c l \nu_l$ decays are suppressed [4, pg. 203]. From the Belle II Physics book [4, pg.200]:

> "A large fraction of the residual backgrounds is due to $B \to X_c l \nu$ events where the charm meson decays to a K_L^0. It is difficult to reconstruct K_L^0 mesons, and to model their hadronic interactions with the KLM and ECL. If precise measurements and reliable calibration of K_L^0 identification can be performed at Belle II via uses of high statistics control modes it would greatly aid in purifying this analysis in the high M_X region. Very few analyses to date have attempted to veto on the presence of K_L^0 in the

signal due to the large differences between data and MC simulation in hadronic interactions."

It can be seen that the introduction of PSD at Belle II to improve K_L^0 identification will allow for improvements in this measurement. In addition, the CsI(Tl) scintillation response simulations methods that are developed in this dissertation and integrated in GEANT4 simulation libraries can also potentially improve the data vs. MC agreement in the calorimeter quantities used in this measurement. This is because using PSD deficiencies in the modelling of hadronic interactions in CsI(Tl) by GEANT4 can be identified, potentially leading to improvements in GEANT4 simulation of hadronic interactions.

2.2.3 Applications in τ Physics Measurements

Shown earlier in Table 2.5, the cross section for $\tau\bar{\tau}$ production at SuperKEKB is comparable to the $\Upsilon(4S)$ production cross section [4]. This high production cross section and the clean e^+e^- collision environment will allow for studies of many rare τ decays modes, allowing for precision tests of the Standard Model.

The dominant τ decay modes are $\tau^\pm \to e^\pm\nu_e\nu_\tau$, $\mu^\pm\nu_\mu\nu_\tau$, $\pi^\pm\nu_\tau$, $\pi^\pm\pi^0\nu_\tau$ and $\pi^\pm\pi^0\pi^0\nu_\tau$, and together account for $\sim$ 80% of all τ decays [2]. The neutrino(s) present in τ decays makes τ's challenging to reconstruct as the neutrinos result in energy escaping the detector. The improvement in photon and π^0 identification that PSD will provide is expected to improve the purities of many τ selections. In addition, the improvements in charged particle identification, particularly in the areas of $e^\pm$ vs $\pi^\pm$ and $\mu^\pm$ vs $\pi^\pm$ identification can lead to improvements in τ selections. This is expected to be achieved in cases where the $\pi^\pm$ produces a hadronic shower in the calorimeter.

A specific example where PSD can have an impact on is the planned measurement of the rare decay $B_{sig} \to \tau\bar{\nu_\tau}$, where B_{sig} is the signal B meson candidate in the event [4]. The projected 50 ab^{-1} dataset to be collected by Belle II is predicted to enable the first 5σ measurement of the branching fraction of this decay [4, p. 158]. Evidence of this decay was observed at Belle at the 3.0σ level [18]. New physics models involving additional Higgs bosons are predicted to impact the branching ratio for this decay [18]. In addition this rare decay allows for the CKM element $|V_{ub}|$ to be measured [18].

In the measurement made by Belle, the variable E_{extra} was used to suppress backgrounds [18]. E_{extra} is defined as the sum of the energy of all neutral calorimeter clusters in the event that were not associated with the B_{sig} or B_{tag} [18]. In this measurement, one of the dominant backgrounds in the signal region is from a B meson decaying semi-leptonically to a D meson followed by the D meson decaying to a final state that includes a K_L^0 [18]. The application of pulse shape discrimination can potentially improve this measurement in multiple ways. The improved K_L^0 and π^0 identification will provide an effective method to apply a K_L^0 veto. In addition, as PSD can identify if a calorimeter cluster is an hadronic or electromagnetic shower, PSD could be used to deconstruct E_{extra} into hadronic and electromagnetic components such as, $E_{\text{extra}} = E_{\text{extra}}^{\text{hadronic}} + E_{\text{extra}}^{\text{EM}}$ where $E_{\text{extra}}^{\text{hadronic}}$ is the extra energy in the event from hadronic showers and $E_{\text{extra}}^{\text{EM}}$ is the extra energy from electromagnetic showers. These new variables can potentially improve the background suppression in all Belle II measurements that have energy that escapes the detector through neutrinos.

Chapter 3

Particle Interactions in Calorimeters

The main objective of the calorimeter sub-detector of a particle detector is to measure the energy of electromagnetically and strongly interacting particles [2]. Calorimeters are typically the densest sub-detectors of a particle detector as the abundance of material increases the probability for an interaction to occur and for the total energy of a particle to be absorbed [2]. For this reason, calorimeters are placed after tracking detectors. Described in Chapter 4, the Belle II calorimeter is constructed from CsI(Tl) scintillator crystals. When a particle interacts in the calorimeter it forms a calorimeter cluster which is defined to be a spatially connected region of the calorimeter where the adjacent crystals each have a significant amount of energy deposited. The types of calorimeter clusters typically formed at Belle II can be classified as either an ionization cluster, electromagnetic shower or an hadronic shower.

3.0.1 Ionization Clusters

Ionization clusters are formed when a heavy ($>> m_e$) charged particle enters the calorimeter and deposits energy primarily through ionization. The process of ionization is illustrated by the diagram in Figure 3.1 and occurs when a charged particle interacts electromagnetically by transferring energy to atomic electrons [2].

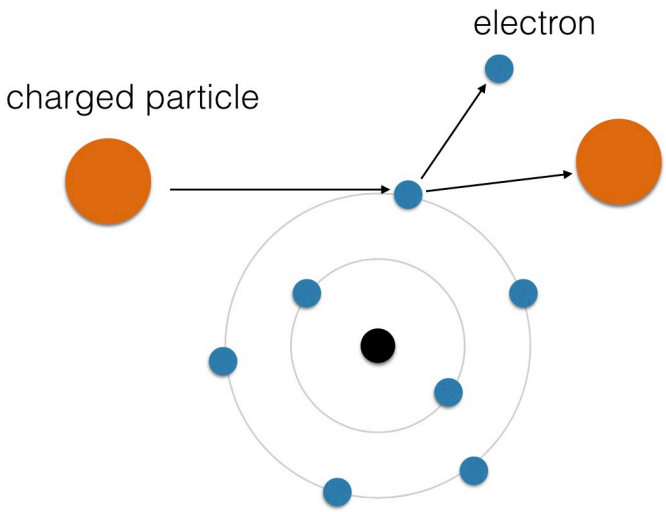

Figure 3.1: Schematic diagram for ionization.

The mean energy loss per unit length-density, $d\mathrm{E}/dx$, for a heavy charged particle passing through a material is given by the Bethe-Bloch equation, defined in equation 3.1 [2].

$$\left\langle -\frac{dE}{dx} \right\rangle = Kz^2 \frac{Z}{A} \frac{1}{\beta^2} \left[\frac{1}{2} \ln \frac{2m_e c^2 \beta^2 \gamma^2 W_{max}}{I^2} - \beta^2 - \frac{\delta(\beta\gamma)}{2} \right] \tag{3.1}$$

In equation 3.1,

$K = 4\pi N_A r_e^2 m_e c^2 \approx 0.307075$ MeV mol^{-1}cm^{-2}

$N_A =$ Avogadro's number.

$r_e =$ classical electron radius.

$m_e =$ electron mass

$c =$ speed of light

$z =$ charge of the incident particle.

$Z =$ atomic number of the material.

$A =$ atomic mass number of the material.

$\beta = v/c =$ speed of the incident particle.

$\beta\gamma = p/Mc$

$p =$ momentum of the incident particle.

$M =$ mass of the incident particle.

$I =$ mean excitation energy of the material.

$\delta(\beta\gamma) =$ density effect correction, important at large $\beta\gamma$ [2].

$W_{\max} =$ maximum energy transfer in a single collision [2], defined in equation 3.2.

$$W_{\max} = \frac{2m_e c^2 \beta^2 \gamma^2}{1 + 2\gamma m_e/M + (m_e/M)^2} \tag{3.2}$$

Equation 3.1 is valid for the range $0.1 < \beta\gamma < 1000$ [2]. In Figure 3.2, equation 3.1 is evaluated, using the properties of CsI(Tl), as a function of momentum for the some of the heavy charged particles that are frequently detected in the Belle II calorimeter. For CsI(Tl), $I = 553.1$ eV and $< Z/A >= 0.41569$ [2]. The parameterization for $\delta(\beta\gamma)$ used is the Sternheimer parametrization from reference [2] [19] and defined in equation 3.3 [2] [19].

$$\delta(\beta\gamma) = \begin{cases} 2(\ln 10)x - \bar{C}, & \text{if } x \geq x_1 \\ 2(\ln 10)x - \bar{C} + a(x_1 - x)^k, & \text{if } x_0 \leq x < x_1 \\ 0, & \text{if } x < x_0 \text{ (nonconductors)} \\ \delta_0 10^{2(x-x_0)}, & \text{if } x < x_0 \text{ (conductors)} \end{cases} \tag{3.3}$$

where $x = \log_{10}(p/Mc)$ and for CsI [19]:

$$\begin{aligned} x_0 &= 0.0395 \\ x_1 &= 3.3353 \\ a &= 0.25381 \\ k &= 2.6657 \\ C &= 6.2807 \end{aligned}$$

Figure 3.2 demonstrates several ways that the mean energy loss by ionization depends on a particles properties. At low momentum, particles with larger mass will have a higher $d\mathrm{E}/dx$. This is expected due to the $1/\beta^2$ factor in equation 3.1. Also seen in Figure 3.2, as a particles slows down, the energy loss from ionization rapidly increases. Thus when a particle ionizing in a material begins to slow down to this region of rapid rise in $d\mathrm{E}/dx$, a positive feedback loop begins resulting in the particle to rapidly deposit its remaining energy in a short distance [6, p.91]. This phenomena is called the Bragg curve/peak as the spatial distribution of the energy deposited peaks at the end of the particles track, just before the particle stops [6, p.91]. Equation 3.1 also shows that the ionization $d\mathrm{E}/dx$ is proportional to the charge of the particle. This means a highly charged particle, such as an α particle which is a helium nucleus and has charge $2e$, will be highly ionizing relative to a proton or pion in the lower momentum region.

Shown in Figure 3.2, at higher momenta the ionization $d\mathrm{E}/dx$ of a particle decreases then begins to plateau at a relatively small value. Particles with momentum in this region of relatively small and constant $d\mathrm{E}/dx$ can be highly penetrating in materials. This is because if the particle does not initiate another interaction in the

material, such as a strong interaction, the particle will ionize with a relatively constant and small $d\mathrm{E}/dx$ through the material. Frequently at Belle II higher momentum heavy charged particles will produce an ionization cluster when the particle ionizes through the calorimeter and escapes to the KLM detector. The energy deposit in an ionization cluster will be spatially contained in a small localized area and the total energy of the cluster will be ~ 200 MeV as the Belle II calorimeter is 30 cm thick [4].

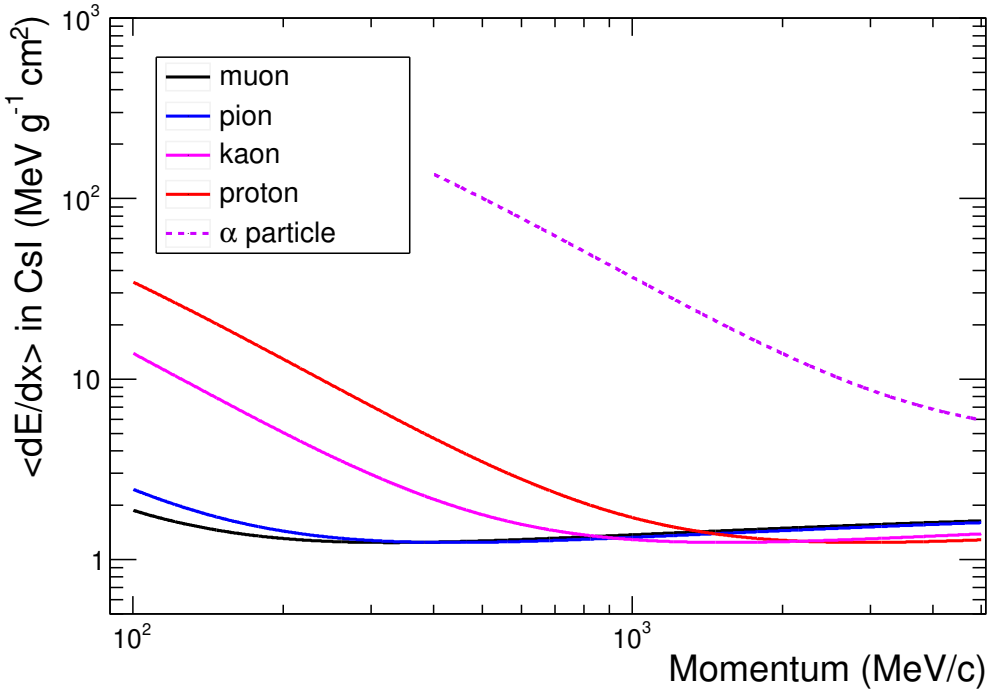

Figure 3.2: $d\mathrm{E}/dx$ in CsI(Tl) computed for $\beta\gamma > 0.1$ using equation 3.1 for the heavy charged particles that frequently interact in the Belle II calorimeter.

3.0.2 Electron Interactions

In addition to ionization, charged particles traversing a material can also lose energy by electromagnetically interacting with an atomic nucleus and emitting photons through bremsstrahlung [2]. This process is illustrated in Figure 3.3 which shows a charged particle interacting with the electric field of a nucleus and radiating a photon. One of the lowest order Feyman diagrams for bremsstrahlung is also shown in Figure 3.3 [6, p.92].

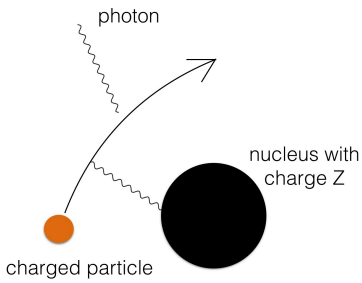

(a)

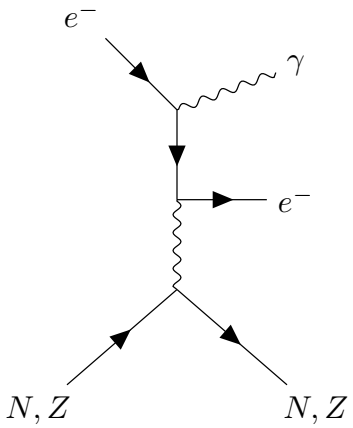

(b)

Figure 3.3: a) Schematic diagram for a charged particle emitting a bremsstrahlung photon by interacting with an atomic nucleus, N, of charge Z. b) One of the lowest order Feynman diagrams for bremsstrahlung [6, p.92].

Energy loss from bremsstrahlung only dominates over ionization energy losses when a particle is highly relativistic [2] [6, p.92]. The energy where a particle's dominant form of energy loss in a material changes from ionization to bremsstrahlung is called the critical energy, E_c [2]. For the majority of the charged particles listed in Table 2.6, E_c in CsI(Tl) is outside the energy range of SuperKEKB. For example in CsI(Tl), muons have a critical energy of $E_c^{\mathrm{CsI},\mu}$ =198 GeV [2]. Electrons however have $E_c^{\mathrm{CsI,electron}} = 11.17$ MeV [2] and thus bremsstrahlung will be the dominant method of energy loss for energetic electrons interacting in the Belle II calorimeter.

The characteristic distance an electron will travel in a material before its energy is reduced to $1/e$ of its initial energy through emission of bremsstrahlung radiation is called the radiation length, X_0 [2] [6, p.92]. For high energy electrons, the energy loss by bremsstrahlung is proportional to the electron's energy and given by equation 3.4 [2] [6, p.92].

$$\left\langle -\frac{dE}{dx} \right\rangle_{\text{bremsstrahlung}} \approx \frac{E}{X_0} \tag{3.4}$$

CsI(Tl) has a radiation length of 1.860 cm [2] and thus when an electron enters the Belle II calorimeter, only a minimal amount of energy will be deposited through ionization before the electron is likely to emit a photon through bremsstrahlung.

3.0.3 Photon Interactions

In the energy range 1 keV−100 GeV the dominant material interaction for photons varies from pair production to Compton scattering to the photoelectric effect depending on the photon energy [2],[9, p. 9-18]. For photons with energy above ~ 5 MeV, the dominant interaction in a material is pair production [9, p. 9-18].

Illustrated in Figure 3.4 is one of the lowest order Feynman diagrams for pair production. This diagram shows that a photon can interact electromagnetically with an atomic nucleus (N) and transforms into an electron position pair [6, p. 94].

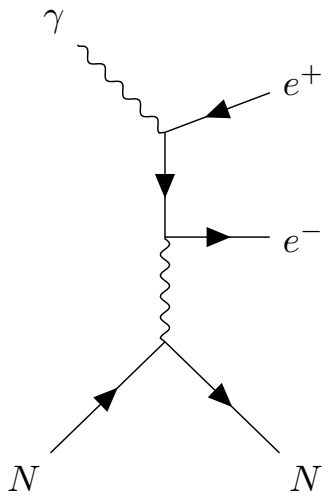

Figure 3.4: One of the lowest order Feynman diagrams for photon pair production through the interaction of the photon with an atomic nucleus, N, of charge Z.[6, p.94].

Comparing the Feynman diagrams for pair production and bremsstrahlung, shown in Figures 3.4 and 3.3, the diagrams are similar with only the top fermion and photon lines interchanged. This leads to the characteristic distance that an energetic photon will travel in a material before undergoing pair production to be given by $\frac{9}{7}X_0$ [2, 9].

In the energy range $\sim 0.5 - 5$ MeV, the cross section for photons to undergo pair

production rapidly decreases due to energy conservation and Compton scattering dominates the material interaction cross-section [2] [9, p.9-19]. Compton scattering describes when a photon loses energy by transferring energy to an atomic electron causing the emission of the electron. Below ~ 1 MeV, the cross section for the photon to undergo the photoelectric effect rapidly increases and dominates the material interaction cross section [2] [9, p.9-18]. The photoelectric effect describes when a photon is absorbed by an atom leading to the emission of an atomic electron [9, p.9-18].

3.0.4 Electromagnetic Showers

An electromagnetic shower describes the cascade of electrons, positrons and photons that forms when a high energy (> 10 MeV) photon, electron or positron enters a dense material such as the CsI(Tl) calorimeter at Belle II [9, p.9-36]. A schematic showing the development of an electromagnetic shower is illustrated in Figure 3.5.

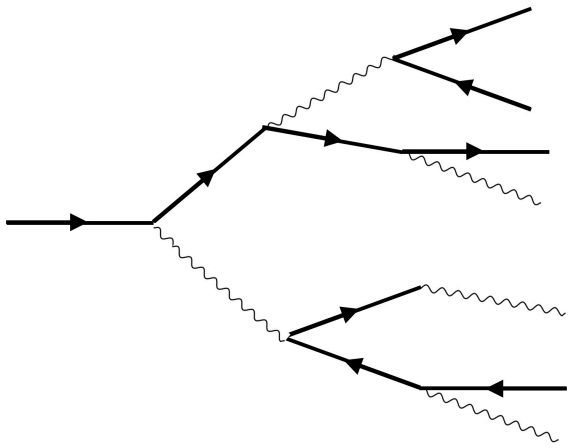

Figure 3.5: Schematic showing the development of an electromagnetic shower. In this figure solid lines pointing left-to-right represent electrons and solid lines pointing right-to-left represent positrons.

In Figure 3.5 an energetic electron initially enters the dense material and begins to ionize. At a distance of $\sim X_0$ the electron then emits an energetic photon through bremsstrahlung. The energetic photon will then be likely to undergo pair production after traversing $\sim X_0$ of material, resulting in the production of an additional electron and positron. The development of the electromagnetic shower then proceeds as illustrated in Figure 3.5 showing alternating stages of electrons and positions emitting bremsstrahlung photons, and photons undergoing pair production. For each radiation

length of material that the electromagnetic shower penetrates, the average energy of the particles decreases and the multiplicity of secondary particles doubles. The electromagnetic shower proceeds until the energy of the photons produced is below the pair production threshold and the electrons reach the critical energy of the material [9, 9-37].

The depth of an electromagnetic shower, d_{EM}, is characterised by the quantity shown in equation 3.5 which is derived by assuming the multiplicity of secondary particles doubles every radiation length until reaching the critical energy [9, p.9-37]

$$d_{EM} = X_0 \ln(E_0/E_c)/\ln(2) \tag{3.5}$$

After d_{EM}, the propagation of energy deposited in the material from the shower decays exponentially with distance [9, p.9-37]. The development of an electromagnetic shower in the direction perpendicular to the initial momentum of the primary particle is characterized by the Moliere radius, R_M [9, p.9-38][2]. R_M is defined such that 90% of the energy of the electromagnetic shower is contained in a cylinder of radius $3.5R_M$ [9, p.9-38]. For CsI(Tl), R_M is equal to 3.531 cm [2].

3.0.5 Hadronic Shower

The quark content of hadrons allows them to undergo strong interactions with the protons and neutrons in materials. This process is referred to as a hadronic interaction. Analogous to the radiation length for bremsstrahlung, the nuclear interaction length, λ, gives the characteristic length that a hadron will traverse in a material before a hadronic interaction occurs [9, p.9-38]. For CsI(Tl), $\lambda^{\mathrm{CsI}} = 38.04$ cm [2]. When a hadron interacts with a proton or neutron in an atomic nucleus, a hadronic shower is produced.

An schematic illustrating the development of a hadronic shower is shown in Figure 3.6. Compared to an electromagnetic shower, hadronic showers are very complex as the secondary interactions of the shower highly depend on the initial hadronic interaction, which depends on the primary particle type and energy. Figure 3.6 illustrates some of the potential interactions that can occur in a typical hadronic shower [10, 20, 21].

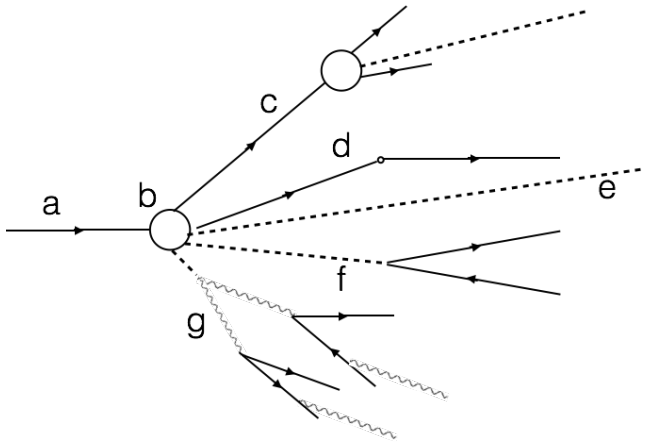

Figure 3.6: Diagram illustrating some of the potential interactions that can occur in the development of a hadronic shower. Diagram is not to scale. Figure is inspired by reference [20].

Region a in Figure 3.6 shows a charged hadron initially ionizing in the material before the primary hadronic interaction occurs at point b. When this happens, the hadron strongly interacts with the protons and/or neutrons in the nucleus. Depending on the energy and type of the primary hadron, this interaction can produce one or more energetic secondary hadrons such as pions, kaons, neutrons, protons, etc [10, 20, 21]. The energetic particles emitted from this interaction are typically produced with momentum at a small angle to the initial momentum of the primary hadron [20]. Cases $c - g$ illustrated in Figure 3.6 show some potential outcomes that can occur during the development of an hadronic shower [10, 20, 21].

- Case c: An energetic secondary hadron is emitted from the hadronic interaction. This charged hadron, then ionizes away from primary interaction. After a distance of $\sim \lambda$ the hadron initiates another hadronic interaction.

- Case d: An energetic hadron is emitted then ionizes away and eventually has an elastic collision with a nucleus. After this collision the hadron continues to ionize away from the primary interaction.

- Case e: A long-lived neutral hadron such as a neutron or K_L^0 is emitted and travels far from the primary interaction without interacting in the material.

The neutral hadron will not leave an ionization trail. If it eventually interacts far from the primary interaction, this will form a calorimeter cluster that will appear to be independent from the primary hadronic shower and potentially will be mis-identified as an independent calorimeter cluster. These mis-identified clusters are called hadronic split-offs.

- Case f: A short-lived neutral hadron, such as a K_S^0, is emitted and travels a short distance before decaying to charged particles.

- Case g: A π^0 is emitted then almost immediately decays as $\pi^0 \rightarrow \gamma\gamma$, forming an electromagnetic shower.

Depending on the primary particle type and energy, several of these interactions can occur in a single hadronic shower [10, 20, 21].

In the hadronic interaction with the nucleus shown in region b, energy will be transferred to the nucleus allowing the nucleus to enter an excited state [20]. After this occurs, the nucleus will de-excite through nuclear evaporations or fissions [20]. In nuclear evaporation the nucleus de-excites by isotropically emitting numerous low energy ($<\sim$ 10 MeV) hadrons such as neutrons, protons, alpha particles and fission fragments etc, in addition to photons [20]. The low energy hadrons emitted in this process will be highly ionizing due to their high mass and electric charge and will thus deposit their energy near the location of the primary interaction. Fission occurs when the configuration of protons and neutrons that comprise the nucleus is unstable. In this process multiple neutrons with energy $\sim$ 1 MeV can be emitted and the nucleus will break apart into into nuclear fragments [9, 5-16].

In general, the energy lost by the primary particle in an hadronic shower can be classified as electromagnetic, invisible or hadronic. Electromagnetic energy refers to the energy that is absorbed from the photons, electrons and $\pi^0 \rightarrow \gamma\gamma$ produced in the hadronic shower [2]. The invisible component refers to the energy that is not absorbed in the material and is lost in the form of binding energies and leakage from neutrons or, neutrinos produced from decays, that will escape the cluster [2]. The hadronic component is the energy deposited by ionization from charged hadrons produced in the shower [2]. Due to the invisible component, the energy absorbed by the calorimeter in an hadronic shower is typically not equal to the energy released by the primary particle and thus the calorimeter cluster energy cannot be used to precisely infer the energy of the primary hadron without applying advanced calibration procedures [2].

3.0.6 Scintillation Emission in CsI(Tl)

The above sections describe how a particle can transfer energy to a material. To measure the magnitude of energy absorbed in a material a method is required that allows an electrical signal to be produced which is a function of the energy deposited. In the case of CsI(Tl), this is achieved by scintillation light emission and detection, because the scintillation light intensity is proportional to the energy deposited [2][22].

Scintillators are materials that emit light in the visible spectrum after absorbing energy [2][22]. Scintillators are classified as organic or inorganic. Organic scintillators are typically made from hydrocarbons and produce scintillation light from the molecules of the material becoming excited by ionizing radiation, followed by de-exciting through the emission scintillation photons [2] [22, p.220]. Inorganic scintillators, such as CsI(Tl), are made from crystals where the crystal lattice has a band gap structure. In general inorganic scintillators have higher densities than organic scintillators and thus are used for constructing electromagnetic calorimeters in particle detectors [2][22].

The process by which an inorganic scintillator produces scintillation light is illustrated in the diagram shown in Figure 3.7 [23][22, p.232]. The initial part of this diagram depicts electrons being excited from the valence band to the conduction band by absorbing the energy deposited by an incident particle [23]. This process leaves positively charged holes in the valence band [23]. In a single energy deposit, many electron-hole pairs are formed and in some cases an electron in the conduction band can become bound to a hole in the valence band forming a bound state called an exciton [22, p.233]. After the electrons, holes and excitons are produced, they can migrate in the crystal lattice away from their production site [23][22, p.233]. In an inorganic scintillator where no dopants are present, the scintillation emission is produced from the annihilation of the excitons which can produce a photon. In this case however, the energy of the photon will be near the band gap energy and thus it is likely that the photon will be re-absorbed before escaping the crystal [22, p.232-233]. To increase the yield of light that escapes the crystal, inorganic scintillators such as CsI(Tl), which is CsI doped with thallium, are doped to allow for luminescence centres to be formed in the crystal lattice [2] [22, p.232]. Shown in Figure 3.7, the luminescence centres allow for energy states in the forbidden region between the conduction and valence band. When electrons, holes and/or excitons excite a luminescence centres, the scintillation photon emitted from the de-excitation will be less likely to be re-absorbed by the

crystal because the photon energy is smaller than the band gap energy [2] [22, p.232].

To convert the scintillation light into an electrical signal, scintillators are instrumented with light detectors such as photomultiplier tubes (PMT) or photodiodes. In the case of a PMT, a material called a photocathode is used to produce electrons from the absorption of the scintillation photons. The electrons are then accelerated by an electric field and made to collide with components called dynodes which allow for electron multiplication. After several dynode stages the small number of electrons initially emitted from the photocathode can be amplified to produce a current that can be easily measured [6, p.104] [2]. For a photodiode, a $p-n$ junction is placed under a reverse voltage bias such that when scintillation light interacts with the junction electron-hole pairs are produced allowing for an electrical signal to be generated in the circuit [2].

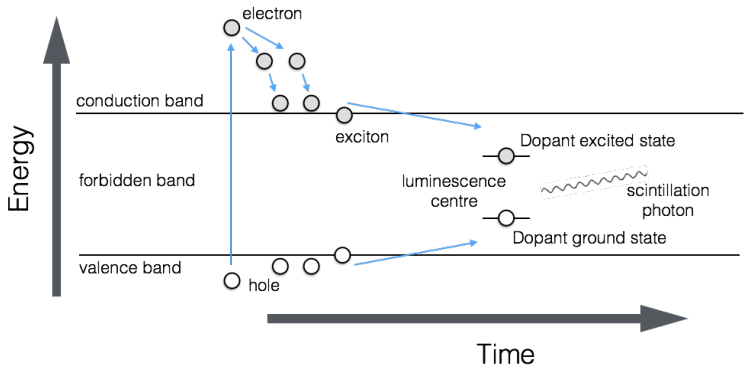

Figure 3.7: Illustration of scintillation in an inorganic scintillator. Figure inspired from reference [23].

The scintillation light emitted by a scintillator as a function of time, $L(t)$, can be described by the sum of multiple exponentials as shown in equation 3.6 where L_{Total} is the total scintillation light emitted, L_i is the relative intensity of light emitted in the i^{th} scintillation component and τ_i is the decay time of the i^{th} component [22].

$$L(t) = L_{\text{Total}} \sum \frac{L_i}{\tau_i} \exp -t/\tau_i \tag{3.6}$$

In CsI(Tl), the scintillation parameters in equation 3.6 depend on the particle type.

For photons there are two primary decay components with lifetimes of $\sim 0.8\mu$s and $\sim 5\mu$s [24] [22, p.238] [25]. In Chapter 5 [25] $L(t)$ will be studied and discussed in detail for hadronic energy deposits which are shown to produce an additional scintillation component with lifetime of $0.63 \pm 0.01\mu$s. Particles with higher ionization $d\mathrm{E}/dx$, such as protons or alpha particles, are observed to emit faster scintillation emission relative to energy deposits from energetic electrons [24]. In addition, energy deposits from highly ionizing particles are observed to have a non-linear scintillation efficiency such that the scintillation light yield can be higher or lower than the light yield emitted from the equivalent energy deposit from an electron [26]. The mechanisms that produce these phenomena are beyond the scope of this work and are active areas of scintillator research [27, 28].

3.1 Hadronic Shower Identification through Pulse Shape Discrimination

The central objective of work completed in this dissertation can now described. Indicated previously in Table 2.6, the Belle II calorimeter is central to detecting all of the electromagnetically and strongly interacting long-lived particles produced in collisions at Belle II. For photons and K_L^0 in particular, the calorimeter can, in many cases, be the only detector where these particles are measured. Photons interacting in the calorimeter will generate an electromagnetic shower and the energy deposit will span a region of a couple Moliere radii. A K_L^0 interacting in the calorimeter will produce a hadronic shower. Described in Section 3.0.5, the details of this interaction will vary on a cases by case basis. At the past e^+e^- experiments, Belle and BaBar, CsI(Tl) calorimeters were used and the information recorded for each energy deposit was limited to the magnitude, location and time of the energy deposit in the CsI(Tl) crystals. Despite the underlying interactions occurring in an electromagnetic and hadronic shower being very different, with only this information a calorimeter cluster produced by a K_L^0 and photon can frequently appear to be very similar from the perspective of the detector. The detector signature for both of these particles can appear just as a spatially connected region of energy deposited in the calorimeter. To identify K_L^0 from photons, Belle and BaBar used shower shape variables that characterize how the energy of the cluster is spatial distributed. The shower shape variables employed at Belle and BaBar however demonstrated limited performance [4] and of-

ten analyses were designed to not rely on K_L^0 identification in the electromagnetic calorimeter. This is despite K_L^0 detection being critical component for many physics measurements, as expanded on in Section 2.2.

As mentioned in Section 3.0.6, the scintillation response of CsI(Tl) is empirically known to depend on the ionization $d\mathrm{E}/dx$ of the particles depositing energy in the crystal [24]. This allows for the application of pulse shape discrimination which refers to the ability to identify the type of particle depositing energy based on the pulse shape of the scintillation emission [22]. The central aim of this work is to explore whether pulse shape discrimination will be a feasible method for improving particle identification at Belle II. Pulse shape discrimination is predicted to be an effective technique for hadronic shower identification because the protons and α particles that are frequently produced in hadronic showers will result in energy deposits that have a faster scintillation emission relative to energy deposits in electromagnetic showers, consisting of only secondary electrons, positrons and photons.

The research objectives of this work are as follows:

- Study the CsI(Tl) scintillation response to the long-lived particles emitted in SuperKEKB collisions in the energy range of $0.1 - 5$ GeV, and evaluate whether pulse shape discrimination is an effective tool for identifying electromagnetic vs hadronic showers.

- Develop simulation methods that can be integrated with GEANT4 particle interactions in matter simulation libraries [5] and allow for precise simulations of the particle dependent CsI(Tl) scintillation response as measured in data. In addition these simulation methods should be integrated into the Belle II simulation framework.

- Implement pulse shape discrimination at the Belle II experiment and evaluate the performance in noise conditions created by SuperKEKB accelerator induced backgrounds.

- Use Belle II collision data to evaluate the performance of pulse shape discrimination at the Belle II experiment for improving K_L^0 vs photon identification and compare with shower shape methods.

- Use Belle II collision data to evaluate the CsI(Tl) scintillation response simulation methods that are developed as a part of this work.

Chapter 4

The Belle II Experiment

Belle II is a B-Factory experiment located at the SuperKEKB e^+e^- collider and is the successor experiment to the past Belle and BaBar B-Factories. Belle II aims to accumulate 50 ab^{-1} of e^+e^- collision data over the experiments lifetime. This dataset will be $\sim 50\times$ the size of the datasets individually collected by BaBar and Belle, and will be used to search for physics beyond the Standard Model through searches for rare and forbidden processes, as well as, precision measurements that test Standard Model predictions [4].

4.1 The SuperKEKB Collider

SuperKEKB is an asymmetric e^+e^- collider, designed to collide 7 GeV/c electrons with 4 GeV/c positrons, corresponding to a total collision energy in the centre-of-mass (CMS) frame of 10.58 GeV. This energy is just above the threshold to produce a strongly bound $b\bar{b}$ quark resonance called the $\Upsilon(4S)$. The $\Upsilon(4S)$ has a significant branching fraction (>96% [2]) to decay to $B^0\bar{B}^0$ or B^+B^- pairs. Due to the large amount of B mesons produced, Belle II is referred to as a B-Factory [4].

The B meson pairs produced in $\Upsilon(4S)$ decays exist in an entangled state which allows a variety of measurements to be conducted that test the flavour sector of the Standard Model [8]. This includes precision tests of the CKM quark mixing model and measurements of CP violation by B mesons. Due to the asymmetric collision energies of SuperKEKB, the $\Upsilon(4S)$ is produced with a boost of $\beta\gamma \approx 0.284$ [4]. The boost increases the separation distance between the decay points of the B mesons, allowing for the potential to distinguish the location of the individual B decay vertices.

Described previously in Chapter 2 Section 2.2.1, by measuring the distance between the B decay vertices, Belle II can perform measurements of time dependent CP violation in the B meson system [4].

Belle II is a luminosity frontier experiment which means the sensitivity of the experiment to new physics primarily comes from precision measurements completed on large datasets. The SuperKEKB collider is designed to achieve an unprecedented instantaneous luminosity of 8×10^{35} cm^{-2}s^{-1}, allowing for a projected 50 ab^{-1} total dataset to be integrated over the lifetime of Belle II. To achieve this instantaneous luminosity, the past KEKB collider, used at the original Belle experiment, is upgraded to SuperKEKB. This upgrade increases the beam currents and reduces the size of the beams at the interaction point to produce an increase in instantaneous luminosity. In particular, the instantaneous luminosity at SuperKEKB is given by equation 4.1 [29, 30].

$$L = \frac{N_- N_+ n_b f_0}{4\pi\sigma_z \phi_x \sqrt{\epsilon_y \beta_y^*}} \tag{4.1}$$

In equation 4.1,

$N_\pm$ is the number of particles per bunch for the beam with the corresponding charge.
n_b is the number of bunches.
f_0 is the revolution frequency.
σ_z is the bunch length.
ϕ_x is the horizontal crossing angle.
ϵ_y is the vertical emittance.
β_y^* is the vertical beta function at the interaction point.

Tables 4.1 summarizes the beam parameters planned to be achieved by SuperKEKB and compares these values to the values achieved by KEKB. SuperKEKB aims to achieve a $\sim \times 40$ increase in instantaneous luminosity relative to KEKB by reducing the beam size at the interaction point as well as increasing the number of bunches and particles per bunch [29, 30].

Table 4.1: Accelerator parameters planned for SuperKEKB compared to the values achieved by the KEKB collider [29, 30].

Parameter	SuperKEKB		KEKB	
	e^+	e^-	e^+	e^-
Beam Energy (GeV)	4.0	7.007	3.5	8.0
N (10^{10})	9.04	6.53	6.47	4.72
σ_z (mm)	6	5	7	7
β_y^* (mm)	0.27	0.30	5.9	5.9
ϵ_y (pm)	8.64	12.9	150	150
Beam Current (A)	3.6	2.6	1.64	1.19
$2\phi_x$ (mrad)	83		22	
n_b	2500		1584	
f_0 (kHz)	99.47		99.47	
L ($\mathrm{cm}^{-2}\mathrm{s}^{-1}$)	8×10^{35}		2.108×10^{34}	
$\int L$ (ab^{-1})	50		1.041	

Accompanying the increase in instantaneous luminosity, a significant increase in beam induced backgrounds will be present at SuperKEKB and will irradiate the Belle II detector. The main contributions to the beam backgrounds at SuperKEKB arise from the following processes [31]:

- Touschek scattering: Intra-bunch Columb scattering of the electron/positions in a single beam bunch. Touschek scattering can cause particles to be scattered out of a beam bunch and into the accelerator components and/or Belle II detector components [31].

- Beam Gas Scattering: Scattering of beam particles with gas molecules in the beam pipe [31].

- Synchrotron Radiation: Photons emitted by beam particles when interacting in the magnetic field of the accelerator [31].

- Radiative Bhabha scattering: Radiative Bhabha scattering corresponds to the process $e^+e^- \to e^+e^-(\gamma)$ and dominates the e^+e^- cross section at SuperKEKB. The radiated photon emitted in this process can interact with accelerator and/or

Belle II detector components producing showers of secondary particles that irradiate the Belle II detector [31].

From these processes the Belle II detector components will accumulate a significant radiation dose from photons and neutrons, relative to the Belle detector [31]. This produces a challenging environment for the Belle II detector to operate in, relative to the BaBar and Belle experiments, and a major focus of the Belle II detector design is to maintain high performance while coping with the increased noise and degradation from beam backgrounds [3].

4.2 The Belle II Detector

Located at the collision point of SuperKEKB, the function of the Belle II detector is to reconstruct and identify the particles emitted in the decay chains that are initiated by SuperKEKB collisions. The Belle II detector achieves this through a combination of sub-detectors that are optimized for specific functions, such as, charged particle detection, energy measurements and particle identification. The layout of Belle II sub-detectors is illustrated by the top-view schematic shown in Figure 4.1 [4, pp. 37]. The operating principles, functions and design performance for each of the Belle II sub-detectors is described in the following sections.

4.2.1 Pixel Detector

The Pixel Detector (PXD) is the first sub-detector radially outward from the interaction point. The PXD is a tracking detector, designed to measure the spatial location of charged particles emitted from the interaction point. The PXD accomplishes this by enclosing the interaction point with a cylindrical assembly of rectangular shaped modules that contain arrays of DEPleted Field Effect Transistors (DEPFET) pixel detectors [3].

DEPFET sensors detect the presence of charged particles by performing as a switch which is activated by a charged particle ionizing through the sensor. The active material of the DEPFET is a depleted bulk region placed under a voltage bias. When a charged particle ionizes through this region, electron-hole pairs are produced and the electric field generated by the voltage bias forces charge to accumulate at the readout contacts attached to the ends of the bulk. The charge activates a transistor switch, signalling a charged particle has crossed the pixel volume [3, 32].

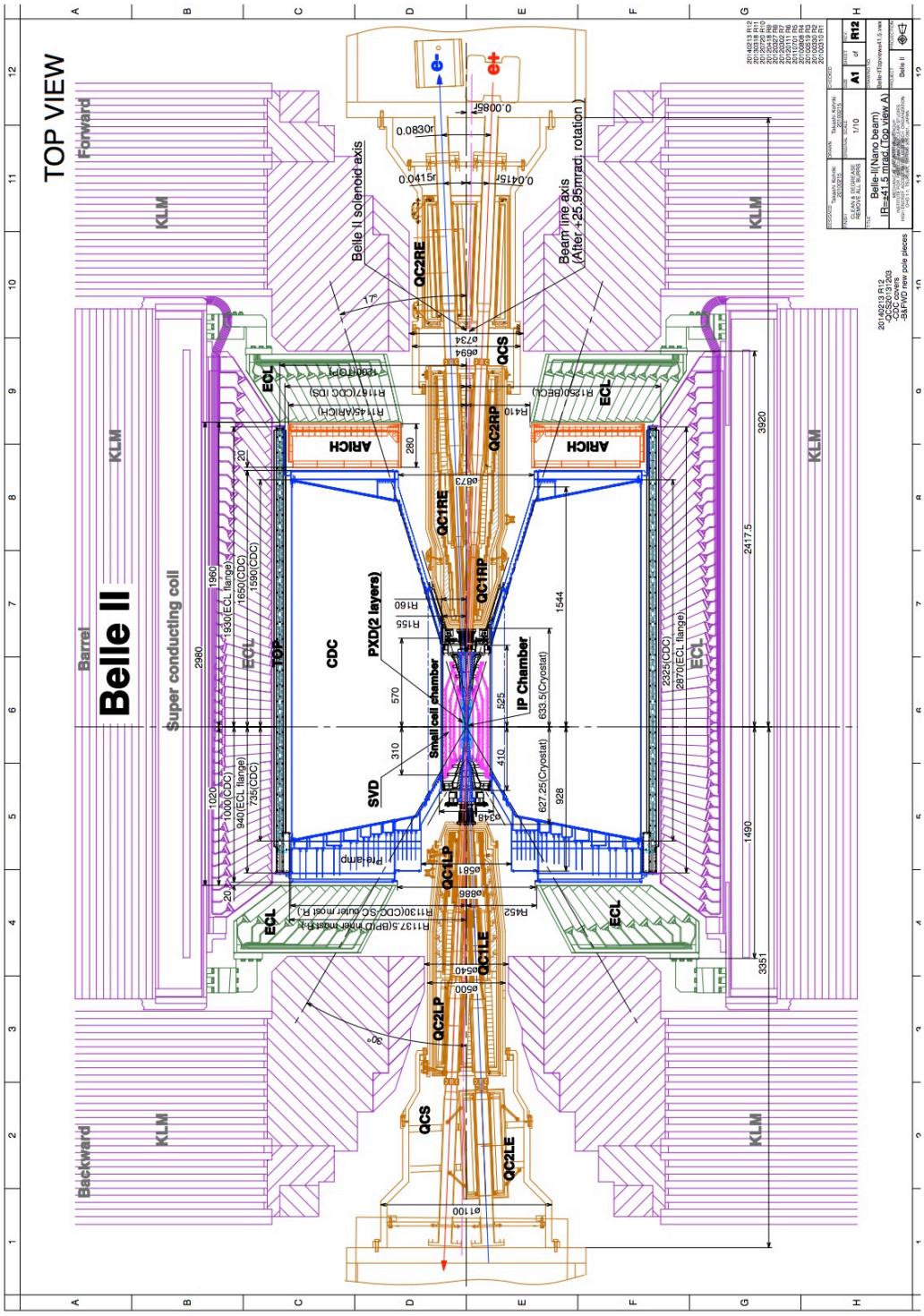

Figure 4.1: Schematic diagram of Belle II detector. Image is from reference [4].

The PXD assembly consists of two concentric cylindrical layers constructed from ladder modules. Each ladder module has two arrays of 768×250 pixels with thickness of 75μm. The inner layer of the PXD is constructed from eight ladder modules and has an inner radius of 14 mm, enclosing the SuperKEKB beam pipe that has a radius of 10 mm. The 256 pixels nearest to the interaction point have an area of $50 \times 55\mu$m and the remaining outer pixels are $50 \times 60\mu$m. The second cylindrical layer of the PXD is constructed from twelve ladder modules and has an inner radius of 22 mm. For the outer layer, the inner 256 pixels of the modules have an area $50 \times 70\mu$m and the outer pixels have area $50 \times 85\mu$m [3, 32].

4.2.2 Silicon Vertex Detector

The detector radially outward that follows the PXD is the Silicon Vertex Detector (SVD). Similar to the PXD, the SVD is designed to measure the spatial location of charged particles emitted from the interaction point.

The SVD uses Double-sided Silicon Strip Detector's (DSSD) to detect charged particles. DSSD's are designed to act as a switch which is activated by a particle ionizing through the sensor. The active material of the DSSD is a 300 μm thick n-type bulk region that has a voltage bias applied across it. The side of the DSSD's facing the interaction point is instrumented with long p^+ strips oriented along the beam axis direction, while the outer face has short n^+ type strips oriented perpendicular to the beam axis. When a charged particle ionizes through the bulk, electron-hole pairs are produced and the electric field forces the charge to accumulate at the nearest p^+ and n^+ strips, producing an electrical signal that is detected. The orthogonally oriented p^+ and n^+ strips allow the spatial location of the particle to be determined [3].

The SVD assembly consists of rectangular modules arranged in four concentric cylindrical layers (numbered layer 3-6 in Figure 4.2) that have inner radii of 38, 80, 115 and 140 mm, as illustrated in Figure 4.2 [3]. Shown in this figure, layers 4-6 of the SVD are slanted inward in the forward region of the detector. This allows the polar angle acceptance of $17 - 150\,\text{deg}$ to be covered with a more cost-effective sensor area [3]. In terms of area and pitch separation, the SVD uses three types of DSSDs as indicated in Figure 4.2 where the blue, green and yellow colour code indicates the DSSD geometry of the corresponding ladder module. Table 4.2 summarizes the number of ladder modules and DSSD sensors per SVD layer [3].

Together the PXD and SVD are referred to at the Vertex Detector (VXD) and

are designed to achieve an impact parameter resolution of $\sigma_{z_0} \sim 20\mu$m for charged tracks originating from the interaction point. This is critical to precisely reconstruct the decay vertex of particles that decay within the radius of the beampipe, such a B mesons [3].

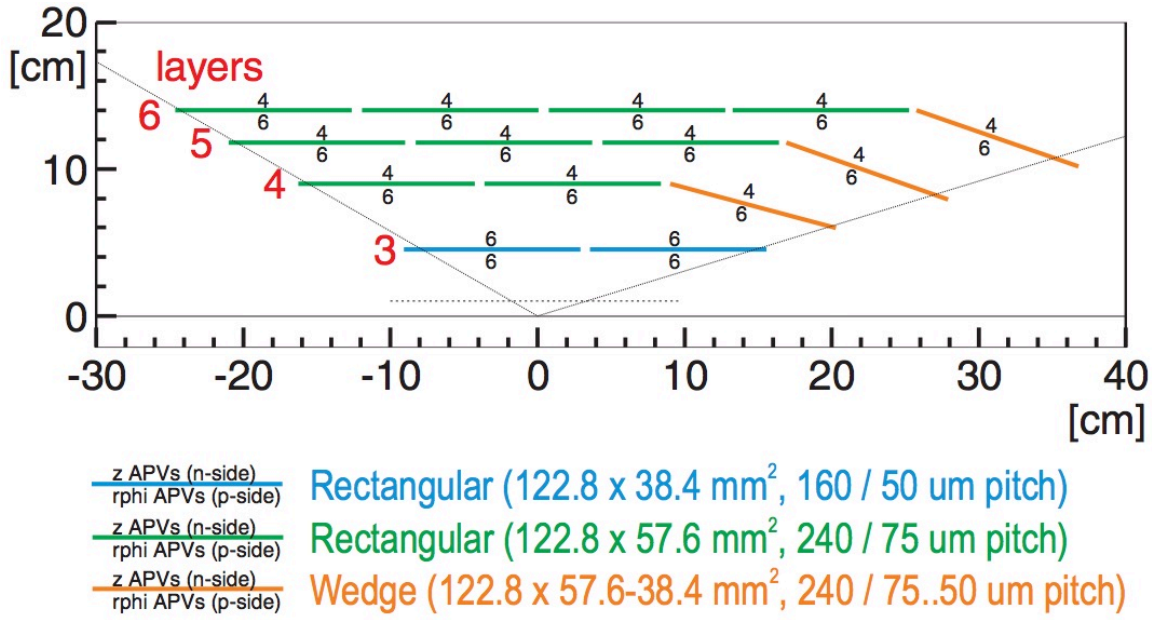

Figure 4.2: Schematic diagram showing layout of the SVD modules. Image is from reference [3].

Table 4.2: SVD assembly parameters from reference [3].

Layer	Radius (mm)	Ladders	Sensors per Ladder
3	38	8	2
4	80	10	3
5	115	14	4
6	140	17	5

4.2.3 Central Drift Chamber and Magnetic Field

The Central Drift Chamber (CDC) is the third sub-detector radially out from the collision point, beginning at an inner radius of 160 mm and extending to an outer radius of 1130 mm [3]. Throughout the VXD and CDC a 1.5 T magnetic field is present and oriented along the beam axis to bend the trajectory of charged particles

travelling through the CDC volume. By measuring the trajectory of the charged particle travelling through the CDC, the particles charge and momentum can be determined. The CDC performs several tasks critical to Belle II operation including measuring the momentum and identity of charged particles, as well as providing Level 1 trigger information to determine if the data measured in a collision event should be recorded offline [3].

The CDC is constructed from a cylinder tube filled with a gas mixture of 50 % helium - 50 % ethane. The CDC is instrumented with 42,240 aluminium field wires with diameter 126 μm and 14,336 tungsten sense wires with diameter 30 μm. These wires run along the length of the cylinder. The field wires induce an local electric field such that when an charged particle travels through the gas and produces free charges by ionization, the charges are accelerated by the local electric field resulting in further ionization to be induced, producing an amplification of the electrical signal that is then detected by the sense wires [3].

A schematic of the CDC geometry is shown in Figure 4.3 [3]. The sense wires are arranged in 56 layers along the radial dimension. From these layers, nine superlayers are formed such that each superlayer contains six layers, except for the innermost superlayer which has eight layers. The superlayers are strung in two different configurations, refereed to as axial and stereo. In the axial configuration, the wires are oriented in the direction of the Belle II magnetic field and in the stereo configuration the wires are in a skewed at a small angle to the axial layers. The superlayers alternate in axial vs stereo configurations allowing the position information along the beam axis to be measured [3].

The CDC is designed to independently achieve a vertex resolution of $\sigma_{r\phi} = 100\mu$m and $\sigma_z = 2$ mm and a momentum resolution of $\sigma_{p_t}/p_t = \sqrt{(0.1\%p_t)^2 + (0.3\%/\beta)^2}$, where p_t is in units of GeV/c. In addition the CDC is designed to measure the ionization $d\mathrm{E}/dx$ of tracks with a resolution of $\sigma_{dE/dx} = 5\%$[3].

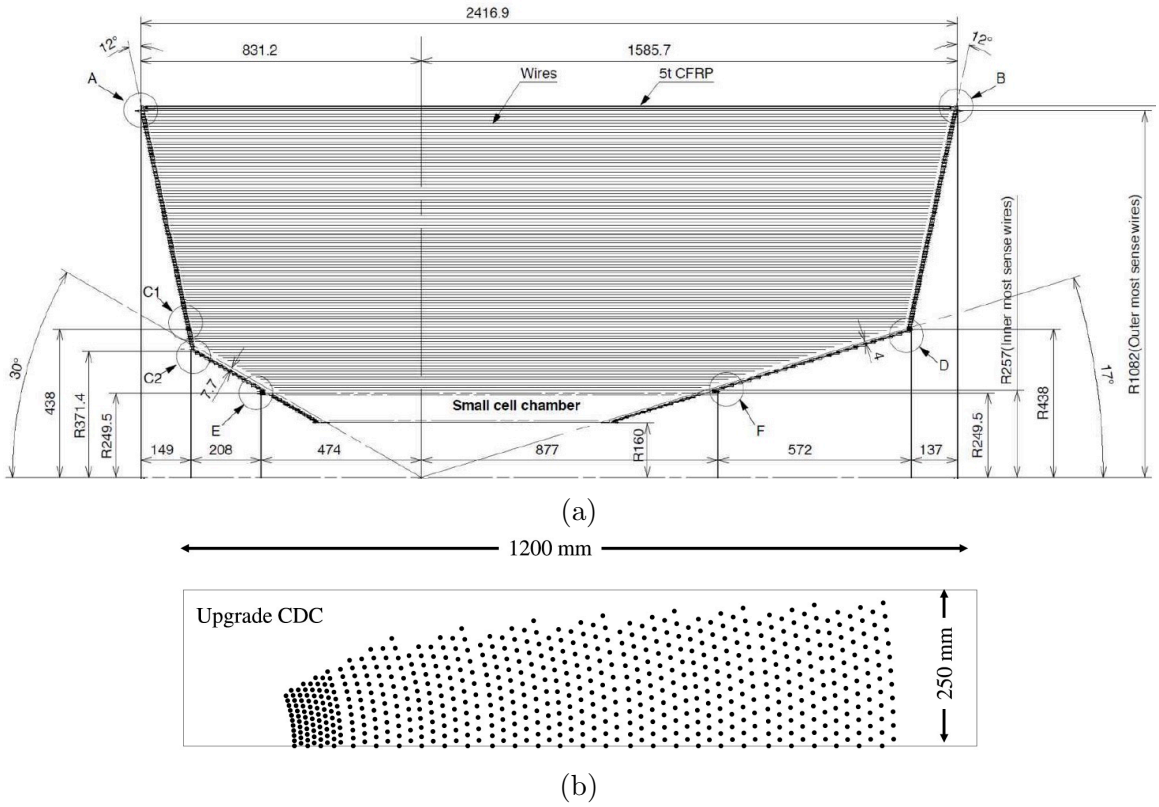

Figure 4.3: Schematic diagram of the Belle II CDC. Image is from reference [3].

4.2.4 Time-Of-Flight Propagation Detector

Surrounding the CDC in the barrel region is the Time-Of-Propagation (TOP) detector. The TOP is designed to perform charged particle identification. A critical function of the TOP in particular is to improve $\pi^{\pm}$ vs $K^{\pm}$ separation as well as providing precise event timing. The TOP detector is designed to achieve a time resolution of $\sigma_t = 40$ ps and a $K^{\pm}/\pi^{\pm}$ separation performance of 99% efficiency at a 0.5% pion fake rate [3].

The TOP detector assembly consists of 16 quartz bar modules with dimensions $440 \times 1200 \times 20$ mm^2. A schematic of a TOP module is shown in Figure 4.4 [3]. One end of a module is instrumented with a focusing mirror while the opposite end has an array of micro-channel plate (MCP) photomultiplier tubes (PMT). The quartz is the active material of the TOP module. When a charged particle enters the quartz at a speed that exceeds the speed of light in quartz, Cherenkov photons are emitted. The Cherenkov photons propagate in the quartz and are total internally reflected, allowing them to be detected by the array of MCP-PMTs mounted on the end of the

module [3].

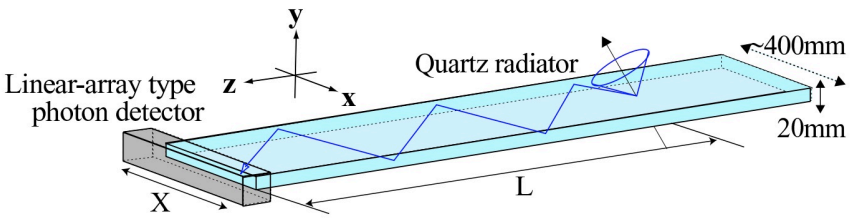

Figure 4.4: Schematic diagram of a TOP module. Image is from reference [3].

The TOP achieves particle identification by using the arrival time and position of the Cherenkov photons to determine the mass of the incident particle. This can be done because the Cherenkov photons are emitted in a cone as shown schematically in Figure 4.4, and the opening angle of the Cherenkov photon emission, θ_c, is given by equation 4.2 [3].

$$\cos\theta_c = \frac{1}{n\beta} \tag{4.2}$$

In equation 4.2, n is the index of refraction and $\beta = v/c$ is the magnitude of the particle velocity divide by the speed of light in vacuum. For the TOP quartz $n = 1.44$ at 405 nm wavelength [33]. Using the momentum of the incident particle measured by the CDC, the mass of the incident particle can be constrained using θ_c. In practice, the TOP identifies particles by comparing the photon arrival times and positions to pre-calibrated probability density functions computed for the charged particle hypothesis's e, μ, π, K, p and d [3, 33].

4.2.5 Aerogel Ring-Imaging Cherenkov Detector

The Aerogel Ring-Imaging Cherenkov Detector (ARICH) detector is located outside the CDC in forward endcap region of the Belle II detector and is used for charged particle identification. Similar to the TOP, the ARICH detector uses information from Cherenkov radiation to perform charged particle identification.

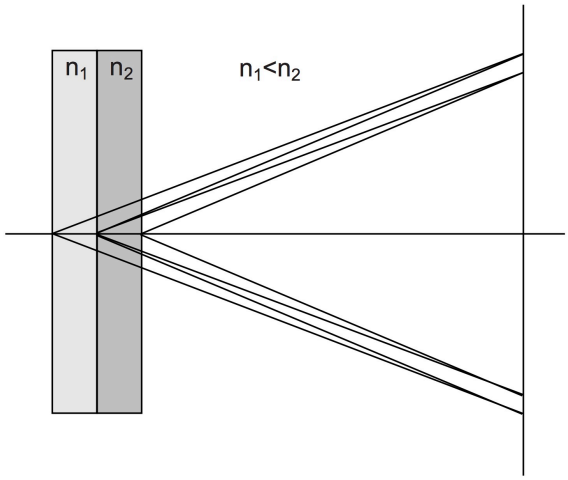

Figure 4.5: Diagram illustrating the operation principle of the ARICH detector. Image is from reference [3].

A side view of the ARICH is shown schematically in Figure 4.5 [3]. The active material of the ARICH is a ring of aerogel, which produces Cherenkov photons when a charged particle enters the aerogel exceeding the speed of light in aerogel. Following the aerogel rings is a 20 cm expansion volume that allows the Cherenkov photons to propagate outward in the shape of a cone. After the expansion volume are nine concentric rings that contain arrays of position sensitive hydrid avalanche photon-detectors (HAPD). The HAPD's measure the position of the Cherenkov photons when they reach the sensors [3].

Shown in Figure 4.5, the ARICH has two rings of aerogel and each ring has indexes of refraction of $n_1 = 1.045$ and $n_2 = 1.055$, respectively [34]. The refractive indices of the two rings are tuned such that when the two sets of Cherenkov photons, one produced by each aerogel ring, reach the HAPD's, the rings will overlap. This design produces an amplified signal relative to if the entire aerogel ring was the same refractive index [3].

Using the position information and the track momentum measured by the CDC, the ARICH can determine the mass of the charged particle using equation 4.2. The ARICH aims to achieve a $K^{\pm}/\pi^{\pm}$ separation performance of 96% efficiency with a 1% pion fake-rate at momenta of 4 GeV/c [3].

4.2.6 Electromagnetic Calorimeter

The Belle II Electromagnetic Calorimeter (ECL) is located outside the TOP and ARICH detectors and consists of three sections referred to as the barrel, the forward endcap and the backward endcap. The layout of the calorimeter is shown in the diagram in Figure 4.6[3]. The ECL covers the polar angle of $12.4 - 155.1$ deg [3]. The main function of the ECL is to measure the energy deposited by particles that interact in the ECL. In particular, the ECL is the primary detector used to detect photons and measure their momentum. The ECL has many other roles including event triggering, neutral hadron detection, and charged particle detection and identification [3]. The central focus of this dissertation is extending the capabilities of the the Belle II ECL in the areas of particle identification by applying CsI(Tl) pulse shape discrimination.

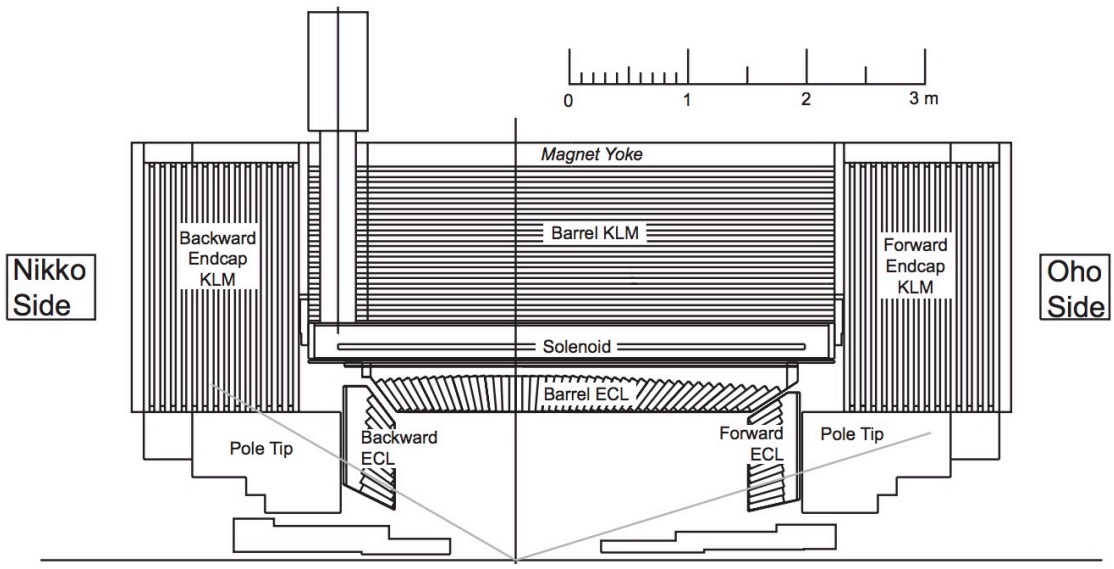

Figure 4.6: Schematic diagram showing locations of the Belle II calorimeter and K_L^0 Muon detectors. Image is from reference [3].

The ECL is constructed from 8736 CsI(Tl) scintillation crystals which are re-used from the past Belle experiment. These crystals are arranged in concentric rings as shown in Figure 4.6. The CsI(Tl) crystals have a trapezoidal geometry with a nominal length of 30 cm, forward face area of $\sim 4 \times 4$ cm^2 and the outward face area of $\sim 5 \times 5$ cm^2. The ECL measures the energy deposited in the CsI(Tl) crystals by detecting the scintillation light emitted by the CsI(Tl) when a particle deposits energy in the crystal volume. Each crystal is instrumented with two Hamamatsu Photonics S2744-08 photodiodes that are glued to the rear of the crystal for scintillation light detection.

Each crystal is wrapped in a 25μm thick aluminium and 25μm thick mylar wrapping to improve the scintillation light yield at the end of the crystal through internal reflection of the scintillation photons. The photodiodes are connected to a series of pre-amplifier electronics that filter, shape and integrate the electrical signal emitted by the photodiodes. The major upgrade from Belle to Belle II for the ECL is through new signal chain electronics that reduce the shaping time relative to Belle and also allow for digitization of the waveforms [3]. The signal chain of the CsI(Tl) crystals in the calorimeter will be described in further detail in Chapter 6 Section 6.1. The Belle II ECL aims to have an energy resolution of $\sigma_E/E = 0.2\%/E \oplus 1.6\%/\sqrt[4]{E} \oplus 1.2\%$, where E is in units of GeV and $\oplus$ indicates addition in quadrature. The ECL also aims to have a position resolution of $\sigma_{\text{pos}} = 0.5 \text{ cm}/\sqrt{E}$, where E is in units of GeV [3].

Due to the work completed in this dissertation, Belle II is the first e^+e^- collider experiment to perform particle identification by applying CsI(Tl) pulse shape discrimination with the electromagnetic calorimeter. The methods by which pulse shape discrimination is achieved at Belle II are described in detail in Chapter 6. At Belle II, CsI(Tl) pulse shape discrimination is enabled by the higher sampling frequency of the new readout electronics, sampling with a 567 ns time bin [35], and the recording of the digitized CsI(Tl) waveforms for crystals with an energy deposit above 30 MeV, allowing for offline pulse shape analysis. The results presented in Chapter 7 and Chapter 8 demonstrate that through the application of CsI(Tl) pulse shape discrimination, the Belle II calorimeter can identify electromagnetic vs. hadronic showers. This allows for improvements in particle identification, particularly in the areas of photon vs K_L^0/neutron separation and $e^\pm$ vs $\mu^\pm$ vs $\pi^\pm$ separation.

4.2.7 K_L^0 and Muon Detector

The K_L^0 and Muon Detector (KLM), as shown in Figure 4.6, is located outside of the superconducting coil which surrounds the electromagnetic calorimeter, producing the Belle II magnetic field. The KLM is designed to detect and identify K_L^0 and muons, in addition to operating as a flux return for the Belle II solenoid. The KLM is segmented into barrel and endcap detectors. In the barrel, the KLM is constructed from alternating layers of 4.7 cm thick iron plates and Resistive-Plate Chamber (RPC) superlayers. The iron plates in the RPC's provide a magnetic field flux return, while also providing a dense material to increase the likelihood for a K_L^0 interaction [3].

The layout of an RPC superlayer is shown in Figure 4.7 [3]. Each superlayer is constructed from two RPC detectors that are separated by a mylar insulator. Each RPC contains a gas gap that contains a mixture of 62% HFC-134a, 30% argon, and 8% butane-silver. When a charged particle travels through the gas, free charges are produced by ionization. A voltage bias is applied across the gas gap, producing an electric field that accelerates and amplifies the charge produced by the ionizing particle. The charge is detected by metal strips at the ends of the gas gap. In the barrel, the KLM aims to achieve a performance of $\Delta\phi = \Delta\theta = 20$ mRad for K_L^0 detection and a 1% hadron fake rate for muon detection [3].

In the KLM endcaps the RPCs in the superlayers are replaced with plastic scintillator detectors because the RPC performance is predicted to degrade from the large level of beam backgrounds in the endcaps relative to the barrel [36]. The scintillators used have a strip geometry with cross section 10×40 mm^2 and length of up to 2.8 m depending on the superlayer geometry [36]. The plastic scintillator used is a polystyrene doped with PTP (p-terphenil) or PPO (2,5-diphenyloxazole) [36]. Each endcap KLM superlayer is instrumented with 75 scintillator strips [36]. In each strip a wavelength shifting fibre is installed to run along the length of the scintillator strip through the centre. The fibre converts the scintillation light emitted by the scintillator to a longer wavelength that is more compatible with the photodiodes that are mounted at the end of the fibre for light detection [36]. In the endcaps, the predicted KLM performance is $\Delta\phi = \Delta\theta = 10$ mRad for K_L^0 detection [3].

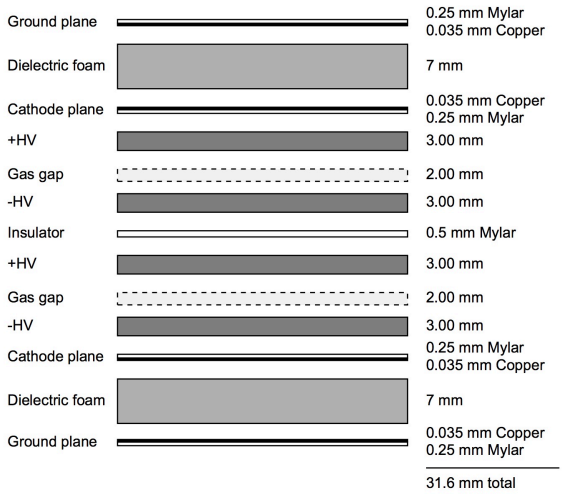

Figure 4.7: Schematic diagram of an RPC superlayer. Image is from reference [3].

4.3 Phase 2 of the Belle II Experiment

The Belle II Experiment is a long term project. The design report was published in October 2010 [3], and completion of the experiment is projected to be after 2027. Over this timeline the SuperKEKB operation periods are divided in three segments referred to Phase 1, Phase 2 and Phase 3. The studies in the dissertation used Belle II collision data collected during Phase 2.

Phase 1 occurred approximately from February 2017 to July 2017. In Phase 1 SuperKEKB operated in single beam mode such that only one beam operated at a time and thus no collisions occurred. During Phase 1 the Belle II detector was not installed at the SuperKEKB interaction point. Instead a collection of dedicated beam background monitoring detectors were installed to measure the beam induced background levels at the interaction point [31].

Phase 2 occurred approximately from March 2018 to July 2018. During Phase 2 the full Belle II detector was installed at the interaction point, with the exception of the PXD and SVD detectors where only a small segment of these detectors was installed. Phase 2 was the first time collisions were initiated by SuperKEKB and the first time collision data was recorded by Belle II. During Phase 2 the instantaneous luminosity of SuperKEKB reached a level of 5.55×10^{33} cm^{-2}s^{-1} [29]. The results in this dissertation presented in Chapters 6, 7 and 8 study Belle II collision data recorded during Phase 2.

Phase 3 of the Belle II experiment began in February 2019 and is projected to run beyond 2027. In Phase 3 the full Belle II detector, including the PXD and SVD, are installed at the interaction point. During Phase 3 the SuperKEKB collider will increase in instantaneous luminosity with plans to achieved 8×10^{35} cm^{-2}s^{-1}, allowing for an integrated luminosity 50 ab^{-1} to be accumulated during Phase 3.

Chapter 5

Hadronic vs. Electromagnetic Pulse Shape Discrimination in CsI(Tl) for High Energy Physics Experiments

This chapter consists of a paper describing research conducted by the author of this dissertation and published in the Journal of Instrumentation as reference [25]. The preprint version of the paper is included in this chapter, with permission, following the brief summary below. The published version of the article [25] can be accessed at the DOI:

https://doi.org/10.1088/1748-0221/13/03/P03018

This paper studies CsI(Tl) scintillation waveforms collected in a testbeam conducted by the author of this dissertation and completed at the TRIUMF proton and neutron irradiation facility. The analysis presented in this paper and the authoring of the paper was completed independently by the author of this dissertation, under the supervision of Dr. J. M. Roney.

The highlights of the paper are summarized below.

- CsI(Tl) scintillation waveforms from energy deposits initiated by neutrons and protons are analysed to show that energy deposits by highly ionizing particles emit a CsI(Tl) scintillation component with decay time of 630 ± 10 ns, referred to as the hadron scintillation component (hadron component), and not present

for energy deposits by photons or low $d\mathrm{E}/dx$ particles, such as muons produced from cosmic rays.

- The magnitude of the scintillation emission in the hadron scintillation component is shown to depend on the magnitude of energy deposited at high ionization $d\mathrm{E}/dx$. This allows energy deposits from interactions that produced a single proton, multiple protons, an alpha particle etc. to be identified by measuring the fraction of scintillation emission present in the hadron scintillation component, defined as the hadron component intensity (hadron intensity).

- A model to compute the magnitude of hadron component scintillation emission in an energy deposit, based on the primary and secondary particles produced, is developed. The Hadron Emission Function is defined to be a function that computes the fraction of hadron component scintillation emission produced in an energy deposit, based on the instantaneous $d\mathrm{E}/dx$ of the particle depositing energy.

- A method for computing the Hadron Emission Function using the proton data is developed.

- The Hadron Emission Function is incorporated into GEANT4, allowing for simulations of the particle dependent CsI(Tl) scintillation response. Using the neutron and proton testbeam data these simulation methods are validated.

- A GEANT4 simulation, that includes particle dependent CsI(Tl) pulse shapes simulations, is used to simulate a 5×5 array of CsI(Tl) crystals and evaluate the potential for CsI(Tl) PSD to be used for photon vs. K_L^0 identification at high energy physics experiments, such as Belle II. The results from these simulations predict that CsI(Tl) PSD will provide an effective method for photon vs. K_L^0 identification at high energy physics experiments.

Prepared for submission to JINST

Hadronic vs Electromagnetic Pulse Shape Discrimination in CsI(Tl) for High Energy Physics Experiments

S. Longo and J. M. Roney

Department of Physics and Astronomy, University of Victoria,
3800 Finnerty Rd, Victoria, BC, V8P 5C2, Canada

E-mail: longos@uvic.ca

Abstract: Pulse shape discrimination using CsI(Tl) scintillators to perform neutral hadron particle identification is explored with emphasis towards application at high energy electron-positron collider experiments. Through the analysis of the pulse shape differences between scintillation pulses from photon and hadronic energy deposits using neutron and proton data collected at TRIUMF, it is shown that the pulse shape variations observed for hadrons can be modelled using a third scintillation component for CsI(Tl), in addition to the standard fast and slow components. Techniques for computing the hadronic pulse amplitudes and shape variations are developed and it is shown that the intensity of the additional scintillation component can be computed from the ionization energy loss of the interacting particles. These pulse modelling and simulation methods are integrated with GEANT4 simulation libraries and the predicted pulse shape for CsI(Tl) crystals in a 5×5 array of $5 \times 5 \times 30$ cm^3 crystals is studied for hadronic showers from 0.5 and 1 GeV/c K_L^0 and neutron particles. Using a crystal level and cluster level approach for photon vs hadron cluster separation we demonstrate proof-of-concept for neutral hadron detection using CsI(Tl) pulse shape discrimination in high energy electron-positron collider experiments.

Contents

1 Introduction

We study the scintillation response of Thallium doped Cesium Iodide (CsI(Tl)) to charged and neutral hadrons in order to evaluate the potential for the application of inorganic scintillator pulse shape discrimination (PSD) to improve electromagnetic vs hadronic calorimeter

cluster identification at high energy e^+e^- collider experiments. In the low energy regime ($E_k < 20$ MeV) it has been established that charged particle identification for electron, proton and alpha particles can be achieved using CsI(Tl) scintillation pulse shape discrimination [1–3]. As a result this technique has been used for charged particle identification in nuclear physics detectors for example in heavy-ion detectors such as AMPHORA [4] and CHIMERA [5]. Pulse shape discrimination has not yet been applied at high energy physics experiments using CsI(Tl) detectors. For example the past *BABAR* [6, 7] and Belle [8] experiments, which made use of CsI(Tl) electromagnetic calorimeters, only extracted pulse amplitude and timing information [6–8]. With upcoming/present experiments such as Belle II [9] and BESIII [10] applying new detector technologies such as online waveform processing with FPGAs in the front-end electronics for the CsI(Tl) calorimeter crystals [11], online pulse shape characterization is now feasible to extract pulse shape information in addition to the standard crystal energy and timing variables. In this study we focus on the objective of applying pulse shape discrimination to improve electromagnetic vs hadron calorimeter cluster identification. Improvements in cluster identification would result in the reduction of systematic uncertainties related to particle identification of photons vs long lived neutron hadrons and low momentum pion vs muon separation. These improvements would complement the large data samples planned to be collected by intensity frontier experiments to perform precision tests of the Standard Model.

The reconstruction of long lived neutral hadrons are an important but challenging task at high energy particle detectors. For example, K_L^0 detection is critical for important physics analyses at e^+e^- B-Factories such as the measurement of the Charge-Parity violation parameter, $\sin 2\beta$, using the decay of $B \rightarrow J/\psi K_L^0$ [12, 13]. The past B-factories *BABAR* and Belle relied on event topologies and calorimeter energy spatial distributions to separate neutral hadrons from photons [12, 13]. In these cases, the neutral hadron experimental signature is characterized by the lack of associated charged particles in the tracking detectors, the transverse spatial distribution of energy deposits in the CsI(Tl) calorimeter and/or the characteristics of energy deposited in detectors behind the CsI(Tl) calorimeter. These methods however have shown to lead to low purities for $J/\psi + K_L^0$ samples (51%) compared to sample purities achieved for $J/\psi + K_S^0$ (96%) as the K_S^0 can be reconstructed using tracking information [12].

The question we address in this paper is: Do the hadronic showers initiated by higher momentum ($|\vec{P}| = 0.1 - 1$ GeV/c) K_L^0 or neutrons produce significant enough energy deposits from secondary charged hadrons such that PSD can be applied to substantially improve the discrimination between electromagnetic and hadronic showers in a CsI(Tl) calorimeter? We focus on separating showers from K_L^0 or neutrons and photons in particular as these particles cannot be identified with tracking detectors however we note that electromagnetic vs hadron shower identification would also have application in improving charged particle identification in high energy experiments as well. This technique has been explored for fast neutron detection using small 2.54 cm diameter CsI(Tl) crystals in references [14, 15] where fast neutron identification was demonstrated using this principle.

These studies show that the secondary charged hadrons created from the inelastic neutron interactions in the crystal can transfer a significant amount of energy to the CsI(Tl) [14, 15]. By applying CsI(Tl) PSD, the different inelastic neutron interactions in the crystal then can be identified [14, 15]. From these studies it is expected that the crystals in K_L^0 initiated showers will have hadronic CsI(Tl) pulse shapes.

We begin in Section 2 with a description of the fast neutron data and proton testbeam data, collected at the TRIUMF Proton Irradiation Facility (PIF) [17], and used in this paper. In addition, the experimental setup is also described in Section 2. In Section 3 we develop a hadron scintillation component model to characterize the CsI(Tl) pulse shape variations observed in the fast neutron data. This model is validated in Section 4 by applying it to the proton testbeam data. In Section 5 simulation methods for the hadron scintillation component model are developed and integrated with GEANT4[1] particle interactions in matter simulation libraries [16]. Simulated results for neutron and proton interactions in a CsI(Tl) crystal are then computed and quantitatively compared with the fast neutron and proton testbeam data collected. Finally in Section 6 the pulse shape characterization and simulation techniques are applied to compute the pulse shape response for a CsI(Tl) crystal cluster to hadronic showers from a sample of simulated K_L^0 and neutron events. By comparing the predicted cluster response for the hadronic and electromagnetic showers, neutral hadron vs photon discrimination using CsI(Tl) PSD is demonstrated.

2 Experimental Data

2.1 Neutron and Proton Data

Proton data from proton testbeams was collected at the TRIUMF Proton Irradiation Facility (PIF) [17]. Scintillation pulses from protons with primary kinetic energies of 67.0, 57.7, 40.1 and 20.0 MeV were recorded. The proton beam in the 57.7, 40.1 and 20.0 MeV runs was partially degraded prior to the CsI(Tl) detector to allow for multiple proton energies in the same beam. The CsI(Tl) detector was self-triggered at rate of approximately 2.1 kHz while recording the proton pulses.

A sample of fast neutron events was also collected in a neutron run. During this run the TRIUMF cyclotron was in operation performing isotope production which involved impinging up to 500 MeV protons on a target located on the other side of a wall of concrete shielding separating the PIF area from target area. From this process a sample of high energy neutrons approximately following a 1/E energy distribution up to a maximum energy of 500 MeV [17] interacted with the detector in the PIF area during a 10 hour run and as a result this run contained a sample of fast neutron events. This dataset also included energy deposits from cosmic muons. Energy calibration was completed using low energy photon peaks from ^{137}Cs (0.662 MeV), ^{40}K (1.46 MeV) and ^{208}Tl (2.61 MeV) backgrounds. As a

[1]Simulation results are computed using GEANT4 version 10.2.2 and the `FTFP_BERT_HP` physics lists with range cuts for all particles set to 0.07 mm.

result, light output yield values throughout this paper are expressed in photon equivalent energy units.

2.2 CsI(Tl) Detector

CsI(Tl) scintillation pulses were digitized using a spare crystal from the past B-factory experiment *BABAR* [6, 7]. The crystal was manufactured by Shanghai Institute of Ceramics and had a length of 30 cm and a trapezoidal geometry with front face size of approximately 4×4 cm^2 and light readout face size of approximately 5×5 cm^2. The crystal had thin wrappings of Teflon and Mylar in order to improve the light collection efficiency. A Hamamatsu R580 photomultiplier tube (PMT) with diameter of 38 mm was used for scintillation light detection [18]. Using a spring assembly, the PMT was pressed against the crystal face and an air optical coupling was used to interface the PMT and crystal. The PMT output was connected to a CAEN V1724 digitizer that was triggered on a voltage threshold. Once triggered the scintillation pulses were digitized with sampling time of 10 ns and saved for offline analysis.

3 Hadronic Scintillation Component Model

3.1 Charge Ratio Characterization

We begin by characterizing the scintillation pulse shapes in the PIF neutron measurement using the short-over-long charge ratio PSD technique that has been applied in past CsI(Tl) PSD studies [3, 15]. This technique takes advantage of the observation that proton and alpha energy deposits in CsI(Tl) result in faster scintillation emission compared to photon energy deposits [1]. This results in a greater percentage of the scintillation emission to occur earlier in the scintillation pulse for hadron energy deposits leading to higher values of the charge ratio. Specifically we use the charge ratio, R_{PSD}, defined in equation 3.1 where $Q(t)$ is the charge output of the PMT as a function of time.

$$R_{\mathrm{PSD}} = \frac{Q(1.2\mu\mathrm{s})}{Q(7.4\mu\mathrm{s})} \tag{3.1}$$

A short charge time of 1.2μs is used so that comparison can be made with reference [15] where the same short gate time was applied and stated to be the optimal time for CsI(Tl) PSD. Our long gate of 7.4μs was chosen as this is the typical length of time available before pile-up effects in high radiation environments such as at e^+e^- collider experiments. Figure 1 displays the two dimensional histogram of R_{PSD} vs $Q(7.4\mu\mathrm{s})$.

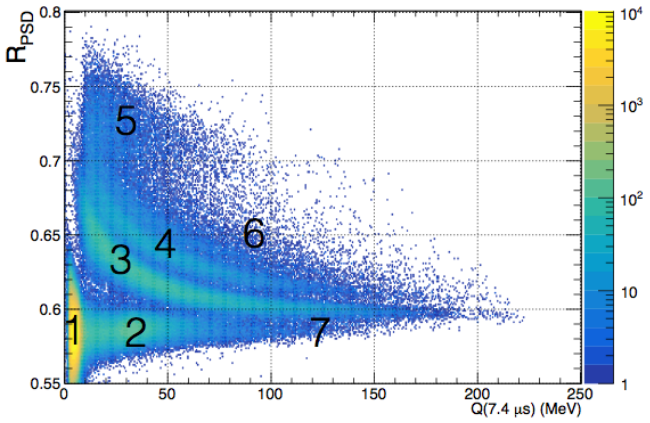

Figure 1. R_{PSD} vs $Q(7.4\mu s)$ pulse shape characterization of pulses recorded in the 10 hour PIF neutron measurement.

From Figure 1, it is observed that a diverse spectra of pulse shapes are present in the 10 hour PIF neutron run. In order to discuss the material interactions causing the band structures observed we label seven regions in Figure 1 for reference. Region 2 is identified as the cosmic muon peak centred around a charge ratio of approximately 0.585. At higher values of R_{PSD}, where hadron pulses are expected, systematic band structures are present. These band structures were reported in two past studies of the response of CsI(Tl) to fast neutrons [14, 15]. In these references the bands are attributed to secondary proton, deuteron and triton particles generated by neutron interactions in the crystal [14, 15]. Using the simulation methods discussed in Section 5, we use Monte Carlo (MC) truth to confirm that the Region 3 band arises from secondary protons from neutron scatters. We find however that the Region 4 band is predominately from neutron interactions where two secondary protons are created. Specifically for all labelled regions we find that the corresponding interaction is given by:

1 - Secondary photons from low energy ($E_k < 10$ MeV) neutrons and natural radioactive background.
2 - Cosmic muon peak.
3 - Neutron scatter where single secondary proton was produced. The value of the deposited energy is determined from the secondary proton kinetic energy as it will stop in the crystal volume.
4 - Neutron scatter where two secondary protons where produced.
5 - Neutron scatter where secondary alpha was produced.
6 - Neutron scatter where secondary proton/deuteron and alpha were produced.
7 - Neutron scatter where high momentum proton was produced and escapes crystal volume.

3.2 Pulse Shape Variations from Photon Pulse

For greater than 1 MeV photon energy deposits in CsI(Tl) it is well established that the scintillation pulse shape can be described using a two component scintillation model consisting of a fast and slow component emission as shown in equation 3.2 in charge form and equation 3.3 in current-form [19].

$$Q_\gamma(t) = L_\gamma(N_{\text{fast}}(1 - e^{\frac{-t}{\tau_{\text{fast}}}}) + N_{\text{slow}}(1 - e^{\frac{-t}{\tau_{\text{slow}}}})) \tag{3.2}$$

$$I_\gamma(t) = L_\gamma\left(\frac{N_{\text{fast}}}{\tau_{\text{fast}}} e^{\frac{-t}{\tau_{\text{fast}}}} + \frac{N_{\text{slow}}}{\tau_{\text{slow}}} e^{\frac{-t}{\tau_{\text{slow}}}}\right) \tag{3.3}$$

Where L_γ is the total light output from the photon energy deposit, τ_{fast} is the time constant of the fast scintillation component, τ_{slow} is the time constant of the slow scintillation component, N_{fast} is the relative intensity of the fast scintillation component yield and N_{slow} is the relative intensity of the slow scintillation component yield defined such that $N_{\text{fast}} + N_{\text{slow}} = 1$.

In order to study the origin of the pulse shape difference between photon pulses and pulses from hadron energy deposits, we construct a template photon pulse by individually fitting equation 3.2 to the pulses in Region 1 (low energy photons) of Figure 1 defined by, $3 < Q(7.4\mu\text{s}) < 6$ MeV and $0.569 < R_{\text{PSD}} < 0.593$. From this large sample of fits we extract the mean values of the four scintillation parameters to define a template photon pulse. The results for the template photon pulse parameters are shown in Table 1. We also include in Table 1 the photon pulse shape parameters found in a previous investigation of the photon CsI(Tl) pulse shape near room temperature by reference [19]. We note that the template photon pulse parameters we measured are in agreement with reference [19].

Table 1. Mean values for photon pulse shape parameters determined by fitting shape parameters to a large sample of 3-6 MeV photon pulses. The systematic uncertainty is ±1% and statistical errors are negligible. Our values are compared to those from Valentine et al [19]. Note that $N_{\text{slow}}/N_{\text{fast}}$ corresponds to Q_2/Q_1 in reference [19] and $N_{\text{slow}} = 1 - N_{\text{fast}}$.

Parameter	τ_{fast}	τ_{slow}	N_{fast}	$N_{\text{slow}}/N_{\text{fast}}$
This Study	851 ± 9 ns	5802 ± 58 ns	0.569 ± 0.006	0.756 ± 0.007
From Ref. [19]	832 ± 42 ns	5500 ± 275 ns	0.568 ± 0.028	0.760 ± 0.038

We calculate for pulses in regions 2-7 the energy normalized charge difference, $\text{D}_Q(t)$, defined by equation 3.4 where we normalize to the charge at 7.4μs.

$$\text{D}_Q(t) = \frac{Q(t)}{Q(7.4\mu\text{s})} - \frac{Q_\gamma(t)}{Q_\gamma(7.4\mu\text{s})} \tag{3.4}$$

From $\text{D}_Q(t)$ we gain insight to the origin of the pulse shape variations observed in non-photon pulses. Typical $\text{D}_Q(t)$ for the pulse regions 2-6 are shown in Figure 2. From

these charge difference plots it is observed that only the amplitude of $D_Q(t)$ is dependent on R_{PSD} and the shape of $D_Q(t)$ remains constant, independent of the charge ratio or energy deposited. This result demonstrates the wide spectrum of the pulse shapes observed in Figure 1 all deviate from the photon pulse in the same way and thus likely occur from the same origin. We note that $D_Q(t)$ was also studied by reference [3] for low energy alpha particles where the same shape was observed. In addition the peak value of $D_Q(t)$ occurs at approximately 1.2μs after the trigger point accounting for why this was found to be the optimal short gate by reference [15].

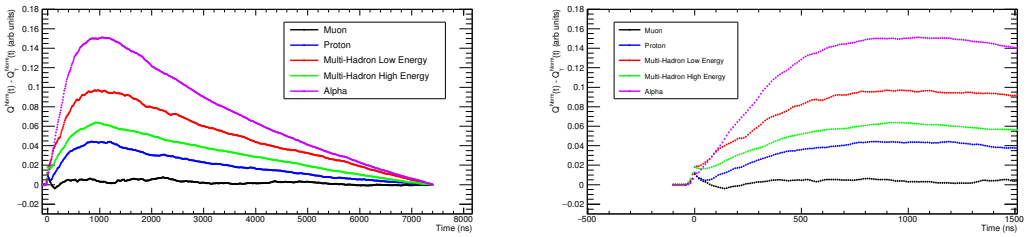

(a) (b)

Figure 2. a) Plots of $D_Q(t)$ for sample pulses in the various regions defined from the pulse shape spectrum in Figure 1. "Muon" is from a sample pulse in from region 2; "Proton", region 3; "Multi-hadron low energy". region 4; "Multi-hadron high energy", region 6; and "Alpha", region 5. b) Zoom in on first microseconds of pulse differences showing approximate form of an integrated exponential.

Studying the shape of $D_Q(t)$, the decay to zero charge difference at 7.4μs is a result of the charge normalization in the definition of $D_Q(t)$. In the initial microseconds shown in the zoom in Figure 2b however it is observed that $D_Q(t)$ has the approximate behaviour of an integrated exponential suggesting that the pulse shape difference arises from an additional scintillation component. To explicitly demonstrate this we calculate the current difference $I^{\text{Diff}}(t)$ defined in equation 3.5.

$$I^{\text{Diff}}(t) = I(t) - \frac{A^{\text{Tail}}}{A_\gamma^{\text{Tail}}} I_\gamma(t) \tag{3.5}$$

Where A^{Tail} is the integrated current in the tail region of the pulse we define by t=10-14μs. As we find the pulse shape in the tail region is independent of particle type we use the charge in this region to scale the current-form of the gamma template when computing $I^{\text{Diff}}(t)$. By computing $I^{\text{Diff}}(t)$ we can observe the shape of the light emission difference which occurs for hadron energy deposits compared to photons. Plots of $I^{\text{Diff}}(t)$ for typical pulses in shape regions 2-7 are shown Figure 3 with a fit overlaid to a exponential with fixed decay time of 630 ns, only fitting for the amplitude, A. From these plots it can be seen that the additional emission present for hadron energy deposits has the identical exponential form for all pulse shape regions. For the muon pulse is it also observed that the difference is zero as the

pulse shape is the same as the low energy photons. This particle-independent exponential shape for the hadron energy deposits indicates that the pulse variations for these particles originate from a third scintillation component which is not present for electromagnetic energy deposits. We find the time constant for this hadronic scintillation component to be τ_{Hadron}=630 ± 10 ns.

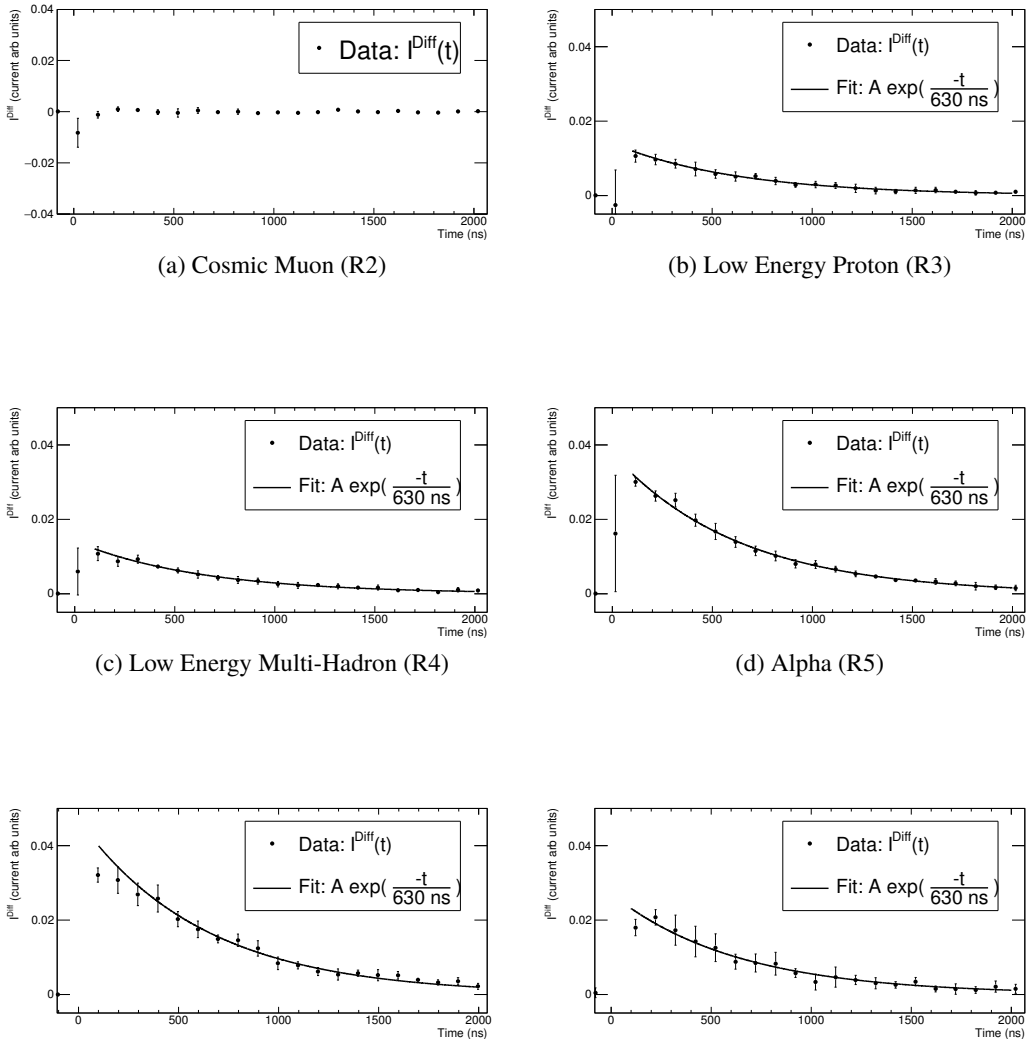

(a) Cosmic Muon (R2)

(b) Low Energy Proton (R3)

(c) Low Energy Multi-Hadron (R4)

(d) Alpha (R5)

(e) High Energy Multi-Hadron (R6)

(f) High Energy Proton (R7)

Figure 3. Plots of $I^{\text{Diff}}(t)$ for the region's R2-R7 indicated Figure 1.

3.3 Hadron Scintillation Component Model

We incorporate this hadron scintillation component into a new three component model for CsI(Tl) scintillation emission defined by equation 3.6. We note that although this model extends the number of scintillation components for CsI(Tl), the only free parameter of the

model is the intensity of the hadron scintillation component defined as N_{Hadron} in equation 3.7 which, in Section 5, we will show depends on the ionization $\frac{dE}{dx}$ and therefore the type of particle and energy it deposits via ionization loss. All of the remaining pulse shape parameters are fixed to the template photon parameters in Table 1 and τ_{Hadron}=630 ns.

$$Q^{\text{Hadron Component Model}}(t) = Q_\gamma(t) + L_{Hadron}(1 - e^{\frac{-t}{\tau_{Hadron}}}) \tag{3.6}$$

$$N_{Hadron} = \frac{L_{Hadron}}{L_\gamma + L_{Hadron}} = \frac{L_{Hadron}}{L_{Total}} \tag{3.7}$$

Where L_{Hadron} is the total scintillation emission of the hadron scintillation component in units of photon equivalent energy.

To test this model, the PIF neutron data is re-analysed by fitting the charge pulses to equation 3.6 and extracting N_{Hadron} for each pulse. Typical fit results for an alpha and muon pulse shape are shown in Figure 4 with the three scintillation components overlaid.

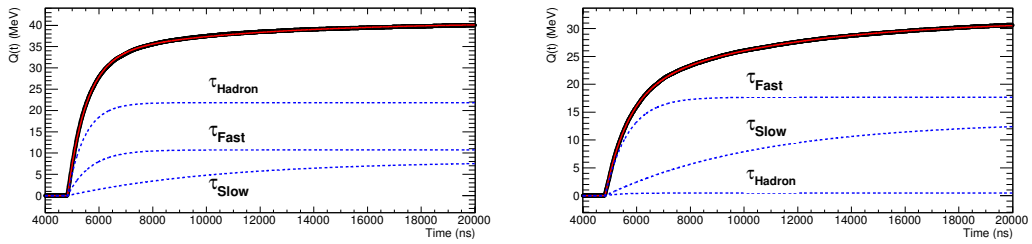

(a) Alpha particle (b) Muon

Figure 4. Sample fits using hadron component model equation 3.6, for typical alpha and muon pulses with pulse amplitudes of 30-40 MeV. The contributions from the different scintillation components is shown.

As shown in Figure 4 we use the charge form of the pulse to fit for the hadron intensity as by integrating the current-form we can reduce noise present in the raw current pulse. In order to evaluate the fit results, however, we use the current-form to avoid the correlations introduced when computing the charge pulse form. The current-form of pulses with the fit result overlaid are shown in Figure 5 for a typical pulse for each of the pulse shape regions 2-7. From these plots we show visually the pulse decay shape for all pulse types is fully described up to 14μs by the addition of a 630 ns exponential at various intensities.

In Figure 6 we plot the N_{Hadron} vs pulse amplitude and observe that the same band structures arises as the R_{PSD} vs $Q(7.4\mu s)$ plot in Figure 1. This demonstrates the pulse shape variations can be described by the parameter N_{Hadron} and can be interpreted as originating from the hadron scintillation component. In agreement with this hypothesis, the intensity of the hadron scintillation component is zero for the cosmic muon energy deposits, as well as those of photons, and increases for the hadron deposits with alpha pulses having up to 70% of the scintillation emission in the hadron component.

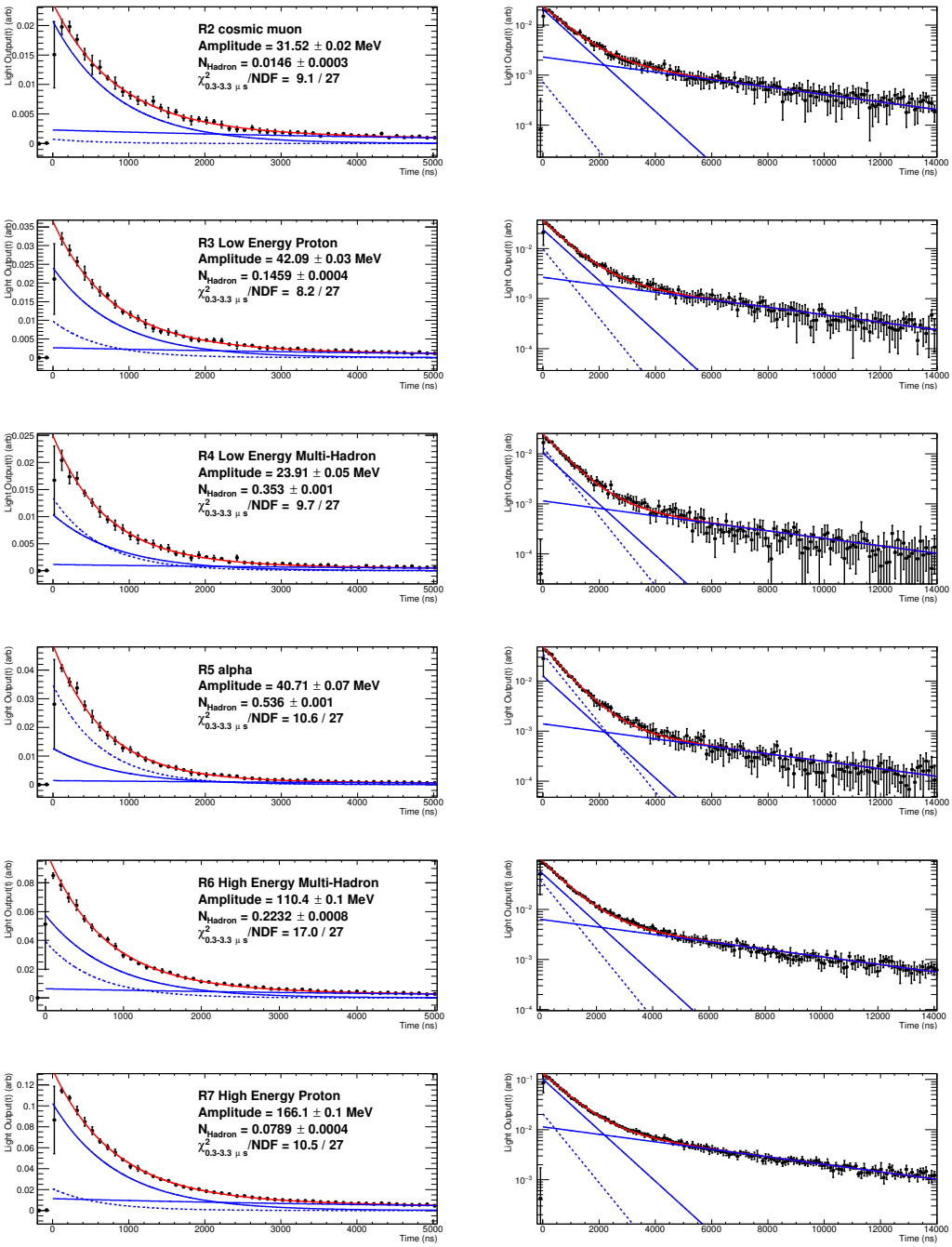

Figure 5. The current-form of typical fit results for pulse region's R2-R7 indicated Figure 1. Fast, slow and hadron components are overlaid. Hadron component indicated by dashed line. The plots on the right use a vertical log scale and expand the time from 5 μs (used for the plots on the left) to 14 μs to show the tail region of pulses.

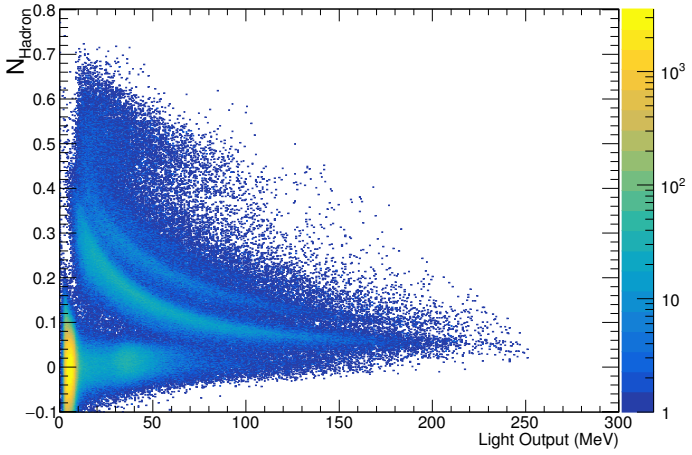

Figure 6. Hadron scintillation component intensity vs pulse amplitude spectrum of PIF neutron data. Light output is in units of equivalent photon energy.

To further demonstrate that all pulse shapes in the PIF neutron sample are well described by the hadron component model we compute the χ^2 in the pulse regions of 300 - 3300 ns where the hadron component has the highest impact in the pulse shape. We restrict the calculation of the fit quality to begin after the initial 300 ns of the pulse in order to avoid systematic effects such as the ultra-fast component and the pulse rise time, which are not included in the model as they contribute a small percentage of total charge. In order to evaluate the goodness-of-fit of the hadron component model we use the current-form of the scintillation pulse binned in 100 ns wide bins. The error of the amplitude in each bin is computed from the standard deviation of the points in the bin, which characterizes the electronic and statistical noise present in the pulse, recognizing that the points within the bin are not independent due to correlations. This conservative approach leads to an overestimate of the errors used in the χ^2 calculation. As a result we focus on the relative comparison of the χ^2 distributions for the photon and hadron pulses shapes as we treat all shapes consistently. In addition sample fit results for the typical waveforms are presented in Figure 5 to visually show how the fit results compare with the data. In Figure 7 we divide the pulses with amplitude greater than 10 MeV into different pulse shape regions and plot the χ^2 for these pulses where the number of degrees of freedom is 27 (30 bins and 3 parameters). From this we find that the model defined in equation 3.6 describes both the hadron and photon pulse shapes equally well. We note that this model does not include delayed hadronic interactions which would result in out of time pile-up pulses and yield a high χ^2. From Figure 7 it can be seen that such effects are small and justifiably neglected.

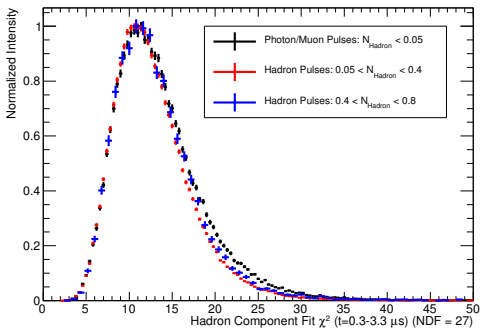

Figure 7. Fit χ^2 histograms for electromagnetic and hadronic pulse shapes for pulses with amplitude greater than 10 MeV. The number of degrees of freedom (NDF) for the fit is 27. Note as discussed in Section 3.3 the errors used for computing the χ^2 are conservatively estimated as correlations within the time bin have not been taken into account, which produces a lower than expected χ^2.

3.4 Discussion of Hadron Component Model

By considering the pulse shape differences between photon and hadron energy deposits we have demonstrated that the pulse shape variations for CsI(Tl) can be characterized using a third scintillation component with decay time of 630 ± 10 ns. Using this model, the pulse shapes for CsI(Tl) are characterized by the parameter N_{Hadron} defined as the scintillation emission intensity of the hadron scintillation component. This single parameter pulse shape description is advantageous compared to present approaches for pulse shape characterizing techniques for CsI(Tl) where the four shape parameters (τ_{fast},τ_{slow}, N_{fast} and N_{slow}) of the two component scintillation model are varied to describe the CsI(Tl) pulse shape spectrum as done in references [2] and [20]. In addition these studies have shown that low energy hadron energy deposits, which result in the largest pulse shape difference from photons, will result in fast time constants in the range of approximately 600-650 ns when fit to the two component model [20]. This is in agreement with our model where it is expected that the τ_{Hadron} component would dominate the scintillation emission for these pulses and thus a pulse shape description using a two component scintillation model is expected to produce a fast time constant consistent with our hadron time constant.

In Section 5 we show that the instantaneous hadron scintillation component emission intensity can be computed from the ionization energy loss of the interaction particle. A detailed analysis of the mechanism resulting in the 630 ± 10 ns scintillation component for only high $\frac{dE}{dx}$ energy deposits is beyond the scope of this paper however we note that the magnitude of this decay time is close to the 575 ± 5 ns thallium centre lifetime measured by reference [21] by observing the single component scintillation emission of CsI(Tl) when exposed pulsed UV light. Considering possible systematic effects such as temperature variations between experimental setups, it is possible that this is the same decay component we observe in the hadronic pulse shapes.

4 Hadron Component Model Applied to Proton Data

In this section we apply the hadron component model to the proton testbeam data collected in addition to the PIF neutron run studied in the previous section. The proton beam data was collected at kinetic energies of 20.0, 40.1, 57.7 and 67.0 MeV corresponding to proton momenta of 0.194, 0.277, 0.344 and 0.360 GeV/c, respectively. For the following proton data runs discussed in this section fit quality cuts were applied to remove out of time pile-up pulses.

4.1 67.0 MeV Proton Data

The pulse amplitude spectrum in units of equivalent photon energy for the 67.0 MeV proton run is shown in Figure 8. Peaks are observed at quantized values in units of total scintillator light output for the full energy deposit of the primary proton kinetic energy. These peaks correspond to events where single, double and triple coincident protons from the beam simultaneously entered the crystal. Similar quantization of peaks were also observed in the other proton runs.

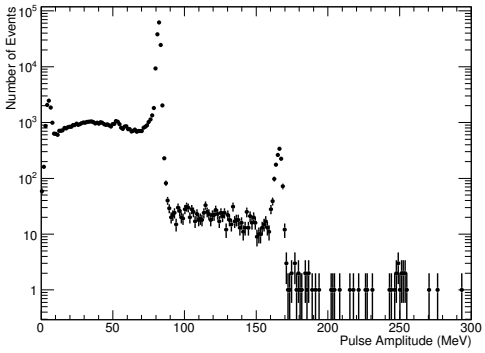

Figure 8. Energy deposited spectrum for recorded pulses in 67.0 MeV proton run data. Note that the peak of the pulse amplitude spectrum for the protons, presented in electron equivalent energy units, is higher than the proton kinetic energy due to the Birk's scintillation efficiency of CsI(Tl) for high $\frac{dE}{dx}$ energy deposits [22–25]. The Birk's scintillation efficiency for the protons is discussed further in Section 5.2.

The N_{Hadron} vs pulse amplitude pulse shape spectrum for the 67.0 MeV proton run data is shown in Figure 9a. The pulses corresponding to full energy deposition from the primary 67.0 MeV protons result in pulse shapes with approximately 10% contribution from the hadron scintillation component. Other features in the spectrum are observed in the continuum events below the main proton peak. As was done with the neutron pulse shape spectrum, these features were understood using truth information from Monte Carlo (MC) simulations described in the Section 5. Simulation truth results are shown in Figure 9b for 67.0 MeV incident protons and as expected the multi-proton peaks are not present

in the simulation results as each simulated event began with a single primary proton. In the simulation results we observe that the proton peak is present in a small number of bins (circled in red) demonstrating the consistency of the proton ionization process. From the simulation truth we identify the pulse shape band originating at the main proton peak and trending towards 0 hadron intensity at 0 MeV as originating from events where the deposited energy by the primary proton was approximately equal to the pulse amplitude followed by the primary proton undergoing an inelastic interaction with a Cs or I atom that resulted in no secondary protons being created. The band beginning at the main proton peak and trending upward occurs when one of the secondary particles created was a proton. The intrinsic broadening of this band in the simulation is due to events containing secondary protons with different kinetic energies. Finally the additional bands trending upward above the main band are identified as proton inelastic interactions which result in two and three secondary protons.

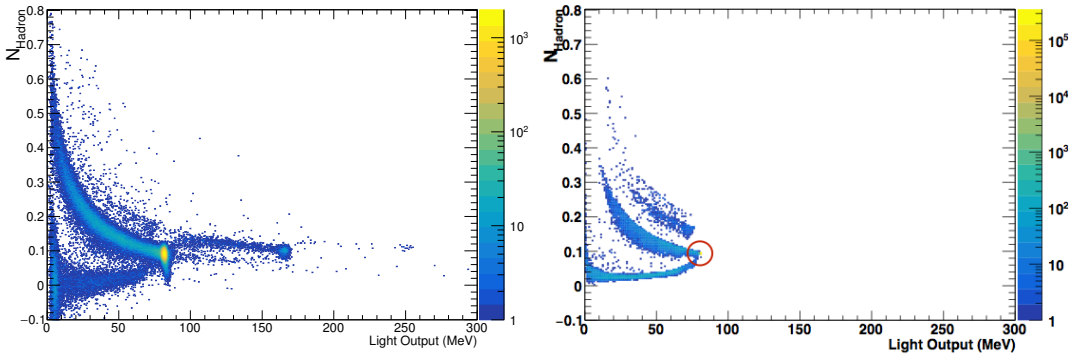

(a) 67.0 MeV Data.

(b) Simulation Truth.

Figure 9. a) Data and b) Simulation truth plots of N_{Hadron} vs pulse amplitude pulse shape spectrum for 67.0 MeV proton run. Note in the simulation truth (b) results, a large number of events from the proton ionizing and stopping in the detector are contained in one histogram bin (circled in red) centred at (80.5 MeV, 0.0935) consistent with the position of the peak in the data plot, (a). Pulse shape and amplitude simulation techniques are described in Section 5.

4.2 20.0, 40.1 and 57.7 MeV Proton Data

During the 20.0, 40.1 and 57.7 MeV runs part of the beam had its energy degraded before reaching the crystal. This provided one additional sample of protons with a lower energy in each of the runs. For these runs we plot the hadron component intensity vs pulse amplitude in Figures 10a, 10b and 10c. In these spectra, similar features as those seen in the 67.0 MeV run are present, such that there is an intense peak at the total light output equivalent for the main beam energies and additional pulses from secondary hadron interactions below the main peak. Using the single proton band in pulse shape spectra for the four proton

runs we extract the hadron component intensity as a function of the total light output by fitting a Gaussian to the intensity distribution in a series of 2 MeV bins of total light output. The extracted N_{Hadron} vs L_{Total} points for the single proton bands are overlaid in Figure 15 in Section 5.4 where they are further discussed and are compared with simulation and numerical calculations developed in the following sections.

To demonstrate that the hadron component model describes the proton data just as well as the neutron data presented in Section 3, we plot in Figure 10d the χ^2 statistic for the pulses in the main energy peak of each proton data run. From the χ^2 distributions it is seen that the hadron component model performance is identical for each proton energy.

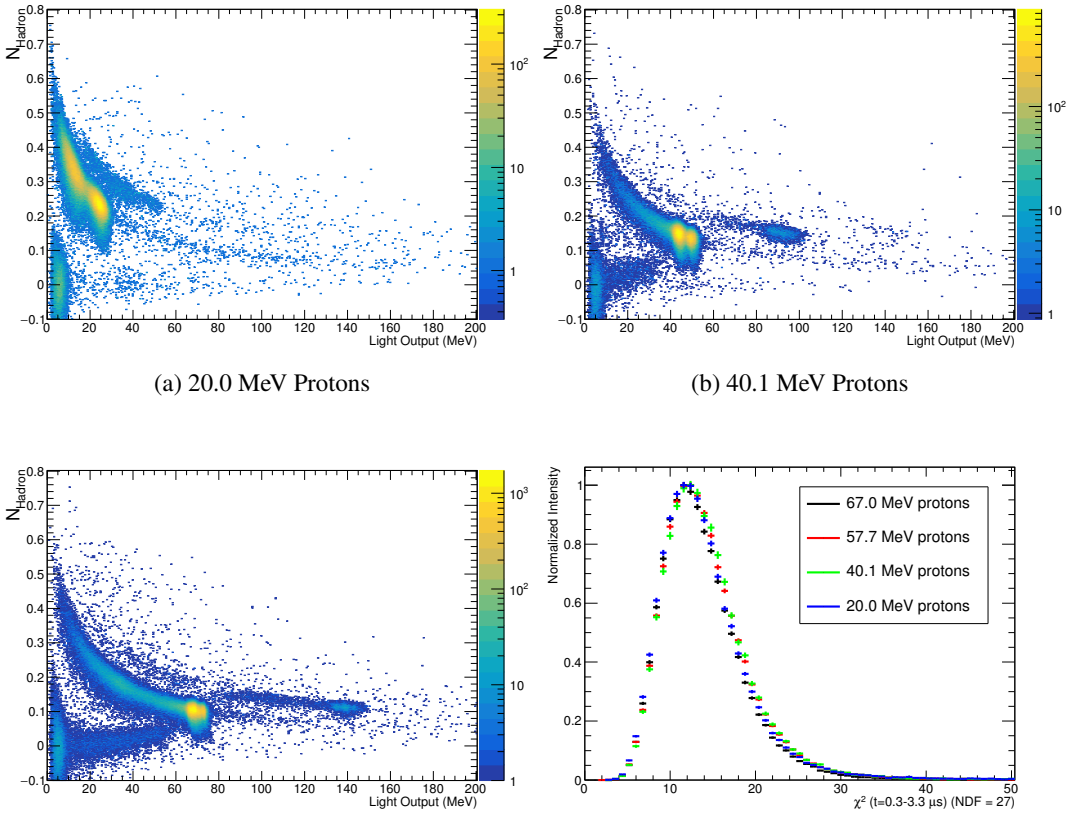

(a) 20.0 MeV Protons

(b) 40.1 MeV Protons

(c) 57.7 MeV Protons

(d)

Figure 10. Data pulse shape spectra for (a) 20.0, (b) 40.1 and (c) 57.7 MeV proton runs. (d) Fit χ^2 for pulses in main proton peaks. The number of degrees of freedom is 27. Note as discussed in Section 3.3 the errors used for computing the χ^2 are conservatively estimated as correlations within the time bin have not been taken into account, which produces a lower than expected χ^2.

5 Simulation Techniques for CsI(Tl) Pulse Shape Variations

5.1 Simulation Methodology

As outlined by the hadron component model developed in Section 3, the total light output of CsI(Tl), L_{Total}, can be divided into two components, L_γ and L_{Hadron}. The shape of CsI(Tl) scintillation pulse is then characterized by the relative intensity of the hadron component, N_{Hadron} defined in equation 3.7 in Section 3. The task of simulating the response of CsI(Tl) is thus reduced to calculating the quantities L_{Total} and L_{Hadron}. Once these quantities are known the output response of the CsI(Tl) dectector can be constructed from equation 5.1.

$$L(t) = (L_{Total} - L_{Hadron})R_\gamma(t) + L_{Hadron}R_{Hadron}(t) \tag{5.1}$$

Where $R_\gamma(t)$ and $R_{Hadron}(t)$ are the normalized detector response shapes for the photon and hadron scintillation emission shapes. In the particular case of PMT readout directly by a digitizer, $R_{Hadron}(t)$ is an exponential with decay time equal to τ_{Hadron} and $R_\gamma(t)$ is given by $I_\gamma(t)/L_\gamma$ where $I_\gamma(t)$ is defined in equation 3.3 and $L_\gamma = L_{Total} - L_{Hadron}$ by construction. For detector systems using additional shaping electronics, $R_\gamma(t)$ and $R_{Hadron}(t)$ should include the response of the signal chain electronics.

In order to compute L_{Total} and L_{Hadron}, equations 5.2 and 5.3 are used, respectively. In these equations the computed light output yields are expressed in calibrated units of photon equivalent energy deposited. Practical effects such as scintillation photon self-absorption in the crystal, absolute total light yield of the crystal and photo-detector responses are not modelled as these effects are not required for the simulation truth pulse shape spectrum results we present.

$$L_{Total} = \sum_{i}^{N_{Particles}} \int_{E_i^{Initial}}^{E_i^{Final}} B\left(\frac{dE}{dx}_i\right) dE_i \overset{MC}{\approx} \sum_{i}^{N_{Particles}} \sum_{j}^{N_i^{Step}} E_{ij}^{Step} B\left(\frac{dE}{dx}_{ij}^{avg}\right) \tag{5.2}$$

$$L_{Hadron} = \sum_{i}^{N_{Particles}} \int_{E_i^{Initial}}^{E_i^{Final}} f\left(\frac{dE}{dx}_i\right) B\left(\frac{dE}{dx}_i\right) dE_i \overset{MC}{\approx} \sum_{i}^{N_{Particles}} \sum_{j}^{N_i^{Step}} E_{ij}^{Step} f\left(\frac{dE}{dx}_{ij}^{avg}\right) B\left(\frac{dE}{dx}_{ij}^{avg}\right) \tag{5.3}$$

Where[2]:

[2]Values for ionization energy loss ($\frac{dE}{dx}$) are computed using the GEANT4 G4EmCalculator class.

$\mathrm{N}_{\mathrm{Particles}}$ = Total number of primary and secondary particles depositing energy inside the crystal volume.

E_i^{Initial} = Initial energy of the i^{th} particle.

E_i^{Final} = Final energy of the i^{th} particle.

$\frac{dE}{dx}_i = \frac{dE}{dx}(P_i, E_i) =$ Ionization energy loss of the particle i, P_i, with instantaneous energy E_i.

$B\left(\frac{dE}{dx}\right) =$ Birk's scintillation efficiency correction for CsI(Tl) defined to be normalized to 1 for 662 keV photon response. See Section 5.2 for additional discussion.

$f\left(\frac{dE}{dx}\right) =$ Hadron component emission function defined to compute the fraction of the instantaneous energy deposit which results in scintillation emission in the hadron scintillation component. See Section 5.3 for additional discussion.

$\mathrm{N}_i^{\mathrm{Step}} =$ Total number of simulation steps inside the crystal volume by the i^{th} shower particle.

$\mathrm{E}_{ij}^{\mathrm{Step}} =$ Energy deposited by the i^{th} shower particle in the j^{th} discrete step of a simulation.

$\frac{dE}{dx}_{ij}^{\mathrm{avg}} = \frac{dE}{dx}$ computed using the average kinetic energy between the post and pre-step simulation points.

In equations 5.2 and 5.3, $\overset{\mathrm{MC}}{\approx}$ is used to indicate the approximation made when Monte Carlo libraries such as GEANT4 [16] are used and the particles are tracked in discrete steps. In this case, using $\frac{dE}{dx}^{\mathrm{avg}}$ is needed to improve the accuracy of modelling the lower energy charged hadron energy deposits where the $\frac{dE}{dx}$ can vary substantially from step-to-step. We emphasize that when simulating the response, equations 5.2 and 5.3 are evaluated for all primary and secondary shower particles created in an event. In addition, the scintillation response of each particle is computed continuously as it deposits energy in the crystal in order to account for the changing $\frac{dE}{dx}$ of the particle along its track.

5.2 Pulse Amplitude Calculation

The Birk's scintillation efficiency defined as, $B(\frac{dE}{dx}) = \frac{dL}{dE}(\frac{dE}{dx})$, is known to vary for CsI(Tl) depending on the particle ionization energy loss, $\frac{dE}{dx}$ [22–27]. Studies of the scintillation

efficiency are typically conducted using measurements independent of the pulse shape variations by integrating the light emission for a long time period compared to the pulse length.

Models of the Birk's scintillation efficiency correction for inorganic scintillators have been discussed in the literature such that the correction empirically has the form of equation 5.4 [23]. This correction is defined to be normalized to 1.0 relative light output for 662 keV photons [23].

$$B(\tfrac{dE}{dx}) = \frac{a}{1 + b\tfrac{dE}{dx} + c(\tfrac{dE}{dx})^{-1}} \tag{5.4}$$

The applicability of two parametrizations for equation 5.4 have been evaluated for protons and alphas by references [23, 25]. These parametrizations, calculated by reference [23], are referred to as the Birk's and Modified Birk's parametrizations and are presented in Table 2.

Table 2. Parametrizations for equation 5.4 studied.

Parametrization	a	b	c	Reference
Birk's	1.08	1.29e-3	0	[23]
Modified Birk's	1.26	1.92e-3	7.47e-1	[23]
This Study	1.52	3.448e-3	2	-

We find that in order to simulate the CsI(Tl) response for protons while maintaining linearity for electromagnetic showers from electrons with energies from 2 MeV - 250 MeV, a re-parametrization of equation 5.4 is required. In particular, we consider three criteria for the scintillation efficiency of CsI(Tl) that a Birk's scintillation efficiency model must follow. These criteria are summarized by Figure 7 of reference [22] and are as follows.

1. As measured by reference [28], the relative light output of electromagnetic showers from electrons over the energy range of 20 MeV - 5.4 GeV must be linear. This requirement translates to $B(\frac{dE}{dx} < 2 \text{ MeV cm}^2/\text{g}) \approx 1$.
2. The relative light output of protons with kinetic energies in the approximate range of 10 - 100 MeV must be greater than 1.
3. The relative light output of low energy heavy particles such as alphas and ions is less than one. This requirement roughly translates to $B(\frac{dE}{dx} > 200 \text{ MeV cm}^2/\text{g}) < 1$.

In order to satisfy these requirements, we use a re-parametrized version of equation 5.4 defined by equation 5.5 with the parameters outlined in Table 2.

$$B_{\text{This Study}}(\tfrac{dE}{dx}) = \begin{cases} 1 & \tfrac{dE}{dx} < 10 \text{ MeV cm}^2/\text{g and } B(\tfrac{dE}{dx}) < 1 \\ B(\tfrac{dE}{dx}) & \text{for all other values of } \tfrac{dE}{dx} \text{ and } B(\tfrac{dE}{dx}) \end{cases} \tag{5.5}$$

We plot in Figure 11 the three parametrizations for $B(\frac{dE}{dx})$.

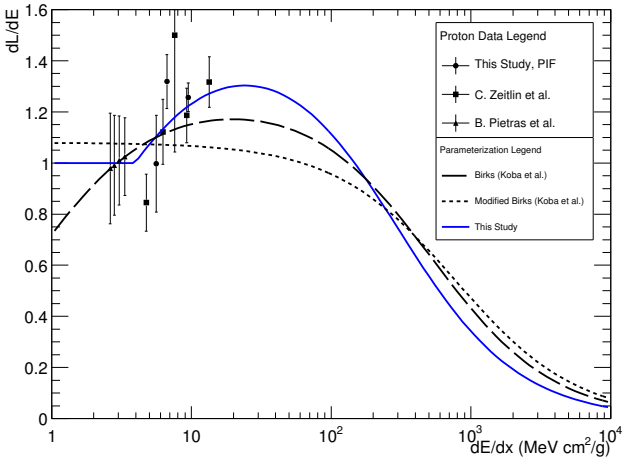

Figure 11. Three parametrizations for CsI(Tl) scintillation efficiency corrections overlaid with experimental data from PIF and references [24] and [25]. Non-PIF proton data points are read from plots in references [24] and [25].

The scintillation efficiency correction parametrization we propose was computed such that the simulated light output of protons at initial kinetic energies of from 2 - 250 MeV are in agreement with the CsI(Tl) response measured with our proton testbeam data and other proton testbeam data in literature from references [24] and [25]. In addition we also require that the three criteria outlined above are satisfied, specifically that the scintillation response to electromagnetic showers is unchanged. Comparisons for the simulated proton and electron response using three parametrization in Table 2 with data are shown in Figures 12a and 12b.

In Figure 12a the simulated CsI(Tl) response to protons is compared to proton testbeam data for the three parametrizations in Table 2. These simulations demonstrate that, unlike the other parametrizations, the re-parametrization used in this study accurately reproduces the lower energy proton data in literature while simultaneously matching the higher energy proton response of the Modified Birk's parametrization. In Figure 12a is it also observed that the Birk's scintillation efficiency corrections can be a significant effect for protons in the low energy region as the light output can reach up to approximately 1.3 times the response with no correction.

In Figure 12b the same parametrizations are evaluated for electrons. Further support for our re-parametrization is observed in these results as both the Birk's and Modified Birk's parametrizations do not maintain a unity response for electromagnetic showers. This indicates that the agreement of the Modified Birk's for the high energy proton response also results in a reduction in the electromagnetic response of CsI(Tl) which is not observed in measurements reported in literature [22, 28]. From these results we conclude that our re-parametrization should be used to simulate the total light emission of CsI(Tl).

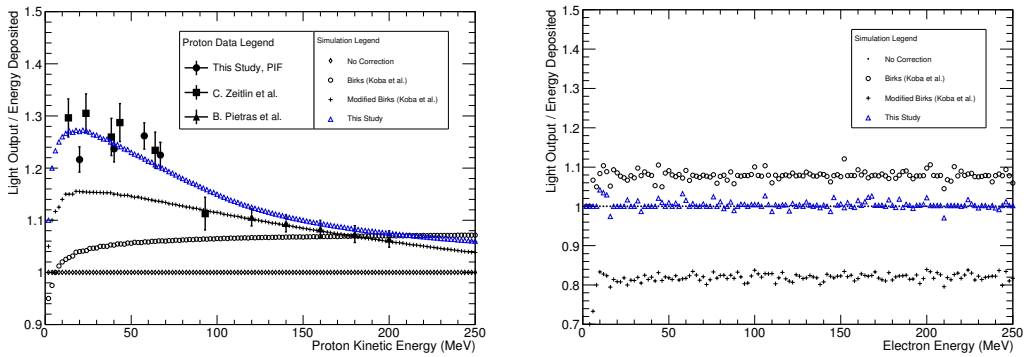

(a) Proton response comparison.

(b) Electron response comparison.

Figure 12. Comparisons of data and MC for simulations employing the three Birk's scintillation efficiency parametrizations outlined in Table 2. Non-PIF proton data points are read from the plots in references [24] and [25].

Using the full simulation approach discussed above to evaluate the scintillation efficiency parametrizations is advantageous as all effects of secondary particle production are included in the calculation. Past studies [22, 23] evaluating $\frac{dL}{dE}$ have used an alternate approach where data taken by various particle types and successive kinetic energies is differentiated and overlaid onto plots of $\frac{dL}{dE}$ such as Figure 11. In the ideal case where the only energy deposited in the event is from the initial primary particle, this technique can be used to compute to the magnitude of $\frac{dL}{dE}$ at a specific value of $\frac{dE}{dx}$. As an additional test of the models we overlay our PIF proton data combined with proton data in references [24] and [25] onto Figure 11. From this analysis approach we again find agreement as expected between our scintillation efficiency re-parametrization with proton testbeam data.

5.3 Pulse Shape Calculation

In the literature the observed pulse shape variations of CsI(Tl) have been correlated with the ionization energy loss of the particle as early as 1959 by Storey et al. where the CsI(Tl) pulse shapes variations were empirically shown to be related to the ionization energy loss of the particle, $\frac{dE}{dx}$ [1]. As a result we assume that the hadron component emission function can be written as $f(\frac{dE}{dx})$, independent of the particle type.

From the neutron data in Figure 6 we begin by estimating the shape and bounds for $f(\frac{dE}{dx})$. As muons and electrons have $N_{Hadron} = 0$ we expect the lower bound $f(\frac{dE}{dx} < 2\ \text{MeV cm}^2/\text{g}) \approx 0$ as this is the ionization region for these particles. In addition, the maximum value of $f(\frac{dE}{dx})$ can also be bound from Figure 6 to be approximately 60-70% emission. This maximum emission is observed for neutron induced alpha and $E_k < 1$ MeV proton events which have $\frac{dE}{dx}$ values beyond 100 MeV cm^2/g. From these bounds it can thus be extrapolated that in the region of approximately 2 MeV cm^2/g $< \frac{dE}{dx} < 100$ MeV cm^2/g, $f(\frac{dE}{dx})$ will transition from 0 to 60-70%. Further evidence for this transition

region is established by the shape of the single proton band in the proton data shown in Figure 9a and Figures 10a - 10c. As the kinetic energy of the primary proton decreases and approaches higher values for $\frac{dE}{dx}$, the pulse shapes continuously approach higher values for N_{Hadron}. From this observation we are able to extract part of the emission function from the single proton bands in the proton data we collected.

Using the single proton bands present in the proton data shown in Figures 9a and 10a-10c we extract $f(\frac{dE}{dx})$ by assuming the proton events to be an ideal case consisting of no secondary shower particles and only proton ionization. Using GEANT4 we verify this assumption holds for protons with kinetic energies less than 100 MeV. In this case, the proton of initial kinetic energy E_k will ionize until it stops in the crystal volume resulting in a total energy deposit equal to the initial proton kinetic energy. The hadron scintillation emission of the final pulse can then be written as equation 5.6.

$$L_{Hadron}(P\text{=proton}, E_k) = \int_0^{E_K} B(P,k) f(P,k) dk \tag{5.6}$$

Where k is the instantaneous kinetic energy of the proton. We solve equation 5.6 to get an expression for the emission function as a function of the instantaneous proton kinetic energy as shown in equation 5.7.

$$f(P\text{=proton}, E_k) = \frac{1}{B(\frac{dE}{dx})} \frac{d}{dk}\bigg|_{E_k} L_{Hadron}(P\text{=proton}, k) \tag{5.7}$$

Applying equation 5.7 to the single proton bands in the PIF proton beam data in Figure 9a and Figures 10a - 10c we plot the values of $f(P\text{=proton}, E_k)$ in Figure 13.

As the goal is to extract the emission function as a function of $\frac{dE}{dx}$, independent of particle type, the final step in computing $f(\frac{dE}{dx})$ is to convert from proton kinetic energy to $\frac{dE}{dx}$. After this conversion[3] the data values for $f(\frac{dE}{dx})$ extracted from the proton bands is shown in Figure 14.

From Figure 14 we see that using the single proton band we are able to extract the hadron emission intensity in a limited ionization region of 5-35 MeV cm^2/g. In order to extrapolate to the higher and lower $\frac{dE}{dx}$ regimes we use equation 5.8.

$$f(P\text{=proton}, k) = \frac{A}{1 + (Bk)^C} \tag{5.8}$$

The functional form of equation 5.8 is empirically driven as it is a simple analytic function that well describes the data in Figure 13 and will satisfy the boundary conditions discussed above. In order to determine the parameters for equation 5.8 we evaluate equation 5.6 numerically in 0.01 MeV step sizes and fit directly to the N_{Hadron} vs L_{Total} PIF proton data points in Figure 15 and overlay the numerical fit result in violet in this Figure. From the fit we find the parameters for equation 5.8 to be $A = 0.612 \pm 0.003$, $B = 0.194 \pm 0.001$ MeV^{-1}

[3]We perform the conversion from proton kinetic energy to ionization energy loss ($\frac{dE}{dx}$) using the GEANT4 G4EmCalculator class.

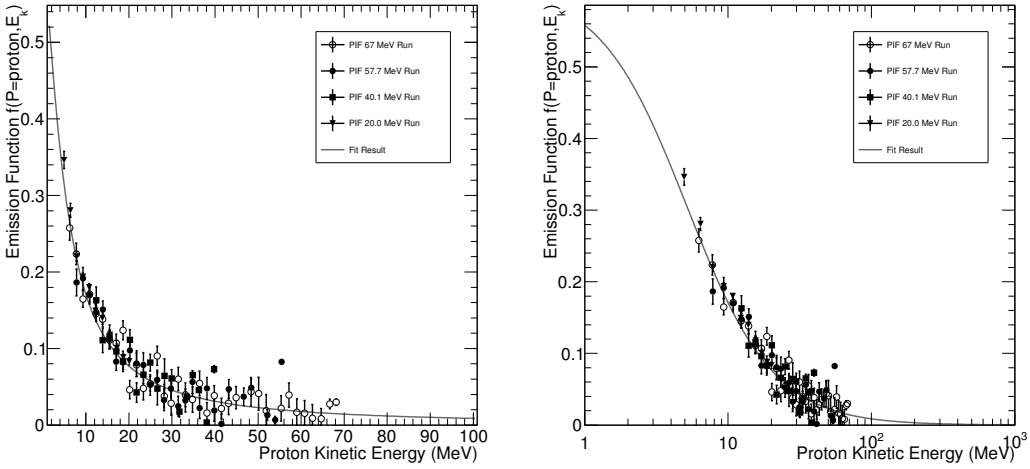

(a) Linear scale. (b) Log scale.

Figure 13. Instantaneous hadron scintillation component emission extracted from single proton bands in PIF proton data using equation 5.7. Analytic result for equation 5.8 is overlaid.

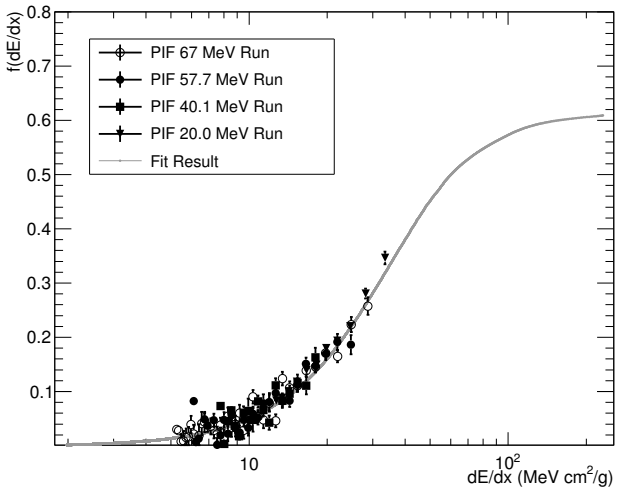

Figure 14. Instantaneous hadron scintillation component emission as a function of $\frac{dE}{dx}$. Analytic result for equation 5.8 is overlaid.

and $C = 1.430 \pm 0.004$. We also overlay equation 5.8 in Figure 13 and in Figure 14 by converting from proton kinetic energy to $\frac{dE}{dx}$. We observe the measured data points for $f(\frac{dE}{dx})$ are in agreement with the numerical fit result as expected. In addition we confirm our expectation for the bound of $f(\frac{dE}{dx})$ at high and low $\frac{dE}{dx}$.

5.4 Simulation Validation with Proton Data

We have now developed the tools to compute the CsI(Tl) pulse amplitude and pulse shape based on the shower particles of the event by using equations 5.2 and 5.3, respectively. As was done with the scintillation efficiency corrections validation, we validate the proton ionization pulse shape simulations by simulating protons runs in the kinetic energy range of 2 to 70 MeV at 2 MeV intervals and extracting the L_{Total} and L_{Hadron} for each simulated proton energy run. The results for the simulated proton response are overlaid in Figure 15 with the N_{Hadron} vs pulse amplitude values measured in the PIF proton data runs discussed in Section 4. From Figure 15 we observe reasonable agreement between data and simulation demonstrating we can accurately simulate the CsI(Tl) scintillation response to protons. This result also demonstrates that the instantaneous hadron scintillation component emission can be computed from the ionization energy loss of the interacting particles of the proton events. A side-by-side data and simulation comparison for 67.0 MeV protons is shown in Figure 9a. This side-by-side comparison is discussed in Section 4 and illustrates that in addition to proton ionization events, the pulse shapes from the proton inelastic interactions are also reproduced in the simulation.

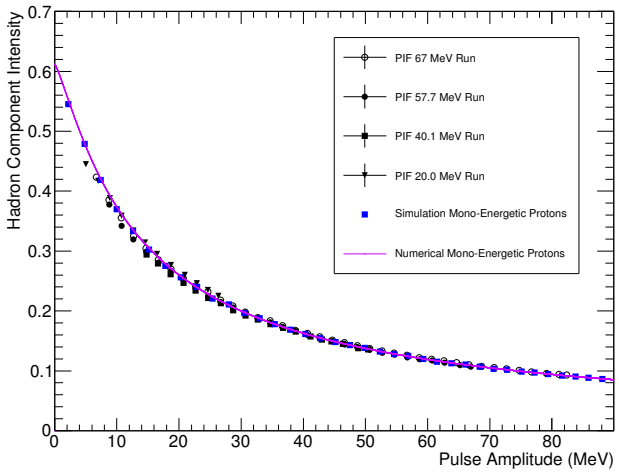

Figure 15. Hadron component intensity as a function of pulse amplitude for the single proton band in the PIF proton data runs shown in Figures 9a and 10a- 10c. The fit result to equation 5.6 is overlaid in violet. Simulation results computed using equations 5.2 and 5.3 are overlaid as blue squares over the full range of 2-88 MeV.

5.5 Simulation Validation with PIF Neutron Data

Using the PIF neutron run we can further validate our simulation methods. The energy spectrum of the PIF neutrons is expected to approximately follow a 1/E energy distribution with a maximum energy of 500 MeV [17]. We note that exact knowledge of the neutron

energy spectrum is not critical for pulse shape validation as we expect this to only effect the relative rate of the different neutron interactions in CsI(Tl) resulting in different relative intensities in the two dimensional pulse shape scatter plots. As long as the energy threshold for an interaction is reached, the location of the hadron bands in the pulse shape spectra is expected to be independent of the neutron energy distribution.

We simulate in GEANT4 neutrons following a 1/E energy distribution between kinetic energies of 1-500 MeV and compute the total light output and total hadron component light output based on the primary and secondary particles of the event. Note detector resolution effects such as electronic noise and photo-electron statistics are not simulated. Simulation truth results for the pulse shape spectrum of neutrons is shown in Figure 16 with points colour coded based on the secondary charged hadrons generated from the neutron interaction in the event. Note for all events in Figure 16 the initial primary particle was a neutron. This simulation result shows the same band structure as was observed in the neutron data presented in Figure 6.

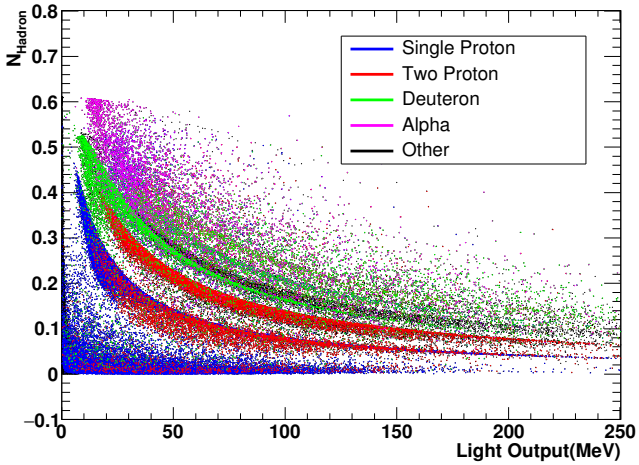

Figure 16. Simulation truth pulse shape distributions for neutron events following a 1/E energy spectrum. Detector resolution is not modelled.

As observed in Figure 16, in addition to the single proton band, the additional band structures arising from other secondary hadrons produced from inelastic neutron interactions are observed. Detailed comparisons between data and simulation projections are plotted for different energy ranges in Figure 17. From these projections it is observed that in addition to correctly simulating the single proton response, the location of the peaks from the multi-proton and deuteron bands are in reasonable agreement between data and MC. This result confirms that although the hadron component emission function was extracted using proton data, when expressed as a function of $\frac{dE}{dx}$ the hadron scintillation component emission function has universal application to other charged hadrons. Note the excess of

events at $N_{Hadron} = 0$ in the data in the lower energy projections is due to the cosmic muon background.

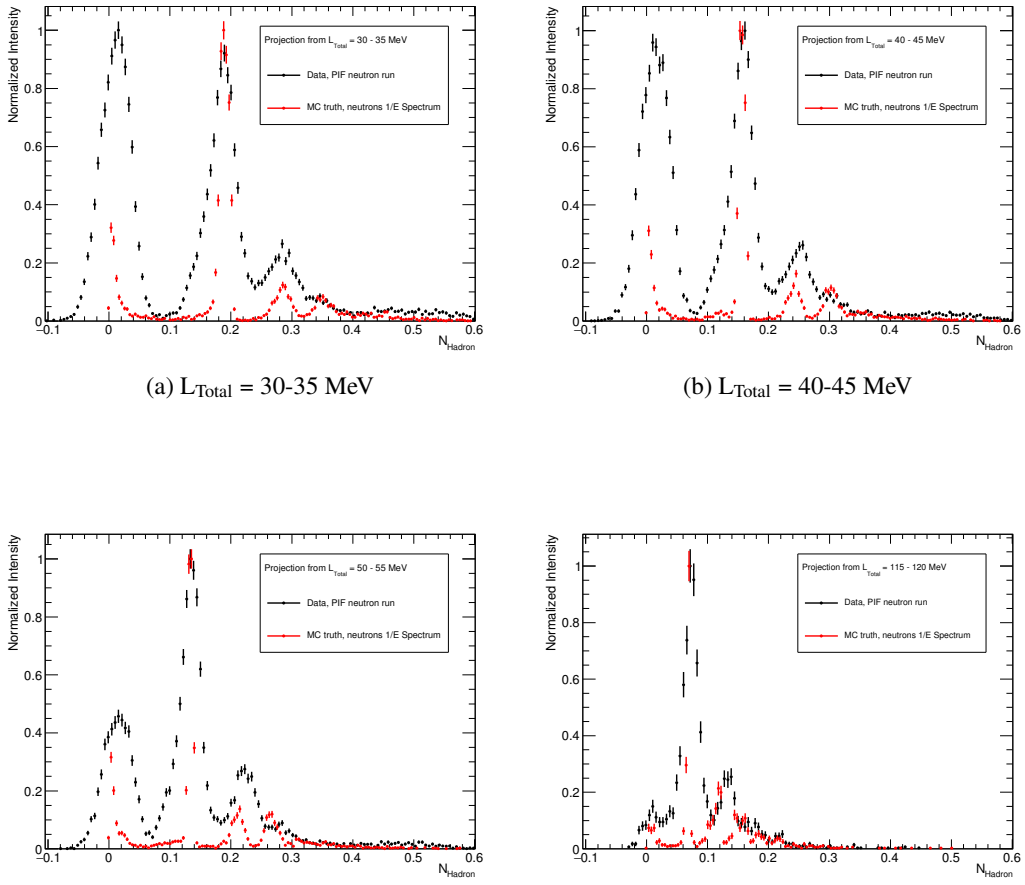

(a) L_{Total} = 30-35 MeV

(b) L_{Total} = 40-45 MeV

(c) L_{Total} = 50-55 MeV

(d) L_{Total} = 115-120 MeV

Figure 17. Data and simulation projections comparing PIF neutron run to MC truth for 1/E neutron energy distributions. Note the cosmic muon background is not included in the simulation and as a result the data has an excess of events at $N_{Hadron} = 0$ in the lower energy projections. Note also that detector resolution effects are not modelled in the simulation.

5.6 Discussion of Simulation Validation Results

In order to improve the accuracy of these simulations additional studies in the high (> 35 MeV cm^2/g) and low (< 5 MeV cm^2/g) $\frac{dE}{dx}$ regions should be pursued to verify our extrapolation of the emission function to these regions. Such studies could potentially be completed using alpha beams for the higher $\frac{dE}{dx}$ region and high kinetic energy (> 80 MeV) protons for the low $\frac{dE}{dx}$ region.

In addition to improving the accuracy for the simulations of the scintillation response of CsI(Tl), the above simulation techniques now give the ability to use CsI(Tl) PSD for

evaluation of the GEANT4 modelling for hadron material cross-sections in CsI(Tl). As accurate hadronic material interaction modelling is important for minimizing the systematic errors in precision measurements made in nuclear and particle physics measurements, improving hadronic cross-section modelling could potentially have a large impact on a broad range of applications which make use of GEANT4 simulations. Specifically by performing two dimensional cuts on the pulse shape distributions one could isolate the energy deposited spectra for specific secondary interactions and in principle measure the cross-sections for the specific inelastic interactions in CsI. This type of analysis for example has been explored, using data only, by reference [29] to separate photon and proton interactions in CsI(Tl). The simulation techniques we developed now allow for data vs simulation comparisons for these studies.

6 Pulse Shape Discrimination for Neutral Hadron vs Photon Separation in e^+e^- Collider Experiments

One of the central questions to determine if PSD will be viable for neutral hadron detection in e^+e^- collider experiments deploying CsI(Tl) crystals (such as Belle II and BESIII) is: will the energy deposited from the secondary charged hadrons of a hadronic shower be significant compared to the electromagnetic component of the shower, so that the CsI(Tl) pulse shape variations can be measured in the crystals associated with a hadronic shower candidate? In this section we address this question using the simulation methods developed and demonstrate the potential for neutral hadron identification using CsI(Tl) PSD. To study cluster effects we simulate in GEANT4 a 5×5 CsI(Tl) crystal cluster constructed from crystals with rectangular prism geometry and dimensions of $5 \times 5 \times 30$ cm^3. These crystal dimensions are similar to the electromagnetic calorimeters used in the Belle II and BESIII experiments [9, 10]. K_L^0 and neutrons of fixed momenta of 0.5 and 1 GeV/c are sent into the centre of the cluster and the quantities $\mathrm{L_{Total}}$ and $\mathrm{L_{Hadron}}$ are computed for all crystals in the cluster. Photons with energy uniformly distributed between 0.2-1 GeV are also generated to serve as the electromagnetic shower control sample. To ensure the particle interacted with the cluster, only events with total cluster light output ($\mathrm{L_{Total}^{Cluster}}$) greater than 10 MeV are analysed. $\mathrm{L_{Total}^{Cluster}}$ is defined as the sum of the light output from all the crystals in the 5×5 matrix of crystals. For the 0.5 and 1 GeV/c K_L^0 samples 44% and 56% of generated events pass the 10 MeV energy threshold, respectively. For the 0.5 and 1 GeV/c neutron samples 41% and 49% of generated events pass the 10 MeV energy threshold, respectively.

6.1 Crystal Level Analysis

In Figure 18 we plot the computed hadron intensity distribution vs total light output for the cluster crystals in showers from 1 GeV/c K_L^0's. From this we see that a large variety of hadron pulse shapes are produced in the cluster crystals. Compared to the distributions in the PIF neutron data, it is observed that the crystals in the high momentum K_L^0 showers

produce similar band structures. From simulation truth we find that in addition to single and double proton bands, there are pulse shape bands also originating from higher multiples such as triple and quadruple proton events and also multiples of secondary deuterons and tritons. In the region of high pulse amplitude and high hadron intensity, a smoother distribution is observed. Pulses in this region are produced by combinations of different secondary hadrons.

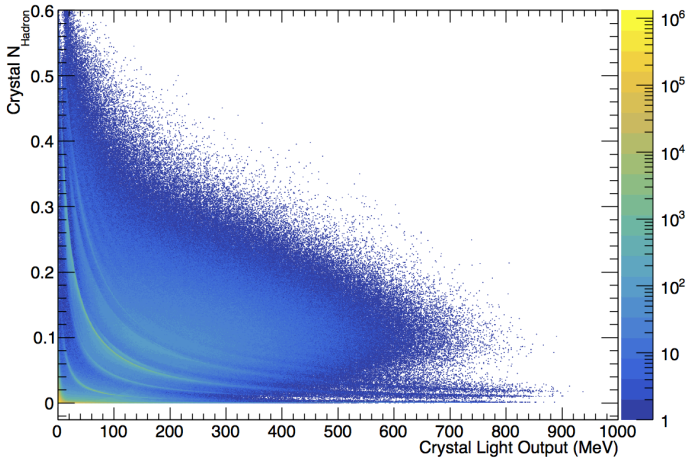

Figure 18. Calculated pulse shapes of cluster crystals contained in hadronic showers from simulated 1 GeV/c (620 MeV kinetic energy) K_L^0.

In addition to the hadron pulse shapes, a number of crystals in the 1 GeV/c K_L^0 clusters result in photon pulse shapes due to the electromagnetic component of the shower. In principle electromagnetic vs hadronic cluster separation however would only require a minimum of one crystal in the cluster to contain large contribution from the hadron scintillation component to allow for that cluster to be classified as hadronic. This is because electromagnetic showers from photons are expected to consistently have zero hadron component intensity, independent of photon energy. To estimate the performance of PSD for neutral hadron ID we compute the fraction of clusters which contained at least one crystal with a significant contribution from the hadronic scintillation component. For a given detector system the pulse shape resolution of the system will determine the minimum amount of hadron component light output which can be resolved. This resolution will be the limiting factor in the effectiveness of PSD. Factors which are expected to degrade the pulse shape resolution such as electronic noise and pulse pile-up from background sources will vary between different detector systems. To illustrate the potential for hadron identification, we define the quantity $\mathrm{L}_{\mathrm{Hadron}}^{\mathrm{Threshold}}$ to be the minimum hadron component light output which a detector system can resolve in the pulse shapes. In order to classify a cluster as hadronic we then require that the hadron component light output of at least one crystal

in the cluster is greater than $L_{Hadron}^{Threshold}$. We show in Figure 19 the efficiency for identifying hadronic clusters as a function of $L_{Hadron}^{Threshold}$.

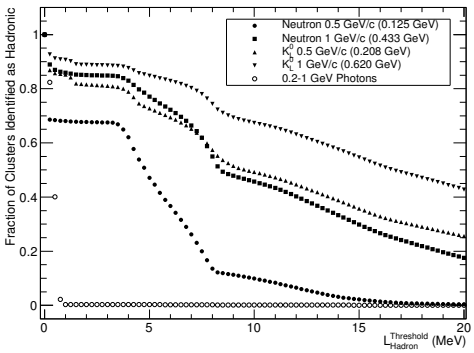

Figure 19. Fraction of clusters with $L_{Total}^{Cluster} > 10$ MeV that contained a minimum of one cluster with $L_{Hadron} > L_{Hadron}^{Threshold}$.

From Figure 19 it is predicted that if a detector is able to resolve 3 MeV or less of hadron component light output then PSD alone has the potential to provide excellent performance for neutral hadron vs photon separation as we see that a very small fraction of photon clusters are mis-identified as hadrons. Quantitatively, at $L_{Hadron}^{Threshold} = 3$ MeV the percentage of photons mis-identified is $< 0.35\%$ and decreases to < 0.14 % at $L_{Hadron}^{Threshold} = 10$ MeV. The majority of photon clusters containing crystals with $L_{Hadron} > 3$ MeV are found to be from events where the photon underwent a photo-nuclear interaction resulting in a secondary proton being produced in the cluster.

Examining the change in hadron identification efficiencies with increasing $L_{Hadron}^{Threshold}$, three $L_{Hadron}^{Threshold}$ regions are identified where the efficiency has a distinct trend. In the initial region corresponding to $L_{Hadron}^{Threshold} < 3$ MeV it is observed that the hadron identification efficiency for all hadron samples studied is approximately constant demonstrating that there is not a significant gain in setting $L_{Hadron}^{Threshold} < 3$ MeV. This is related to the minimum energy threshold for secondary proton production by a hadronic interaction in CsI(Tl). Specifically for neutrons, the kinetic energy threshold for secondary proton production in CsI is 8 MeV [14]. As a result the minimum secondary proton kinetic energy generated in a single proton neutron scatter event is expected to be approximately 8 MeV. This 8 MeV kinetic energy threshold can be seen in our neutron data presented in Figure 6 where it is observed that 8 MeV is the total light output threshold for pulses with hadron intensity greater than 10%. Now considering the event where a single 8 MeV proton is produced from a hadronic scatter in a crystal, we expect from the proton data shown in Figure 15 that this will result in 0.38×8 MeV = 3.0 MeV of hadron component light output. Thus due to the CsI(Tl) energy threshold for secondary charged hadron production, ~3 MeV is the minimum magnitude of hadron component light output expected in a hadronic scatter.

In the region of 3 MeV $< L_{Hadron}^{Threshold} <$ 8 MeV these simulations predict that as $L_{Hadron}^{Threshold}$ increases there is a noticeable drop in identification efficiency for all particles. This drop is a result of the $L_{Hadron}^{Threshold}$ surpassing the hadron component light output of the single proton band in the pulse shape spectrum. As single proton production is dominant for lower energy hadrons, the impact of not resolving the single proton band is largest for the 0.5 GeV/c (0.125 GeV kinetic energy) neutrons. In the final region of $L_{Hadron}^{Threshold}$ >8 MeV, the efficiency does not drop as quickly as the previous region. This is observed for all particles studied and is because in this region of high hadron component light out, multiple different charged hadrons are produced in the hadronic shower creating large amounts of hadron component light output.

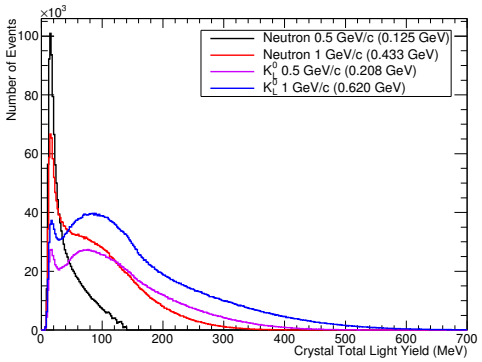

Figure 20. Total energy distribution for cluster crystals with $L_{Hadron} > 3$ MeV.

To study the energy distribution of hadron identified crystals we plot in Figure 20 the distribution of the total light output for all cluster crystals with $L_{Hadron}^{Threshold}$ >3 MeV. From Figure 20 we see for the higher kinetic energy samples studied, that a significant number of hadron identified cluster crystals are expected to also have relatively high energy deposits. We now consider a more constrained case where an experiment might only be able to characterize higher energy deposits in the calorimeter. We study this by applying a tighter criteria for hadron identification where in addition to a cluster containing a crystal with $L_{Hadron} > L_{Hadron}^{Threshold}$, we also require that the same crystal has a total light output greater than 50 MeV in order to be identified as hadronic. We show in Figure 21, the expected hadron identification efficiencies after applying this tighter criteria. Compared to the results shown in Figure 19 where no crystal energy threshold was applied, we see that applying a 50 MeV crystal total light output threshold has the greatest impact for all hadron samples on the hadron detection efficiencies for low $L_{Hadron}^{Threshold}$ values. This means that detectors with good pulse shape resolution will have the largest impact. This result is expected as events with low hadron component light output are typically from lower energy single proton energy deposits. The drop in efficiency in Figure 21 thus is a result of now requiring the threshold hadronic interaction to be a single secondary proton with total light output above 50 MeV. For a single proton event with total light output of 50 MeV

the equivalent hadron component light output is ~7 MeV as shown in our proton data in Figure 15. As a result the 50 MeV total light output threshold results in the efficiency in the low $L_{Hadron}^{Threshold}$ region to be reduced to approximately the value of the efficiency curve in Figure 19 evaluated at $L_{Hadron}^{Threshold} = 7$ MeV. For the region of $L_{Hadron}^{Threshold} > 8$ MeV in Figure 21 the detection efficiency is not significantly affected by the 50 MeV total light output requirement as hadron events in this region of high hadron component light output will typically also have high total light output and pass the 50 MeV cut.

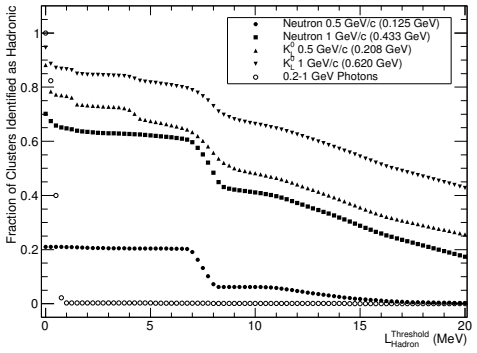

Figure 21. Fraction of clusters studied that contain one crystal with both $L_{Hadron} > L_{Hadron}^{Threshold}$ and $L_{Total} > 50$ MeV.

6.2 Cluster Level Analysis

The analysis's presented in Figures 19 and 21 are completed using the cluster crystal information individually. Considering an alternative algorithm for hadron shower identification, we now combine the crystal information of a 5×5 cluster and compute the cluster hadron component light output, $L_{Hadron}^{Cluster}$, by summing the hadron component light output of all cluster crystals. Analogous to the single crystal, the cluster hadron intensity defined by $L_{Hadron}^{Cluster}/L_{Total}^{Cluster}$ is also computed. In Figure 22 we plot the distribution of cluster hadron intensity vs $L_{Total}^{Cluster}$, for the same 1 GeV/c K_L^0 events as Figure 18. Using the cluster variables it is predicted that the individual band structures are now less prominent and the intensity of the events in the smooth high energy and high hadron intensity region increases compared to the individual crystal distribution in Figure 18. This is expected to improve the PSD performance as pulses in this region have the largest magnitude of hadron component light output.

We evaluate the hadron identification efficiency using the cluster variables by plotting in Figure 23a the fraction of clusters with $L_{Hadron}^{Cluster} > L_{Hadron}^{Threshold}$ as a function of $L_{Hadron}^{Threshold}$. Comparing with the crystal level analysis in Figure 19, it is predicted for the 0.5 and 1 GeV/c K_L^0 that combining the crystal information in the cluster will have significant impact in improving the $L_{Hadron}^{Threshold} > 10$ MeV region of the efficiency plot. This is because the high energy particles produce many secondary charged hadrons throughout the cluster.

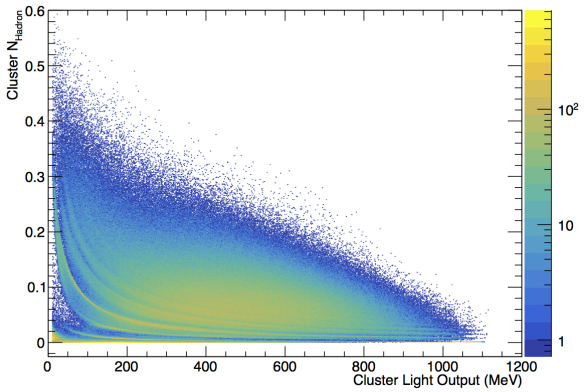

Figure 22. Calculated cluster hadron intensity vs total light output distribution for 1 GeV/c (620 MeV) K_L^0.

This result demonstrates that detectors with higher noise resulting in high $L_{Hadron}^{Threshold}$ values can have significant benefit from combining the crystal information in a cluster. In the 0.5 GeV/c neutron case the increase in performance is not as significant compared to the higher energy neutron and K_L^0 cases. This is because the dominant interaction for the low energy neutrons is single proton production which is expected to be contained in a single crystal volume thus the other cluster crystals will likely not contain additional hadron component light output.

In Figure 23b we consider a second scenario of the cluster algorithm where only cluster crystals with greater than 50 MeV of total light output are used for computing $L_{Hadron}^{Cluster}$. In this case the hadron identification efficiencies are shown in Figure 23b. In Figure 23b we see a similar trend as observed in the crystal level analysis when only high energy deposits were used for hadron identification, that is the hadron identification efficiently for low values of $L_{Hadron}^{Threshold}$ are the most affected by the energy threshold.

6.3 Discussion of Neutral Hadron PSD Results

In the above section we demonstrate that the hadron component light output from charged secondary particles in hadronic showers will be large enough for CsI(Tl) PSD to provide discrimination between electromagnetic and hadronic showers. The analysis presented in the previous sections used only the magnitude of the hadron component light output as a discrimination variable and predicts the ability to cleanly discriminate between neutral hadron clusters with high efficiency using PSD alone. In general we observe the trend that the PSD performance is predicted to improve with increasing hadron energy as multi-hadron production becomes more likely. It is important to recognize that this PSD observable uses information that is independent of information used in existing techniques to discriminate between hadronic and electromagnetic showers, such as differences in the spatial distribution of energy deposited by hadronic and electromagnetic showers as captured in e.g.

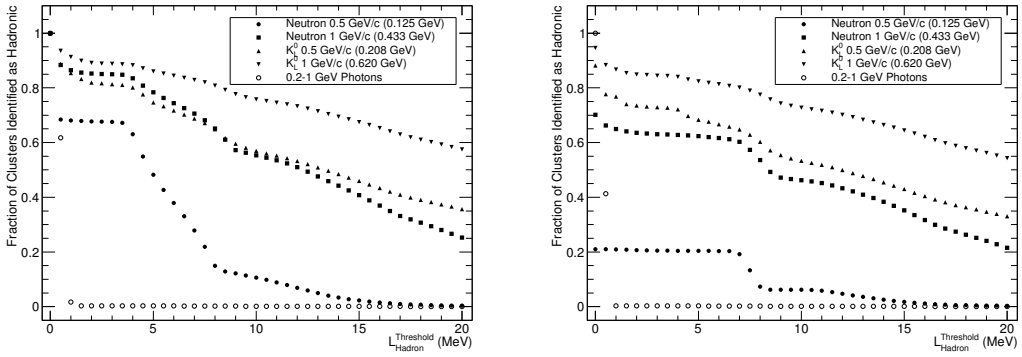

Figure 23. a) Fraction of clusters with $L_{Hadron}^{Cluster} > L_{Hadron}^{Threshold}$. b) Fraction of clusters with $L_{Hadron}^{Cluster} > L_{Hadron}^{Threshold}$ where $L_{Hadron}^{Cluster}$ is computed using only cluster crystals with total light output greater than 50 MeV.

lateral shower shape variables and longitudinal shower properties. Combining the PSD information with these existing shower spatial discriminators in multivariate analyses will lead to significantly improved performance in distinguishing between hadronic and electromagnetic showers. Moreover, the differences in PSD characteristics for K_L^0 and neutrons suggest that there is potential for using CsI(Tl) PSD as a tool for identifying different types of hadrons.

7 Conclusions

The results in this paper show that PSD can be an effective tool for neutral hadron vs photon separation at current and upcoming high energy physics experiments using CsI(Tl) calorimeters. With experiments such as Belle II and BESIII applying FPGA waveform analysis in the front-end electronics, online pulse shape characterization is now feasible for these experiments. In addition we focus in this article on using CsI(Tl) scintillators for PSD however we note that the same principles we use may be applied to other inorganic scintillators which are known to have analogous pulse shape discrimination properties, such as NaI(Tl) [14].

To demonstrate the potential for CsI(Tl) PSD we began by using neutron data and proton beam data collected at the TRIUMF PIF to analyse the pulse shape differences observed in CsI(Tl) for photon and charged hadron energy deposits. From the pulse shape differences, we demonstrated that the pulse shape variations observed in CsI(Tl) for the charged hadron energy deposits can be characterized using a third scintillation component with decay time of 630 ± 10 ns, referred to as the hadron scintillation component. This defined a new hadron scintillation component model for CsI(Tl) where the pulses shapes are characterized by the relative intensity of the hadron scintillation light output to the

total light output. This new method for pulse shape description reduces the number of parameters required to describe the pulse shape variations in CsI(Tl) compared to present techniques.

Techniques for computing the total and hadron scintillation component light output as a function of the shower particle's instantaneous ionization energy loss were developed in order to simulate these pulse shape variations. By incorporating these methods in the GEANT4 simulation libraries we were able to reproduce the pulse shape distributions observed in the neutron and proton data.

Using the pulse modelling and simulation techniques, the predicted pulse shape vs pulse amplitude spectra for $5 \times 5 \times 30$ cm^3 CsI(Tl) crystals in a 5×5 array was computed for hadronic showers generated by 0.5 and 1 GeV/c samples of simulated neutron and K_L^0 mesons entering the 5×5 array. Using a couple of simple identification algorithms we demonstrate that if the detector system can resolve the single proton band, excellent separation efficiency can be achieved for K_L^0 vs photon clusters using PSD alone.

Acknowledgments

The authors would like to thank TRIUMF for provision of the PIF facility as well its support and kind hospitality. We particularly thank E.W. Blackmore and M. Trinczek for their operation of the PIF facility and technical assistance provided for this experiment. The assistance of C. Hearty, J. Coffey and Z. Li during data-taking is also gratefully acknowledged. This work is supported by the Natural Sciences and Engineering Research Council (Canada).

References

[1] R. S Storey et al., *The Fluorescent Decay of CsI(Tl) for Particles of Different Ionization Density*, *Proc. Phys. Soc.* **72** (1958) pg. 1

[2] F. Benrachi et al., *Investigation of the Performance of CsI(Tl) for Charged Particle Identification by Pulse-Shape Analysis*, *Nuc. Instr. Meth. A* **281** (1989) pg. 137

[3] W. Skulski and M. Momayezi, *Particle identification in CsI(Tl) using digital pulse shape analysis*, *Nuc. Instr. Meth. A* **458** (2001) pg. 759

[4] D. Drain et al., *The Particle Detector Array AMPHORA*, *Nuc. Instr. Meth. A* **281** (1989) pg. 528

[5] M. Alderighi et al., *Particle identification method in the CsI(Tl) scintillator used for the CHIMERA 4 π detector*, *Nuc. Instr. Meth. A* **489** (2002) pg. 257

[6] B. Aubert et al., *The BABAR detector*, *Nuc. Instr. Meth. A* **479** (2002) pg. 1

[7] B. Aubert et al., *The BABAR detector: Upgrades, operation and performance*, *Nuc. Instr. Meth. A* **729** (2013) pg. 615

[8] A. Abashian et al., *The Belle Detector*, *Nuc. Instr. Meth. A* **479** (2002) pg. 117

[9] T. Abe et al., *Belle II Technical Design Report*, *KEK-REPORT-2010-1* (2010)

[10] M. Ablikim et al., *Design and Construction of the BESIII Detector*, *Nuc. Instr. Meth. A* **614** (2010) pg. 345

[11] V. Aulchenko et al., *Time and energy reconstruction at the electromagnetic calorimeter of the Belle-II detector*, 2017 *JINST* **12** C08001

[12] B. Aubert et al., *Observation of CP violation in the B^0 meson system*, *Phys. Rev. Lett.* **87**, (2001) 091801

[13] A. Abashian et al., *Measurement of the CP violation parameter* $\sin 2\phi_1$ *in* B^0_d *meson decays*, *Phys. Rev. Lett.* **86**, (2001) pg. 2509

[14] C. M Bartle and R.C. Haight, *Small inorganic scintillators as neutron detectors*, *Nuc. Instr. Meth. A* **422** (1999) pg. 54

[15] D. McLean et al., *CHELSI: Recent developments in the design and performance of a high-energy neutron spectrometer*, *Nuc. Instr. Meth. A* **562** (2006) pg. 793

[16] S. Agostinelli et al., *GEANT4 - a simulation toolkit*, *Nuc. Instr. Meth. A* **506** (2003) pg. 250

[17] E. W. Blackmore, *Operation of the TRIUMF (20-500 MeV) Proton Irradiation Facility*, *IEEE Radiation Effects Data Workshop* (2000). DOI: 10.1109/REDW.2000.896260.

[18] HAMAMATSU Photonics, *Photomultiplier tube R580 Specifications.* https://www.hamamatsu.com/us/en/R580.html

[19] J. D. Valentine et al., *Temperature dependence of CsI(TI) gamma-ray excited scintillation characteristics*, *Nuc. Instr. Meth. A* **325** (1993) pg. 147

[20] F. Amorini et al., *Investigation of the Dependence of CsI(Tl) Scintillation Time Constants and Intensities on Particle's Energy, Charge and Mass Through Direct Fitting of Digitized Waveforms*, *IEEE Transactions on Nuclear Science* **59** NO. 4 (2012)

[21] M. M. Hamada et al., *Dependence of Scintillation Characteristics in the CsI(Tl) Crystal on Tl+ Concentrations Under Electron and Alpha Particles Excitations*, *IEEE Transactions on Nuclear Science* **48** NO. 4 (2001)

[22] R. Gwin and R.B. Murray, *Scintillation Process in CsI(T1). I. Comparison with Activator Saturation Model*, *Phys. Rev.* **131** (1963) pg. 2

[23] Y. Koba et al., *Scintillation Efficiency of Inorganic Scintillators for Intermediate-Energy Charged Particles*, *Progress in Nuclear Science and Technology* **1** (2011) pg. 218

[24] C. Zeitlin et al., *Calibration and Characterization of the Radiation Assessment Detector (RAD) on Curiosity*, *Space Sci Rev* **201** (2016) pg. 201

[25] B. Pietras et al., *First testing of the CALIFA Barrel Demonstrator*, *Nuc. Instr. Meth. A* **814** (2016) pg. 56

[26] C. J. W. Twenhofel et al., *The Response Function of a CsI(Tl) Scintillator with Photodiode*

Readout to Light and Heavy Ions in the Intermediate Energy Range, *Nuc. Instr. Meth. B* **51** (1990) pg. 58

[27] M. Pârlog et al., *Response of CsI(Tl) scintillators over a large range in energy and atomic number of ions Part I: recombination and δ-electrons*, *Nuc. Instr. Meth. A* **482** (2002) pg. 674

[28] H. Ikeda et al., *A detailed test of the CsI(Tl) calorimeter for BELLE with photon beams of energy between 20 MeV and 5.4 GeV*, *Nuc. Instr. Meth. A* **441** (2000) pg. 401

[29] M. Bendel et al., *RPID - A new digital particle identification algorithm for CsI(Tl) scintillators*, *Eur. Phys. J. A* **49** (2013) pg. 69

Chapter 6

Pulse Shape Discrimination with the Belle II Calorimeter

The testbeam results presented in Chapter 5 [25] demonstrate the potential to improve particle identification at the Belle II experiment by applying PSD with the CsI(Tl) crystals that comprise the Belle II calorimeter. Particle identification through pulse shape discrimination relies on the precise understanding of the CsI(Tl) scintillation response to electromagnetic vs. hadronic energy deposits. As a result, extending the pulse shape characterization methods developed in the TRIUMF testbeam analysis, where a single crystal was used, to application at the full Belle II calorimeter consisting of 8736 unique CsI(Tl) crystals, poses significant challenges. In particular the CsI(Tl) crystals used at Belle II are re-purposed from the original Belle experiment and originate from several manufacturers and crystal production batches. In addition the response of the crystals light detection, shaping electronics and noise characteristics can vary crystal-to-crystal. Detailed in this chapter are the calibration, reconstruction and simulation methods that were developed to apply PSD at Belle II.

6.1 CsI(Tl) Scintillation Light Detection at the Belle II Calorimeter

The signal chain for a single calorimeter crystal channel at Belle II begins with the CsI(Tl) crystal that emits scintillation light stimulated from energy deposits in the crystal volume. The time structure of the scintillation light emitted by CsI(Tl) can be

modelled by a sum of exponential components with decay times on the order of 600 ns to several microseconds [25]. Shown by the results in Chapter 5 [25], the relative intensity of the these scintillation components depends on the ionization energy loss of the particles depositing energy in the crystal. As a result the exact shape of the CsI(Tl) scintillation signal depends on the nature of the energy deposit in the crystal.

Each CsI(Tl) crystal in the Belle II calorimeter is instrumented with two Hamamatsu S2744-08 PIN photodiodes for detecting CsI(Tl) scintillation light. The diodes are glued to the rear face of the crystal and each have an area of 10×20 mm^2 [3, 35]. Following the diodes are a series of pre-amplifier circuits that process the electrical signal emitted from the diodes by applying signal shaping and filtering. The primary stages for a single Belle II CsI(Tl) crystal channel are illustrated in Figure 6.1[37].

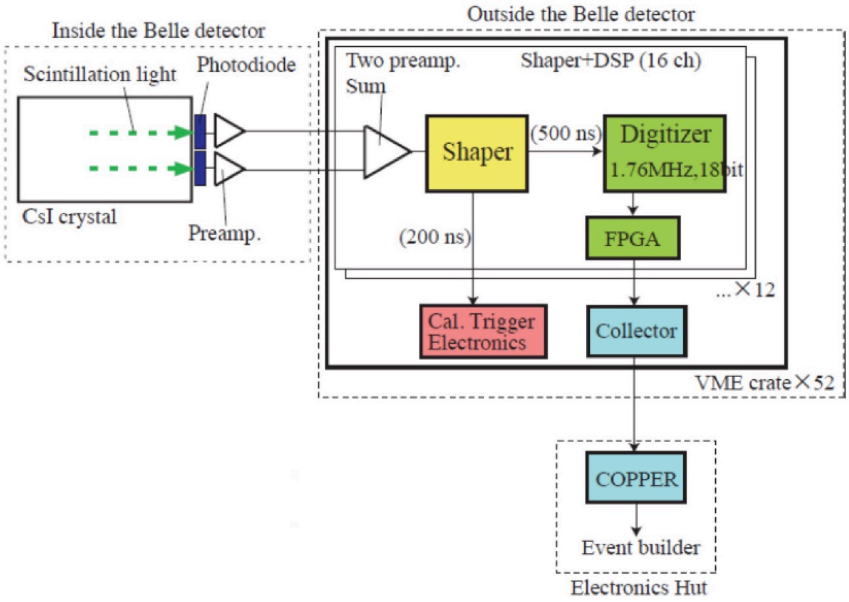

Figure 6.1: Schematic diagram illustrating main signal chain components for a single crystal channel in the Belle II calorimeter. Image is from reference [37].

The main function of the electronics following the diodes are to measure the integrated CsI(Tl) scintillation emission as this quantity is related to the energy deposited in the crystal. This is accomplished by several stages of signal shaping electronics that integrate, filter and shape the initial signal detected. For each diode, there is a pre-amplifier that is also mounted on the rear of the crystal. These pre-amplifiers integrate and shape the electrical signal emitted by the diodes. After these initial pre-amplifiers the two signals, one from each diode, are summed and the pulse is sent to a shaping amplifier called the ShaperDSP. The ShaperDSP is new to Belle

II and was designed to achieve good energy resolution in the high accelerator induced background that is expected to be present during SuperKEKB operation. This is achieved by applying a $\mathrm{CR}-(\mathrm{RC})^4$ shaping amplifier with a short shaping time of 0.5 μs [35]. The ShaperDSP also performs a tail subtraction that suppresses the electronics response to the several micro-second long CsI(Tl) scintillation component [3].

After the ShaperDSP, the signal is digitized into 31 ADC points with a 1.76 MHz clock frequency at 18-bit ADC [35]. The digitized waveform is then characterized by a Field Programmable Gate Array (FPGA) that performs a template fit. The template used in the FPGA fit is calibrated to model the full channel response to an energy deposit from a photon. From the single template fit by the FPGA, the waveforms amplitude, time and a single bit fit quality flag are returned. In each event these three quantities are saved offline for all crystals with energy greater than 1 MeV.

6.2 Waveform Readout for PSD

The first proposal to use CsI(Tl) PSD at Belle II for particle identification was in October 2016 [38], relatively late in the development stage of the Belle II calorimeter electronics and FPGA firmware that began development as early as 2009. As a result the signal chain in Figure 6.1 was not developed with PSD included as a design goal. In particular the online waveform analysis performed by the FPGA does not explicitly perform a pulse shape characterization as required for PSD. To accommodate PSD with the Belle II calorimeter, the FPGA firmware was modified by the Belle II Calorimeter group to allow for the digitized waveforms emitted by the ShaperDSP to be saved offline if the energy of the waveform is above an energy threshold, $\mathrm{E}^{\mathrm{Readout}}_{\mathrm{Threshold}}$. By saving the waveforms offline, PSD can be achieved during offline data processing. The primary constraint for $\mathrm{E}^{\mathrm{Readout}}_{\mathrm{Threshold}}$ is the total data size of the offline waveforms. Uncompressed, each digitized waveform corresponds to 31 ADC points $\times$ 18 bits = 558 bits. This is much larger than the 36 bits required for storing only the energy, time and fit quality flag normally returned by the FPGA.

To establish an optimal value of $\mathrm{E}^{\mathrm{Readout}}_{\mathrm{Threshold}}$ to implement in the FPGAs, the number of waveforms saved per event was studied as a function of $\mathrm{E}^{\mathrm{Readout}}_{\mathrm{Threshold}}$ using Monte-Carlo simulations (MC). In Figure 6.2 the average number of waveforms saved per event, $\langle n^{\mathrm{event}}_{\mathrm{waveforms}} \rangle$, is computed as a function of $\mathrm{E}^{\mathrm{Readout}}_{\mathrm{Threshold}}$ for several MC modes. In Figure 6.2a the SuperKEKB beam background levels applied in the simulation correspond

to predictions for the conditions that were expected to be present in Phase 2. In Figure 6.2b the background levels applied in the simulation correspond to Phase 3 predictions, where the luminosity will be much higher. The results in Figure 6.2 predict that $\langle n^{\text{event}}_{\text{waveforms}} \rangle$ rapidly increases at lower $\text{E}^{\text{Readout}}_{\text{Threshold}}$ values, independent of the MC mode. This rapid rise is due to the presence of numerous energy deposits by lower energy (< 10 MeV) photons produced by beam backgrounds. The energy threshold where this rapid increase begins for the Phase 2 conditions is predicted to be ~ 15 MeV, and for Phase 3 conditions is predicted to be ~ 25 MeV. As expected the rapid rise begins at a larger $\text{E}^{\text{Readout}}_{\text{Threshold}}$ value for Phase 3 conditions because the higher luminosities in Phase 3 are expected to produce higher levels of beam backgrounds. At larger values of $\text{E}^{\text{Readout}}_{\text{Threshold}}$, the Phase 2 and Phase 3 distributions are similar as energy deposits above 100 MeV are primarily from non-beam background sources. From these studies, a 20 MeV threshold was initially set in the FPGAs for online readout during Phase 2 operations. Early in Phase 2 however this threshold was increased to 30 MeV. As a result all calorimeter crystals with an energy deposit measured by the FPGAs to be greater than 30 MeV have a digitized waveform recorded for offline pulse shape analysis.

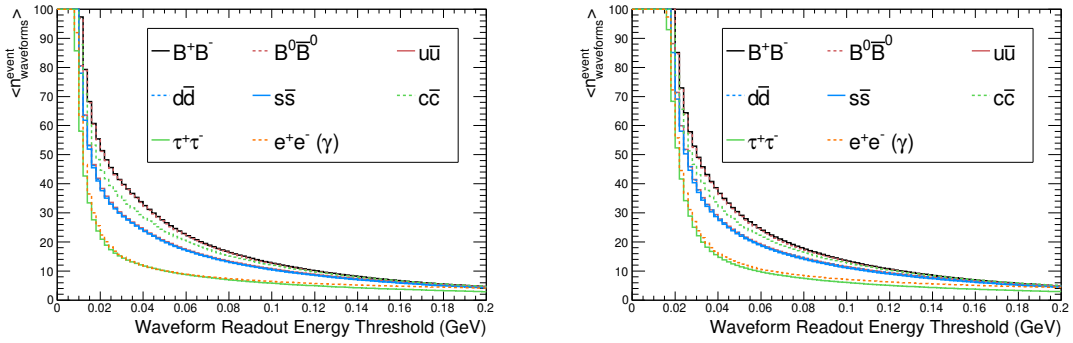

(a) Phase 2 beam backgrounds

(b) Phase 3 beam backgrounds

Figure 6.2: Simulation results to predict the average number of waveforms saved per event as a function of $\text{E}^{\text{Readout}}_{\text{Threshold}}$.

As Phase 2 data became available, the analogous measurement computed for simulation in Figure 6.2 could be measured for different data runs in Phase 2 data. Shown in Figure 6.3 is $\langle n^{\text{event}}_{\text{waveforms}} \rangle$ as a function of $\text{E}^{\text{Readout}}_{\text{Threshold}}$, computed for the largest data runs ($> 10^6$ events) in Phase 2. Shown by this result, the distributions in data for the different runs have a consistent trend and, as predicted by the MC studies,

$\langle n^{\text{event}}_{\text{waveforms}} \rangle$ rapidly increases as $\text{E}^{\text{Readout}}_{\text{Threshold}}$ decreases below 20 MeV. For $\text{E}^{\text{Readout}}_{\text{Threshold}}$ above 100 MeV the data distributions in Figure 6.3 are similar to the $e^+e^- \rightarrow e^+e^-$ MC predictions as the SuperKEKB cross section is dominated by Bhabha scattering.

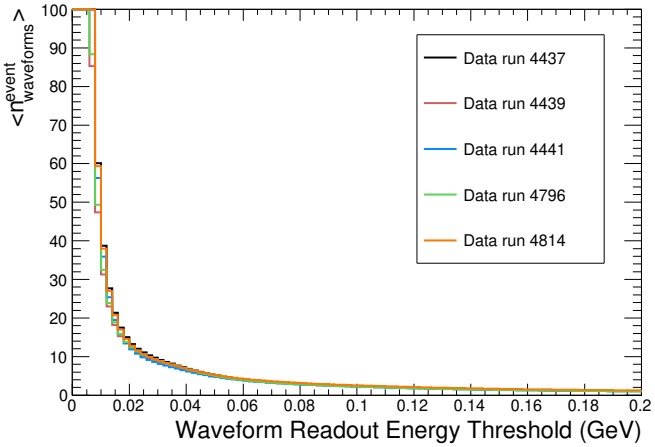

Figure 6.3: $\langle n^{\text{event}}_{\text{waveforms}} \rangle$ as a function of $\text{E}^{\text{Readout}}_{\text{Threshold}}$ measured for the five largest runs in Phase 2 data.

The distributions presented in Figure 6.2 allow an optimal value of $\text{E}^{\text{Readout}}_{\text{Threshold}}$ to be established by setting $\text{E}^{\text{Readout}}_{\text{Threshold}}$ to be as low a possible while maintaining a safety margin to avoid from the rapid rise from beam backgrounds. This optimization criteria motivated the $\text{E}^{\text{Readout}}_{\text{Threshold}}$=30 MeV setting for Phase 2. Another quantity that had to be determined with regards to the offline waveforms is the expected total raw data size the saved waveforms would occupy with $\text{E}^{\text{Readout}}_{\text{Threshold}}$=30 MeV. For a set $\text{E}^{\text{Readout}}_{\text{Threshold}}$ value the total offline data size can be estimated by scaling the simulation results in Figure 6.2 using the corresponding "accepted cross section", σ^{accepted}, determined by the Belle II trigger settings. In Table 6.1 and Table 6.2 the predicted data size for the offline waveforms is shown for Phase 2 and Phase 3 background conditions respectively. In this table the σ^{accepted} values from reference [39] are used.

Table 6.1: Predicted offline data sizes for different modes in with Phase 2 beam background conditions. σ^{accepted} values are from reference [39].

Mode	σ^{accepted} (nb)	$\langle n^{\text{event}}_{\text{waveforms}} \rangle$ (30 MeV threshold)	Waveform Data Size Gb/fb^{-1}	Fraction of all Waveform Data	Fraction of all non-waveform ECL Data
$B\bar{B}$	1.1	41.3	3.2	0.01	< 0.01
$u\bar{u}$	1.5	30.4	3.2	0.01	< 0.01
$d\bar{d}$	0.4	30.0	0.8	< 0.01	< 0.01
$s\bar{s}$	0.4	29.9	0.8	< 0.01	< 0.01
$c\bar{c}$	1.3	35.8	3.2	0.02	< 0.01
$\tau^+\tau^-$	0.8	15.2	0.8	< 0.01	< 0.01
$e^+e^-(\gamma)$	184.0	15.7	201.6	0.94	0.19

Table 6.2: Predicted offline data sizes for different modes in with Phase 3 beam background conditions. σ^{accepted} values are from reference [39].

Mode	σ^{accepted} (nb)	$\langle n^{\text{event}}_{\text{waveforms}} \rangle$ (30 MeV threshold)	Waveform Data Size Gb/fb^{-1}	Fraction of all Waveform Data	Fraction of all non-waveform ECL Data
$B\bar{B}$	1.1	52.7	4.0	0.02	< 0.01
$u\bar{u}$	1.4	41.4	4.0	0.02	< 0.01
$d\bar{d}$	0.4	41.3	1.2	< 0.01	< 0.01
$s\bar{s}$	0.4	40.4	1.1	< 0.01	< 0.01
$c\bar{c}$	1.3	46.7	4.2	0.02	< 0.01
$\tau^+\tau^-$	0.8	25.0	1.4	< 0.01	< 0.01
$e^+e^-(\gamma)$	103.3	27.0	194.5	0.92	0.16

Tables 6.1 and 6.2 show that although $B\bar{B}$ events on average have the largest number of waveforms saved per event, the waveforms from Bhabha events are predicted to occupy over 90% the total waveform data due to the large Bhabha cross section. In Tables 6.1 and 6.2, the total waveform data size is also shown as a fraction of the total non-waveform calorimeter data. The non-waveform calorimeter data includes

the crystal amplitude, timing and quality flag for all crystals in the event with energy above 1 MeV. As a fraction of the non-waveform data, the total waveform data is predicted to be $\sim$ 19% for Phase 2 and $\sim$ 16% for Phase 3. This data fraction is predicted to be lower for Phase 3 because although for Phase 3 the backgrounds are much larger, σ^{accepted} for $e^+e^-(\gamma)$ is reduced for Phase 3 data-taking due to prescaling.

With Phase 2 data the data-size of the waveforms as a fraction of non-waveform calorimeter data was computed for the largest Phase 2 data runs and the results are presented in Table 6.3. From this table the waveform data fraction was measured to be run-dependent and ranging 12-16 %. This variations of these values could be caused by changes in accelerator conditions between the different runs causing different levels of beam background. This range is slightly lower than the predicted 19% shown in Table 6.1.

Table 6.3: Fraction of offline ECL raw data that is from offline waveforms saved measured for several of the larger runs in Phase 2 data.

Phase 2 Data Run	$\frac{\text{Waveform Data}}{\text{Non-Waveform ECL Data}}$
4796	0.14
5239	0.15
5240	0.12
5241	0.16
5553	0.13

6.3 Offline Waveform Fitting

Outlined in the previous section, during Belle II data-taking all calorimeter waveforms with energy above 30 MeV are saved for offline pulse shape characterization. During offline reconstruction, waveform shape characterization is performed by fitting the waveform to $G(t)$ defined in equation 6.1

$$G(t) = L_{\text{Photon}} R_{\text{Photon}}(t - t_0) + L_{\text{Hadron}} R_{\text{Hadron}}(t - t_0) \tag{6.1}$$

where,

t is time.

t_0 is the time of the energy deposit.

R_{Photon} is the photon template which describes the shape of the signal emitted by the full Belle II crystal channel signal chain corresponding to input scintillation CsI(Tl) emission produced by an electromagnetic shower.

R_{Hadron} is the hadron template which describes the shape of the signal emitted by the full Belle II crystal channel signal chain for pure hadron scintillation component emission.

L_{Photon} is the photon scintillation component light output yield.

L_{Hadron} is the hadron scintillation component light output yield.

From the quantities measured by the multi-template fit, the crystal energy, $\text{E}_{\text{Total}}^{\text{crystal}}$, and crystal hadron intensity, N_{H}, are computed using equations 6.2 and 6.3, respectively.

$$\text{E}_{\text{Total}}^{\text{crystal}} = L_{\text{Photon}} + L_{\text{Hadron}} \tag{6.2}$$

$$\text{Hadron Intensity} = \text{N}_{\text{H}} = \frac{L_{\text{Hadron}}}{L_{\text{Photon}} + L_{\text{Hadron}}} \tag{6.3}$$

The multi-template fit computes L_{Photon}, L_{Hadron} and t_0 by minimizing the χ^2 defined in equation 6.4.

$$\chi^2 = \mathbf{D}\mathbf{C}^{-1}\mathbf{D} \tag{6.4}$$

where

$$\mathbf{D} = \mathbf{A} - \mathbf{G} \tag{6.5}$$

$\mathbf{A} = a_1..a_{31}$: Data points of digitized waveform.
$\mathbf{G} = g_1..g_{31}$: Fit hypothesis function evaluated at times corresponding to the waveform data points.
$\mathbf{C}^{-1}$: Noise matrix defined as the inverse of the covariance matrix, $\mathbf{C}$.

To evaluate equation 6.4 and $G(t)$, the templates R_{Photon} and R_{Hadron} need to be known, in addition to the covariance matrix. The procedures developed to compute and validate these quantities are outlined in the following sections.

6.3.1 Hadron Response Template Calibration

The photon and hadron templates in equation 6.4 are defined as the response of the full electronics chain in Figure 6.1 to an input CsI(Tl) scintillation signal corresponding to a pure photon scintillation component emission and pure hadron scintillation component emission, respectively. In the testbeam study in Chapter 5 [25] the PMT output was directly digitized and as a result these templates corresponded to exponential curves describing the time structure of CsI(Tl) scintillation emission. As described in Section 6.1, waveforms at BelIe II are digitized only after the CsI(Tl) emission is processed by several stages of pulse shaping and filtering. As a result the photon and hadron component templates used to describe Belle II waveforms are not exponential curves.

The output signal shape of the ShaperDSP is modelled using a 11 parameter function. Calibration of the photon and hadron templates requires computing the 11 parameters that describe the signal chain output that corresponds to a pure photon and hadron scintillation component emission input. The photon and hadron templates are calibrated individually for each calorimeter crystal channel as small channel-to-channel perturbations in the electronics and crystal scintillation response are expected.

For the photon template which corresponds to the signal chain response to electromagnetic showers, the template parameters are computed by the ECL group using energy deposits from high energy electrons in Bhabha scattering events. As Bhabha events are readily available and contain single crystals with energy deposits above 1 GeV, the 11 template parameters for describing the photon response are computed for a single crystal by simultaneously fitting a set of high energy (> 1 GeV) waveforms. This procedure is done individually for each calorimeter channel and is advantageous as it does not require of exact knowledge of the CsI(Tl) scintillation response.

Calibrating the hadron templates is more challenging as the majority of hadronic energy deposits in Belle II data are at lower energies (< 0.5 GeV) and the energy

deposits with hadron pulse shapes are observed to always be a combination of photon and hadron scintillation component emission. In addition prior to the first SuperKEKB beams in April 2018 a data sample of waveforms from hadronic energy deposits was not available. As a result the following procedure was developed for calibrating the ShaperDSP hadron templates for each channel in the Belle II calorimeter without requiring pulse shape data from hadronic energy deposits.

The input signal, $R_i^{\mathrm{IN}}(t)$, of the Belle II signal chain corresponds to the CsI(Tl) scintillation emission, where i = photon or hadron and t is time. The electronics chain in Figure 6.1 converts $R_i^{\mathrm{IN}}(t)$ to the output signal from the ShaperDSP , R_i. The output signal R_i can be computed from input signal $R_i^{\mathrm{IN}}(t)$ using equation 6.6 if the impulse response of the signal chain $h(t)$ is known.

$$R_i(t) = h(t) * R_i^{\mathrm{IN}}(t) \tag{6.6}$$

where $*$ indicates a convolution. In equation 6.6 it is assumed that $h_{\mathrm{Photon}}(t) = h_{\mathrm{Hadron}}(t) = h(t)$. Proceeding with this assumption there are two equations, one for i =Photon and i = Hadron, and the four unknowns $R^{\mathrm{IN}}_{\mathrm{Photon}}(t)$, $R^{\mathrm{IN}}_{\mathrm{Hadron}}(t)$, $h(t)$ and R_{Hadron}. Next an approximation is made that the CsI(Tl) scintillation emission shapes for an electromagnetic shower and hadron component emission are given by the parameters measured in the testbeam study in Chapter 5 [25] (Table 1 in Chapter 5 [25]), for all crystals in the calorimeter. That is, $R^{\mathrm{IN}}_{\mathrm{Photon}}(t) = I_{\gamma}^{\mathrm{PMT}}(t)$, and $R^{\mathrm{IN}}_{\mathrm{Hadron}}(t) = I^{\mathrm{PMT}}_{\mathrm{Hadron}}(t)$. This approximation assumes that the crystal-by-crystal variations in the decay time structure of the CsI(Tl) crystals are small relative to the noise in the waveform. In Section 6.5.3 the accuracy of this approximation is evaluated.

With this approximation the unknowns remaining are $h(t)$ and R_{Hadron}. This allows the hadron template to be computed using equations 6.7 and 6.8.

$$R_{\mathrm{Hadron}}(t) = \mathrm{IFT}(H(w) \times \mathrm{FT}(I^{\mathrm{PMT}}_{\mathrm{Hadron}}(t))) \tag{6.7}$$

$$H(w) = \frac{\mathrm{FT}(R_{\gamma}(t))}{\mathrm{FT}(I_{\gamma}^{\mathrm{PMT}}(t))} \tag{6.8}$$

where FT is the Fourier Transform, IFT is the inverse Fourier Transform and w is frequency, such that:

$$H(w) = FT(h(t)) \tag{6.9}$$

$$h(t) = IFT(H(w)) \tag{6.10}$$

Applying equation 6.7, the signal chain response to a pure hadron scintillation component input is computed for each calorimeter channel. Typical results are shown in Figure 6.4 where the photon template and the predicted hadron template for a typical crystal channel are overlaid.

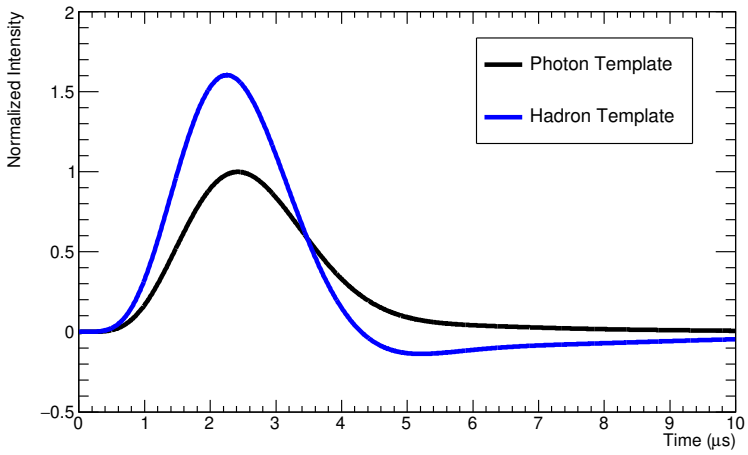

Figure 6.4: Typical results for a photon template and hadron template used in photon+hadron fit perform offline to Belle II calorimeter waveforms. The photon template corresponds to the Belle II single chain response to scintillation component emission produced by an electromagnetic shower. The hadron template corresponds to the predicted signal chain response to hadron component scintillation emission.

In Figure 6.4 the critical observation is made that the signal chain in Figure 6.1 is predicted to be sensitive to changes in input scintillation signal. The hadron scintillation component emission by the CsI(Tl) crystal, produced by high $d\mathrm{E}/dx$ energy deposits, is predicted to result in a signal chain response that has an undershoot in the tail region of the pulse and is distinct from the response from photon scintillation component emission. This observation answers one of the main questions posed at the beginning of this research work of whether the signal chain electronics at Belle II are sensitive to changes in the input CsI(Tl) scintillation response.

Another observation made in Figure 6.4 is that the normalized response of the photon and hadron templates are different. By definition, the photon template is normalized to peak at one. The predicted hadron template shape however peaks at $\sim 1.6\times$ the photon template amplitude. When computing the hadron template,

the input CsI(Tl) decay curve is normalized to have unit total charge to ensure that one energy unit of emission in the photon decay curve corresponds to one unit of amplitude in the output photon template. The different relative normalization in Figure 6.4 indicates the signal chain electronics are non-linear for changes in the input signal decay time. A consequence of this is that the response of the signal chain to hadron scintillation component emission is actually amplified relative to the response to photon scintillation component emission. For a constant input signal shape where only the pulse amplitude is changing the ShaperDSP electronics are measured to deviate from linearity by only 0.3% [40]. This characteristic is predicted for all channels in the Belle II calorimeter as shown by the histogram shown in Figure 6.5 where the normalization of the hadron template is shown for all 8736 calorimeter channels.

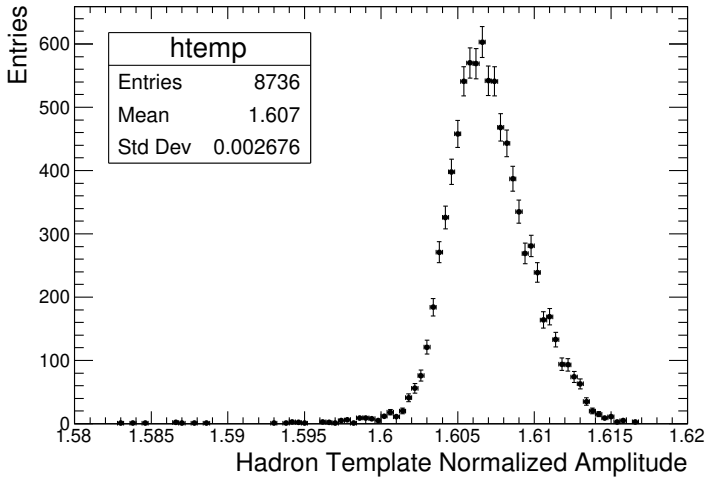

Figure 6.5: Hadron template normalization relative to photon template amplitude computed for all 8736 crystals in the Belle II calorimeter.

6.3.2 Initial Validation of Hadron Template Calibration with Data

This section uses a general selection of clusters from $B\bar{B}$ and $q\bar{q}$ like events to perform an initial validation of the hadron template calibration procedure and verify the hadron template features shown in Figure 6.4 are observed in the data.

$B\bar{B}$ and $q\bar{q}$ like events are selected by requiring the event to have 4 or more tracks

satisfying the requirements below.

- $p_T > 0.15$ GeV/c
- $|d_0| < 0.5$ cm
- $|z_0| < 1$ cm

This track requirement is applied reject Bhabha events. From these events all calorimeter clusters not matched to a track are selected.

For all crystals in the selected clusters that have a waveform saved offline, the waveform is fit to equation 6.1. From this fit the total energy and the hadron component intensity, defined as the fraction of the hadron component energy to the total energy, are computed. The distribution for the crystal hadron intensity vs crystal total energy are shown in Figure 6.6 for all waveforms in the clusters selected with fit $\chi^2 < 60$.

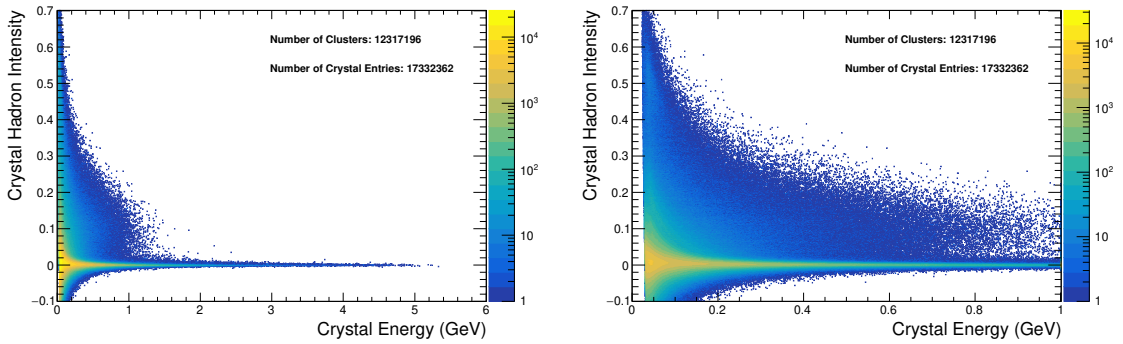

(a) (b)

Figure 6.6: Distribution of crystal hadron intensity vs crystal energy for all crystals with waveforms saved offline from crystals in neutral calorimeters clusters in all data events after Bhabha veto is applied. a) Crystal energy extends to 6 GeV. b) Zoom into crystal energy below 1 GeV.

In the distribution shown in Figure 6.6 a variety of pulse shapes are observed as indicated by the range of hadron intensity values extending from ~ 0 to ~ 0.60. This hadron intensity range is consistent with the TRIUMF testbeam studies in Chapter 5 [25] and provides a validation of the relative normalization difference that was predicted for the photon and hadron template shapes. In Figure 6.6 many of the waveforms are seen to have hadron intensity of zero. These waveforms are well

described by only the photon template, and thus the energy deposits are likely from electromagnetic showers. Sample fits for waveforms with photon-like pulse shapes are shown in Figure 6.7. As expected, the photon templates well describe the data and the hadron component contribution to these fits is minimal.

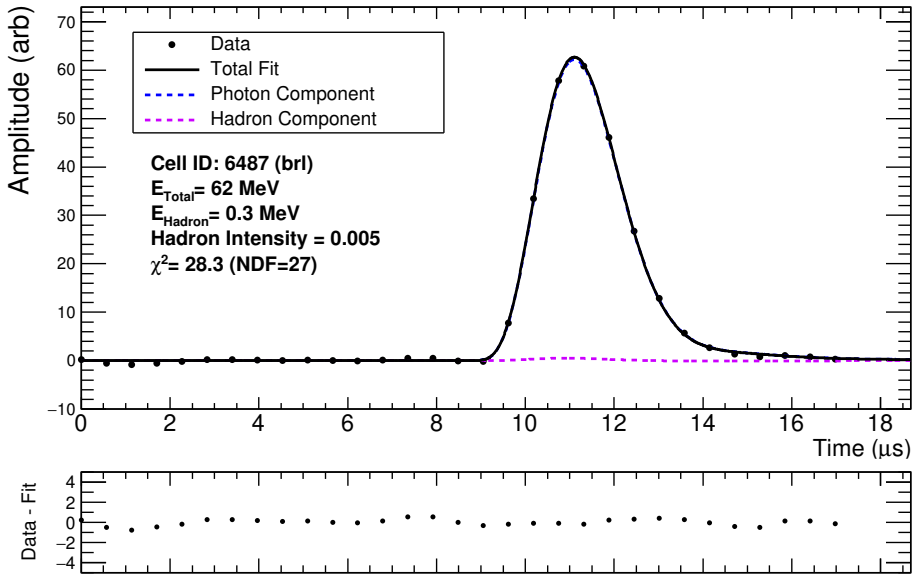

(a)

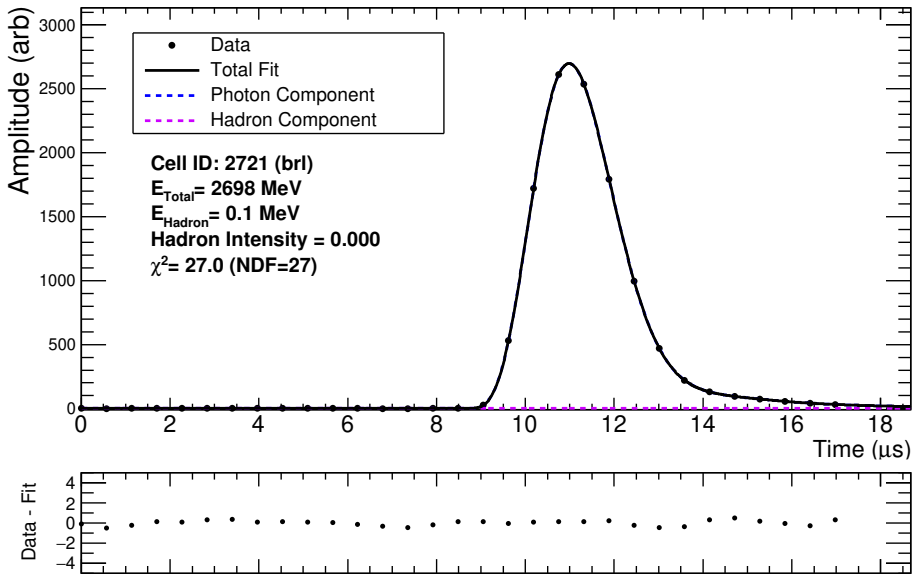

(b)

Figure 6.7: Example photon+hadron fit results for Belle II calorimeter crystal waveforms in data with photon-like pulse shapes. a) Lower energy deposit. b) Higher energy deposit.

Accompanying the large sample of waveforms with photon-like pulse shapes, the distribution in Figure 6.6 includes a significant sample of crystals with waveforms that have hadron intensity much greater than zero. In particular, in the low energy zoom shown in Figure 6.6b pulse shape bands from energy deposits by multiples of secondary protons are visible. In addition an excess of crystals with hadron intensity of 0.60 is present, as expected from energy deposits by secondary alpha particles. At crystal energies above 100 MeV waveforms with hadron-like pulse shapes are consistent with energy deposits by a mixture of various secondary charged hadrons. The presence of these features verifies that the hadron templates applied in the fits are correctly measuring the hadron scintillation component light output yield of the crystals.

Displayed in Figure 6.8 are typical photon+hadron fit results to waveforms from data with hadron-like pulse shapes. Sample fits are shown for waveforms with a range of hadron intensity and total energy values. The total fit contributions from the photon and hadron templates overlaid illustrate that several features which were predicted to be present are observed in the data. In particular the waveforms have an undershoot in the tail region of the waveform which is modelled by the hadron

template. It is also clearly observed in Figure 6.8 these waveforms are not well described by only the photon template and require the photon+hadron template fit to describe the data.

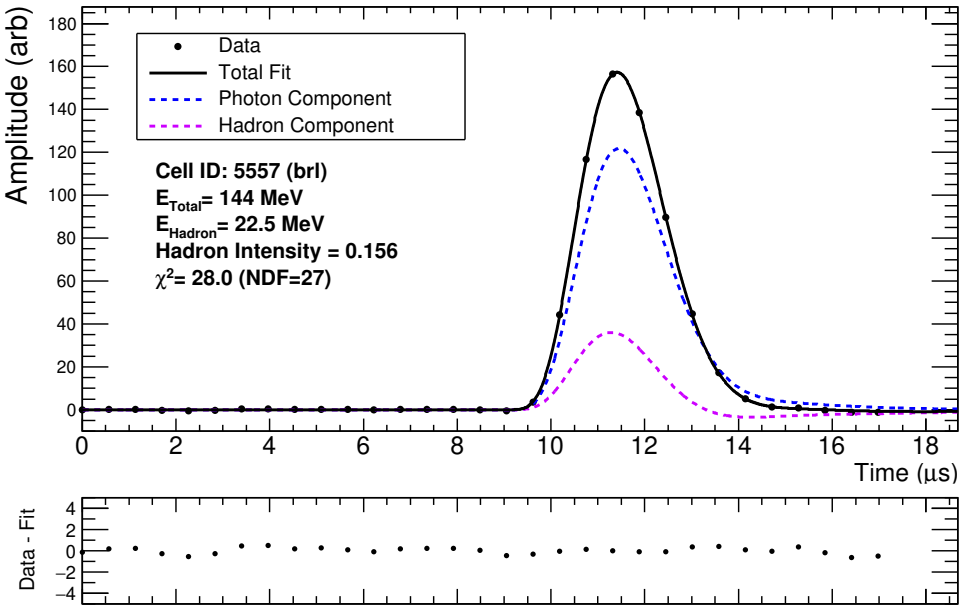

(a)

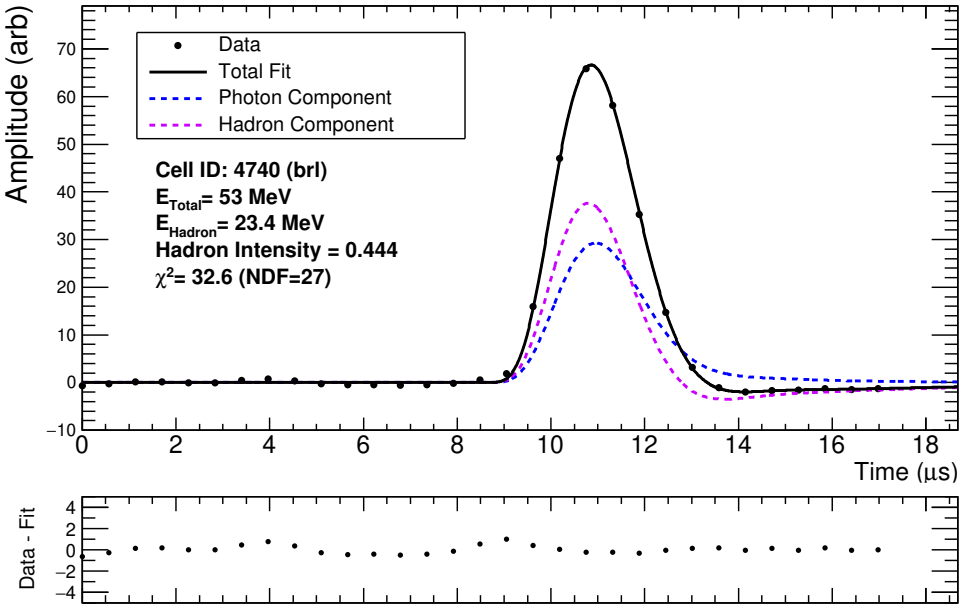

(b)

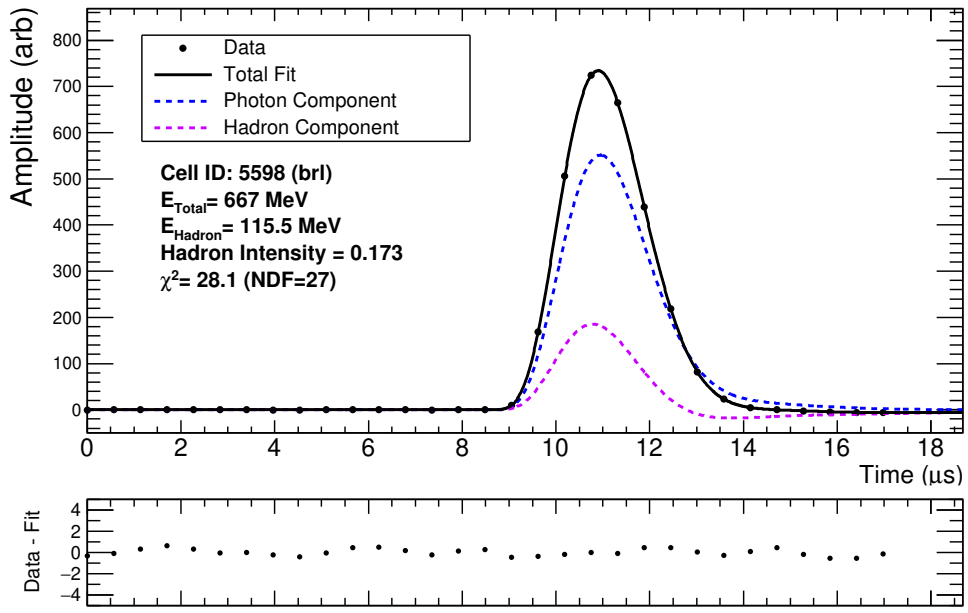

(c)

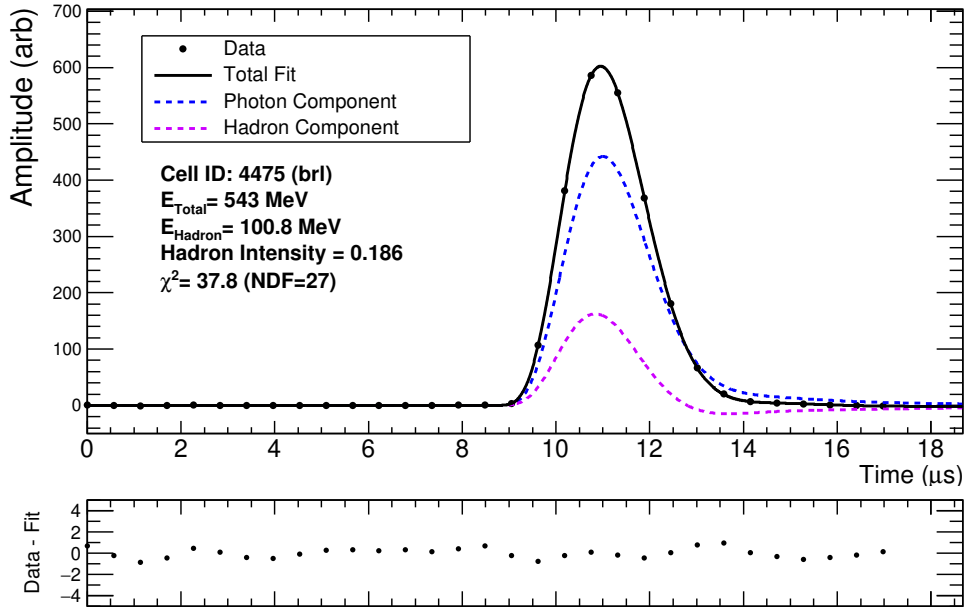

(d)

Figure 6.8: Example photon+hadron offline fit results for Belle II calorimeter crystal waveforms with hadron-like pulse shapes. a) Lower energy and higher hadron intensity. b) Lower energy and medium hadron intensity. c) and d) Higher energy and medium hadron intensity.

6.4 Covariance Matrix

The covariance matrix is a critical component to the waveform fit defined in equation 6.4. When evaluating the χ^2 of the waveform fit the covariance matrix is used to compute the error for the waveform data-points. The ideal covariance matrix will thus model the noise level of the waveform.

In the simplistic case, the covariance matrix takes the form of the identity matrix multiplied by a noise scale. In this case, the point-to-point correlations in the waveform noise are ignored. If these correlations are non-negligible however then using the identity matrix as the covariance matrix will result in an underestimation of the error and larger χ^2 values. As only waveforms with $\chi^2 < 60$ are used for pulse shape discrimination, larger χ^2 values result in a decrease in the fitting efficiencies which thus degrade the particle identification performance at cluster level. It is thus important that the covariance matrix models the correlated and uncorrelated noise in an optimal way such that the fitting efficiency and resolution in the fit parameters are maximized.

The covariance matrix is defined in equation 6.11,

$$C_{(i,j)} = \frac{1}{n-1}\sum_{k=1}^{n}(A_{k,i} - \bar{A}_i)(A_{k,j} - \bar{A}_j) \tag{6.11}$$

where:

$A_{k,i} = a_{k,1}..a_{k,31}$ = is the k^{th} baseline subtracted noise waveform, which has a length of 31 ADC points.

n = Total number of noise waveforms in the sample.

$\bar{A}_i = \frac{1}{n}\sum_{k=1}^{n}(a_{k,i} - b_i)$ = baseline subtracted average of noise waveform sample, which has a length of 31 ADC points.

$b_1..b_{31} = \frac{1}{n}\sum_{k=1}^{n} a_{k,i}$ = average baseline of noise waveform sample, which has a length of 31 ADC points.

The noise waveform dataset used to compute the covariance matrix is a parameter that should be optimized for fit performance. During SuperKEKB operation the noise components to a waveform originate from three primary sources:

1. $\delta_{\text{electronic}}$: Correlated and uncorrelated electronic noise in the signal channel.

2. $\delta_{\text{Low Energy Pile-up}}$: Noise from pile-up hits, approximately continuous in time and from low energy ($\ll\sim$ 1 MeV) photons generated by accelerator backgrounds.

3. $\delta_{\text{High Energy Pile-up}}$: Out-of-time, higher energy ($>\sim$ 5 MeV) pile-up hits from photons generated by accelerator backgrounds.

Of these sources of noise, $\delta_{\text{electronic}}$ is expected to be approximately constant for different accelerator conditions. The characteristics of $\delta_{\text{Low Energy Pile-up}}$ and $\delta_{\text{High Energy Pile-up}}$ however are expected to vary depending on accelerator conditions such as beam currents, collimator settings and beam sizes [31]. These parameters can vary run-to-run or even in a single run causing $\delta_{\text{Low Energy Pile-up}}$ and $\delta_{\text{High Energy Pile-up}}$ to potentially vary event-to-event. The run dependence of $\delta_{\text{Low Energy Pile-up}}$ and $\delta_{\text{High Energy Pile-up}}$ was especially prevalent in Phase 2 data as this data was the first time SuperKEKB operated with collisions and accelerator tuning was on-going throughout Phase 2.

To account for $\delta_{\text{High Energy Pile-up}}$ noise, a second fit hypothesis was implemented and is described in Section 6.6. For $\delta_{\text{Low Energy Pile-up}}$, the optimal method to account for this background had to be determined. As the covariance matrix is central to the offline waveform fit it was important to study the impact that increasing the noise scale of the noise waveforms used to compute the covariance matrix has on the fitting performance. To explore this the following study was completed.

6.4.1 Impact of Covariance Matrix on Fitting Performance

The goal of this study is to determine how the χ^2 and hadron intensity distributions are impacted by using covariance matrices that are computed from samples of noise waveforms with different noise levels. For simplicity this study only uses crystals in the calorimeter barrel and the same covariance matrix is applied to all crystals. Note this differs from true reconstruction where the noise matrix is crystal dependent. To study a sample of waveforms with photon and hadron-like pulse shapes, a data sample is used where only the High Energy Ring (HER) of SuperKEKB was in operation with a current of 0.15 mA and no injections. During this run all calorimeter crystals, independent of energy, had their waveform recorded every 1000 events. The waveforms recorded in these full readout events correspond to the sample of "noise waveforms".

The noise level of a noise waveform was estimated using $\mathrm{E_{noise}}$ defined in equation 6.12,

$$\mathrm{E_{noise}} = (\max A - \min A) d_{\mathrm{crystal}} \tag{6.12}$$

where d_{crystal} is a crystal channel dependent calibration constant to convert from ADC to energy units and $\max A (\min A)$ is the maximum (minimum) value of the waveform. The distribution of $\mathrm{E_{noise}}$ for run 03116 (HER ON), is shown in Figure 6.9. Overlaid is also the $\mathrm{E_{noise}}$ distribution for a run with SuperKEKB OFF where comic ray data was collected. From Figure 6.9 it is observed that the run with HER ON has slightly higher noise levels than the cosmics run where no beam was present. This increase in noise is caused by the $\delta_{\text{Low Energy Pile-up}}$ noise contribution.

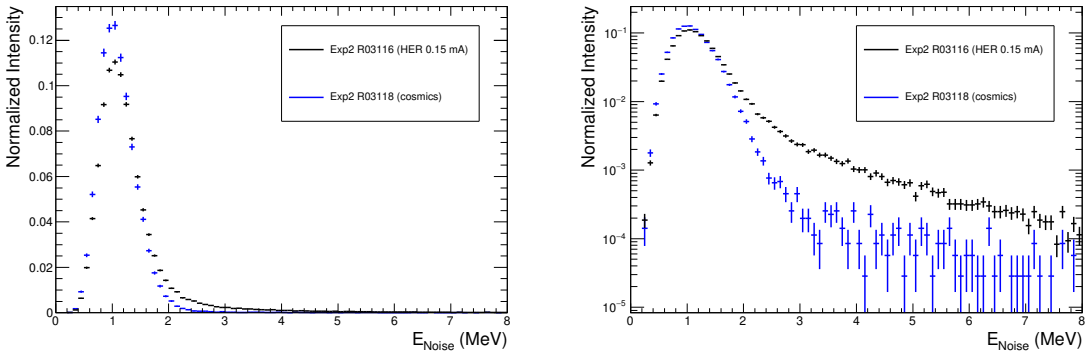

(a) (b)

Figure 6.9: Distribution of $\mathrm{E_{noise}}$ measured for noise waveforms in run 03116 (HER at 0.15 mA) and run 03118 (cosmic ray run, electronic noise). a) Linear scale b) Log scale.

To evaluate the impact of applying a covariance matrix computed from a sample of noise waveforms corresponding to different noise levels, the noise waveforms from run 03116 were divided into the follow three samples:

- Sample 1: $\mathrm{E_{noise}} < 2$ MeV (electronics noise)
- Sample 2: $2 < \mathrm{E_{noise}} < 3.5$ MeV
- Sample 3: $3.5 < \mathrm{E_{noise}} < 8$ MeV

Shown by Figure 6.9, Sample 1 contains primarily noise waveforms where the contribution from $\delta_{\text{Low Energy Pile-up}}$ is small relative $\delta_{\text{electronic}}$. In Sample 2 the

$\delta_{\text{Low Energy Pile-up}}$ noise contribution is non-negligible and in Sample 3, $\delta_{\text{Low Energy Pile-up}}$ and $\delta_{\text{High Energy Pile-up}}$ have significant contributions. Using these three samples, three covariance matrices are computed, one from each sample.

The noise matrix, defined as the inverse of the covariance matrix, is a symmetric matrix and as the noise is uniformly distributed in time across the waveform, the noise matrix is approximately constant along the matrix diagonals. These symmetries allow the structure of the noise matrix to be summarized by a projection along a middle column of the matrix as shown in Figure 6.10.

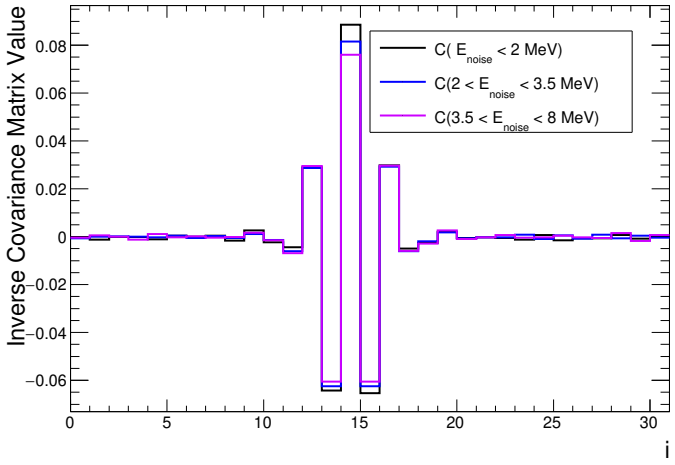

Figure 6.10: Projections along middle column for noise matrices computed from noise waveform samples with different levels of noise.

The three noise matrices in Figure 6.10 are observed to have a similar structure such that the centre diagonal elements have the highest magnitude and the absolute magnitude of each adjacent diagonal decreases. This demonstrates that as the separation between waveform points increases, the correlations in noise between the points decreases. Observing the differences in the noise matrices for different noise regions, as the noise level of the sample increases, the relative weight of the main diagonal decreases indicating the noise correlations increase in the higher noise samples.

To evaluate the fitting performance for the different covariance matrices, the waveforms in the triggered events in run 03116 are processed with each covariance matrix and the identity matrix. As run 03116 included HER beam, calorimeter clusters from protons and fast neutrons produced by accelerator backgrounds were present. These hadronic energy deposits allow the impact of each noise matrix to be studied on a sample containing photon and hadron pulse shapes. To evaluate the changes in fitting

performance, the χ^2 and hadron intensity distributions for each processing are shown in Figures 6.11 and 6.12, respectively.

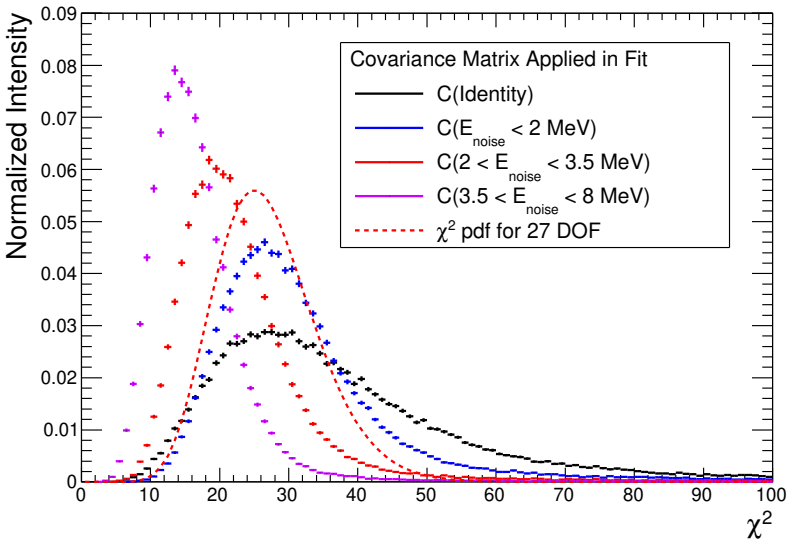

Figure 6.11: χ^2 distributions of photon+hadron fit to non-noise waveforms recorded in data run with HER beam ON. Each distribution corresponds to the same waveforms however the fit uses a different covariance matrix. χ^2 probability distribution function for 27 degrees-of-freedom is also overlaid for reference.

The χ^2 distribution for each re-processing is overlaid in Figure 6.11, in addition to the χ^2 probability distribution function for 27 degrees of freedom. In the ideal scenario where the noise of each waveform is perfectly modelled, the χ^2 distribution of the fits would match this distribution. The C(Identity) distribution in Figure 6.11 corresponds to the re-processing where the identity matrix was used as the covariance matrix. This represents the simplest noise modelling scenario as the correlated noise is not modelled. Comparing this distribution to the other distributions in Figure 6.11. it is evident that this case has the lowest fitting efficiency. The C(E_{noise} <2 MeV) distribution in Figure 6.11 is the χ^2 distribution for the re-processing that applied the covariance matrix computed from noise waveforms in the electronic noise dominated region. Unlike C(Identity), this matrix accounts for the correlated electronic noise in the signal chain. By accounting for the noise correlations, the results in Figure 6.11 show an improvement in the fitting efficiency. Compared to the χ^2 pdf overlaid however, the C(E_{noise} <2 MeV) distribution is observed to have a higher χ^2 on average. This indicates that for some of the waveforms in the data sample, C(E_{noise} <2 MeV)

is underestimating the noise level. Also overlaid in Figure 6.11 are the results for the re-processing's applying a covariance matrix computed for the higher noise regions. These distributions demonstrate the trend that as the noise level increases, the χ^2 distribution shifts to lower values, thus increasing the fitting efficiency. The mean of these distributions however is lower than the ideal distribution. This suggests that these matrices are overestimating the noise levels for the majority of the waveforms.

Although this improves the fitting efficiency, the hadron intensity resolution is degraded when the noise is overestimated. This is shown by Figure 6.12 where the distribution of the hadron intensity for waveforms in run 03116 with energy between 30 and 40 MeV is shown. In this Figure the peak at zero hadron intensity is from photon-like pulse shapes produced by electromagnetic showers and the secondary peak at hadron intensity of $\sim$ 0.11 are waveforms from energy deposits by single protons stopping in the crystal. Comparing the hadron intensity distributions in Figure 6.12 corresponding to the C(Identity) and C(E_{noise} <2 MeV) re-processings, it is observed that the resolution of the hadron intensity is essentially unchanged. This demonstrates that accounting for the electronic noise correlations results is a net positive gain in the fitting performance as the mean of the χ^2 distribution in Figure 6.11 improved without significantly degrading hadron intensity resolution. Seen in Figure 6.12, the re-processings that applied a covariance matrix computed from the higher noise levels result in a noticeable degradation in the hadron intensity resolution. This occurs because the covariance matrix's in these cases are over-estimating the noise level and beginning to filter the high frequency components of the waveform that are expected to correspond to the fast hadron scintillation component contribution which the fit is aiming to measure. Thus although the χ^2 mean shifts to lower values, the overall pulse shape discrimination performance decreases.

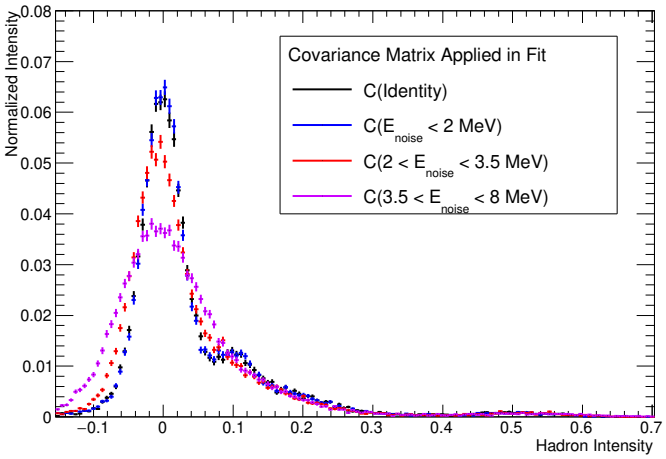

Figure 6.12: Hadron intensity distribution for crystals in energy range 30-40 MeV computed using photon+hadron fit to non-noise waveforms recorded in data run 03116. Each distribution corresponds to the same waveforms however the fit uses a different covariance matrix.

This study shows that to achieve optimal fitting performance, in terms of fitting efficiency and hadron intensity resolution, it is important that the covariance matrices applied in the fit do not over-estimate the noise level. If the covariance matrix over-estimates the noise levels then the fit χ^2 distribution will have a lower than expected mean given the number degrees of freedom however the sensitivity to pulse shape variations decreases. Conversely if the covariance matrix significantly underestimates the noise levels then the fit χ^2's will be larger than expected and leading to lower fit efficiencies, however the hadron intensity resolution is not degraded.

From these conclusions, for Phase 2 data processing the approach taken was to model only the electronic noise contributions with the covariance matrices used in the offline waveform fits. With this approach, each crystal channel in the Belle II calorimeter has a unique covariance matrix that is computed by the Belle II Calorimeter group such that the noise waveform input dataset was from a cosmic ray run when the SuperKEKB beams were OFF. As Phase 2 was the first commissioning run of SuperKEKB and Belle II, the luminosity was still relatively low compared to the projected instantaneous luminosities expected to be reached in Phase 3. As a result the $\delta_{\text{Low Energy Pile-up}}$ noise contribution was found to be small enough that by omitting this noise contribution from the covariance matrices, only a small decrease in the fit efficiency was observed (Section 6.5.1). For future Belle II operation during

Phase 3, where background conditions are expected to be more consistent relative to Phase 2, leading to longer data runs, a more optimal strategy would likely be to apply run-dependent covariance matrices computed from noise waveforms recorded during each data run. In addition the fitting performance of an alternate approach can be studied such that the covariance matrices model only electronic electronics noise, thus underestimating the total waveform noise, however, the χ^2 thresholds are adjusted on a run-by-run basis to maintain a predetermined fitting efficiency.

6.5 Evaluating Crystal-by-Crystal Covariance matrix, Photon Template and Hadron Template Calibrations

The end application of PSD at Belle II is through cluster variables that are derived from the information measured by the photon+hadron fits. The performance of the cluster variables is thus dependent on the fitting performance. If the templates, covariance matrices or fit hypothesis are not optimal or well calibrated then the low fitting performance, with regard to fitting efficiency and parameter resolution, will propagate to the cluster variables. As discussed above, the crystal properties and noise characteristics vary channel-by-channel and for this reason, the photon templates, hadron templates and covariance matrices are calibrated individually for each crystal channel. It is thus important to evaluate the performance of the waveform template calibration and fitting procedures discussed above for each crystal channel in the calorimeter. In this section the performance of these calibrations are evaluated.

6.5.1 Covariance Matrix Calibration Validation

To evaluate how well the covariance matrices model the noise levels in collision data, a sample of waveforms from electromagnetic showers are used. By assuming the photon templates are well-calibrated, the mean of the χ^2 distribution for this sample, $\langle\chi^2\rangle_{\mathrm{EM}}$, can be used to measure how well the covariance matrices are modelling the noise. Ideally $\langle\chi^2\rangle_{\mathrm{EM}}$ would equal 27 as this is the number of degrees-of-freedom in the fit, however as demonstrated by the study in Section 6.4.1, in order to avoid over-estimating the noise and degrading the hadron intensity resolution, the approach taken is to slightly under-estimate the noise levels. Thus $\langle\chi^2\rangle_{\mathrm{EM}}$ is expected to be

slightly higher then the ideal value of 27.

As there are 8736 crystal channels in the Belle II calorimeter, a large statistics sample of energy deposits from electromagnetic showers is required to evaluate crystal-by-crystal performance. For this reason crystals from clusters produced by $e^{\pm}$ from Bhabha scattering events is used.

An overall picture of the covariance matrix performance is shown by Figure 6.13 showing the χ^2 distribution for the photon+hadron fits to the waveforms in this sample. The mean of this distribution is observed to be slightly higher than the ideal value of 27, however, this is expected as the covariance matrices do not account for the $\delta_{\text{Low Energy Pile-up}}$ noise component.

The χ^2 distributions shown in Figure 6.13 differ between the e^+ vs e^- samples. This is seen for data and MC, and is due to the $\delta_{\text{Low Energy Pile-up}}$ background component varying across the calorimeter. Although the distributions in Figure 6.13 include all the crystals in the calorimeter barrel, due to the kinematics of $e^+e^- \to e^+e^-$ scattering, the majority of e^- clusters are in the forward region of the calorimeter and majority of the e^+ clusters are in the backward region of the calorimeter.

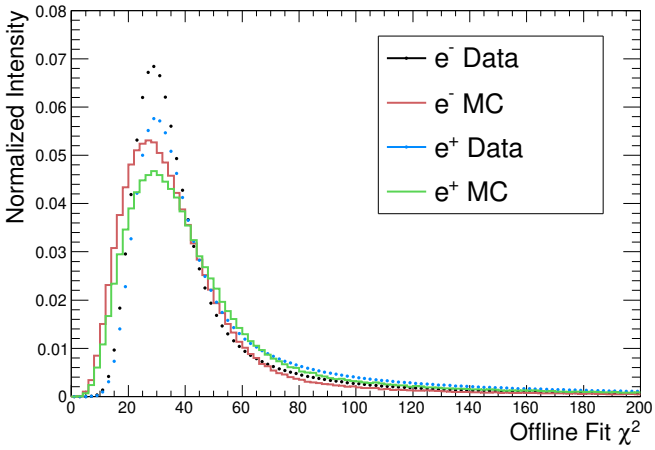

Figure 6.13: Distributions of χ^2 for photon+hadron template fit for all crystals in barrel region of the calorimeter selected from clusters produced by $e^{\pm}$ from $e^+e^- \to e^+e^-$.

To evaluate crystal-by-crystal performance, the analogous χ^2 distribution to Figure 6.13 is produced for each crystal and $\langle\chi^2\rangle_{\text{EM}}$ is computed for each crystal. In Figure 6.14 $\langle\chi^2\rangle_{\text{EM}}$ is shown for all crystals in the calorimeter. In this figure Cell ID is a labelling system used to identify the crystals in the Belle II calorimeter. Cell ID

= 1-1007 corresponds to the crystals in the forward endcap, 1008 - 7776 the barrel and 7777 - 8737 backward endcap.

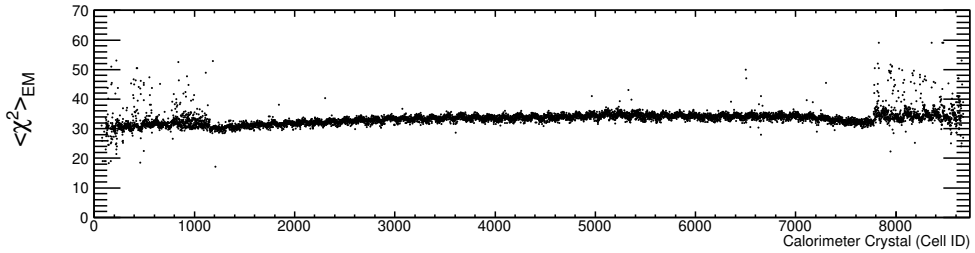

(a) Data

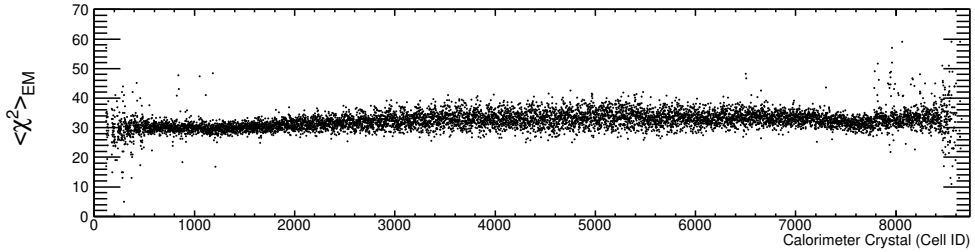

(b) MC

Figure 6.14: $\langle\chi^2\rangle_{\mathrm{EM}}$ for each crystal channel in the Belle II calorimeter measured with crystals with photon-like pulse shapes. Error bars are not shown for clarity. The larger spread in values for MC is due to the MC having lower statistics relative to the data.

The data in Figure 6.14 demonstrates the covariance matrix performance is consistent across the calorimeter as $\langle\chi^2\rangle_{\mathrm{EM}}$ is observed to not have large crystal-to-crystal variations. For the majority of crystals in the calorimeter, $\langle\chi^2\rangle_{\mathrm{EM}}$ is slightly above the ideal value of 27, as expected from the discussion above. In the barrel a small number of outlier crystals are present with anomalously high/low $\langle\chi^2\rangle_{\mathrm{EM}}$ values. For these crystal channels the electronics noise likely has changed since the calibration was performed and thus the covariance matrix modelling in these few cases can be improved in a future calibration. In the endcap regions the majority of the covariance matrices are also shown to be well-calibrated, however the rate of outlier crystals is higher relative to the barrel. This is attributed to higher beam backgrounds in the endcaps. Comparing the data and MC, similar behaviour is observed and several of the outlier crystals are identical in the MC and data, verifying that for these few crystals the noise in the crystal channel changed since the calibration was initially performed.

To quantify the covariance matrix performance in data vs MC, the ratio of $\langle\chi^2\rangle_{\rm EM}$ in data over MC, $\langle\chi^2\rangle_{\rm EM}$(Data)/ $\langle\chi^2\rangle_{\rm EM}$(MC), is computed for each crystal in the barrel. The results are summarized by the histogram in Figure 6.15 where each entry corresponds to one crystal. The mean of the histogram in Figure 6.15 demonstrates that $\langle\chi^2\rangle_{\rm EM}$ in data is on average 3% higher relative to the MC. This difference between data and MC can be attributed to differences in the noise present in data vs. MC. The noise characteristics are not expected to be identical in data vs MC as the background overlay data, used to reproduce the detector conditions in simulation, were only recorded during the latter end of Phase 2 data-taking.

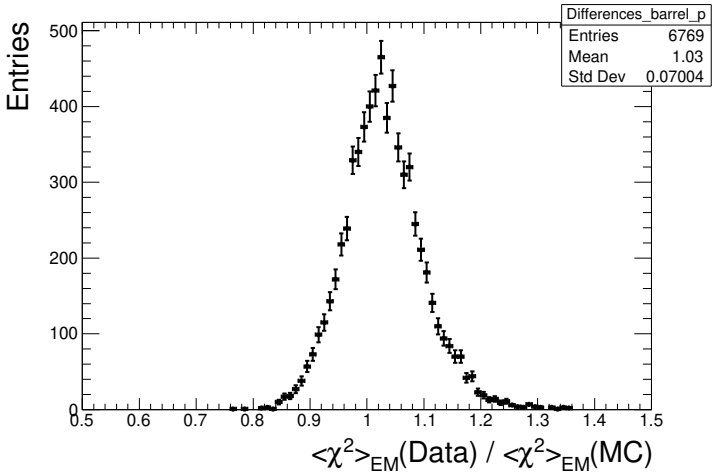

Figure 6.15: Histogram of the ratio of $\langle\chi^2\rangle_{\rm EM}$ in data over MC for all crystals in the calorimeter barrel.

6.5.2 Photon Template Calibration Validation

From the definition of the photon templates, if they are well-calibrated then when the photon+hadron fit is applied to a sample of waveforms from electromagnetic showers, the hadron intensity measured by the photon+hadron fits will be zero. In practice due to small variations in noise between different waveforms, the photon+hadron fit will sometimes add or subtract a small contribution of the hadron template to compensate for noise in the waveform. This results in the hadron intensity for waveforms from a sample of electromagnetic showers to sometimes have small positive and negative values. This is demonstrated by Figure 6.16 showing for data and MC the crystal hadron intensity vs crystal energy for the crystals in the e^+ clusters selected from Bhabha events. At the simulation level, the simulated hadron scintillation com-

ponent emission is always greater or equal to zero, however after reconstruction small negative values in MC are observed as fit artifacts due to noise in the waveforms. This feature is also observed in the data.

To evaluate the photon template calibrations, the mean of the hadron intensity distribution for the sample of waveforms from electromagnetic showers, $\langle N_H \rangle_{EM}$, can be used. This is because if the photon template is mis-calibrated, then the photon+hadron fit will consistently compensate by adding or subtracting a small fraction of the hadron template, resulting in a shift $\langle N_H \rangle_{EM}$ from zero. In Figure 6.16 a small energy dependence in $\langle N_H \rangle_{EM}$ is observed in the data which will be quantified and discussed in Section 6.7.

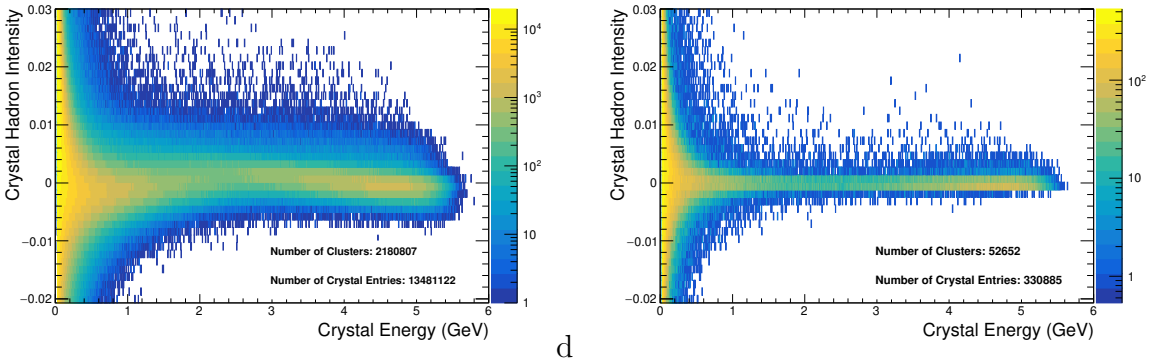

(a) Data (b) MC

Figure 6.16: Crystal hadron intensity vs crystal energy for crystals in e^+ clusters selected from Bhabha scattering. Distribution is shown to demonstrate photon template calibration performance. The energy dependence observed in the data is discussed in Section 6.7. Additional discussion on this sample is also in Chapter 7 Section 7.2.

To evaluate $\langle N_H \rangle_{EM}$, a histogram of the hadron intensity for all waveforms in the crystal energy range 0.075-0.5 GeV with photon+hadron fit $\chi^2 < 60$ is produced for each crystal and the mean of the distribution is computed. This crystal energy range is used to be consistent with the hadron template validation in Section 6.5.3. In Figure 6.17 $\langle N_H \rangle_{EM}$ is shown for all crystals in the calorimeter. From this result any systematic fluctuations in the photon template calibrations for crystal channels in the barrel are found to produce deviations from zero in $\langle N_H \rangle_{EM}$ that are smaller than ± 0.005, indicating the photon templates are well-calibrated for the majority of crystals. In the endcaps larger systematic variations are observed indicating that the photon template calibrations can be improved.

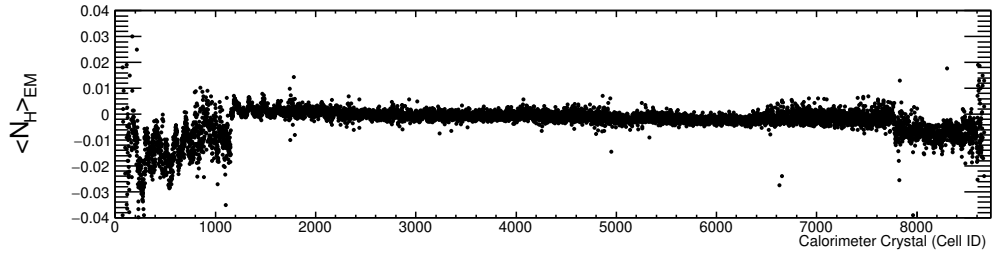

(a) Data

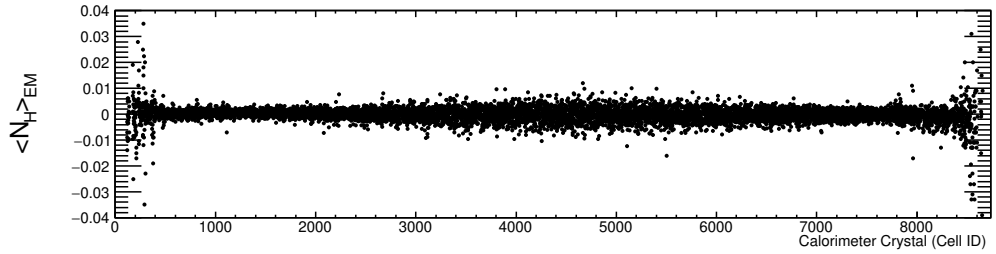

(b) MC

Figure 6.17: $\langle \mathrm{N_H} \rangle_{\mathrm{EM}}$ for each crystal channel in the Belle II calorimeter measured for crystals in energy range $0.075 - 0.5$ GeV from clusters produced by $e^{\pm}$ selected from Bhabha events. Error bars are not shown for clarity.

To quantify the photon template calibration in data vs. MC, the difference between $\langle \mathrm{N_H} \rangle_{\mathrm{EM}}$ in data and MC is computed for each crystal and is shown in the histogram in Figure 6.18. Note only crystals in the barrel region are shown. The mean value of the histogram is observed to be near ideal with 99% of crystals with $\langle \mathrm{N_H} \rangle_{\mathrm{EM}}$ within ± 0.01.

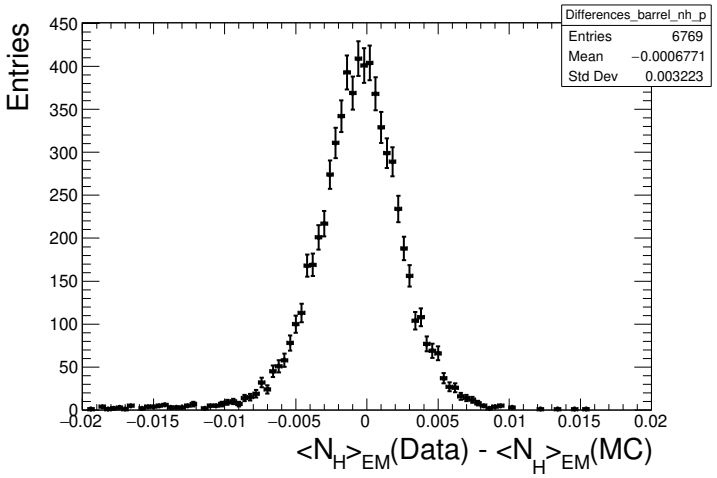

Figure 6.18: Histogram of the difference between $\langle \mathrm{N_H} \rangle_{\mathrm{EM}}$ in data vs. MC for all crystals in the calorimeter barrel.

6.5.3 Hadron Template Calibration Validation

The initial hadron template validation presented in Section 6.3.2 demonstrated that the hadron template calibration procedure developed in Section 6.3.1 produces hadron templates that correctly model the primary features of the waveforms observed in data and produced by hadronic energy deposits. In this calibration procedure, however, an approximation is made such that the CsI(Tl) emission shape for a pure photon and hadron energy deposit is identical for all crystals. As a result, the hadron templates are expected to only be approximations of the true hadron scintillation response of the crystal channel. In this section the precision of this calibration procedure is evaluated.

A challenge in evaluating the hadron template calibration on a channel-by-channel basis is selecting a sample of waveforms in data with hadronic pulse shapes such that sufficient statistics is available for each crystal channel. From the $\sim$ 0.5 fb^{-1} of collision data collected during Phase 2, there was not a single control sample that provided enough statistics. To accumulate a large sample of waveforms from Phase 2 data with hadron-like pulse shapes, all tracks in Phase 2 data are selected that pass the following criteria:

- Event has 4 or more tracks originating from the interaction point. (Bhabha veto)

- Cluster energy is greater than 50 MeV.
- $|d_0| < 0.5$ cm
- $|z_0| < 1$ cm
- $0.3 < p_{\text{lab}} < 3$ GeV/c
- $\text{E}_{\text{ecl}}/p_{\text{lab}}$ is outside the range $0.9 - 1.05$ (electron veto)
- E_{ecl} is outside the range $0.15 - 0.25$ GeV. (Ionizing cluster veto)

For this sample of clusters, the crystal hadron intensity vs crystal energy distribution is shown in Figure 6.19, demonstrating the abundance of crystals present with hadron-like pulse shapes. In addition the pulse shape bands from protons and multi-protons are clearly observed in data and MC. Note in Chapter 7 the crystal hadron intensity vs crystal energy distributions for control samples of $\pi^{\pm}, K^{\pm}$ and $p/\bar{p}$ are studied in detail.

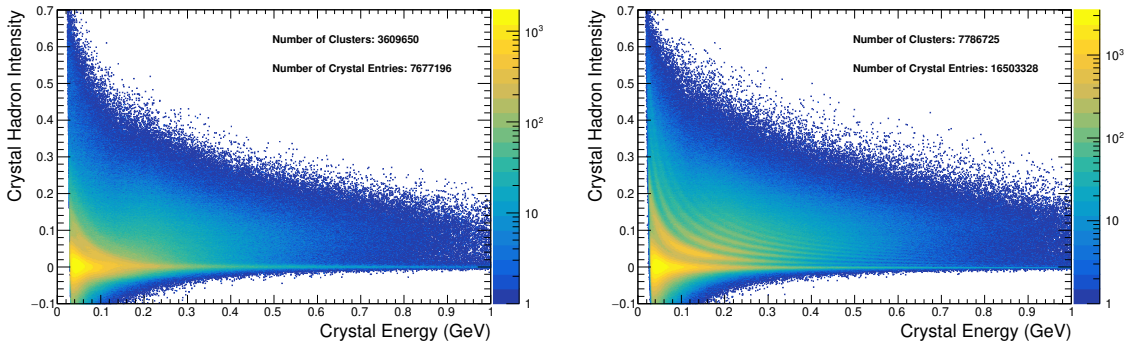

(a) Data (b) MC

Figure 6.19: Crystal hadron intensity vs crystal energy for crystals in clusters selected from general hadron track selection. Note in Chapter 7 the crystal hadron intensity vs crystal energy distribution for control samples of $\pi^{\pm}, K^{\pm}$ and $p/\bar{p}$ are studied in detail.

From this hadron track selection, all waveforms from crystals in the energy range $0.075-0.5$ GeV and with hadron intensity above 0.03 are used to define the hadron-like waveform sample. Using this sample of waveforms, a histogram of the photon+hadron fit χ^2 is produced for each crystal and $\langle\chi^2\rangle_{\text{Had}}$ is computed for each crystal. In Figure 6.20 $\langle\chi^2\rangle_{\text{Had}}$ is shown for all crystals in the calorimeter.

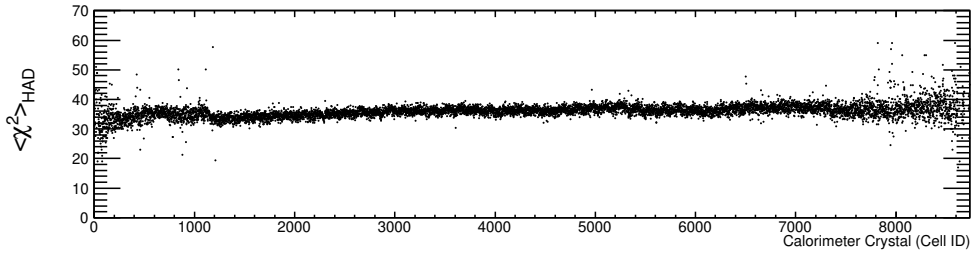

(a) Data

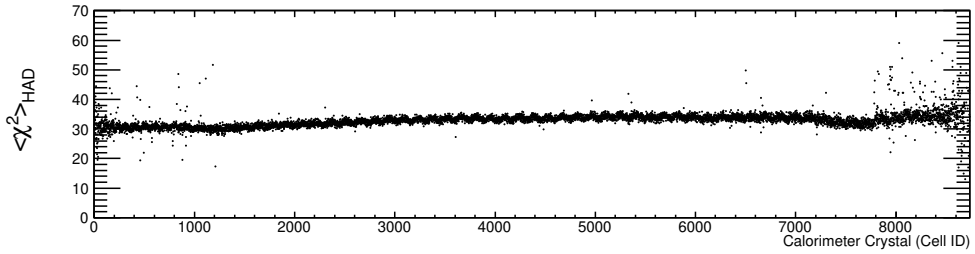

(b) MC

Figure 6.20: $\langle\chi^2\rangle_{\text{Had}}$ for each crystal channel in the Belle II calorimeter measured for crystals with hadron-like pulse shapes. Error bars are not shown for clarity.

Studying the data in Figure 6.20, $\langle\chi^2\rangle_{\text{Had}}$ is observed to be consistent for the majority of the crystals across the calorimeter demonstrating the hadron templates are well-calibrated. In the data there are a few outliers present however the same crystals in the MC are also found to be outliers and thus the anomalously high/low χ^2 are due to the covariance modelling and not the hadron template calibrations. Detailed in Section 6.8 where the simulation methods for Belle II are discussed, the same photon and hadron templates used for simulation are also used for fitting simulated waveforms. This means the MC in Figure 6.20 shows the results expected if the hadron templates are perfectly calibrated. Relative to the data, the MC has slightly lower $\langle\chi^2\rangle_{\text{Had}}$ values. To quantify the difference in data vs. MC the ratio of $\langle\chi^2\rangle_{\text{Had}}$ in data over MC is computed for each crystal and shown in the histogram in Figure 6.21. From this result it is observed that the mean of the histogram is shifted from 1.0 by 9.8%. Referring back to the covariance matrix evaluation in Figure 6.15, of the 9.8% data vs MC difference, 3% can be attributed to differences in the background modelling in data vs. MC. This results in a difference in 6.8% on average across the calorimeter for the χ^2 mean for waveforms with hadron-like pulse shapes. With improved hadron template calibrations that would be possible with more data, this can be improved.

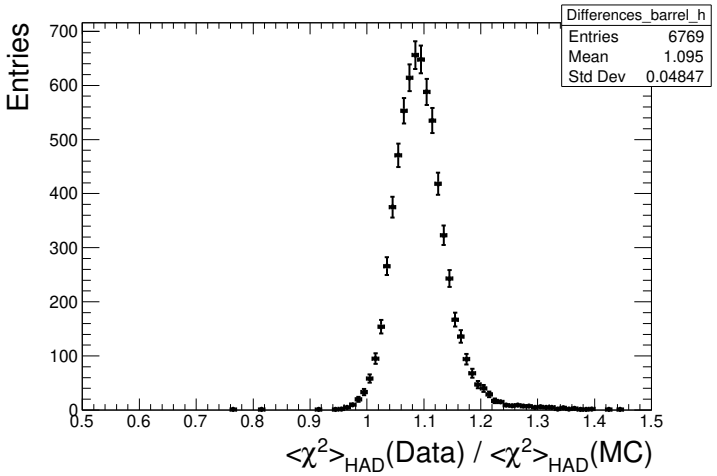

Figure 6.21: Histogram of the ratio of $\langle\chi^2\rangle_{\text{Had}}$ in data over MC for all crystals in the calorimeter barrel.

6.5.4 Method to Improve Hadron Template Calibration

The procedure described above to compute the hadron templates was developed such that a sample of hadron-like pulse shapes was not required to calibrate the templates. This procedure however required the exact nature of the scintillation emission response of the crystals to be assumed. Shown in Section 6.5.3, this approach allowed the primary features of the waveforms to be modelled to a precision of 6.8%. One potential method to improve this calibration is to use a similar procedure as done with the photon template calibration such that a set of hadron-like waveforms are simultaneously fit to calculate the 11 parameters that define the hadron template. The advantage of this procedure is that the precise modelling of the scintillation emission shape for each crystal is not required, however, the disadvantage is that a large dataset of hadron-like waveforms would be required such that each crystal in the calorimeter has a sample of hadron-like waveforms to simultaneously fit.

6.6 Pile-up Photon Fit

The noise source $\delta_{\text{High Energy Pile-up}}$ corresponds to when an significant ($>\sim 5$ MeV) energy deposit occurs in the crystal and is out-of-time relative to the primary energy deposit. When this occurs a secondary pulse in the waveform is formed and the waveform cannot be modelled with the default photon+hadron template fit due to

the extra pile-up pulse. To model this background, the photon+hadron+pile-up fit hypothesis defined in equation 6.13 was implemented.

$$G^{\text{Pile-up}}(t) = G(t - t_0) + L_{\text{Pile-up}} R_{\text{Photon}}(t - t_1) \tag{6.13}$$

In equation 6.13, $G(t)$ is the standard photon+hadron fit that was previously defined in equation 6.1 and is still used to model the primary pulse in the waveform. The additional term $L_{\text{Pile-Up}} R_{\text{Photon}}(t - t_1)$ in equation 6.13 models the pile-up pulse in the waveform using the photon template. In equation 6.13 $t_0 \neq t_1$.

In Figure 6.22, example fits to waveforms in Belle II data that failed the photon+hadron fit but passed the photon+hadron+pile-up hypothesis are shown. In these figures the out-of-time energy deposits are clearly visible and are well modelled by the additional photon template added to the fit. During offline reconstruction when the multi-template waveform fitting is performed, the photon+hadron fit is initially attempted. If this fit has a $\chi^2 > 60$ then the fit is classified as a failed fit and the pile-up fit hypothesis is attempted.

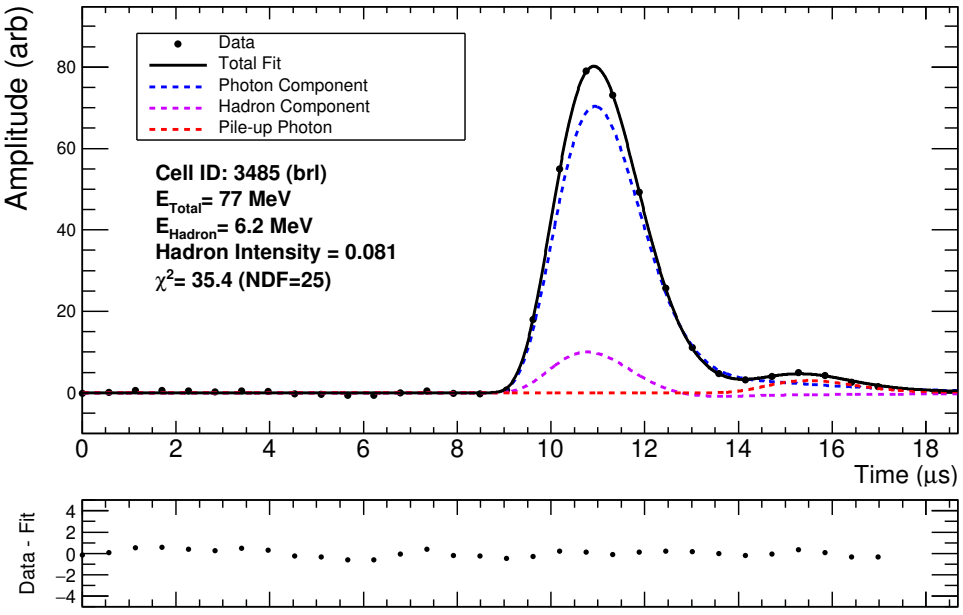

(a)

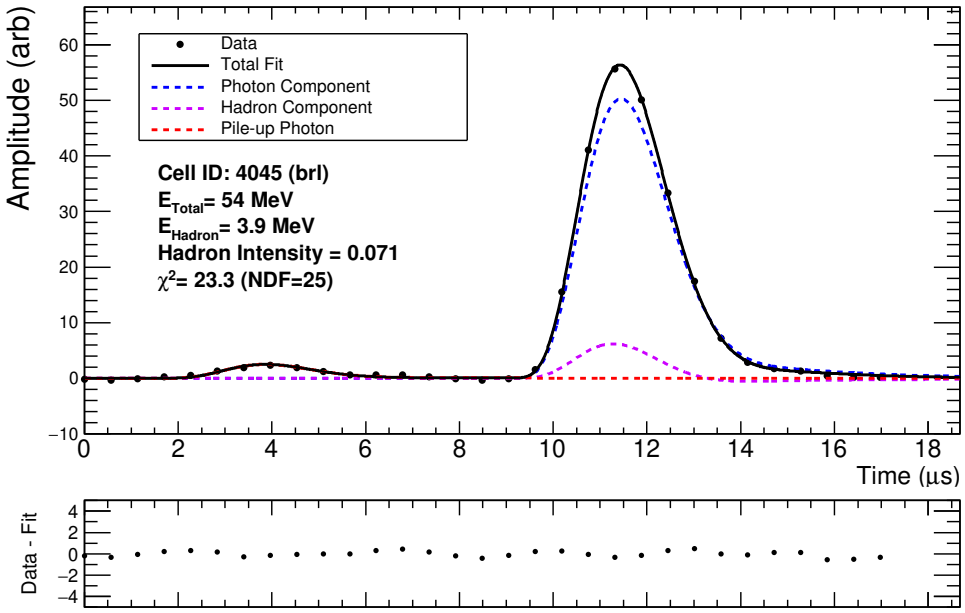

(b)

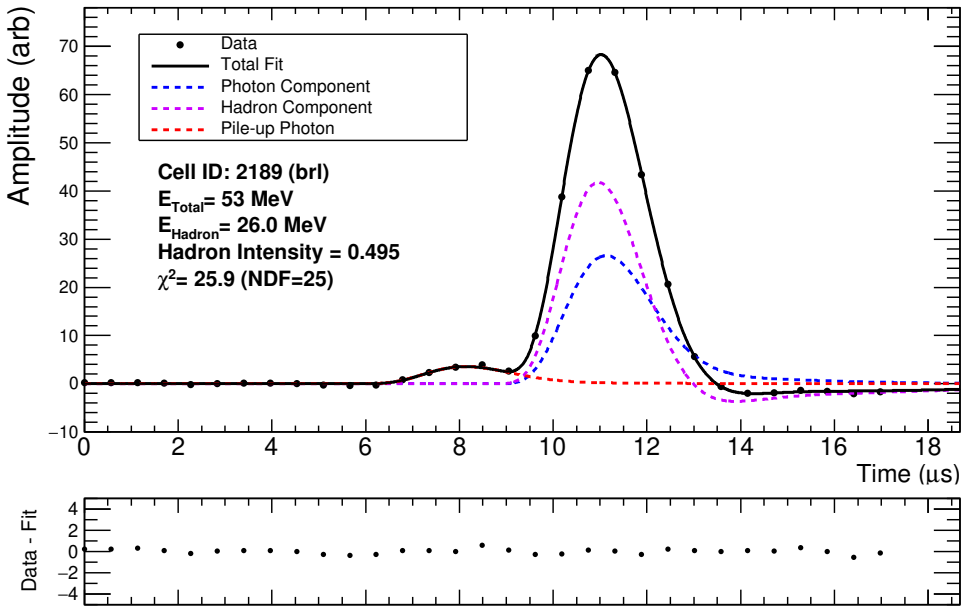

(c)

Figure 6.22: Examples of photon+hadron+pile-up offline fits for Belle II calorimeter crystal waveforms in data. a) Pile-up photon in tail. b) Pile-up photon in baseline. c) Pile-up photon in baseline near primary pulse.

With the photon+hadron+pile-up fit the pulse shape features from hadronic energy deposits can still be resolved in data. This is demonstrated in Figure 6.23 showing for the photon+hadron+pile-up fits the crystal hadron intensity vs crystal energy distribution for crystals in clusters from the hadron track selection. For these crystals the waveform failed the photon+hadron fit but passed the photon+hadron+pile-up fit. In this figure the proton band can be still be seen in the data and MC. Note however in the photon+hadron+pile-up fits the hadron intensity resolution is degraded relative to the photon+hadron fits as discussed in Section 6.7.1.

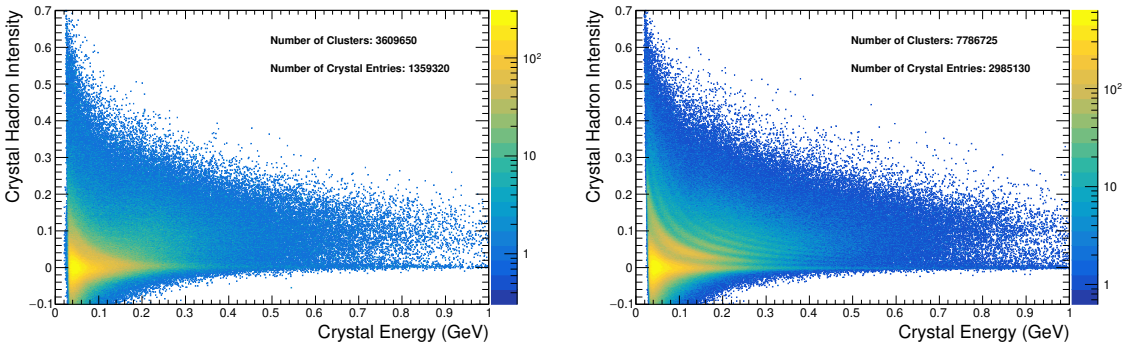

(a) Data (b) MC

Figure 6.23: Crystal hadron intensity vs crystal energy for crystals in clusters selected from general hadron track selection where the waveform fit failed the photon+hadron fit and passed the photon+hadron+pile-up fit.

6.6.1 Diode-crossing Fit Type

The final fit hypothesis implemented was a Photon+Diode-crossing template fit. This fit models when a particle deposits energy directly in the PIN diodes mounted on the rear of the CsI(Tl) crystal. The waveform template to model the diode-crossing response is computed by using an input pulse with decay time of 10 ns to model an energy deposit directly in the PIN diode. A typical diode-crossing template is shown in Figure 6.24a overlaid with a typical photon template and hadron template for comparison. In this figure it is seen that the diode-crossing template has a more pronounced undershoot in the tail region compared to the hadron template, and in addition the pulse is narrower and peaks earlier than the hadron template. These features allow the diode-crossings to be distinguished from hadron component scintillation emission. In Figure 6.24b a sample diode-crossing fit is shown. In the Phase

2 data, only a small fraction, less than a couple percent, of waveform fits were found to pass the Photon+Diode-crossing hypothesis.

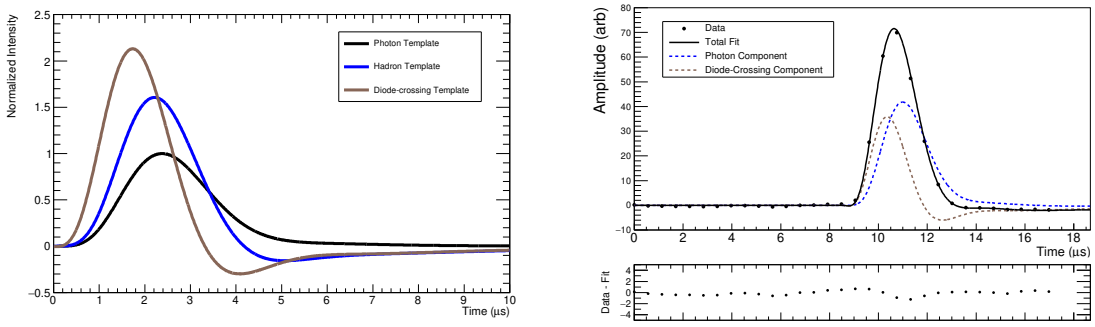

(a) (b)

Figure 6.24: a) Typical results for diode-crossing waveform template with typical photon template and hadron template overlaid. b) Sample Photon+Diode-crossing fit from data.

6.6.2 Distribution of Fit Types

Discussed above, multiple waveform fit hypothesis were implemented in the Belle II reconstruction. During offline reconstruction the photon+hadron fit is initially attempted to the waveforms saved offline. If that fit fails the $\chi^2 < 60$ requirement, then the photon+hadron+pile-up fit is attempted. If that fit has a poor χ^2 then a photon+diode-crossing fit is applied. If a waveform fails the $\chi^2 < 60$ requirement for all fit hypotheses then it is not used for computing the PSD cluster variables. Shown in Figure 6.25 is the fraction of waveform fits with $\chi^2 < 60$ for one of the fits attempted in reconstruction, for various control samples of particles. Selections requirements for these samples are detailed in Appendix A. Across all samples the fitting efficiency ranges from $80\% - 95\%$. Recall the covariance matrices applied correspond to electronics noise only. With improved covariance matrices that model $\delta_{\text{Low Energy Pile-up}}$ noise this fit efficiency can be improved in future studies. The variation between samples can be caused by a variety of factors such as geometric distribution of the backgrounds in the calorimeter and the crystal energy scale of the sample. Differences in data vs. MC are found to be less than a few percent in most cases.

In Figure 6.25b the absolute fraction of photon+hadron fits is shown across the samples. For this fit hypothesis, the fit efficiency ranges from $70 - 80\%$ depending on the sample. In Figure 6.25c the absolute fraction of waveforms passing the

photon+hadron+pile-up hypothesis is shown and a found to account for $\sim 14\%$ of all fits. This indicates the $\delta_{\text{High Energy Pile-up}}$ background component is significant during SuperKEKB operation.

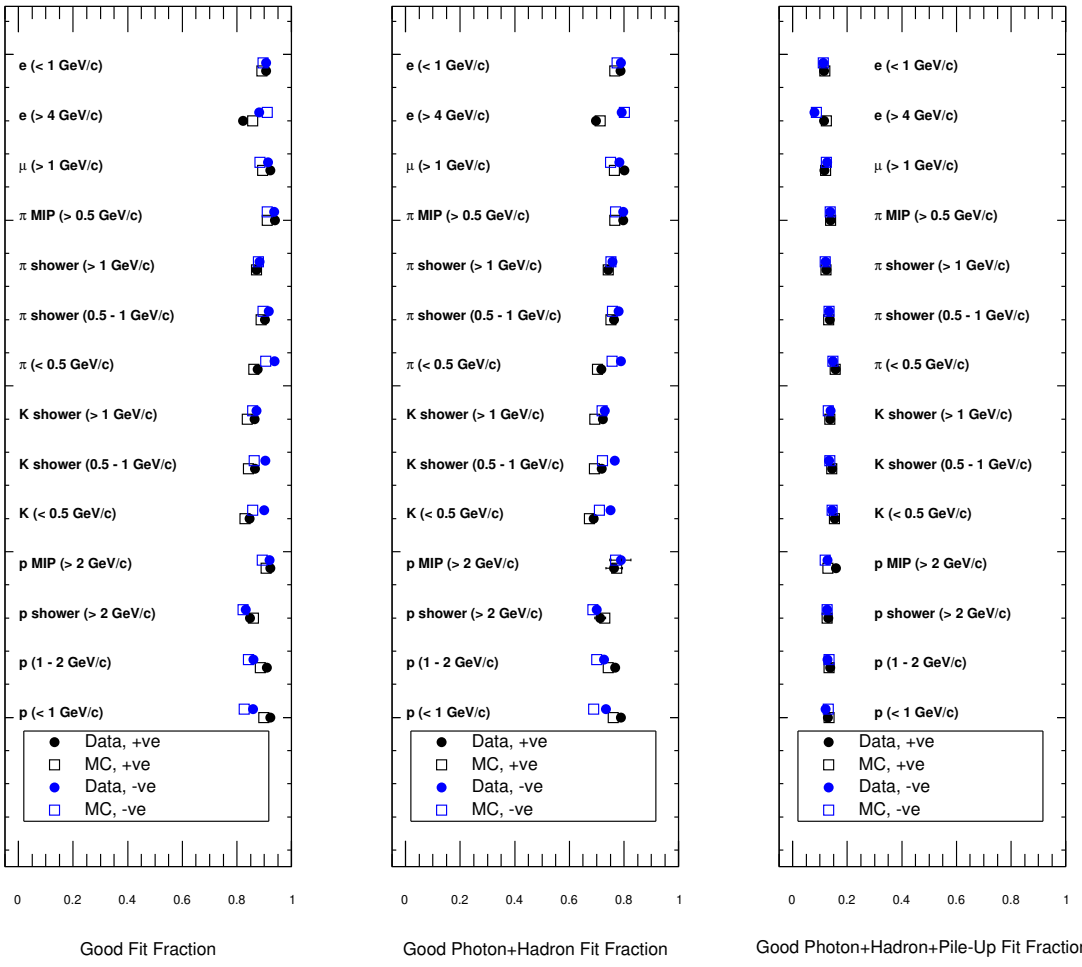

(a) (b) (c)

Figure 6.25: Absolute fraction of waveform fits that: a) Pass any fit hypothesis b) Pass the Photon+Hadron fit Hypothesis c) Fail Photon+Hadron fit and pass the Photon+Hadron+Pile-Up fit Hypothesis for various control samples selected from Phase 2 data and MC.

6.6.3 Other Potential Fit Hypotheses

Shown above, with the current reconstruction the current fitting efficiency ranges from $80\% - 95\%$ depending on the particle sample. A potential improvement to the waveform fitting could be to implement additional fit hypotheses such as:

- Photon+Hadron+Two Pile-up Photons: Two pile-up photons are added to the fit to model waveforms with two pile-up pulses. As $\sim 14\%$ of all fits had one pile-up photon it is expected that $\sim 2\%$ of all waveforms will have this form assuming the noise is uniformly distributed.
- Photon+Hadron+Pile-Up Hadron: Analogous to the photon+hadron+pile-up photon fit already implemented, this fit would model the pile-up pulse with a photon and hadron template. This would account for the scenario where the pile-up hit is from a hadron such as a background neutron.
- Photon+Hadron+Diode-Crossing: The primary pulse is fit with the photon+hadron+diode-crossing template.
- Repeat fit with covariance matrix computed for a higher noise level: This case is for if photon+hadron fit failed because the waveform had a higher than normal noise level. In this case, a second fit would be attempted using a covariance matrix that models a higher noise level.

6.7 Hadron Intensity Energy Dependence and Resolution

The resolution of the hadron intensity characterizes how precisely the photon+hadron fit can measure the hadron intensity of an energy deposit. The resolution of the hadron intensity can be measured with the sample of waveforms from electromagnetic showers because the true hadron intensity is expected to be zero and thus is well known. The sample of waveforms from crystals in clusters produced by $e^{\pm}$ selected from Bhabha scattering events are used to measure the hadron intensity resolution. With this sample, the hadron intensity mean and sigma is measured as a function of crystal energy by fitting energy slices of the distributions in Figure 6.16 to a Gaussian. Applying this procedure, the mean and sigma is measured as a function

of crystal energy for the photon+hadron fit and are shown in Figures 6.26 and 6.27, respectively.

Comparing the data and MC distributions in Figure 6.26, the hadron intensity mean for the sample of crystals from electromagnetic showers is observed to be within ± 0.0025 of the expected zero value, for crystal energy deposits above 100 MeV. Within this band, systematic fluctuations are observed in the data that are not observed in the MC. The systematic fluctuations observed in the data have the same general features for the e^+ and e^- samples. The slight difference between the e^+ vs e^- samples are likely due to differences in the calibration performance for crystals in the forward vs backward region of the calorimeter. As the scale of these deviations from zero are small, they can be caused by a variety of factors such as small non-linearities in the electronic response or mis-calibrations in the photon template, hadron template or covariance matrices. Overall these fluctuations are small relative to the scale of hadron energy deposits that produce hadron component intensities in the range of $\sim 0.03 - 0.60$. For energy deposits below 100 MeV the mean hadron intensity value increases as the energy decreases. This trend is observed in the MC and data.

The resolution of the hadron intensity as a function of crystal energy is shown in Figure 6.27. From this figure the resolution of the hadron intensity is observed to improve as the crystal energy increases, as expected due to the improvement in the signal-to-noise at higher crystal energies. At crystal energies above ~ 1 GeV the resolutions for e^+ vs e^- are very similar. At lower crystal energies, the e^+ clusters have worse resolution then the crystals in the e^- cluster. This trend is observed in data and MC and is likely due to geometric distribution of the background in the detector. In general the resolution in MC is observed to be better than the data. This is likely due to small crystal-by-crystal variations in the accuracy of the photon template calibrations in data. Due to the technical limitations discussed in Section 6.8, in simulation crystal-by-crystal variations in the scintillation response are not modelled and the photon and hadron templates are perfectly calibrated for MC.

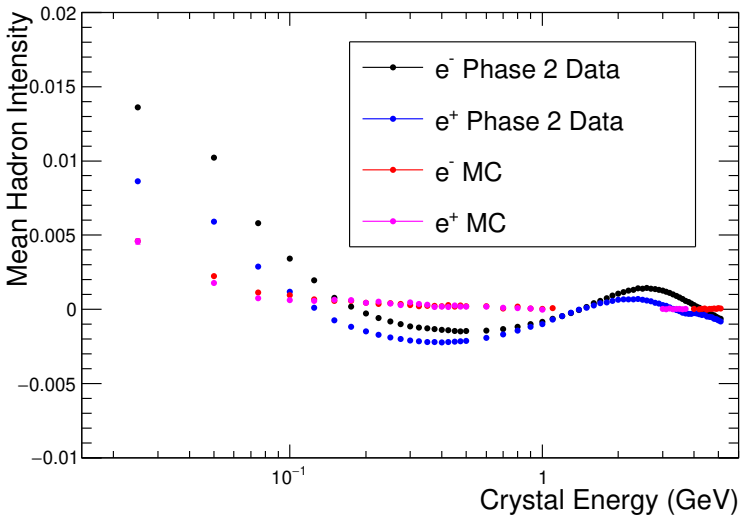

Figure 6.26: Mean of the hadron intensity distribution measured with energy deposits from electrons from Bhabha scattering. Gap in MC between 1 and 3 GeV is due to low MC statistics.

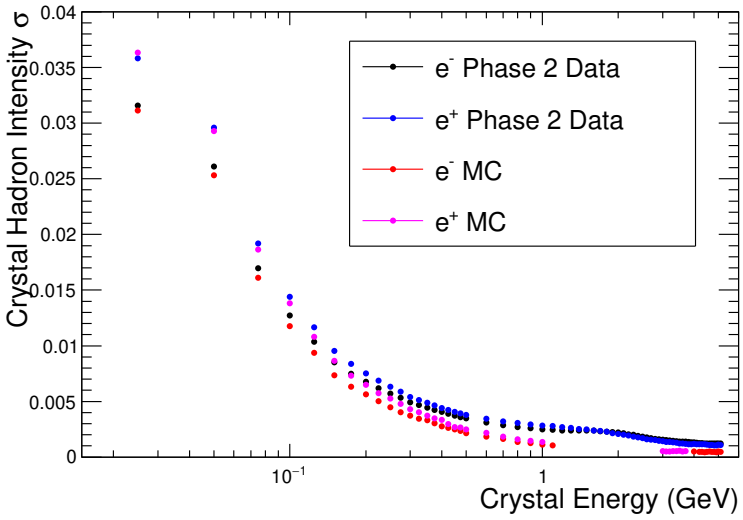

Figure 6.27: Resolution of the hadron intensity as a function of the crystal energy, measured with crystals in Bahbha clusters. Gap in MC between 1 and 3 GeV is due to low MC statistics.

6.7.1 Impact of Pile-Up Photon Fit on Pulse Shape Resolution

In Phase 2 data, $\sim$ 14% of all waveform fits fail the photon+hadron fit and pass the photon+hadron+pile-up photon fit as shown earlier in Figure 6.25c. For the photon+hadron+pile-up photon fit, the resolution of the hadron component intensity is slightly degraded relative to the photon+hadron fits.

Following the same procedure applied in the previous section, the hadron intensity resolution for waveforms passing the photon+hadron+pile-up fit hypothesis is measured using crystals in the e^+ cluster sample. This is shown in Figure 6.28 as a function of crystal energy and overlaid with the photon+hadron resolution for comparison. From this figure it is observed that the pile-up fit type degrades the hadron intensity resolution mainly for crystal energies below 0.5 GeV. Above 0.5 GeV the resolution between the two fit types is similar. As shown earlier in Figure 6.23, although the hadron intensity resolution is degraded, hadron pulse shape features can still be resolved in the data using the photon+hadron+pile-up fits.

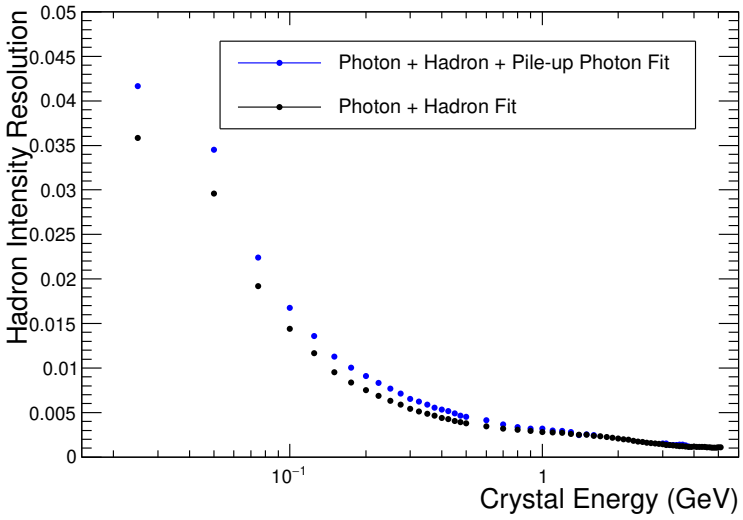

Figure 6.28: Comparison of the hadron intensity resoltion the photon+hadron vs photon+hadron+pile-up fits.

6.8 Simulation of Pulse Shape Discrimination for Belle II

Particle dependent scintillation response for CsI(Tl) is not included in GEANT4 simulations by default. To simulate pulse shape discrimination at Belle II, the CsI(Tl) scintillation response simulation methods that were developed in Chapter 5 [25] are applied. If these simulation methods are not applied, then all simulated waveforms would have photon-like pulse shapes, independent of the type of energy deposit.

To simulate the particle dependent scintillation response the following items are required:

- Hadron emission function, $f(dE/dx)$. Computes the fraction of scintillation emission emitted in the hadron scintillation component for an instantaneous energy deposit.
- Photon template, $R_{\text{Photon}}(t)$, and hadron template, $R_{\text{Hadron}}(t)$, corresponding to full Belle II signal chain response to scintillation emission from an electromagnetic shower and hadron scintillation component emission, respectively.

With these items, the simulation procedure applied at Belle II, with regards to pulse shape discrimination, is outlined below:

1. GEANT4 simulates the material interactions of the particles in the event with the CsI(Tl) crystals. From GEANT4, the magnitude of the discrete energy deposits by each particle (primary and secondary) are acquired and given by Δ^i_{EDEP} where i is the GEANT4 step.
2. The discrete GEANT4 energy deposit, Δ^i_{EDEP}, is converted into an electron equivalent light yield, $\Delta^i_{\text{L,Total}}$, using the Birk's scintillation efficiency model discussed in Chapter 5 [25]. Recall, for energy deposits from electromagnetic showers the Birks factor is equal to one. Thus the electron equivalent light yield in this case is equal to the GEANT4 energy deposit.
3. Using $f(dE/dx)$, the magnitude of the hadron scintillation component emission for the discrete light output yield, $\Delta^i_{\text{L,Hadron}}$, is computed. By definition, the remaining energy is emitted in the shape of the photon template, $\Delta^i_{\text{L,Photon}} = \Delta^{,i}_{\text{L,Total}} - \Delta^i_{\text{L,Hadron}}$.

4. Steps 1- 3 are repeated for each discrete step computed by GEANT4 and the values $\Delta^i_{\mathrm{L,Total}}$ and $\Delta^i_{\mathrm{L,Hadron}}$ are saved in addition to the time of the step t^i.

5. At the end of the event, the simulated waveform, $G^{\mathrm{sim}}(t)$, is constructed using equation 6.14 by incrementally adding the photon template and hadron templates, scaled by the $\Delta^i_{\mathrm{L,Photon}}$ and $\Delta^i_{\mathrm{L,Hadron}}$ values, for all discrete GEANT4 steps, n_{steps}.

$$G^{\mathrm{sim}}(t) = \sum_{i=0}^{n_{\mathrm{steps}}} \Delta^i_{\mathrm{L,Photon}} R_{\mathrm{Photon}}(t - t^i) + \Delta^i_{\mathrm{L,Hadron}} R_{\mathrm{Hadron}}(t - t^i) \qquad (6.14)$$

6. After the simulated pulse, $G^{\mathrm{sim}}(t)$, is constructed, a noise waveform, recorded from random trigger events from data, is added to $G^{\mathrm{sim}}(t)$. This allows the noise conditions in data to be modelled in simulation.

The procedure outlined above is performed for each crystal in the Belle II simulation allowing a simulated waveform to be constructed for each crystal such that waveform shape is determined by the interactions of the primary and secondary particles that entered the crystal volume during the event. During reconstruction, the simulated waveforms are fit using the identical fit procedures as data, as described previously in this chapter. Figure 6.29 shows an example of a simulated waveform (black points) with a sample fit to the photon+hadron hypothesis overlaid, illustrating the same procedures used to fit waveforms in data are also applied to the simulated waveforms.

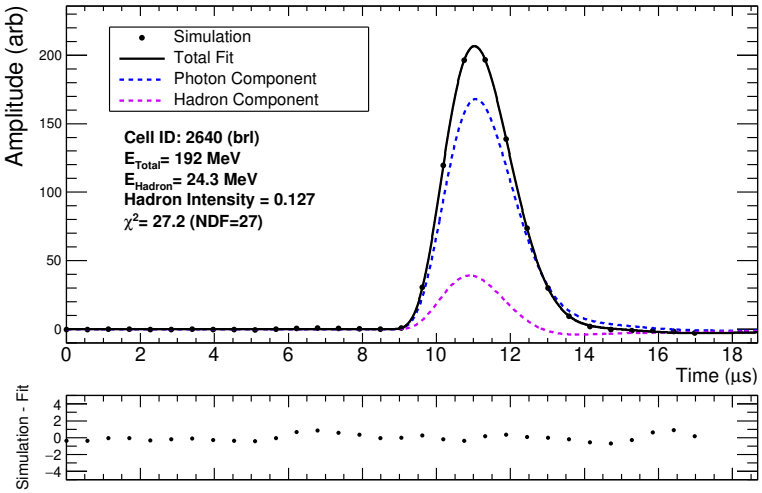

Figure 6.29: Sample simulated waveform with hadron-like pulse shape. Fit applied during reconstruction is overlaid.

6.8.1 Hadron Emission Function Calibration for Belle II Simulation

Formulated in Chapter 5 [25], $f(dE/dx)$ computes the fraction of scintillation emission that is emitted in the hadron scintillation component for an instantaneous energy deposit using the ionization $d\mathrm{E}/dx$ of the interacting particle when it deposited the energy. Also detailed in Chapter 5 [25], $f(dE/dx)$ is derived from the single proton band that is observed in the crystal hadron intensity vs crystal energy distribution. This is achieved because a single proton ionizing then stopping in the crystal provides a controlled scenario such that the range of ionization $d\mathrm{E}/dx$ values the proton takes are known and from the pulse shape, the corresponding hadron scintillation component emission is known. The procedure to compute $f(dE/dx)$ is described in detail in Chapter 5 [25] and validated with the testbeam data. Recall that although the $f(dE/dx)$ is extracted using the single proton band, $f(dE/dx)$ has universal application to all particles and only depends on the ionization $d\mathrm{E}/dx$ of the particle. This was demonstrated in Chapter 5 [25] where the simulations using $f(dE/dx)$ reproduced the pulse shape bands observed for other secondary particles such as deuterons and the multi-hadron pulse shapes in the neutron data. In addition a primary focus of Chapter 7 of this dissertation is evaluating the performance of this simulation method using control samples of charged particles selected from Belle II

collision data.

To isolate the single proton band with Belle II data, a general selection of tracks in Phase 2 data was applied such that there were no requirements on the track d_0 and z_0. As no d_0 and z_0 requirements are applied, the number of protons in the sample is greatly increased because many protons that are produced by beam background interactions in the detector material are included in the selection. From this general sample of tracks, a requirement is placed such that the calorimeter cluster energy is consistent with the track's kinetic energy when the track entered the calorimeter. To compute the kinetic energy, the proton mass hypothesis was applied. This criteria allows the protons in the selection that only ionized and stopped in the calorimeter to be isolated. For the crystals in these clusters, the crystal hadron intensity vs crystal energy distribution is shown in Figure 6.30. In this figure, the single proton band is clearly observed. This is expected as by requiring the cluster energy to be consistent with the proton's kinetic energy when it entered the calorimeter, the sample is dominated by protons that only ionized then stopped in the calorimeter, thus producing an energy deposit with pulse shape on the single proton band. In Figure 6.30 an additional band below the single proton band is also observed. This band, that is below the single proton band, is due to energy deposits from the higher energy protons in the sample. When these protons initially enter the calorimeter they can ionize through a section of a crystal before exiting, and then stopping in the adjacent crystal. In this case the energy deposited in the first crystal will be at a low $d\mathrm{E}/dx$ since the proton is not highly ionizing until stopping in the adjacent crystal. Note in Chapter 7 Section 7.6 control samples of protons that originate from the interaction point are studied and the similar pulse shape features as in Figure 6.30 are observed in data and MC.

From the simulation model developed in Chapter 5 [25], the energy deposits where the proton still has low $d\mathrm{E}/dx$, are expected to have zero hadron intensity. As observed from Figure 6.30 however, the secondary band, and the asymptotic limit of the proton band band, is shifted to a small negative hadron intensity value of -0.02. This -0.02 offset in the data is interesting as it is not present for crystals in electromagnetic showers and suggests that the energy deposits by the higher energy protons in this case produces a different scintillation emission shape than electromagnetic energy deposits. By fitting a Gaussian to energy projections along the two bands in Figure 6.30, the mean values of the proton band and band below the proton band are measured. The mean values measured from this procedure are overlaid in Figure

6.30.

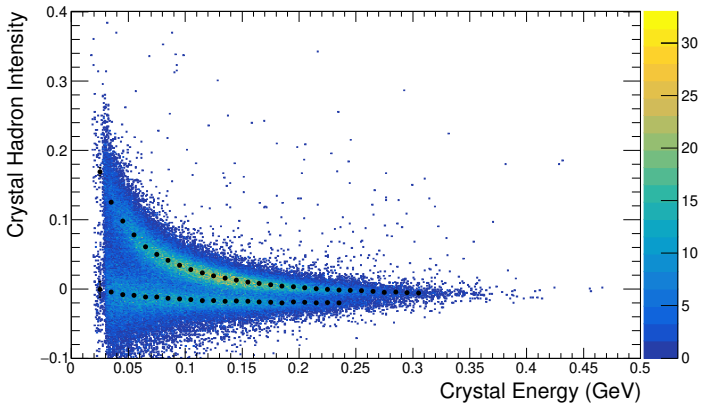

Figure 6.30: Crystal hadron intensity vs crystal energy for ionizing proton clusters in data. Points overlaid measure the mean values of the two bands observed.

A detailed evaluation of the hadron intensity values of the single proton band in the Belle II data show that the Belle II CsI(Tl) channel response to protons was not identical to the response of the CsI(Tl) crystal used in the study in Chapter 5 [25]. That is, although all of the pulse shape features are present in such as particle bands, alpha particle excess and multi-hadron pulse shapes, the precise location of the hadron intensity band structures in the Belle II data are found to be shifted to lower hadron intensity values relative to the results form the TRIUMF testbeam study. This is shown by Figure 6.31 showing the single proton band data points measured in Belle II data overlaid with the predicted response using the $f(dE/dx)$ model derived from the testbeam data in Chapter 5 [25], labelled "Simulation with Uncalibrated $f(dE/dx)$". Although in this result the Belle II data and the uncalibrated simulation have a similar shape, a vertical offset is clearly observed, indicating a difference in hadron scintillation response between the crystal channel used in the TRIUMF testbeam and the Belle II crystal channels. This can be caused by a variety of factors.

The ability to resolve the proton band in the Belle II data suggests that this small difference in the measured CsI(Tl) response is likely caused by a systematic effect that equally affects all crystals in the Belle II calorimeter. This is because the result shown in Figure 6.30 includes all crystals in the calorimeter barrel, and thus if the crystal-by-crystal variations were significant, then the proton band would not be resolved in this plot. A potential cause of this difference in the measured CsI(Tl) response is due to the difference in the spectral response between the PMT

used in the TRIUMF testbeam study and the diodes used at Belle II. The spectral response of the PMT used in the TRIUMF testbeam peaks in the region of 400-500 nm and rapidly drops off for wavelengths above 600 nm [41]. For the diodes used in the Belle II calorimeter however, the spectral response is significant for wavelengths in the range 500-1000 nm, peaking at ∼950 nm [42]. A second significant difference between the experimental setups is that in the TRIUMF testbeam the PMT signal was directly digitized, however in the case of the crystals in the Belle II calorimeter, the signal emitted from the diodes is digitized only after several stages of pre-amplifiers, filtering and shaping. The accumulation of factors such as different spectral response between the PMT and diodes, as well as potentially different frequency responses by the signal chain electronics could lead to the small systematic difference in absolute hadron scintillation emission that is observed.

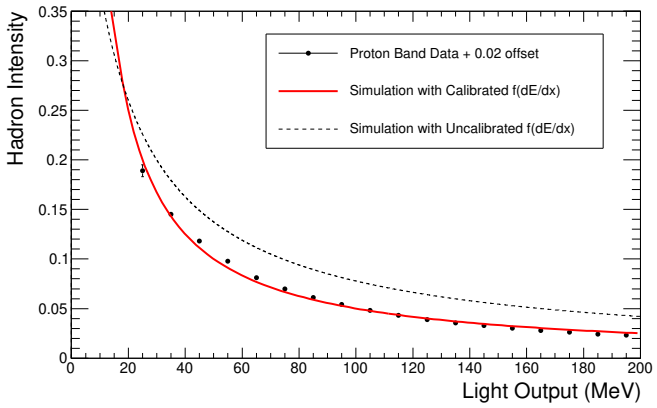

Figure 6.31: Crystal hadron intensity vs. crystal energy for ionizing proton clusters with data points overlaid.

To improve the data vs. MC agreement for Belle II simulations, the ionization proton sample from Belle II data was used to calibrate $f(dE/dx)$ for use in Belle II simulations. When computing $f(dE/dx)$, a complication however arises due to the -0.02 asymptotic limit of the single proton band in Belle II data as $f(dE/dx)$ cannot be negative. In order to proceed with the calibration, a $+0.02$ correction is applied to the measured data points allowing the proton band data used for the $f(dE/dx)$ calibration to have an asymptotic limit that is positive. This $+0.02$ correction is only applied in this special case to calibrate $f(dE/dx)$. With this corrected curve, the calibrated $f(dE/dx)$ is computed using the same procedures applied in Chapter 5 [25] by fitting to the single proton band data (including the $+0.02$ correction) shown

in Figure 6.31. Recall in equation 5.8 in Chapter 5 [25] the $f(dE/dx)$ curve was empirically parametrized by three parameters, A, B and C. When fitting to the Belle II data in Figure 6.31, the parameter A, which determines the maximum value of $f(dE/dx)$ for large $d\mathrm{E}/dx$, was fixed to the value of $A = 0.612$. This was the value computed in Chapter 5 [25] and was fixed in the fit to Belle II data because the 30 MeV energy threshold for Belle II waveforms made it challenging to constrain the curve in the high $d\mathrm{E}/dx$ limit. In addition, the pulse shape distributions in Belle II data such as Figures 6.6b and 6.19 support this limit as the maximum hadron intensity of crystals is observed to be consistent with this value.

The fit result is shown in Figure 6.31 and is labelled "Simulation with Calibrated $f(dE/dx)$". The values for remaining parameters computed in this fit were $B = 0.152 \pm 0.003$ MeV^{-1} and $C = 9 \pm 6$ and the resulting $f(dE/dx)$ function is shown in Figure 6.32. The $f(dE/dx)$ emission function computed from this procedure is applied in the Belle II simulations. The overlay in Figure 6.31 demonstrates that the simulated proton response when using the calibrated $f(dE/dx)$ matches the proton band data with the +0.02 correction, as expected. In Chapter 7, the performance of the CsI(Tl) scintillation response simulations are evaluated with control samples of $e^{\pm}$, $\mu^{\pm}$, $\pi^{\pm}$, $K^{\pm}$ and $p/\bar{p}$ selected from Belle II data and simulation. Those results demonstrate that all of the hadron pulse shape features observed in the data are reproduced by the pulse shape simulations. This is also seen from the simulation results shown earlier in this chapter such as in Figures 6.6b and 6.19, where the hadron pulse shape features such as particle bands, alpha particle excess and multi-hadron pulse shapes are reproduced in the simulation. The main exception however is the +0.02 systematic offset that is present between location of the single proton band in MC vs data. Revisited in Chapter 7 at the end of Section 7.6, this systematic shift can be explored in future studies as an area for improving the CsI(Tl) pulse shape simulations.

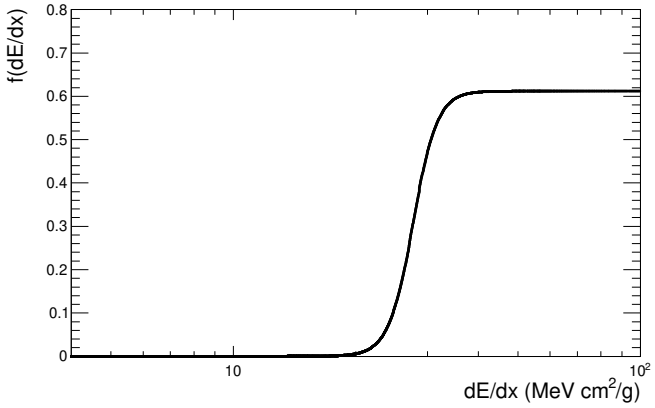

Figure 6.32: Hadron emission function computed from calibration using proton band in Belle II data.

6.8.2 Areas for Improvement in Simulation

The simulation methods outlined above allow for the particle dependent CsI(Tl) scintillation response to be reproduced in simulation in a realistic way such that simulated waveforms such as the one shown Figure 6.29 are produced. In the current version of the simulation however, there are some approximations made that allow for potential improvements in future studies. Due to a technical limitation related to the memory requirements that are needed to simulate the one component fit done in the FPGAs, an approximation is made in the simulation such that all crystals in the Belle II calorimeter are constructed using the same photon template and hadron template shape. In addition, the same photon template and hadron template used for the pulse construction, is also used in the pulse fitting.

Another approximation applied in the pulse shape simulations in Belle II is that all crystals in the calorimeter use the same $f(dE/dx)$ function to model the CsI(Tl) scintillation response to hadrons. As mentioned above, the observation of the single proton band in the Belle II data shown in Figure 6.30 is an indication that the crystal-by-crystal variations in the hadron response cannot be large. However, small variations are still expected to be present, potentially due to crystal-by-crystal differences in impurities, thallium concentration and radiation damage. The impact of this approximation is that when the crystal hadron intensity is studied by combining numerous crystals (for example all crystals in the barrel), the resolution of the hadron features in the crystal hadron intensity vs. crystal energy distributions will

be improved in MC relative to the data. This is illustrated for example in Figure 6.6 and 6.19 earlier in this chapter and in some of the data vs MC comparisons throughout Chapter 7. With a larger dataset $f(dE/dx)$ can potentially be calibrated on a crystal-by-crystal basis however, shown throughout Chapter 7, the overall impact of this approximation in many cases is not the dominant source of data and MC disagreement, relative to independent factors such as the modelling of the hadronic interactions in GEANT4. In additional in Phase 3 where the waveform noise is expected to increases, the additional $\delta_{\text{Low Energy Pile-up}}$ noise will likely become a larger factor in degrading the hadron intensity resolution.

Chapter 7

Studies of Charged Particle Interactions in CsI(Tl) using Calorimeter Pulse Shape Discrimination

This chapter studies the pulse shapes of crystals in calorimeter clusters produced by $e^{\pm}$, $\mu^{\pm}$, $\pi^{\pm}$, $K^{\pm}$ and $p/\bar{p}$ tracks in Belle II Phase 2 data and Monte Carlo Simulations (MC). The selection criteria for each sample is detailed in Appendix A. As the CsI(Tl) scintillation response is determined by the ionization $d\mathrm{E}/dx$ of the particles depositing energy in the crystal, the analysis of the pulse shapes presented in this chapter provides insight into the material interactions, which the primary particles initiate when interacting in the calorimeter. Discussed in detail in Chapter 5 [25], energy deposited in CsI(Tl) by highly ionizing secondary particles will generate emission of a fast CsI(Tl) scintillation component resulting in different scintillation pulse shapes relative to energy deposits from an electromagnetic shower. The fast scintillation emission is referred to as the hadron scintillation component. By measuring the fraction of hadron scintillation component emission relative to the total scintillation emission, defined as the hadron intensity, the types of secondary particles produced in the crystal can be inferred. At Belle II the hadron intensity of crystals with energy above 30 MeV is measured by applying the waveform fitting methods detailed in Chapter 6.

The main focus of this chapter is to survey the hadron intensity distributions

of crystals in clusters produced by the long-lived charged particles frequently produced in the e^+e^- collisions at SuperKEKB. From this analysis the simulation methods developed in Chapter 5 [25] for computing the CsI(Tl) scintillation response to hadronic energy deposits can be evaluated in further detail. In addition to evaluating the CsI(Tl) response simulations, the information provided by the pulse shapes also provides a unique and new method of evaluating the accuracy of GEANT4 simulation models. This allows for the multiplicity, energy and types of secondary particles in a cluster to be compared in data and simulation. Throughout this chapter the GEANT4 modelling of hadronic interactions is compared with the data and using the pulse shape distributions, potential sources of data and MC disagreements are identified. The simulation results in this chapter are computed using the Belle II Analysis Software Framework (basf2) `release-03-00-03` which uses the GEANT4 Physics List `FTFP_BERT`.

After studying the crystal pulse shapes in the clusters produced by charged particles, Section 7.7 demonstrates, and briefly discusses, the application of pulse shape discrimination to improve muon vs pion identification at lower momenta ($p_{\text{lab}} < 1$ GeV/c). In the final section of this chapter "Areas for Future Study" are discussed, outlining some of the many additional studies that can be pursued using PSD to improve the understanding of hadronic interactions in CsI(Tl). In addition potential methods to improve charged particle identification with PSD are briefly discussed. Note in Chapter 8, the application of using PSD to identify hadronic vs electromagnetic showers at Belle II is studied in detail.

7.1 Crystal Requirements

The results in this chapter only discuss the crystals/clusters that pass the following requirements.

- Crystals are required to have an offline waveform saved. This restricts the analysis to crystals with energy above 30 MeV.
- The crystal weight, computed by the calorimeter clustering algorithm to measure the association of the crystal to the cluster, is required to be > 0.95. This weight ranges from $0 - 1$ and in general, most crystals have a weight of 1.0.
- The waveform fit to the photon+hadron templates is required to have a $\chi^2 < 60$

(27 DOF). This requirement mainly excludes crystals with high noise from beam backgrounds. The same pulse shape features discussed below for the photon+hadron fits are also seen in photon+hadron+pile-up fit distributions however crystals passing the photon+hadron+pile-up fit are not included below as these fits had lower statistics and slightly lower resolution in hadron intensity. Additional details and comparisons of these two fit types are discussed in Chapter 6 Section 6.6.

- The distributions include all clusters in the barrel of the calorimeter. This will degrade the energy and hadron intensity resolution in data due to small crystal-by-crystal variations in scintillation response, however this is required to have sufficient statistics. Clusters in the end-caps have similar pulse shape features but for most samples had lower statistics and lower resolution in the hadron intensity and thus are excluded from these studies.

- The one dimensional histograms of crystal hadron intensity are normalized to the number of tracks in the corresponding sample, unless specified in the figure caption.

- All MC cluster energy distributions are normalized to the integrated luminosity of the data sample, unless specified in the figure caption.

7.2 Electrons and positrons

Electrons in the momentum range $0.3 < p_{\text{lab}} < 7$ GeV/c will primarily generate electromagnetic showers when entering the CsI(Tl) calorimeter. The thickness of the Belle II calorimeter corresponds to 30 cm/1.86 cm $\approx$ 16 radiation lengths [2] and thus a large fraction of the primary electrons energy is typically contained in the calorimeter. Described in Chapter 4, the crystals in the Belle II calorimeter have a front face area of $\sim 4 \times 4$ cm^2. The Moliere radius for CsI is 3.531 cm [2] thus the energy deposit from an electromagnetic shower will tend to be distributed over multiple adjacent crystals. Crystals closer to the initial track entrance will have higher energies than crystals at the edges of the cluster thus producing a range of crystal energies present in an cluster from an electromagnetic shower. This is demonstrated in Figure 7.1 showing the crystal hadron intensity vs crystal energy for the crystals in the clusters from electrons in the $e^+e^- \to e^+e^-e^+e^-$ selection. As the momentum

of the electrons in this sample is primary below 1 GeV/c, most of the crystal energies in Figure 7.1 are at lower energies.

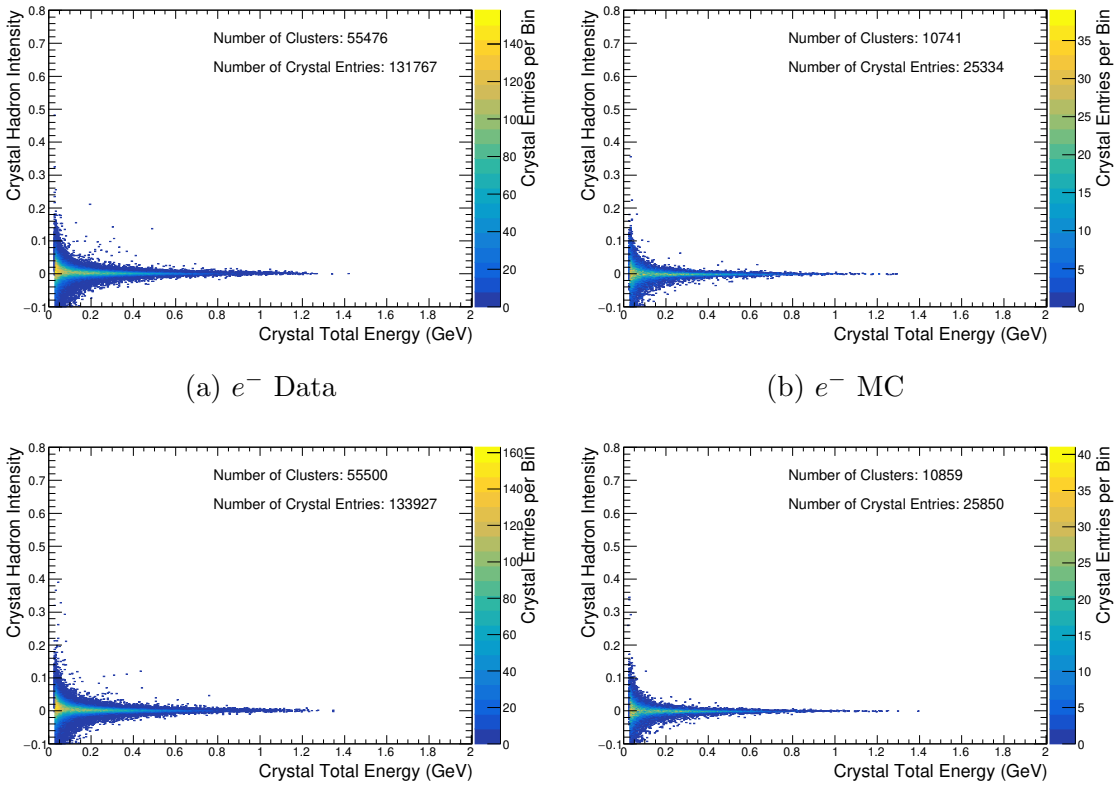

(a) e^- Data (b) e^- MC

(c) e^+ Data (d) e^+ MC

Figure 7.1: Crystal hadron intensity vs crystal energy distributions for crystals in electron clusters from $e^+e^- \to e^+e^-e^+e^-$ selection. MC distributions have lower statistics relative to the data.

In Figure 7.1 nearly all of the crystals in data and MC are observed to have hadron intensity values distributed close to zero. This indicates no high $d\mathrm{E}/dx$ secondary particles are produced in the electron clusters. This is expected as electromagnetic showers consist only of secondary electrons, positrons and photons. In the energy ranges at Belle II, this shower composition is independent of the primary electron momentum and independent of the energy of the crystals in the electron cluster. The small negative and positive hadron intensity values in Figure 7.1 are artifacts of the two template fit arising from noise in the waveform. These fluctuations are observed in the data and MC distributions. Note in simulation at generator level the hadron scintillation emission is always greater or equal to zero. As the crystal energy increases

the hadron intensity fluctuations about zero decrease in magnitude due to the increase in signal-to-noise of the waveforms. The width of this distribution gives the hadron intensity resolution that is related to the PSD separation power. In Chapter 6 Section 6.7 this resolution is measured as a function of the crystal energy using crystals in clusters from Bhabha scattering. Comparing the electron and positron distributions in Figure 7.1, the CsI(Tl) response is seen to be independent of the primary particle charge, as expected due to the charge symmetry in the development of electromagnetic showers.

The CsI(Tl) pulse shapes produced by 4 $<p_{\rm lab}<$ 7 GeV/c electrons are studied using the Bhabha selection outlined in Appendix A. For these clusters the crystal hadron intensity vs crystal energy distributions are shown in Figure 7.2. Due to the large momentum of the tracks in the sample, the energy of the crystals in these clusters can extend to several GeV. In Figure 7.2 it is observed that independent of the crystal energy the pulse shapes are consistently found to have minimal hadron intensity. This demonstrates that crystals with energy deposits up to several GeV from electromagnetic showers do not have a significant hadron scintillation component emission as the energy is deposited at a relativity low ionization dE/dx and over the volume of the crystal.

In the following chapter, applying PSD to identify electromagnetic and hadronic showers is discussed and it is found that one of the factors allowing PSD to be effective in hadronic shower identification is the consistency for electromagnetic showers to not generate hadron pulse shapes. This consistency is demonstrated by the Bhabha cluster distributions in Figure 7.2. Despite having very high statistics and large range of crystal energies relative to the other samples studied in this chapter, the clusters have very few crystals with significant hadron intensity values.

Comparing the simulation and data distributions in Figures 7.1 and 7.2, the distributions are qualitatively found to be very similar. The mean of these distributions as a function of crystal energy was measured and discussed in Chapter 6 Section 6.7. That analysis found the data distributions to have systematic shifts in the mean hadron intensity on the scale of ± 0.005. These shifts are attributed to be caused by the limited precision of the calibrations for the pulse templates and covariance matrices, electronics non-linearities and small differences in the noise characteristics of calorimeter channels. As will be demonstrated in the following sections, the $\sim \pm 0.005$ hadron intensity fluctuations are small relative to the hadron intensity values produced by high dE/dx energy deposits from charged hadrons.

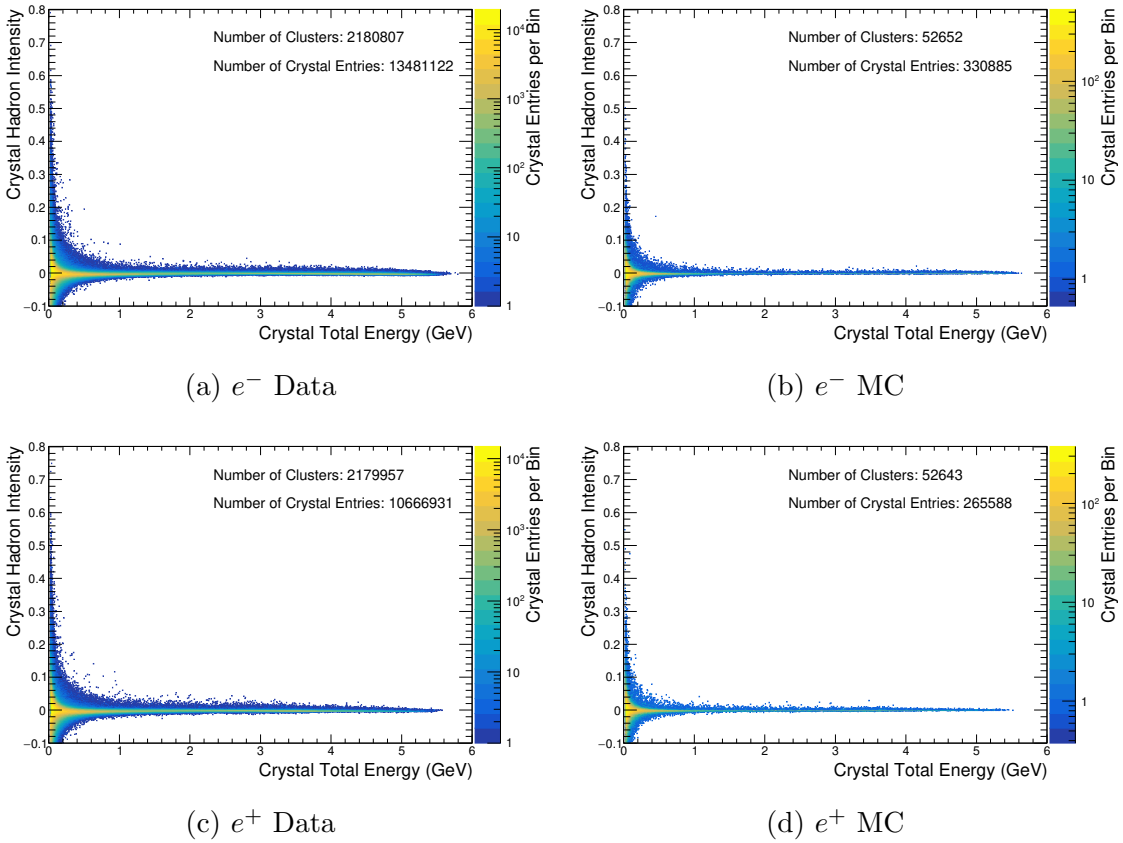

(a) e^- Data (b) e^- MC

(c) e^+ Data (d) e^+ MC

Figure 7.2: Crystal hadron intensity vs crystal energy distributions for crystals in electron clusters from the $e^+e^- \to e^+e^-$ selection. The z-axis is log scale. MC distributions have lower statistics relative to the data.

7.3 Muons

The large mass of muons relative to electrons, increases the critical energy in CsI(Tl) for muons to be 198 GeV [2], well beyond the energy of muons produced at SuperKEKB. This results in the dominant interaction for muons in the Belle II calorimeter to be ionization.

7.3.1 $p_{\mathbf{Lab}} \geq 1$ GeV/c muons

Tracks in the Belle II detector with $p_{\text{lab}} > 4$ GeV/c have relativity small deflections by the magnetic field such that the tracks can enter the calorimeter at large angles to crystal face. As a result muons with $p_{\text{lab}} > 4$ GeV/c will frequently enter only 1-2 crystals when ionizing through the length of the crystals. Muons with $p_{\text{lab}} > 1$ GeV/c

also have a relativity low ionization $d\mathrm{E}/dx$ that slowly varies with the muon momentum. This approximately momentum independent ionization $d\mathrm{E}/dx$, and relatively constant track length in the CsI(Tl), results in a consistent total energy deposition by ionization in the range of $0.15 - 0.25$ GeV for the majority of muons in the sample selected. This is demonstrated in Figure 7.3 showing the cluster energy of the muons selected with $p_{\mathrm{Lab}} \geq 1$ GeV/c. In Figure 7.3 a small fraction of clusters with energies > 0.3 GeV are observed due to Landau fluctuations in the energy of the secondary electrons produced from muon ionization. By studying the secondary particles produced by GEANT4 in these clusters it was verified that the additional energy in these clusters is from an energetic electron (> 0.1 GeV) produced by muon ionization. After production the electron showers, contributing the additional energy to the cluster.

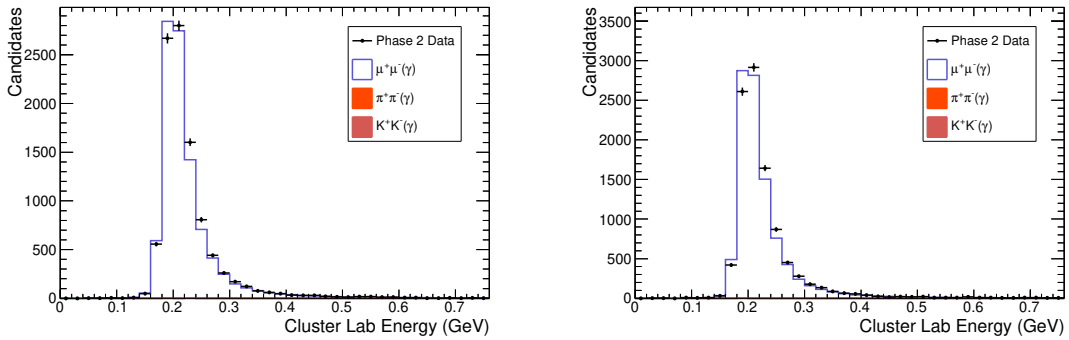

(a) μ^- (b) μ^+

Figure 7.3: Cluster energy distribution of clusters from $p_{\mathrm{Lab}} \geq 1$ GeV/c muons selected from $e^+e^- \to \mu^+\mu^-(\gamma)$. Many of the muons in this sample deposit almost all the cluster energy in a single crystal.

In Figure 7.4 the crystal hadron intensity vs crystal energy distributions for the crystals in the $p_{\mathrm{Lab}} \geq 1$ GeV/c muon clusters are shown. In this figure the same features are seen in the μ^- and μ^+ distributions such that there are a large number of crystals with total crystal energy of 200 MeV followed by a tail of higher and lower energy crystals. The crystals with energy below 200 MeV are from the muon ionizing through multiple crystals and thus the total 200 MeV cluster energy is split between multiple lower energy crystals. Figure 7.4 demonstrates that independent of the muon traversing multiple crystals or concentrating the cluster energy deposit in a single crystal, the resulting CsI(Tl) pulse shapes have close to zero hadron intensity. This demonstrates the muon ionization $d\mathrm{E}/dx$ is too low to produce significant hadron

scintillation component emission. The broadening of the distribution at lower crystal energies is the same effect seen in the electron distributions in the previous section and is due to the lower signal to noise present at lower crystal energies. In these distributions several crystals with energies > 0.3 GeV, which is outside the energy range for muon ionization in 30 cm of CsI(Tl), are also seen. The large energy deposit in these crystals correspond to electromagnetic showers by energetic electrons produced by muon ionization. These crystals correspond to clusters in the high energy tails in Figure 7.3. As demonstrated by Figure 7.4 these energetic crystals have photon pulse shapes, as expected from electromagnetic showers.

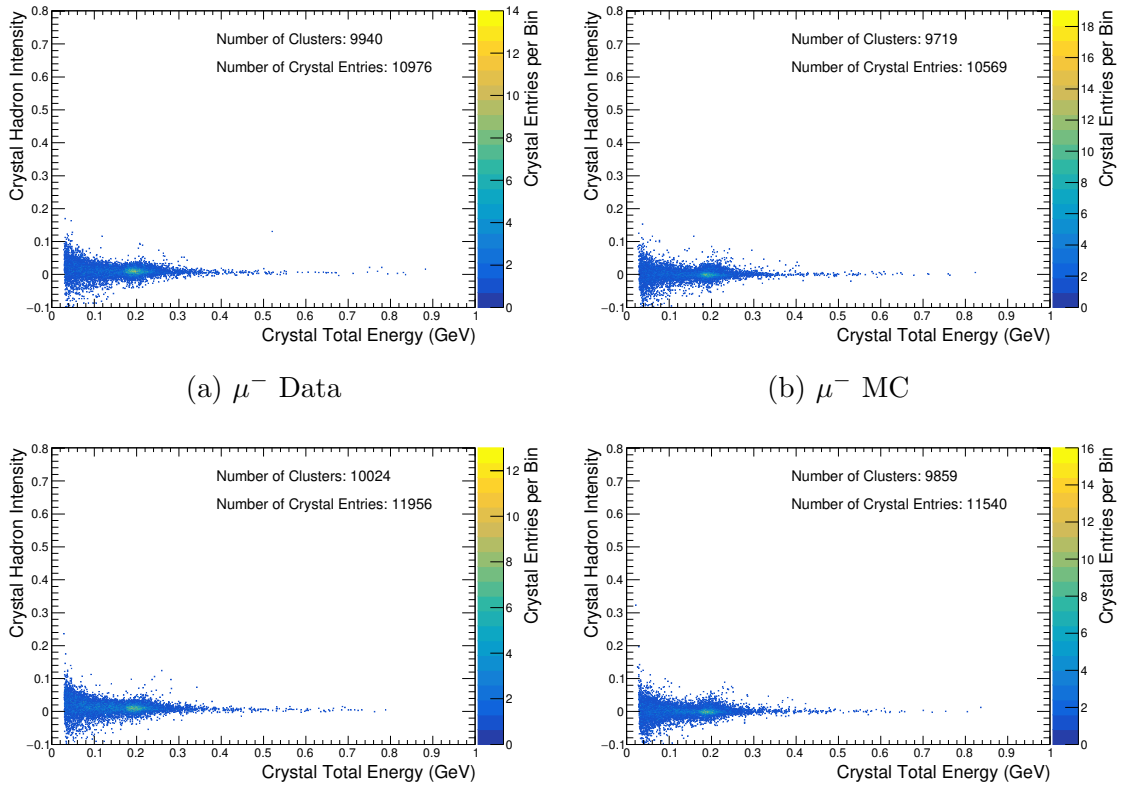

(a) μ^- Data (b) μ^- MC

(c) μ^+ Data (d) μ^+ MC

Figure 7.4: Crystal hadron intensity vs crystal energy distributions for crystals in clusters from muons with $p_{\text{Lab}} \geq 1$ GeV/c from $e^+e^- \rightarrow \mu^+\mu^-(\gamma)$ selection.

Several clusters in the $p_{\text{Lab}} \geq 1$ GeV/c muon sample are produced by a muon concentrating the ~ 200 MeV energy deposit in a single crystal. It is interesting to study the pulse shapes of these crystals in detail. In Figure 7.5 a histogram of the crystal hadron intensity for crystals in the energy range $0.15 \leq \text{E}_{\text{crystal}} < 0.25$ GeV

is shown for the $p_{\text{Lab}} \geq 1$ GeV/c muon clusters and also for the e^- clusters from the $e^+e^- \rightarrow e^+e^-e^+e^-$ sample previously studied. The values of the mean and standard deviations (σ) of the distributions in Figure 7.5 are listed in Table 7.1. Seen in Figure 7.5 and Table 7.1, the hadron intensity distributions are independent of the muon charge in both data and MC. In the data however the mean of muon distributions is found to be higher by +0.005 relative to the mean of the electron distributions. This observation indicates that an energy deposit from a $p_{\text{Lab}} \geq 1$ GeV/c muon ionizing through the length of the crystal will produce slightly different CsI(Tl) scintillation response relative to if the energy deposit was from an electromagnetic shower. This offset is not observed in the MC distributions as the hadron component emission function used for computing the hadron scintillation emission in simulations is only non-zero for very high ionization $d\text{E}/dx$ values. This offset will be further discussed at the end of the following section.

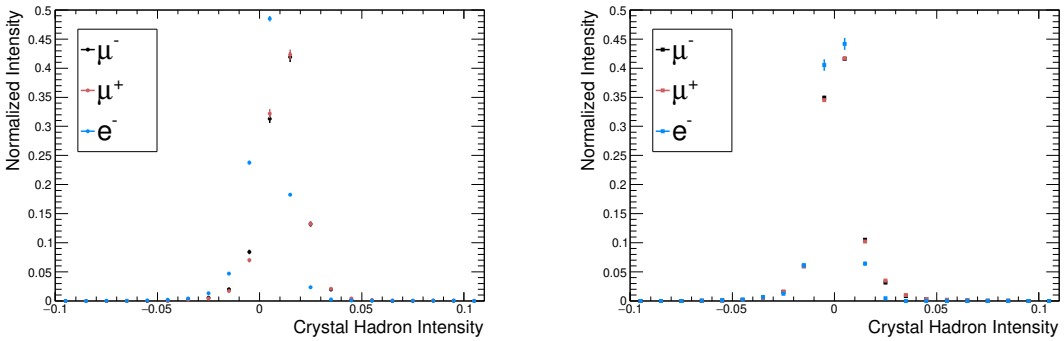

(a) Data (b) MC

Figure 7.5: Crystal hadron intensity for crystals in the energy range of $0.15 \leq \text{E}_{\text{crystal}} < 0.25$ GeV in $p_{\text{Lab}} \geq 1$ GeV/c muon clusters. Distributions are area normalized. These muons deposit almost all of the cluster energy in a single crystal. See Table 7.1 for mean and sigma of distributions.

Table 7.1: Mean and σ computed for hadron intensity distributions shown in Figure 7.5

Sample	Mean $\times 10^{-2}$	$\sigma \times 10^{-2}$
μ^- Data	1.10 $\pm$ 0.01	1.06 $\pm$ 0.01
μ^- MC	0.17 $\pm$ 0.01	1.114 $\pm$ 0.004
μ^+ Data	1.16 $\pm$ 0.01	1.07 $\pm$ 0.01
μ^+ MC	0.19 $\pm$ 0.01	1.145 $\pm$ 0.004
e^- Data	0.34 $\pm$ 0.01	1.007 $\pm$ 0.005
e^- MC	-0.04 $\pm$ 0.01	0.88 $\pm$ 0.01

7.3.2 $0.5 \leq p_{\mathbf{Lab}} < 1$ GeV/c muons

A small sample of $0.5 \leq p_{\mathrm{Lab}} < 1$ GeV/c muons was available from the $e^+e^- \to \mu^+\mu^-(\gamma)$ selection. In Figure 7.6 the energy distribution of the clusters from the muons in this lower momentum sample are shown.

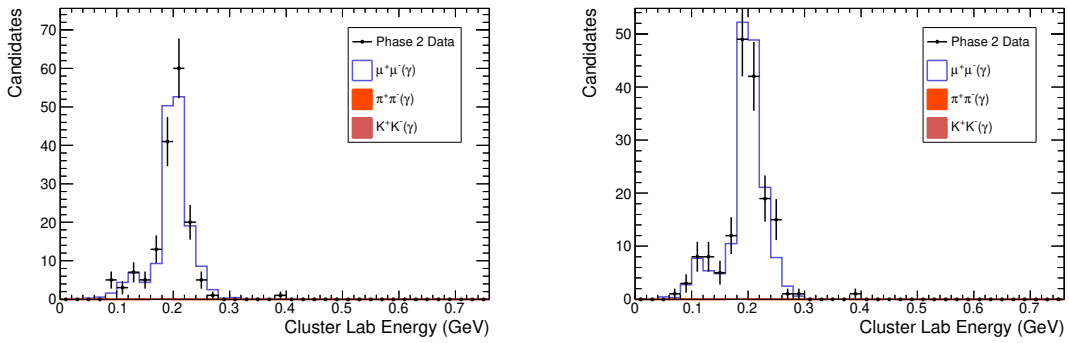

(a) μ^- (b) μ^+

Figure 7.6: Cluster energy distribution of clusters from muons with $0.5 \leq p_{\mathrm{Lab}} < 1$ GeV/c selected from $e^+e^- \to \mu^+\mu^-(\gamma)$.

As seen in Figure 7.6, many of the muons in this sample continue to deposit $\sim$ 200 MeV of energy in the calorimeter as they are still ionizing though the 30 cm thick calorimeter. Although the cluster energy distributions are similar to the high momentum muon sample, the energy deposits in the $0.5 \leq p_{\mathrm{Lab}} < 1$ GeV/c clusters are typically not concentrated in a single crystal. This is seen from Figure 7.7 showing the crystal hadron intensity vs crystal energy distribution for the crystals in the $0.5 \leq p_{\mathrm{Lab}} < 1$ GeV/c muon clusters. Compared to the analogous distribution

in Figure 7.4 for the $p_{\text{Lab}} \geq 1$ GeV/c muons, the abundance of crystals with energy of 200 MeV is not observed due to the increased track curvature resulting in the total cluster energy to be divided in multiple crystals. As observed in Figure 7.7 the pulse shapes of crystals in these clusters remains to be primarily photon-like.

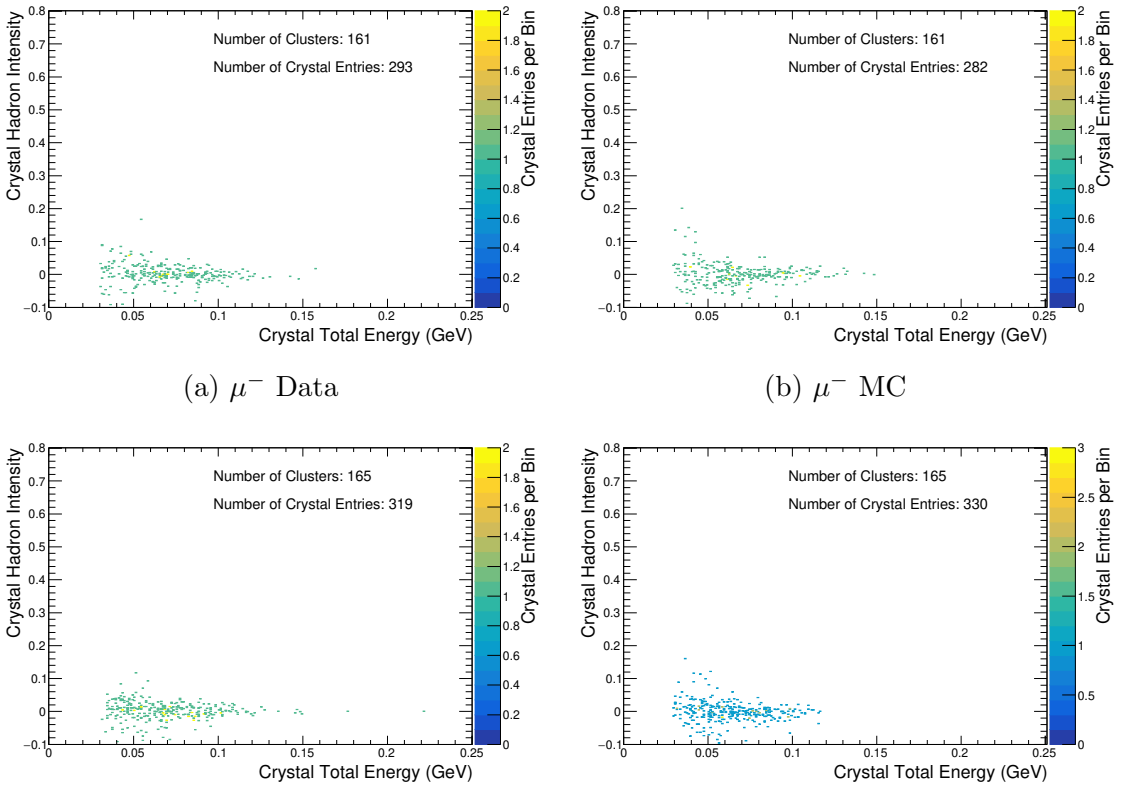

(a) μ^- Data (b) μ^- MC

(c) μ^+ Data (d) μ^+ MC

Figure 7.7: Distribution of pulse shapes from crystals in clusters from muons selected with $0.5 \leq p_{\text{Lab}} < 1$ GeV/c.

In Figure 7.8 a histogram of the hadron intensity is shown for crystals in the energy range $0.05 < \text{E}_{\text{crystal}} < 0.15$ GeV from clusters produced by $0.5 \leq p_{\text{Lab}} < 1$ GeV/c $\mu^{\pm}$'s, $p_{\text{Lab}} \geq 1$ GeV/c μ^-'s and e^-'s. The mean and standard deviation of the distributions in Figure 7.8 are listed in Table 7.2. As seen from Figure 7.8 and Table 7.2 the +0.005 offset in the mean hadron intensity seen in the previous section is only observed for the crystals from the $p_{\text{Lab}} \geq 1$ GeV/c μ^- clusters and not the $0.5 \leq p_{\text{Lab}} < 1$ GeV/c $\mu^{\pm}$ clusters that are found to have mean hadron intensity equal to zero. This result is interesting as it demonstrates the offset in the hadron intensity mean seen in the previous section is still present when the high momentum muon

crosses multiple crystals. This demonstrates the difference in pulse shape is due to the high momentum muon interactions in the crystal and not the path of the muon through the crystal. Another interesting observation from Figure 7.8 is that this shift is not present for the lower momentum muons that are found to have the same pulse shapes as electromagnetic showers. The cause of the offset seen for the higher momentum muons was not determined however overall the shift is small relative the the hadron intensity values produced by high $d\mathrm{E}/dx$ charged hadron energy deposits as will be shown in the following sections.

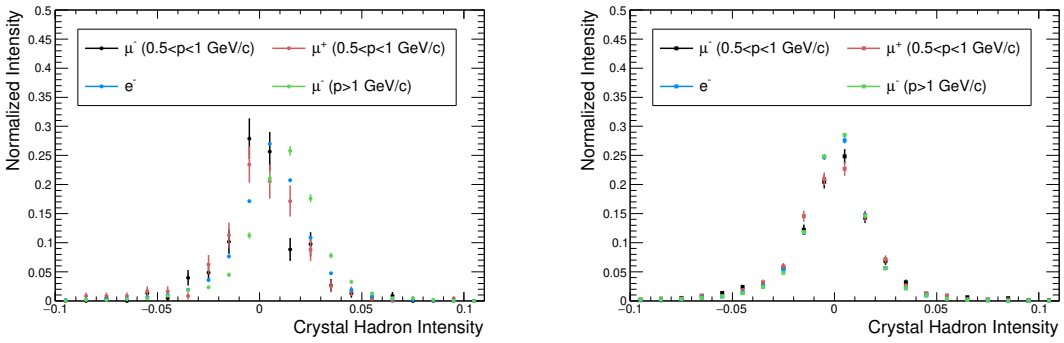

(a) Data (b) MC

Figure 7.8: Histograms of the hadron intensity for crystals in the energy range of $0.05 < \mathrm{E}_{\mathrm{crystal}} < 0.15$ GeV from clusters produced by $0.5 \leq p_{\mathrm{Lab}} < 1$ GeV/c $\mu^{\pm}$, $p_{\mathrm{Lab}} \geq 1$ GeV/c μ^{-} and e^{-}. See Table 7.2 for mean and σ of distribution's.

Table 7.2: Mean and σ computed for hadron intensity distributions shown in Figure 7.8

Sample	Mean $\times 10^{-2}$	$\sigma \times 10^{-2}$
$\mu^{-} 0.5 \leq p_{\mathrm{Lab}} < 1$ GeV/c Data	0.06 ± 0.13	1.96 ± 0.09
$\mu^{-} 0.5 \leq p_{\mathrm{Lab}} < 1$ GeV/c MC	0.00 ± 0.06	2.32 ± 0.04
$\mu^{+} 0.5 \leq p_{\mathrm{Lab}} < 1$ GeV/c Data	0.01 ± 0.15	2.34 ± 0.11
$\mu^{+} 0.5 \leq p_{\mathrm{Lab}} < 1$ GeV/c MC	-0.09 ± 0.06	2.29 ± 0.04
e^{-} Data	0.54 ± 0.01	2.04 ± 0.01
e^{-} MC	-0.06 ± 0.02	1.93 ± 0.01
μ^{-} $p_{\mathrm{Lab}} \geq 1$ GeV/c Data	1.14 ± 0.03	2.05 ± 0.02
μ^{-} $p_{\mathrm{Lab}} \geq 1$ GeV/c MC	-0.03 ± 0.01	1.92 ± 0.01

7.3.3 $p_{\mathbf{Lab}} < 0.5$ GeV/c muons

A limited sample of $p_{\mathrm{Lab}} < 0.5$ GeV/c muons was available from the $e^+e^- \to \mu^+\mu^-(\gamma)$ selection. In Figure 7.9 the energy distribution of the clusters from the muons in this lower momentum sample are shown. From this figure the data and MC have a similar distributions such that the majority of the muons in this momentum range are observed to produce cluster energies below 0.2 GeV.

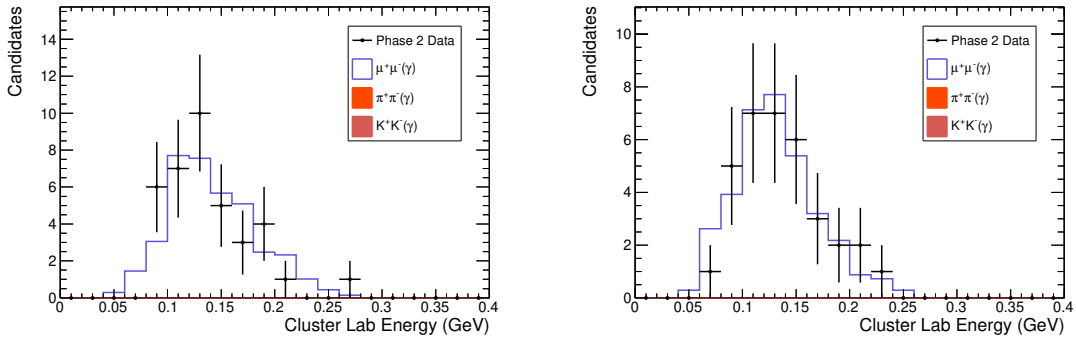

(a) μ^- (b) μ^+

Figure 7.9: Cluster energy distribution of clusters from muons with $p_{\mathrm{Lab}} < 0.5$ GeV/c selected from $e^+e^- \to \mu^+\mu^-(\gamma)$.

Shown in Figure 7.10 are the crystal hadron intensity vs crystal energy distributions for the selected muons with $p_{\mathrm{Lab}} < 0.5$ GeV/c. In this figure the small sample of crystals are observed to have photon-like pulse shapes, independent of the muon charge, for both data and MC. This demonstrates the ionizing muons in this momentum range do not produce significant amounts of hadron scintillation component emission.

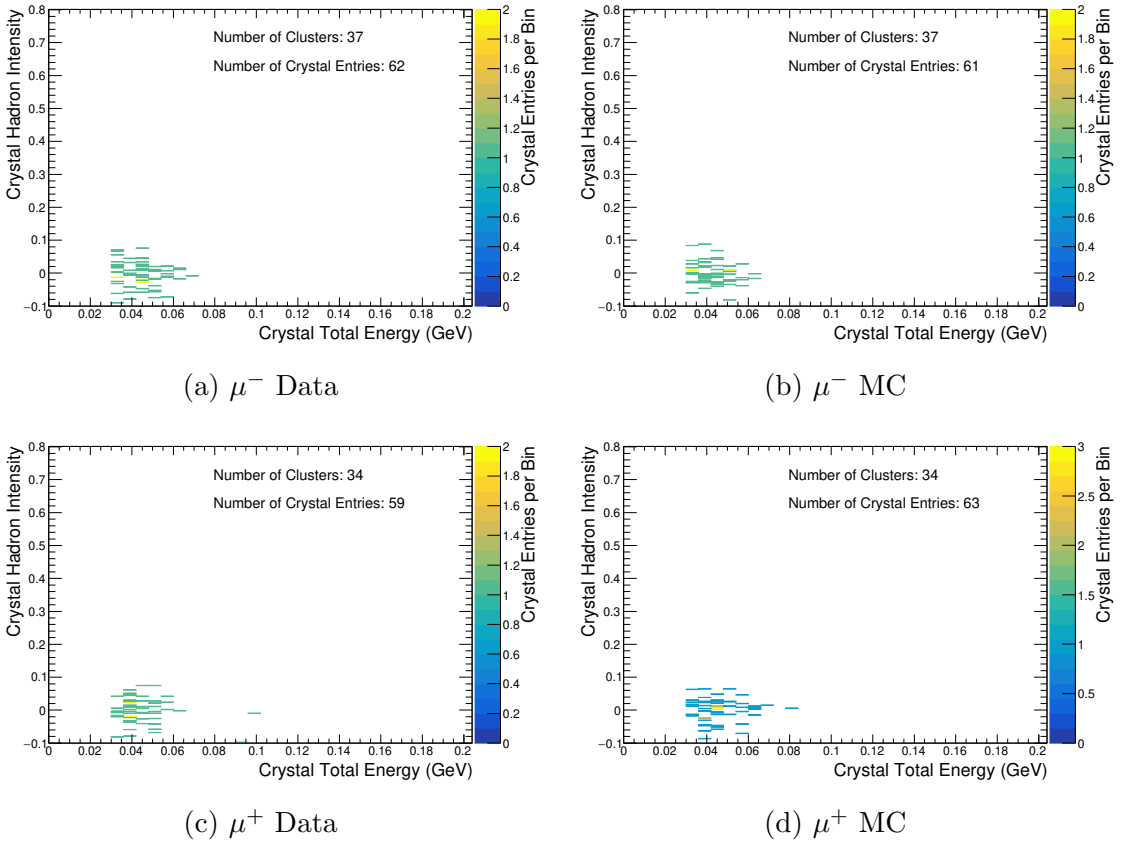

(a) μ^- Data (b) μ^- MC

(c) μ^+ Data (d) μ^+ MC

Figure 7.10: Distribution of pulse shapes from crystals in clusters from muons selected with $p_{\text{Lab}} < 0.5$ GeV/c.

7.4 Charged Pions

As with muons, the dominant electromagnetic interaction in CsI(Tl) for pions in the momentum range studied is ionization. As pions are composed of quarks they can strongly interact with nuclei. The nuclear interaction length for pions in CsI(Tl) is 44.12 cm [2], corresponding to roughly a 50% probability for a pion to have a nuclear interaction in 30 cm of CsI(Tl). This results in a distinct division in the types of calorimeter clusters formed by pions. About half of the pions selected will deposit a total energy of $150-250$ MeV by ionizing through calorimeter, similar to muons. The remaining pions in the sample will initially ionize in the CsI(Tl) before interacting with a nucleus and forming a hadronic shower.

Pions with momenta above 1 GeV/c have more inelastic interactions available and are expected to produce higher energy secondary particles that can re-scatter in

the cluster [10, 21]. In addition lower momentum tracks in the Belle II detector have higher track curvatures due to the magnetic field, leading to longer track lengths in the calorimeter and increasing the probability for a nuclear interaction. To decrease the variance of these effects across the pion sample, the sample is divided into momentum bins of $p_{\text{Lab}} < 0.5$ GeV/c, $0.5 \leq p_{\text{Lab}} < 1$ GeV/c and $p_{\text{Lab}} \geq 1$ GeV/c.

7.4.1 $p_{\text{Lab}} \geq 1$ GeV/c Pion Hadronic Showers

$p_{\text{Lab}} \geq 1$ GeV/c pions have a low enough track curvature and sufficient kinetic energy (> 0.87 GeV) to fully traverse the calorimeter if a nuclear interaction does not occur. This is demonstrated by the peak observed at 200 MeV in Figure 7.11 showing the cluster energies of the selected pions with $p_{\text{Lab}} \geq 1$ GeV/c. In addition to the peak mainly from ionizing pions, a large fraction of clusters have energies outside the range $0.15 < \text{E}_{\text{ecl}} < 0.25$ GeV primarily from hadronic showers generated by the pion.

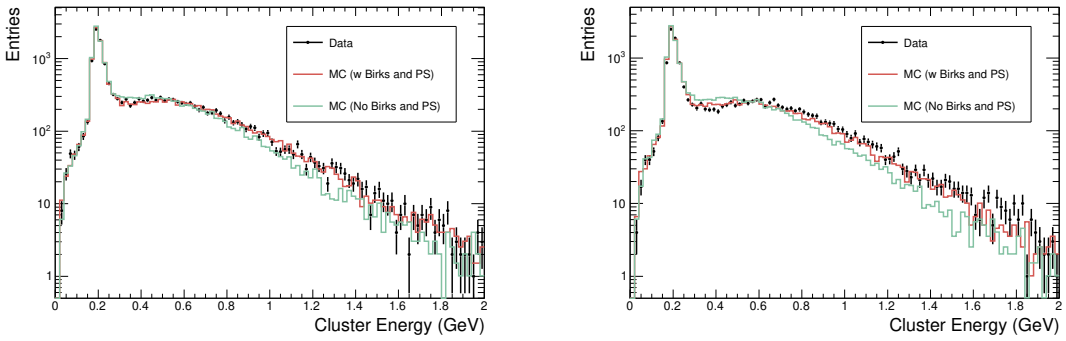

(a) π^- (b) π^+

Figure 7.11: Total cluster energy distribution from pions with $p_{\text{Lab}} \geq 1$ GeV/c selected from $K^0_S \to \pi^+\pi^-$ as described in Appendix A Section A.4.

In Figure 7.11 two versions of simulation are overlaid. The *No Birks and PS* simulation is the standard GEANT4 output whereas the *w Birks and PS* simulation includes the simulation of the CsI(Tl) scintillation response including the Birks correction and scintillation pulse shape variations from high $d\text{E}/dx$ hadronic energy deposits. Note that neither Belle nor BaBar used Birks Corrections in their simulations and that, prior to this work, the Belle II simulation was to deploy the standard GEANT4 version without Birk's Corrections. Outlined in detail in Chapter 5 [25], the CsI(Tl) scintillation response is simulated by computing the hadron scintillation component emission produced by the secondary particles in the cluster. In addition

the CsI(Tl) response simulations also convert the GEANT4 energy deposit to a light output yield by accounting for the ionization $d\mathrm{E}/dx$ dependent CsI(Tl) scintillation efficiency. From Figure 7.11 it is seen that including the more complete CsI(Tl) scintillation response in simulation results in improved agreement between data and MC. The general effect of adding the full CsI(Tl) response is a slight increase in the energies of the hadronic shower clusters. This occurs because ionization from secondary protons contributes a significant fraction to the cluster energy. As protons tend to have CsI(Tl) scintillation efficiencies greater than those from electromagnetic showers, this results in energy deposits from protons to produce more CsI(Tl) light output relative to energy deposits from electromagnetic showers. As a result the measured cluster energy, that is calibrated with electromagnetic showers, will be slightly higher than the true energy deposited by the proton. As observed in Figure 7.11 when this effect is modelled in the simulation by including the Birks correction which accounts for this effect, there is improved agreement between data and MC.

As the secondary particle composition and thus CsI(Tl) scintillation emission of crystals in ionizing vs hadronic shower clusters is expected to largely differ, the $p_{\mathrm{Lab}} \geq$ 1 GeV/c pion sample is loosely divided into *ionization* and *shower* clusters based on the total cluster energy. The *ionization* clusters are classified as clusters with total energy in the range of $0.15 < \mathrm{E_{ecl}} < 0.25$ GeV and *shower* clusters are the remaining clusters outside of this range. The crystal hadron intensity vs crystal energy for the crystals in the *shower* clusters from the selected pions with $p_{\mathrm{Lab}} \geq 1$ GeV/c are shown in Figure 7.12.

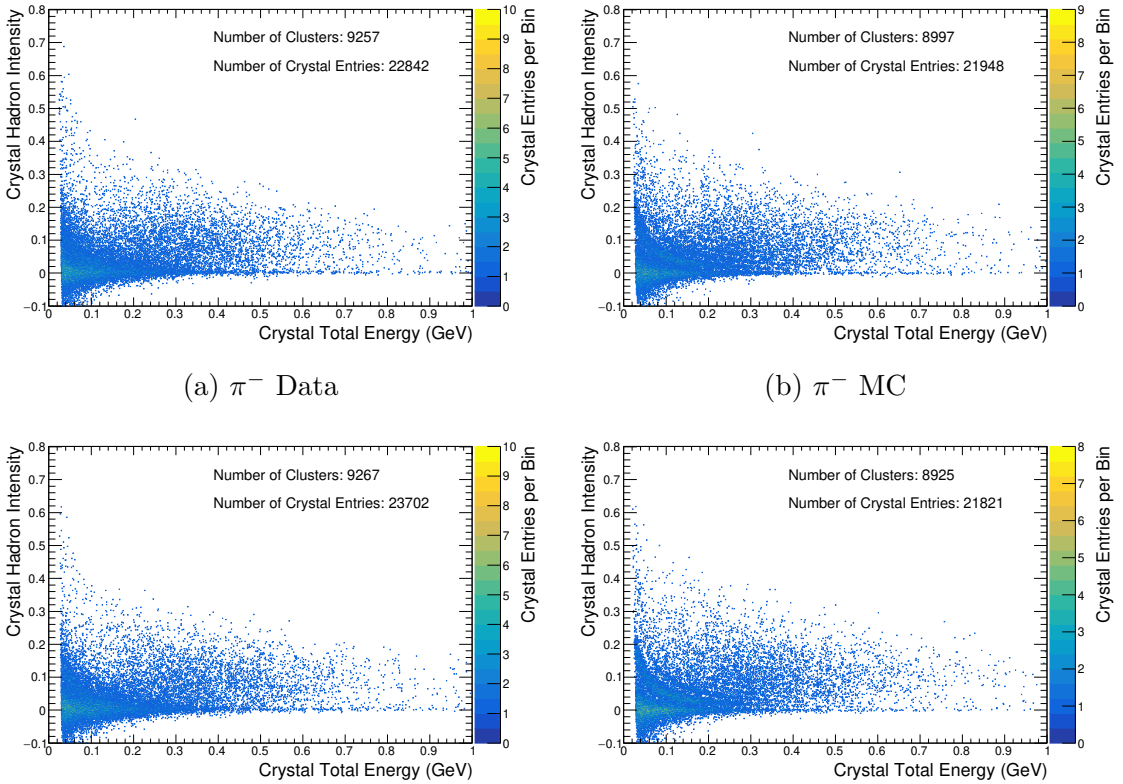

(a) π^- Data (b) π^- MC

(c) π^+ Data (d) π^+ MC

Figure 7.12: Crystal hadron intensity vs crystal energy for crystals in clusters from pions with $p_{\rm Lab} \geq 1$ GeV/c and cluster energy outside the range of $0.15 < E_{\rm ecl} < 0.25$ GeV. Histograms of hadron intensity for different crystal energy ranges are shown in Figure 7.13.

An immediate observation in Figure 7.12 is the variety of CsI(Tl) pulse shapes present in crystals from $p_{\rm Lab} \geq 1$ GeV/c pion *shower* clusters, as demonstrated by the range of hadron intensity values observed. The significant presence of crystals with hadron pulse shapes in these clusters is a distinct difference from the electron and muon clusters studied in the previous sections where only photon-like pulse shapes were observed. In addition the observation of hadron pulse shape features in the MC demonstrate the success of the CsI(Tl) response modelling methods that were developed in Chapter 5 [25], as when the full CsI(Tl) response is not modelled in the simulation then all crystals would have photon pulse shapes. The abundance of hadron pulse shapes is expected in $p_{\rm lab} = 1-3$ GeV/c pion clusters as the corresponding kinetic energy range is $0.87 - 2.86$ GeV and thus many inelastic interactions are above threshold. Typically in these clusters the primary pion interacts with a Cs

or I nucleus producing multiple energetic secondary hadrons such as protons, pions and neutrons. When these secondary hadrons do not have an nuclear interaction, the higher energy neutrons will escape the cluster and the protons frequently will deposit their kinetic energy by ionizing with high $d\mathrm{E}/dx$.

Several of the hadron pulse shape features studied in detail in the TRIUMF test-beam study in Chapter 5 [25] are observed in the data and MC results in Figure 7.12. At lower crystal energies and lower hadron intensity values a faint single proton band is observed in the data and MC distributions. Outlined in Chapter 5 [25], a crystals pulse shape will fall along the single proton band if the primary source of the energy deposit is from a single proton stopping in the crystal. This is because as the proton ionizes and approaches low energies the proton has high ionization $d\mathrm{E}/dx$ thus producing a significant and consistent yield of hadron scintillation component emission. The total energy of crystals along the single proton band is approximately equal to the protons kinetic energy when it was produced or entered the crystal. The observation of the single proton band in Figure 7.12 demonstrates the hadronic showers from the $p_{\mathrm{Lab}} \geq 1$ GeV/c pions selected frequently produce energetic protons in the cluster.

In the MC distributions in Figure 7.12 additional pulse shape bands above the single proton band are clearly resolved. These secondary bands are produced when the energy deposit in the crystal was from multiplies of identical charged hadrons (ie two protons, three protons...), or deuterons, stopping in the crystal. The bands are formed due to the consistency of these interactions as, protons and deuterons always ionize through the same $d\mathrm{E}/dx$ range thus producing consistent yields of hadron component light output. In the data, these secondary bands are not clearly resolved, however, an excess of crystals is observed in the region above the single proton band that could be evidence of a double proton band. In general the hadron pulse shape features in the MC distributions in Figure 7.12 can be seen to have improved resolution relative to the data. This can be attributed to crystal-by-crystal variations in the hadron response in the data. Recall the distributions in Figure 7.12 integrate over the 6622 crystals in the barrel of the calorimeter to have sufficient statistics. By including this large number of crystals degradation in the resolution of the hadron intensity is expected to occur due to crystal-by-crystal variations in the CsI(Tl) hadron scintillation response. This degradation does not occur in the simulation as the same hadron scintillation emission function, used for computing the hadron scintillation component emission, is used for each crystal. As a result each crystal in the simulation has identical scintillation

response to high $d\mathrm{E}/dx$ particles. As discussed in Chapter 6, small variations in crystal responses are expected to be present due variations in thallium concentration, radiation damage and diode spectral response etc. In addition differences in the absolute light output yield for different crystals can cause variations in the hadron intensity resolution for different crystals. Due to the accumulation of these effects the overall resolution of the data is expected to be degraded relative to the simulation. The fact that after combining the results of the 6622 crystals in the barrel a single proton band is still observed in the data is an indication that the crystal-by-crystal variations in the hadron scintillation response cannot be large, and that the hadron and photon templates are well calibrated across the calorimeter. If a similar analysis is done on a crystal-by-crystal basis the resolution of a single crystal is expected to be close to the resolution of the simulation.

At crystal energies above 0.25 GeV in Figure 7.12, the hadron pulse shapes are observed to be scattered between hadron intensity values of $\sim 0.02 - 0.2$. In Chapter 5 [25] it was found by studying GEANT4 truth information that crystals in this pulse shape region originate from energy deposits by numerous low energy hadrons (protons, neutrons, deuterons, tritons, alphas) produced in the crystal. The characteristics of such interactions correspond to nuclear evaporation when an excited nucleus de-excites by emitting numerous low energy hadrons [20]. As the energy, type and multiplicity of the secondary hadrons emitted in these crystals greatly varies for different de-excitations, a scatter in the multi-hadron pulse shapes is observed.

In addition to the hadron pulse shape features in Figure 7.12, many photon-like pulse shapes are also observed, particularly at crystal energies below 100 MeV. Shown later in this section, energetic pions ionizing in CsI(Tl) produce photon-like pulse shapes, similar to the muons in the previous section. The majority of photon-like pulse shapes at these lower crystal energies are from the primary pion initially ionizing though a 5-20 cm section of CsI(Tl) before leaving that crystal and initiating a nuclear interaction in an nearby crystal. This scenario frequently occurs when the pion first enters the calorimeter on its curved trajectory. If the pion interaction produces secondary pions they are also likely to ionize through crystals producing < 100 MeV photon-like energy deposits. In addition photons and electrons produced in the hadronic shower could produce these crystals. The photon-like pulse shapes observed at crystal energies > 0.25 GeV however are more likely to originate from photons/electrons rather than pion ionization. This is because a > 0.25 GeV crystal energy deposit in a single crystal from only pion ionization is unlikely due to the

crystal dimensions. As a result the very high energy photon-like crystals are mostly from energetic $\pi^0 \to \gamma\gamma$ produced in the hadronic shower.

The two-dimensional histograms in Figure 7.12 allows the general characteristics of the pulse shapes of crystals in the clusters to be visualized. To perform a detail study of the crystal hadron intensity distributions, histograms of the crystal hadron intensity are shown in Figure 7.13 for crystal energy ranges of $0.05 < \mathrm{E_{crystal}} < 0.15$ GeV, $0.15 \leq \mathrm{E_{crystal}} < 0.25$ GeV, and $\mathrm{E_{crystal}} \geq 0.25$ GeV. These energy ranges account for the change in hadron intensity resolution with crystal energy.

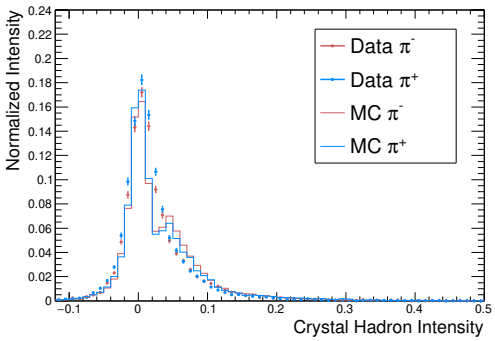

(a) $0.05 < \mathrm{E_{crystal}} < 0.15$ GeV

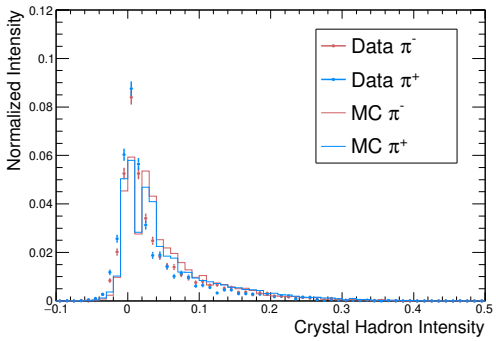

(b) $0.15 \leq \mathrm{E_{crystal}} < 0.25$ GeV

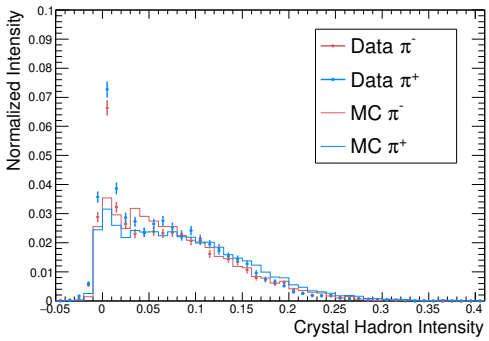

(c) $\mathrm{E_{crystal}} \geq 0.25$ GeV

Figure 7.13: Histograms of the hadron intensity of crystals in *shower* clusters from pions selected with $p_{\mathrm{Lab}} \geq 1$ GeV/c.

Comparing the π^+ and π^- distributions in Figure 7.12, the hadron intensity of crystals in the $p_{\mathrm{Lab}} \geq 1$ GeV/c *shower* pion clusters are observed to be independent of the pion charge across the different crystal energy ranges. This trend is seen in the data and MC, demonstrating the π^+ and π^- interactions in CsI(Tl) are similar in this momentum range.

The histograms in Figure 7.13 also provide a detailed evaluation of the simulation methods developed in Chapter 5 [25] for computing the CsI(Tl) scintillation response. Recall if the CsI(Tl) response is not included in the simulation then no hadron pulse shapes would be observed in the MC as all crystals would have photon-like pulse shapes. In the crystal energy ranges of $0.05 < \mathrm{E_{crystal}} < 0.15$ GeV and $0.15 \leq \mathrm{E_{crystal}} < 0.25$ GeV the data and MC are found to produce similar distributions. In MC there is a slight excess of crystals with hadron intensity in the range 0.05-0.1 for the $0.05 < \mathrm{E_{crystal}} < 0.15$ GeV histogram. In the $0.15 \leq \mathrm{E_{crystal}} < 0.25$ GeV histogram the excess is in the hadron intensity range of 0.02-0.04. These excesses correspond to crystals in the single proton band. The difference between data and MC is understood to be due to a systematic offset of +0.02 present in the hadron intensity of the crystals in the single proton band in simulation relative to data. This offset is discussed in detail in Chapter 6 Section 6.8.1. In the crystal energy range $\mathrm{E_{crystal}} \geq 0.25$ GeV the hadron intensity values of crystals corresponding to hadron energy deposits are observed to be well modelled. An excess of photon-like pulse shapes is found, however, in the data relative to the simulation for both the π^- and π^+ cluster crystals. As there can be several interactions occurring in a single hadronic shower it is difficult to identify the source of this excess however one potential cause could be if the MC is under-producing charge-exchange interactions such as $\pi^- p \to \pi^0 n$ or $\pi^+ n \to \pi^0 p$ as the π^0 produced by this interaction would likely result in high energy crystals with photon-like pulse shapes.

7.4.2 $0.5 \leq p_{\mathbf{Lab}} < 1$ GeV/c Pion Hadronic Showers

The cluster energies of the selected pions in the momentum range $0.5 \leq p_{\mathrm{Lab}} < 1$ GeV/c are shown in Figure 7.14. Compared to the $p_{\mathrm{Lab}} \geq 1$ GeV/c pion clusters, the $0.5 \leq p_{\mathrm{Lab}} < 1$ GeV/c pion clusters have similar features including a peak at total cluster energy of 200 MeV from pions ionizing through the calorimeter in addition to a distribution of higher energy clusters from hadronic showers.

In Figure 7.14 it is found that including the CsI(Tl) scintillation response in the simulations causes the π^- shower clusters to have slightly higher cluster energies than the data. For the π^+ clusters adding the CsI(Tl) response results in an improvement in the agreement between data and simulation, although the overall agreement is still not ideal. These trends differ from the $p_{\mathrm{Lab}} \geq 1$ GeV/c clusters where including the CsI(Tl) response improved agreement between data and MC for both pion charges.

The change in this trend is an indication that as the pion momentum decreases the dominant components of the pion-nucleus interaction cross-section are changing. In particular it is expected that in the momentum range of $0.5 \leq p_{\text{Lab}} < 1$ GeV/c, corresponding to kinetic energies of $0.38 - 0.87$ GeV/c, less inelastic interactions are available, and the cross-section for pion-nuclear absorption starts to become a larger contribution to the total nuclear interaction cross section [43]. To investigate this discrepancy between data and MC, the pulse shape distributions are studied below. At the end of this section the disagreement between data and MC is discussed further with the conclusion that the π^- MC is producing a greater number of secondary protons relative to the data causing the excess in the MC cluster energies, which is evident when the full CsI(Tl) scintillation response is added.

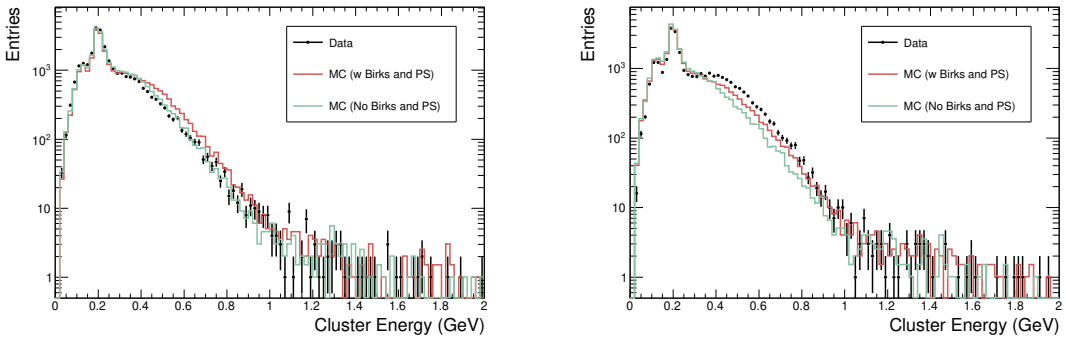

(a) π^- (b) π^+

Figure 7.14: Total cluster energies of pions with $0.5 \leq p_{\text{Lab}} < 1$ GeV/c selected from $K^0_S \to \pi^+\pi^-$.

The crystal energy vs crystal hadron intensity distributions for the $0.5 \leq p_{\text{Lab}} < 1$ GeV/c pion *shower* clusters are shown in Figure 7.15. In this figure, several of the pulse shape features studied in the $p_{\text{Lab}} \geq 1$ GeV/c pion *shower* clusters are observed. In particular the single proton band is seen in the data and MC indicating energetic protons are still frequently produced in these clusters. In the MC, several additional pulse shape bands are observed above the proton band. In the data these bands are not resolved, however, an excess of crystals with pulse shapes in this region are observed supporting the conclusion discussed above that the resolution of the data is degraded due to crystal-to-crystal variations in CsI(Tl) response to hadrons.

Comparing the distributions in Figure 7.15 to Figure 7.12, the decrease in the average crystal energies is expected due to the decrease in the primary particle energy.

It is interesting however to observe the corresponding effect the decrease in primary particle energy has on the pulse shapes of the crystals in the clusters. In the clusters from the higher momentum pions many crystals were observed to be scattered in the multi-hadron pulse shape region ($E_{crystal} > 0.2$ GeV and hadron intensity > 0.02), however as the pion energy decreases the crystals tend to be more concentrated in the region of various pulse shape bands from proton, multi-proton and deuterons. This observation indicates the nuclear interactions in these clusters are emitting lower multiplicities of charged hadrons.

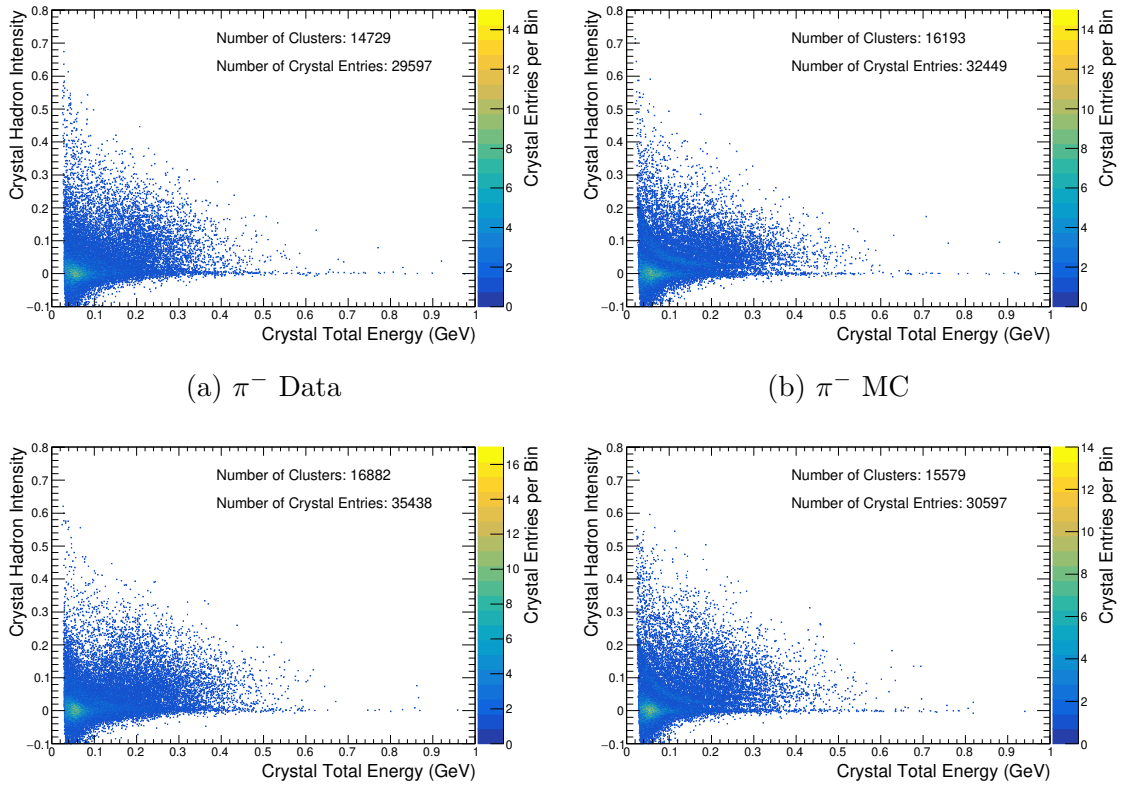

(a) π^- Data (b) π^- MC

(c) π^+ Data (d) π^+ MC

Figure 7.15: Crystal hadron intensity vs crystal energy for crystals in clusters from pions selected with $0.5 \leq p_{Lab} < 1$ GeV/c and cluster energy outside the energy range of $0.15 < E_{ecl} < 0.25$ GeV. Histograms of hadron intensity for different crystal energy ranges are shown in Figure 7.16.

In Figure 7.16 histograms of the hadron intensity for the crystal energy ranges of $0.05 < E_{crystal} < 0.15$ GeV, $0.15 \leq E_{crystal} < 0.25$ GeV, and $E_{crystal} \geq 0.25$ GeV are shown for crystals in the $0.5 \leq p_{Lab} < 1$ GeV/c pion *shower* clusters. From these

histograms several insights into the disagreement in the cluster energy distributions seen in Figure 7.14 can be gained. In the crystal energy ranges $0.05 < \mathrm{E_{crystal}} < 0.15$ GeV it is found that the π^+ data and π^- data are nearly identical. This trend however is not found in the MC where the π^- MC is seen to have two peaks. The peak at zero hadron intensity corresponds primarily to crystals from a π^- ionizing through a crystal without an inelastic interaction occurring. The second less intense peak at higher hadron intensity corresponds to crystals in the single proton band. As the fraction of crystals in the single proton band peak in the π^- MC is larger relative to the π^+ MC this demonstrates the π^- MC is producing a greater number of energetic protons relative to the π^+ MC and π^- data. In the $0.15 \leq \mathrm{E_{crystal}} < 0.25$ GeV energy range difference between the π^- and π^+ distributions in data develop however the trend is still observed that the π^- MC has an excess, relative to π^- data and π^+ MC, of crystals with pulse shape corresponding to the single proton band. This is seen from the peak in the π^- MC at hadron intensity of 0.03.

In the crystal energy range $\mathrm{E_{crystal}} \geq 0.25$ GeV, differences between the π^- and π^+ distributions are observed in data and MC. The π^+ data is found to have a greater number of crystals in multi-hadron pulse shape region relative to the π^- data indicating the π^+ are producing more crystals containing multiple secondary charged particles. The opposite trend however is found in the MC where the π^- MC crystals have an excess of multi-hadron crystals relative to the π^+ MC. Comparing data and MC distributions, the π^- MC is found to be producing a greater number of hadron crystals relative to the π^- data whereas the π^+ MC is under-producing hadron crystals relative to the π^+ data.

These observations lead to a better understanding of the origin of the disagreement between data and MC in the cluster energy distributions discussed at the beginning of this section. The results in Figure 7.16 suggest that in the momentum range $0.5 \leq p_{\mathrm{Lab}} < 1$ GeV/c, the π^- MC is producing a greater number of energetic protons/charged hadrons relative to the data, whereas the π^+ MC is producing slightly less charged hadrons relative to the data. This accounts for the disagreement seen in the cluster energies for the π^- as if the π^- MC is over-producing protons then adding the CsI(Tl) scintillation efficiency produces larger than expected cluster energies.

For the π^+ cluster energies, before and after including scintillation response the cluster energies were lower than the data. However as demonstrated by the $\mathrm{E_{crystal}} \geq 0.25$ GeV result in Figure 7.16, the cause of this lower than expected cluster energy is due to the MC generating less charged hadrons than observed in the data. By

producing more charged hadron final states this would produce a greater number of $E_{crystal} \geq 0.25$ GeV crystals with high hadron intensity thereby also increasing the total cluster energies and improving the data and MC agreement in Figures 7.16 and 7.14. As will be discussed in Section 7.4.4 when the $p_{Lab} < 0.5$ GeV/c pion clusters are studied, it is suspected that the MC modelling of pion absorption is the source of the data vs MC disagreement as these trends continue in the lower momentum sample where pion absorption has a significant cross-section.

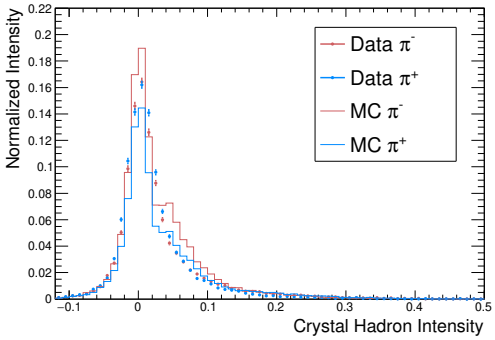

(a) $0.05 < E_{crystal} < 0.15$ GeV

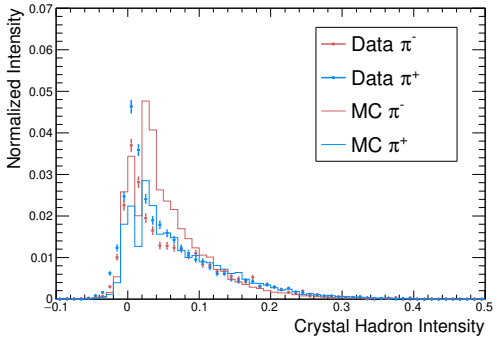

(b) $0.15 \leq E_{crystal} < 0.25$ GeV

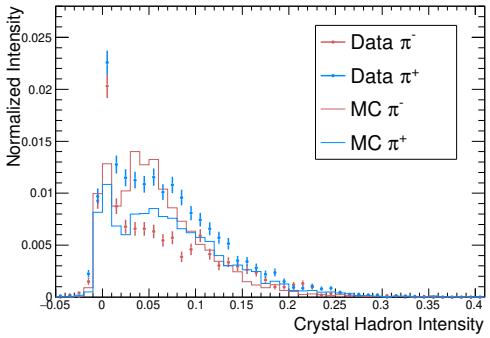

(c) $E_{crystal} \geq 0.25$ GeV

Figure 7.16: Histogram of the hadron intensity for $0.5 \leq p_{Lab} < 1$ GeV/c pion *shower* clusters for different crystal energy ranges.

7.4.3 Pion Ionization Clusters

In this section clusters from pions with ≥ 0.5 GeV/c and cluster energy in range $0.15 < E_{ecl} < 0.25$ GeV are studied. This cluster energy range is consistent with the pion ionizing through the calorimeter without having an inelastic interaction. In Figure 7.17 the crystal hadron intensity vs crystal energy distributions are shown for

crystals in *ionization* clusters from $p_{\text{lab}} \geq 0.5$ GeV/c pions.

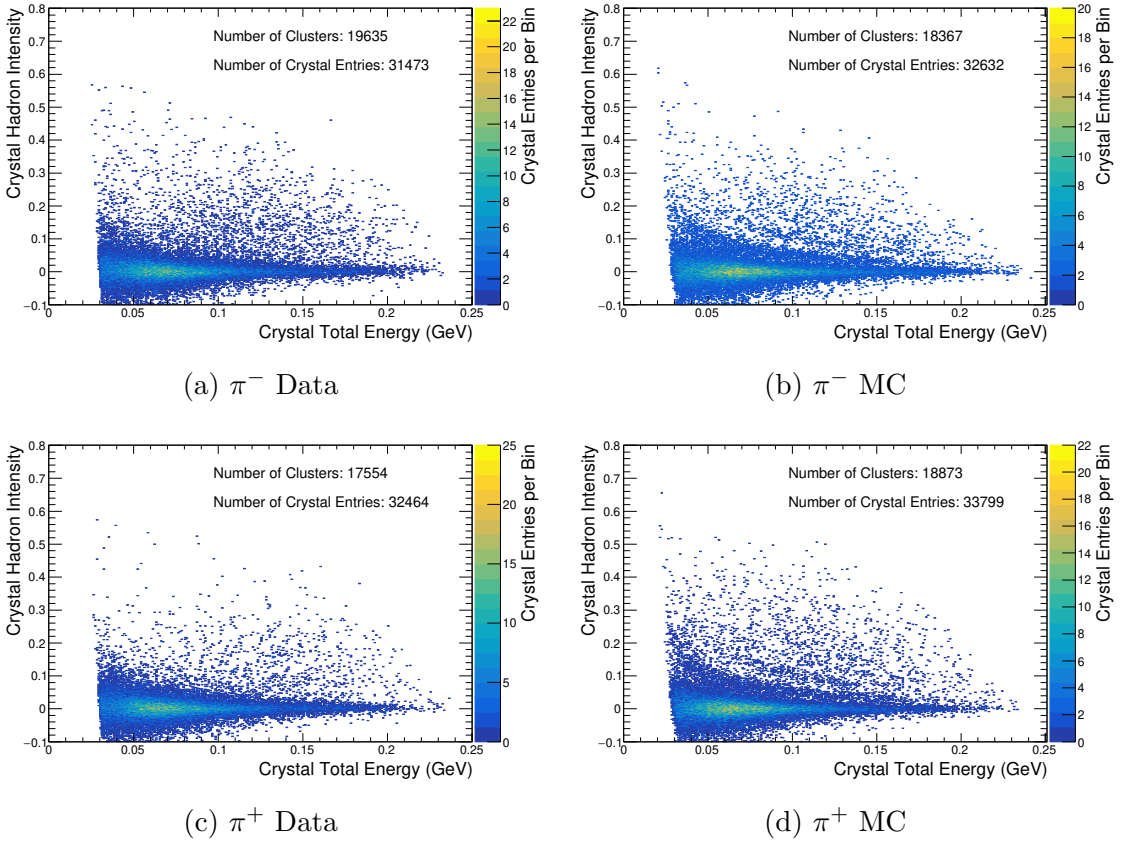

(a) π^- Data (b) π^- MC

(c) π^+ Data (d) π^+ MC

Figure 7.17: Distribution of pulse shapes from crystals in clusters with 0.15 <E_{ecl}< 0.25 GeV from pions with p_{lab}> 0.5 GeV/c

The pulse shapes in Figure 7.17 are found to be dominated by photon-like pulse shapes demonstrating the ionization dE/dx of pions at these energies is too low to produce significant hadron scintillation component emission in CsI(Tl). This is expected as the pion ionization dE/dx is similar to the muon dE/dx at these energies thus the crystals in the pion ionization clusters should closely resemble the muon ionization clusters. Note that there remains a small fraction of hadron-like pulse shapes is seen in Figure 7.17 from hadronic showers that had a cluster energy in the *ionization* cluster energy range, as expected from Figures 7.11 and 7.14.

To compare the pulse shapes of ionizing pions and muons a histogram of the crystal hadron intensity for crystals in the energy range of $0.05 < E_{\text{crystal}} < 0.15$ GeV is shown in Figure 7.18 for the *ionization* pion clusters and the $0.5 \leq p_{\text{Lab}} < 1$ GeV/c muon clusters. Recall the crystal energy is lower than 200 MeV as the muons and

pions are crossing multiple crystals. In Table 7.3 the mean and standard deviations of the distributions are shown. In addition Table 7.3 shows I_{tail} defined as the fraction of crystals in the sample with hadron intensity above 0.03. In Figure 7.18 the pulse shapes of the muons and pions are observed to be identical, independent of the charge or particle type, within precision of these studies. From I_{tail} is it also seen that in the *ionization* pion sample there is a greater fraction of crystals in the clusters with hadron intensity from 0.03-1.0, relative to the muon sample. This is expected as the only requirement for an *ionization* cluster is for the cluster energy to be in the range $0.15 < E_{\text{ecl}} < 0.25$ GeV and thus the pion sample will have some crystals from pion hadronic showers with cluster energy in this range. This observation demonstrates the potential for improved pion vs muon identification using pulse shape discrimination. In Section 7.7 of this Chapter this is explored in further detail.

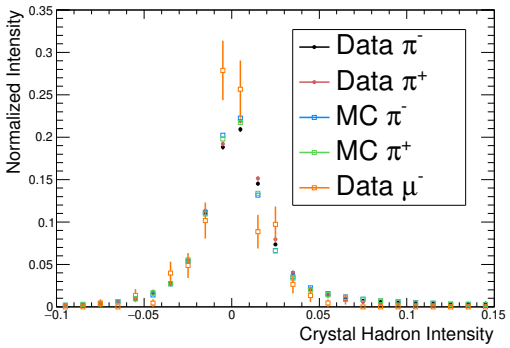

Figure 7.18: Histogram of the hadron intensity of crystals in energy range of $0.05 < E_{\text{crystal}} < 0.15$ GeV from pion *ionization* clusters and muon clusters.

Table 7.3: Mean, σ and I_{tail} computed for hadron intensity distributions shown in Figure 7.18

Sample	Mean $\times 10^{-2}$	σ $\times 10^{-2}$	I_{tail}
π^- Data	1.09 ± 0.03	4.93 ± 0.02	0.147 ± 0.003
π^- MC	0.93 ± 0.02	4.45 ± 0.01	0.144 ± 0.002
π^+ Data	0.57 ± 0.02	3.74 ± 0.02	0.115 ± 0.002
π^+ MC	1.13 ± 0.02	5.21 ± 0.02	0.147 ± 0.002
μ^- Data	0.02 ± 0.17	2.56 ± 0.12	0.058 ± 0.016

7.4.4 $p_{\mathbf{Lab}} < 0.5$ GeV/c pions

$p_{\mathrm{Lab}} < 0.5$ GeV/c tracks in the Belle II detector have highly curved trajectories due to the magnetic field. Tracks with $p_{\mathrm{lab}} < 0.3$ GeV/c typically do not reach the calorimeter and tracks with $p_{\mathrm{Lab}} < 0.5$ GeV/c that do reach the calorimeter enter at small angles to the crystal face. This trajectory allows pions to potentially ionize through several crystals forming an extended track in the calorimeter before hadronically interacting or stopping.

In Figure 7.19 the distribution of cluster energies for the selected pions with $p_{\mathrm{Lab}} < 0.5$ GeV/c is shown. Unlike the higher momentum pion samples studied above, a peak from ionization clusters at 0.2 GeV is not observed. This is due to the highly curved trajectories resulting in the pions in this sample to rarely ionize directly through the 30 cm depth of the calorimeter and escape the calorimeter.

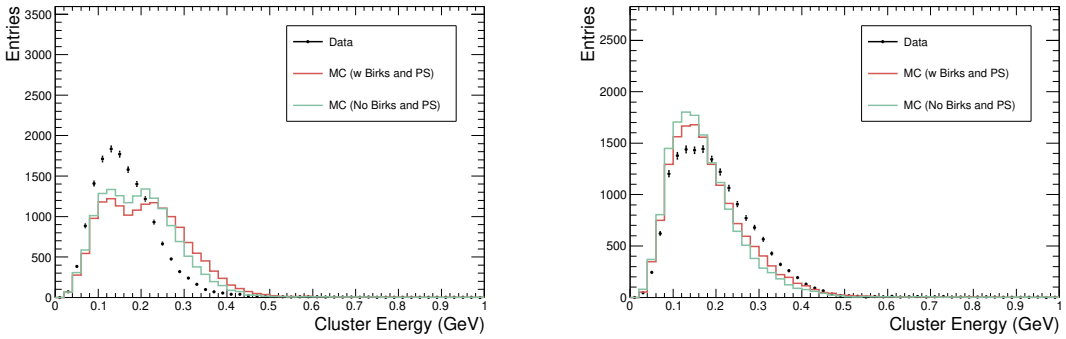

(a) π^- (b) π^+

Figure 7.19: Cluster energies of $p_{\mathrm{Lab}} < 0.5$ GeV/c pion sample.

Comparing the data and MC energy distributions in Figure 7.19, the π^- MC clusters are found to produce higher cluster energies than the data and the π^+ MC produces lower cluster energies relative to the data. This is the same trend that was present in the cluster energy distributions for the $0.5 \leq p_{\mathrm{Lab}} < 1$ GeV/c pion sample. In addition the π^- MC is found to have two merged peaks that are not observed in the data. To gain further insight into the interactions occurring in these clusters the pulse shapes of the crystals in these clusters are studied below.

In Figure 7.20 the crystal energy vs crystal hadron intensity distribution for the crystals in the $p_{\mathrm{Lab}} < 0.5$ GeV/c pion clusters are shown. In this figure a large number of ~ 45 MeV photon-like crystals are observed to be present. The majority of these crystals are produced by the primary pion initially ionizing through a ~ 7 cm section

of CsI(Tl) when the track initially enters the calorimeter at a small angle. In these distributions a significant presence of hadron pulse shapes is also observed. In the data and MC the single proton band is observed for both pion charges and in the MC additional pulse shape bands above the single proton band are also clearly resolved. In the data these additional bands are not resolved, however, an excess of crystals with pulse shapes in corresponding region are observed. As discussed above, the bands are likely not resolved in the data due to crystal-to-crystal variations smearing the distribution.

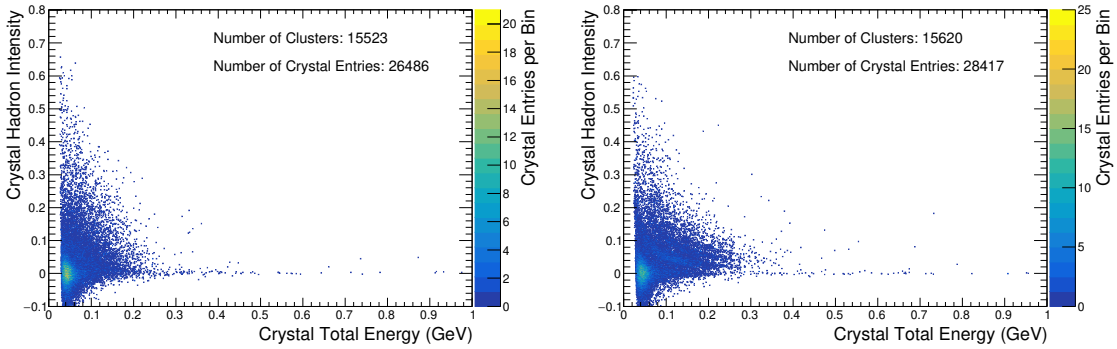

(a) π^- Data (b) π^- MC

(c) π^+ Data (d) π^+ MC

Figure 7.20: Crystal hadron intensity vs crystal energy for crystals in clusters from pions selected with $p_{\text{Lab}} < 0.5$ GeV/c. Histograms of hadron intensity for different crystal energy ranges are shown in Figure 7.21.

The momentum range of $0.3 < p_{\text{lab}} < 0.5$ GeV/c for pions corresponds to kinetic energies in the range $0.19 - 0.38$ GeV. In the kinetic energy range of $0.1 - 0.3$ GeV the pion-nucleus interaction cross-section is known to increase significantly due to the Δ resonance [10, 21, 43]. For cesium and iodide nuclei the main components of the

total pion-nucleus interaction cross section in this energy region are $\sim$ 40% elastic scattering, $\sim$ 35% absorption (no pion in final state), $\sim$ 20% inelastic scattering (pion in final state) and single charge exchange (π^0 in final state) ($\sim$ 5%) [43]. The pulse shape features in Figure 7.20 can provide insight into the interactions of the $p_{\rm Lab} < 0.5$ GeV/c pions. A pion in this sample will initially enter the calorimeter at a low angle and ionize potentially across multiple crystals, as evident from the abundance of $\sim$ 45 MeV photon-like crystals in the clusters. Eventually the pions energy will be reduced into the Δ resonance region and the probability of a nuclear interaction will significantly increase [10, 21, 43]. If the pion has an inelastic interaction this will produce protons and neutrons and the outgoing pion will have very low energy remaining and will then continue to ionize before stopping in the crystal. A stopped π^- can then undergo atomic capture followed by nuclear absorption whereas a π^+ is likely to decay as π^+ atomic capture is suppressed due to the electromagnetic repulsion between the π^+ and nucleus [44]. In pion nuclear absorption the total pion energy is absorbed by the nucleus and energetic protons and neutrons are then emitted. In the GEANT4 Bertini model the charged pion absorption processes included are: $\pi^+nn \rightarrow pn$, $\pi^+pn \rightarrow pp$, $\pi^-pn \rightarrow nn$ and $\pi^-pp \rightarrow pn$ [45]. Thus assuming neutrons escape the cluster, the absorption final states with protons are expected to produce crystals with pulse shapes corresponding to the single proton band observed in Figure 7.20.

In Figure 7.21 histograms of the hadron intensity for crystal energy ranges of $0.05 < {\rm E_{crystal}} < 0.15$ GeV, $0.15 \leq {\rm E_{crystal}} < 0.25$ GeV, and ${\rm E_{crystal}} \geq 0.25$ GeV are shown for the $p_{\rm Lab} < 0.5$ GeV/c pion clusters. From these histograms the types of pulse shapes in the π^+ vs π^- clusters can be compared in detail. In the crystal energy range $0.05 < {\rm E_{crystal}} < 0.15$ GeV the data distributions are very similar for π^+ vs π^-. In the crystal energy ranges $0.15 \leq {\rm E_{crystal}} < 0.25$ GeV and ${\rm E_{crystal}} \geq 0.25$ GeV however the π^+ clusters in data are found to produce a greater number of hadron crystals than the π^- clusters indicating the low momentum π^+ are generating a greater number of crystals with multiple secondary charged hadrons.

Comparing the data and MC in Figure 7.21, in general the π^+ MC has reasonable agreement with the π^+ data. For the π^-, in the crystal energy range $0.05 < {\rm E_{crystal}} < 0.15$ GeV and $0.15 \leq {\rm E_{crystal}} < 0.25$ GeV the π^- MC is found to have a large peak from crystals in the single proton band that is not seen/resolved in the data. In addition crystals with ${\rm E_{crystal}} \geq 0.25$ GeV in the π^- MC are seen to have an excess of multi-hadron pulse shapes relative to the π^- data. As pion absorption is a significant

contribution to the interaction cross section for the pions in this lower momentum sample, these observations suggest the π^- absorption modelling is overproducing secondary charged hadrons. This would also explain the data vs MC difference in the total cluster energy discussed at the beginning of this section where the π^- MC cluster energies were higher than in the data. If the π^- MC is over-producing protons then this could cause the observed differences between data and MC in the pulse shape distributions and cluster energy distributions.

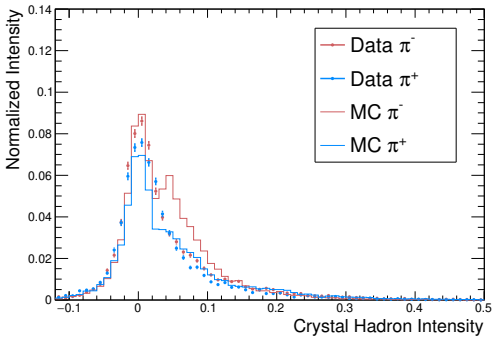

(a) $0.05 < \mathrm{E_{crystal}} < 0.15$ GeV

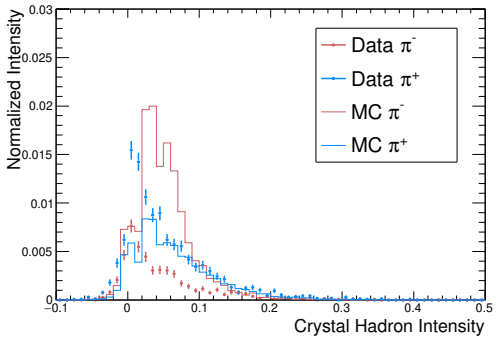

(b) $0.15 \leq \mathrm{E_{crystal}} < 0.25$ GeV

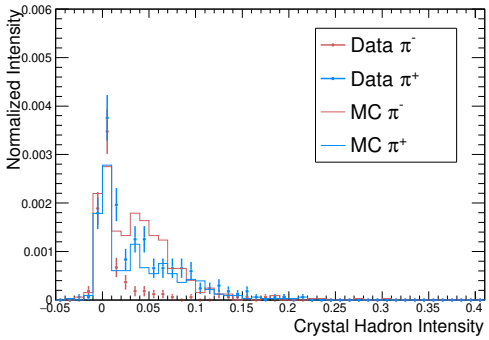

(c) $\mathrm{E_{crystal}} \geq 0.25$ GeV

Figure 7.21: Histograms of the crystal hadron intensity for different crystal energy range for crystals from selected pions with $p_{\mathrm{Lab}} < 0.5$ GeV/c .

7.5 Charged Kaons

Similar to pions, kaons typically will produce ionization clusters or hadronic showers. A distinct difference from pions however is that kaons contain strange quarks. The strangeness of kaons is well known to have a significant role in the material interactions for K^- vs K^+ causing large differences in the interaction cross sections,

particularly at low energies [10, 46, 47]. To reduce the variation of these effects and the track lengths in the calorimeter, the sample of kaons is studied in momentum bins of $p_{\mathrm{Lab}} \geq 1$ GeV/c, $0.5 \leq p_{\mathrm{Lab}} < 1$ GeV/c and $p_{\mathrm{Lab}} < 0.5$ GeV/c, as done with the pions in the previous section.

7.5.1 $p_{\mathrm{Lab}} \geq 1$ GeV/c Kaon Hadronic Showers

The cluster energy distribution for the selected kaons with $p_{\mathrm{Lab}} \geq 1$ GeV/c is shown in Figure 7.22. These distributions display a peak at ∼200 MeV from kaons ionizing through the calorimeter without an inelastic interaction occurring. Outside the energy range of 0.15 <$\mathrm{E_{ecl}}$< 0.25 GeV, many clusters are observed corresponding mostly to hadronic showers.

In Figure 7.22 the impact of including the full CsI(Tl) scintillation response in the MC is found to improve the data vs MC agreement for the K^+ clusters. For K^- clusters an improvement at cluster energies below 0.7 GeV and above 1.2 GeV is observed whereas between 0.7 and 1.2 GeV the MC cluster energies are slightly higher than the data.

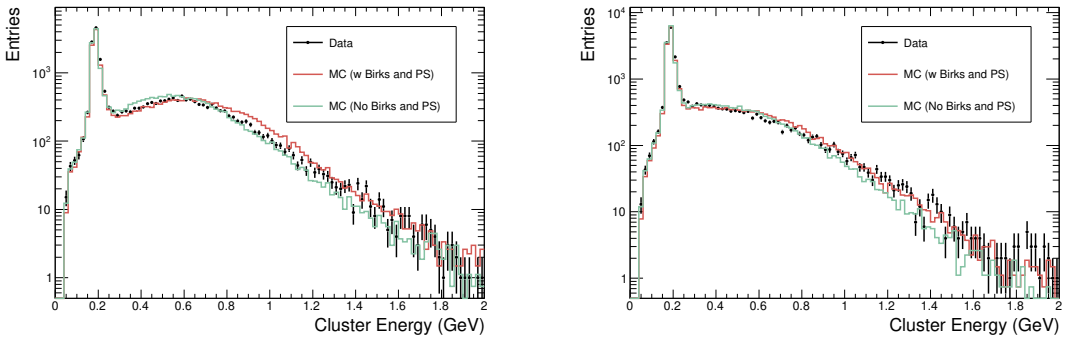

(a) K^- (b) K^+

Figure 7.22: Total cluster energy distribution for kaons selected with p_{lab}> 1 GeV/c.

The clusters from $p_{\mathrm{Lab}} \geq 1$ GeV/c kaons are divided into *ionization* and *shower* clusters based on the total cluster energy. For $p_{\mathrm{Lab}} \geq 1$ GeV/c kaons with cluster energy outside the energy range of 0.15 <$\mathrm{E_{ecl}}$< 0.25 GeV, the crystal hadron intensity vs crystal total energy distributions are shown in Figure 7.23.

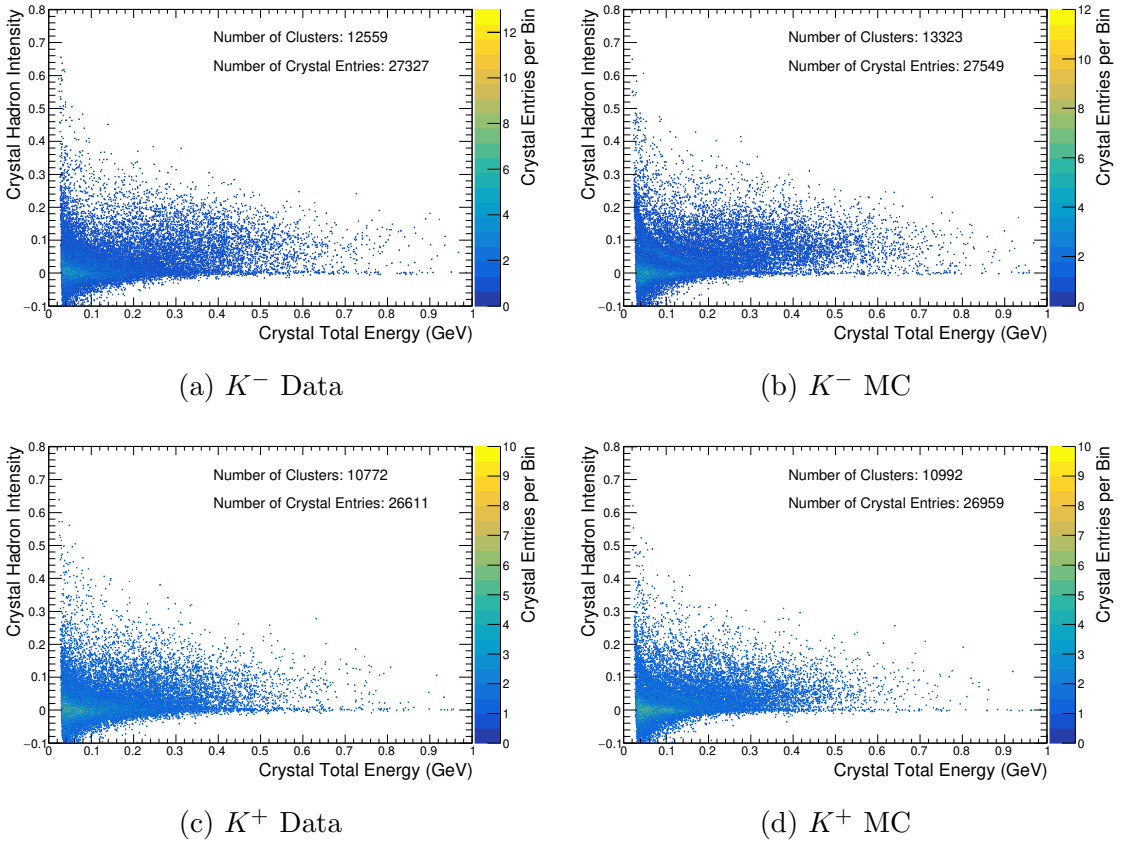

(a) K^- Data (b) K^- MC

(c) K^+ Data (d) K^+ MC

Figure 7.23: Crystal hadron intensity vs crystal total energy distribution for crystals in *shower* clusters from kaons with $p_{\text{Lab}} \geq 1$ GeV/c. Histograms of hadron intensity for different crystal energy ranges are shown in Figure 7.24.

In Figure 7.23 several of the pulse shape features that were present in the $p_{\text{Lab}} \geq 1$ GeV/c pion *shower* cluster crystals are observed. At lower crystal energies, a large number of crystals have photon-like pulse shapes. These crystals are mostly from the energetic kaons initially ionizing through a 7-20 cm segment of CsI(Tl) before interacting in a nearby crystal. The low energy photon-like crystals can also produced from energetic charged pions emitted from the kaon nuclear interactions. Above the photon-like pulse shapes at lower crystal energies the single proton band is visible in both kaon distributions in the data and MC indicating energetic secondary protons are being generated in the hadronic showers.

At higher crystal energies in Figure 7.23 a scatter of crystals in the multi-hadron pulse shape region are observed in all distributions. As discussed above, these energy deposits are from high multiples of low energy charged hadrons emitted by nucleus de-excitations following an energetic interaction with a nucleus. These multi-hadron

pulse shapes are observed to extend to crystal energies up to 1 GeV with relatively large hadron intensity values indicating very large amounts of hadron scintillation component emission in a single crystal. As the energy of these multi-hadron crystals span a large range while the range of hadron intensity values of these crystals remains roughly constant in the range of $0.02 - 0.2$, this means the fraction of energy deposited at high $d\mathrm{E}/dx$ is also remaining roughly constant in these crystals while the total energy deposit is increasing. This demonstrates that as the energy of the multi-hadron crystals increases the multiplicity of charged hadrons produced in these crystals is increasing. For the very high energy photon-like crystals in Figure 7.23, it was confirmed by studying the secondary particles produced by GEANT4 that the large energy deposits are typically from secondary π^0's that decay to two photons in the crystal.

The similarity between the K^+ and K^- distributions in Figure 7.23 is interesting given the difference in strangeness between the K^+ and K^-. It well established that due to strangeness conservation in strong interactions, there are several inelastic channels available to K^- that are forbidden for K^+ when interacting with protons/neutrons/nuclei [10, 46, 47]. This causes the inelastic K^+-p cross-section to only become significant above $>$ 1 GeV/c as between 1 $<p_{\mathrm{lab}}<$ 3 GeV/c the cross-sections for several inelastic interactions involving final states consisting of pions, proton/neutrons and the scattered K^+ become significant [46]. Once produced, the secondary pions can further interact producing additional charged hadrons. The scattered K^+ from these collisions typically will have low energy that will be deposited by ionization before the K^+ decays, producing mainly muons or pions. In addition to the K^+ inelastic collisions that include a scattered K^+, a charge exchange interaction between a K^+ and neutron can also occur producing a K^0_S or K^0_L [46]. If a K^0_S is produced and decays to charged pions, the pions will ionize and potentially initiate additional interactions in the cluster that can produce charged hadrons. If the K^0_S decays to π^0's then these will likely decay to two photon's, producing an electromagnetic shower component to the hadronic shower. The various hadron pulse shapes observed the K^+ distributions in Figure 7.23 are from these different interactions.

For the K^-, the analogous K^+ interactions are possible in addition to a number of interactions where the K^- and a neutron/proton interact to produce a final state with a free hyperon and pion such as $\pi^0\Lambda^0$, $\pi^{\pm}\Sigma^{\mp}$ and $\pi^0\Sigma^0$. These additional channels are forbidden for the K^+ due to strangeness conservation [10, 21, 46]. Once produced the hyperon can further interact in the cluster and/or eventually decay, most often

to states including a proton/neutron. As a result of these additional channels, K^- are known to have higher nuclear interaction cross-sections than K^+ [10, 46].

The difference in K^- and K^+ interactions is especially seen Sections 7.5.2 and 7.5.4 where the lower momentum kaons are studied, however even in the $p_{\text{Lab}} \geq 1$ GeV/c sample the K^- hadronic showers are observed to produce more crystals with hadron pulse shapes compared to the K^+ shower clusters. This difference in the K^- and K^+ interactions can be seen in Figure 7.24 showing histograms of the crystal hadron intensity for different crystal energy ranges for the crystals in the $p_{\text{Lab}} \geq 1$ GeV/c kaon *shower* clusters. In the crystal energy ranges $0.05 < \text{E}_{\text{crystal}} < 0.15$ GeV and $0.15 \leq \text{E}_{\text{crystal}} < 0.25$ GeV the K^+ and K^- distributions are found to be similar however in the crystal energy range $\text{E}_{\text{crystal}} \geq 0.25$ GeV a large difference between the hadron intensity values of crystals in K^+ vs K^- is observed such that the K^- clusters contain more hadron crystals relative to the K^+ clusters.

Comparing the data and MC in Figure 7.24, the lower crystal energy ranges show reasonable agreement by displaying similar features. The MC proton band peak is shifted by +0.02 relative to the data as expected and discussed above. In the $\text{E}_{\text{crystal}} \geq 0.25$ GeV crystal energy range the K^+ and K^- data distributions are found to have an excess of photon-like crystals relative to the simulation. This result was also seen in the pion distribution studied in the previous section. For hadron crystals in these distributions, there is good agreement between the K^+ MC and data demonstrating the K^+ interactions and CsI(Tl) scintillation response is well modelled. For the K^-, the data and MC show a similar distribution however the MC is found to have an excess of crystals with hadron intensity in the region of 0.025-0.15. As there can be several secondary interactions occurring in these clusters from pion/protons etc it is hard to identify a specific process that could cause this excess in the MC. In general, however, the excess hadron crystals in this energy range suggests the nuclear evaporations occurring in the high momentum K^- MC are emitting a greater number of charged hadrons relative to the data.

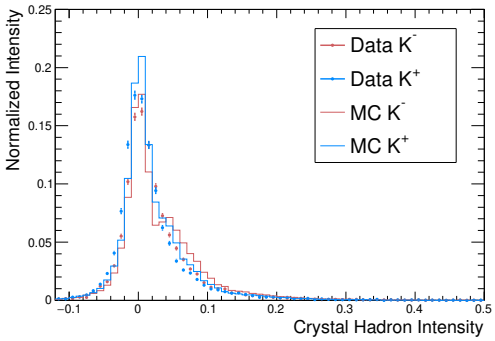

(a) $0.05 < \mathrm{E_{crystal}} < 0.15$ GeV

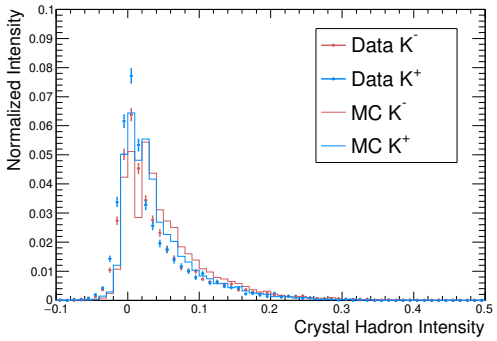

(b) $0.15 \leq \mathrm{E_{crystal}} < 0.25$ GeV

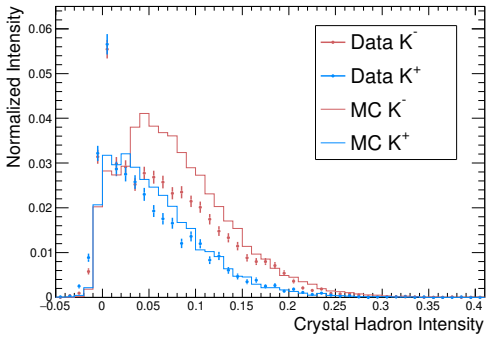

(c) $\mathrm{E_{crystal}} \geq 0.25$ GeV

Figure 7.24: Hadron intensity histograms for crystals in *shower* clusters from kaons with $p_{\mathrm{Lab}} \geq 1$ GeV/c.

7.5.2 $0.5 \leq p_{\mathbf{Lab}} < 1$ GeV/c Kaon Hadronic Showers

The distribution of cluster energies for the selected kaons in the momentum range $0.5 \leq p_{\mathrm{Lab}} < 1$ GeV/c is shown in Figure 7.25. In these distributions a significant asymmetry is observed between K^- and K^+. This is in contrast to the $p_{\mathrm{Lab}} \geq 1$ GeV/c clusters where similar features were observed for both kaon charges. The difference in cluster energy distributions is caused by the decreases in the number of K^+ inelastic channels available at lower energies. In particular as the momentum drops below 1 GeV/c, the K^+ interactions producing pions quickly become below threshold [46]. In the momentum range $0.5 \leq p_{\mathrm{Lab}} < 1$ GeV/c kaons have corresponding kinetic energies in the range $0.2 - 0.62$ GeV and thus the higher momentum kaons in this sample can still ionize through the calorimeter if an inelastic interaction does not occur. This is evident from the peak observed at 200 MeV in the K^- and K^+ distributions.

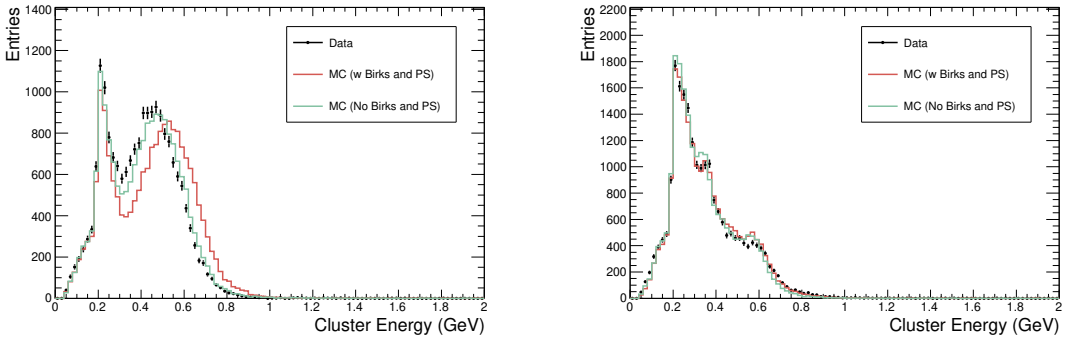

(a) K^- (b) K^+

Figure 7.25: Total cluster energy distribution for selected kaons with $0.5 \leq p_{\text{Lab}} < 1$ GeV/c.

In Figure 7.25 the impact of including the full CsI(Tl) scintillation response in the simulations is observed to produce different results for the K^- vs K^+. For the K^+ clusters, adding the CsI(Tl) response results in a slight improvement in the data vs MC agreement. For the K^-clusters, the cluster energies in MC tend to be larger than the data. However the K^- MC cluster energies are in general found to be higher than the data even prior to including the CsI(Tl) response. This is an indication that the K^- MC is producing more secondary protons relative to the data as adding the CsI(Tl) response would amplify this effect. As will be shown below, the pulse shapes of the crystals in these clusters suggest the nuclear de-excitations in the K^- clusters are the source of the excess protons.

As many clusters with energy 0.15 $<\text{E}_{\text{ecl}}<$ 0.25 GeV are present in the $0.5 \leq p_{\text{Lab}} < 1$ GeV/c sample due to kaons ionizing through the calorimeter, the kaon hadronic showers in the $0.5 \leq p_{\text{Lab}} < 1$ GeV/c sample are isolated by selecting the clusters outside the *ionization* cluster energy window. The distribution of crystal hadron intensity vs crystal energy for the crystals in these clusters are shown in Figure 7.26

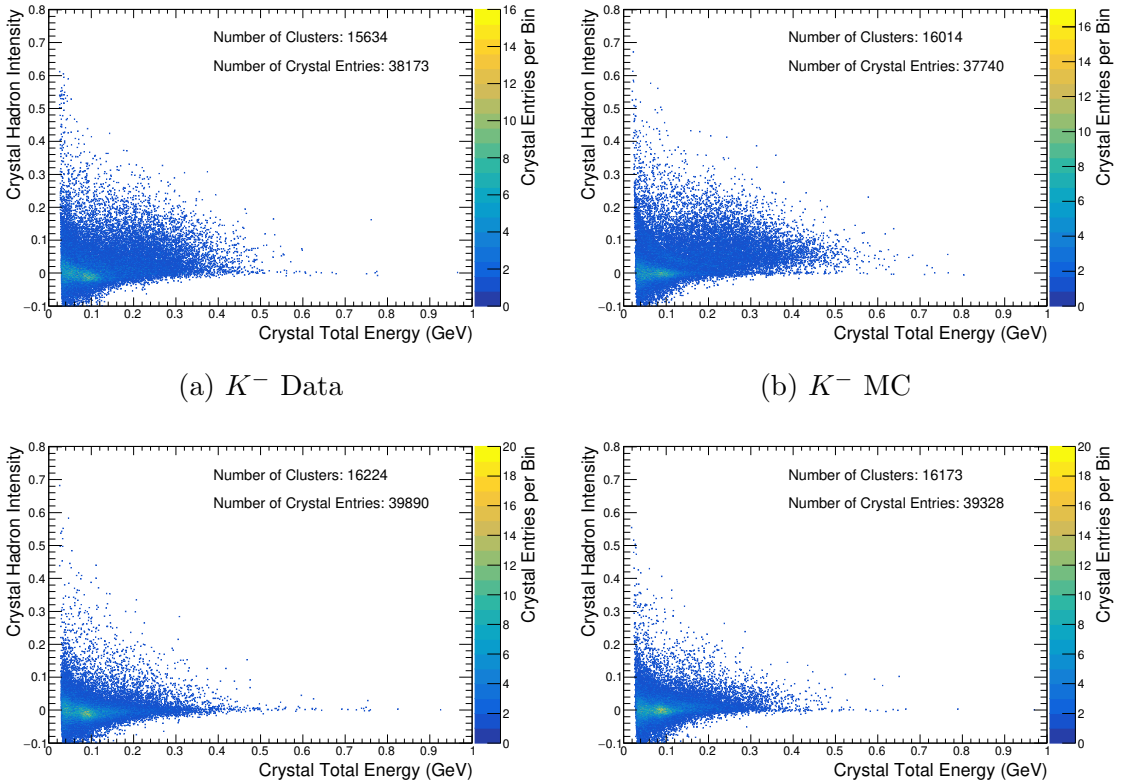

(a) K^- Data (b) K^- MC

(c) K^+ Data (d) K^+ MC

Figure 7.26: Crystal hadron intensity vs crystal energy for crystals in *shower* clusters from kaons with $0.5 \leq p_{\text{Lab}} < 1$ GeV/c. Histograms of the crystal hadron intensity for different crystal energy ranges are shown in Figure 7.27.

As the kaon momentum drops below 1 GeV/c several inelastic interactions become below threshold [46]. This can be seen from Figure 7.26 to have a significant impact on the types of pulse shapes produced in crystals in the $0.5 \leq p_{\text{Lab}} < 1$ GeV/c kaon clusters, particularity for the K^+ clusters. In Figure 7.26 the single proton band is only clearly observed in the K^- distributions, and in general very few crystals with hadron pulse shapes are present in the K^+ clusters. The deficit of hadron pulse shapes at lower K^+ momentum demonstrates that less K^+ inelastic interactions are occurring as the momentum decreases. By studying the GEANT4 truth of the MC clusters where the K^+ cluster did have a crystal with a hadron pulse shapes, the majority of the corresponding energy deposits are found to be from charge exchange interactions that produced protons/neutrons and a K^0_S or K^0_L.

In the K^- distributions numerous crystals with hadron pulse shapes are observed. This is consistent with expectations as several inelastic interactions producing $\pi\Lambda$ and

$\pi\Sigma$'s are still possible for K^- in this momentum range [10, 46]. These interactions are expected to produce nuclear excitations and energetic protons from the hyperon decays. The charged hadrons produced from these interactions would then produce crystals with hadron pulse shapes as seen in the crystals in the K^- clusters. The main difference observed in the K^- distributions between the $p_{\text{Lab}} \geq 1$ GeV/c and $0.5 \leq p_{\text{Lab}} < 1$ GeV/c ranges is a decrease in the crystal energy for the multi-hadron crystals. This demonstrates the decrease in momentum results in a decrease in energy transferred to the nucleus as the multiplicity of charged hadrons emitted from the nucleus de-excitations in the clusters is decreasing.

The significant difference in pulse shapes present in the $0.5 \leq p_{\text{Lab}} < 1$ GeV/c K^- vs K^+ clusters can also be seen from the hadron intensity histograms in Figure 7.27. In these histograms, the K^+ clusters are observed to have less hadron pulse shapes relative to the K^- in all three crystal energy ranges. This trend is different from the higher momentum sample where the asymmetry was only observed for $\text{E}_{\text{crystal}} \geq 0.25$ GeV crystals. In Figure 7.27 the histogram for crystals with $\text{E}_{\text{crystal}} \geq 0.25$ GeV in particular shows a large asymmetry between the K^- and K^+. These trends are observed in the data and MC.

Comparing the data and MC distributions in Figure 7.27, in the $0.05 < \text{E}_{\text{crystal}} < 0.15$ GeV crystal energy range the data and MC have reasonable agreement with the tail of crystals with higher hadron intensity values being well modelled. In the $0.15 \leq \text{E}_{\text{crystal}} < 0.25$ GeV and $\text{E}_{\text{crystal}} \geq 0.25$ GeV energy ranges however the MC is found to produce more hadron crystals relative to the data in both the K^- and K^+ clusters. The excess of charged hadrons in the K^- MC is consistent with the excess K^- cluster energies seen at the beginning of this section and suggests the K^- MC is producing more secondary protons than the data.

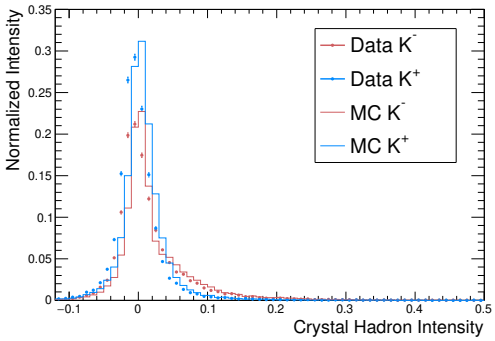

(a) $0.05 < \mathrm{E_{crystal}} < 0.15$ GeV

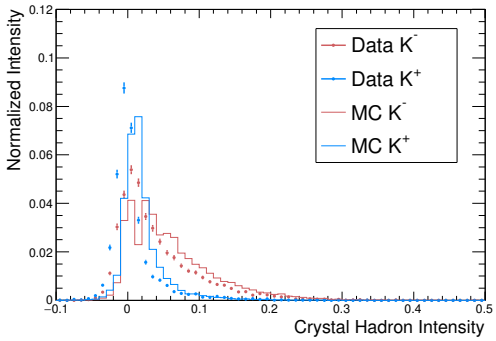

(b) $0.15 \leq \mathrm{E_{crystal}} < 0.25$ GeV

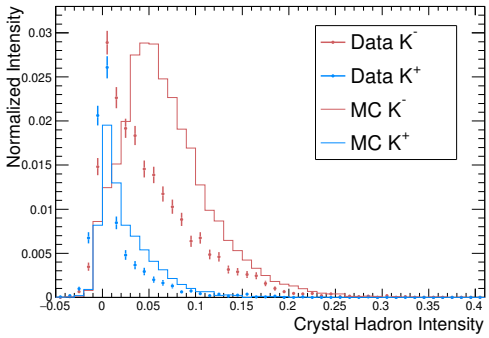

(c) $\mathrm{E_{crystal}} \geq 0.25$ GeV

Figure 7.27: Hadron intensity histograms for crystals in *shower* clusters from charged kaons with $0.5 \leq p_{\mathrm{Lab}} < 1$ GeV/c.

7.5.3 Kaon Ionizing Clusters

The previous section studied $p_{\mathrm{lab}} > 0.5$ GeV/c kaons with total cluster energy outside the range of $0.15 < \mathrm{E_{ecl}} < 0.25$ GeV/c to remove clusters from a kaon ionizing through the calorimeter. In this section the clusters in the energy range $0.15 < \mathrm{E_{ecl}} < 0.25$ GeV from $p_{\mathrm{lab}} > 0.5$ GeV/c kaons are studied. For these clusters the crystal hadron intensity vs crystal energy distributions are shown in Figure 7.28. From this figure it is observed that when the kaon ionizes though the crystals, photon-like pulse shapes are produced. This is similar to the pion *ionization* clusters and muon clusters and demonstrates the kaon ionization dE/dx is not large enough to generate significant amounts of hadron component scintillation emission. In these distributions some hadron pulse shapes are visible from hadronic showers with cluster energy in the *ionization* cluster energy window.

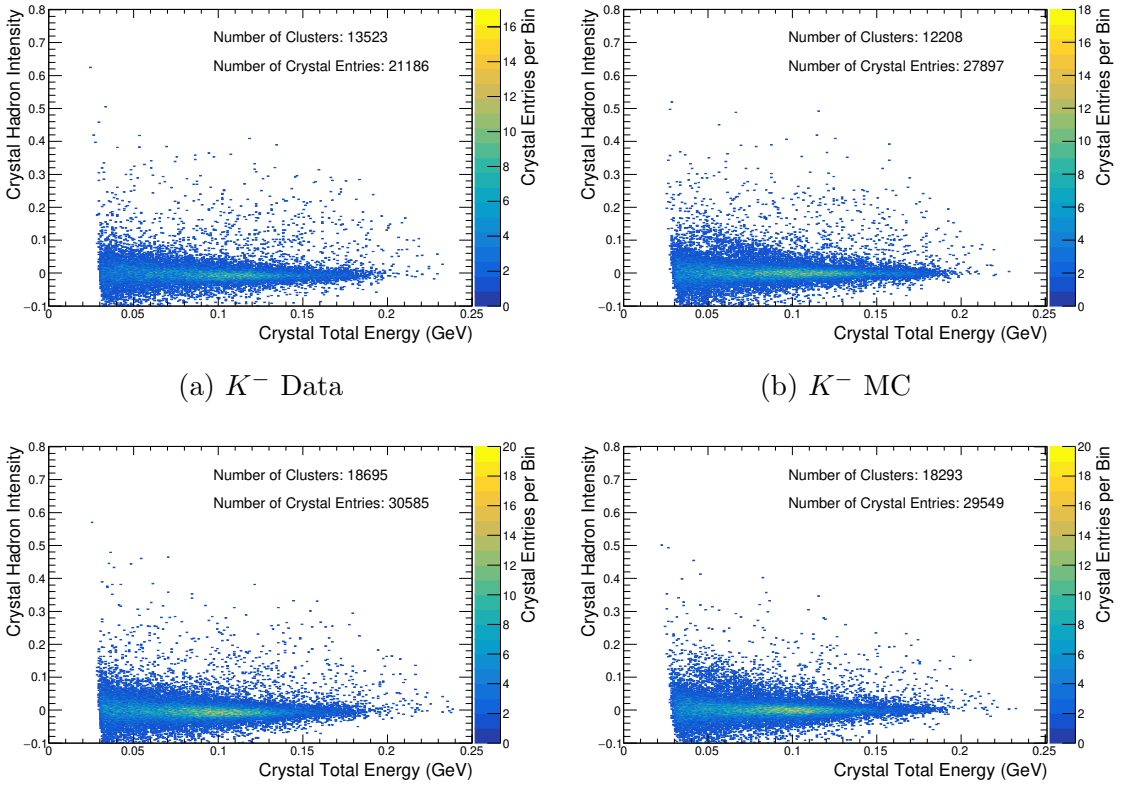

(a) K^- Data (b) K^- MC

(c) K^+ Data (d) K^+ MC

Figure 7.28: Crystal hadron intensity vs crystal total energy distribution for crystals in clusters from kaons with $p_{\text{lab}}>$ 0.5 GeV/c and total cluster energy in the range 0.15 $<\text{E}_{\text{ecl}}<$ 0.25 GeV/c.

7.5.4 $p_{\text{Lab}} < 0.5$ GeV/c Kaons

As discussed above, the magnetic field in the Belle II detector forces $p_{\text{Lab}} < 0.5$ GeV/c tracks to have highly curved trajectories allowing the tracks to enter the calorimeter a small angles. This has the effect to increase the available track length in the calorimeter allowing the kaons to potentially ionize through several crystals horizontally before interacting or stopping. In Figure 7.29 the total cluster energy distribution for the kaons selected with $p_{\text{Lab}} < 0.5$ GeV/c is shown.

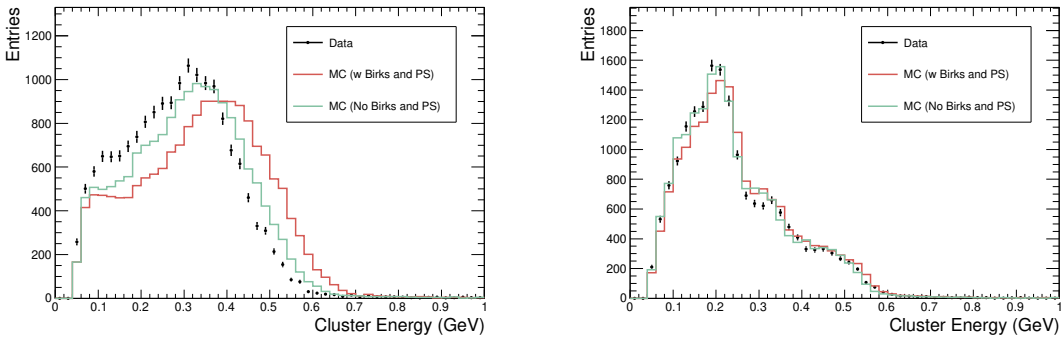

(a) K^- (b) K^+

Figure 7.29: Cluster energy distributions for selected kaons with $p_{\text{Lab}} < 0.5$ GeV/c.

As seen in Figure 7.29 the cluster energy distributions for the kaons selected with $p_{\text{Lab}} < 0.5$ GeV/c shows different features depending on the kaon charge. This is the same trend that was observed in the $0.5 \leq p_{\text{Lab}} < 1$ GeV/c sample and is related to the difference in strangeness for the K^- vs K^+ allowing for different material interactions. In the case of the K^+ clusters, including the CsI(Tl) response in the MC does not cause a significant change in the distribution and there is reasonable agreement between the data and MC. For the K^- clusters the MC is found to tend to produce higher cluster energies than the data both with and without including the CsI(Tl) response. By including the CsI(Tl) response the clusters shift to even higher energies. As discussed in the previous sections, this trend suggests the K^- MC is producing more secondary protons than the data.

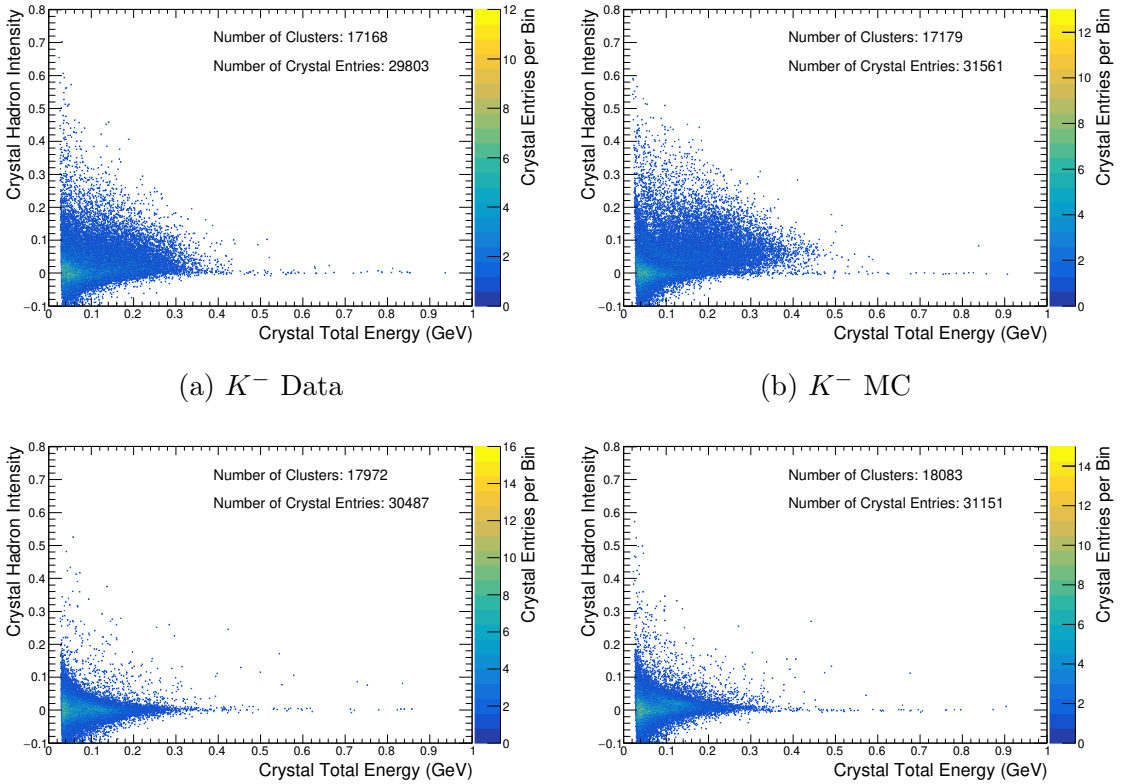

(a) K^- Data (b) K^- MC

(c) K^+ Data (d) K^+ MC

Figure 7.30: Crystal hadron intensity vs crystal energy distribution for crystals in clusters from kaons with $p_{\text{Lab}} < 0.5$ GeV/c. Histograms of hadron intensity for different crystal energy ranges are shown in Figure 7.31.

In Figure 7.30 the crystal hadron intensity vs crystal energy distributions for the $p_{\text{Lab}} < 0.5$ GeV/c kaon clusters is shown. In Figure 7.30 the K^- and K^+ clusters are observed to have an significant number of crystals with photon-like pulse shapes at crystal energies < 100 MeV. These crystals primarily correspond to a kaon initially ionizing through ~ 7 cm of CsI(Tl) when initially entering the calorimeter. In terms of hadron pulse shape features, significant differences are observed between the K^- and K^+ clusters. The K^+ clusters are found to contain very few crystals with hadron pulse shapes whereas the K^- clusters have numerous crystals with hadron pulse shapes. This observation indicates that the K^+ clusters are rarely producing secondary charged hadrons in the cluster and is demonstrative of the interactions of low energy kaons in materials. Only K^- can undergo strong nuclear absorption due to strangeness conservation [10, 46, 47]. When K^- absorption occurs at lower energies, a Λ or Σ is produced and can then become bound to the nucleus and form a

hypernuclei [47]. In addition about 80% of K^- absorptions in heavier nuclei will also emit a pion [47]. After production the hyperon will eventually decay typically producing pions, protons or neutrons. In addition the nucleus will de-excite by emitting photons, neutrons and/or protons [47]. In the GEANT4 Bertini Cascade, hypernuclei are modelled by adding the decay products of a low energy hyperon to the simulation [48]. Thus from these interactions numerous charged hadrons are expected to be produced in the K^- clusters leading to the abundance of hadron pulse shapes observed in the K^- distributions in Figure 7.30.

The low energy K^+ material interactions are very different from K^- as K^+ nuclear absorption is forbidden/highly suppressed due to strangeness conservation [10, 46, 47]. For the majority of K^+ in this sample the calorimeter interaction will proceed with the K^+ depositing all of its kinetic energy (< 0.2 GeV) by ionization then stopping in a crystal. Following this the K^+ will decay. The different features in the total cluster energy distribution in Figure 7.29 arise from the different K^+ decay modes. The majority of K^+ clusters with energy below 0.25 GeV are from the K^+ decaying by: $K^+ \to \mu^+\bar{\nu}_\mu$ (branching fraction is 64% [2]). From this decay the neutrino has 235.5 MeV of energy that escapes the cluster. The muon produced has a kinetic energy of 152 MeV that will then also typically be deposited by ionizing in the calorimeter. Thus when this decay occurs there will typically be a least a total energy deposit of 352 MeV by kaon and muon ionization. Depending on the event, however, the muon when ionizing can escape the calorimeter or be classified as a separate cluster by the clustering algorithm. For this reason many of the K^+ clusters have lower energies. Another option is if the K^+ decays by $K^+ \to \pi^+\pi^0$ (branching fraction is 21% [2]). In this case the π^+ is produced with 110 MeV of kinetic energy and the total energy of the π^0 is 244 MeV that gets deposited electromagnetically after decaying to two photons. The low energy π^+ can then potentially have an inelastic interaction or decay. As a result many of the few hadron crystals that are observed in the K^+ distribution in Figure 7.31 are from interactions initiated by secondary pions produced by K^+ decays.

In Figure 7.31 histograms of the hadron intensity for different crystal energy ranges are shown for the crystals in the $p_{\text{Lab}} < 0.5$ GeV/c kaon clusters. From these distributions the excess of hadron crystals in K^- relative to K^+ clusters can clearly be seen in all crystal energy ranges in both the MC and data. In the crystal energy ranges $0.15 \leq \text{E}_{\text{crystal}} < 0.25$ GeV and $\text{E}_{\text{crystal}} \geq 0.25$ GeV, the K^- MC is found to produce an excess of hadron crystals relative to the K^- data. This observation sug-

gests that the MC modelling for K^- nuclear absorptions is over-producing charged particles. This would also account for the larger cluster energies observed in the K^- MC relative to the data as shown at the beginning of this section.

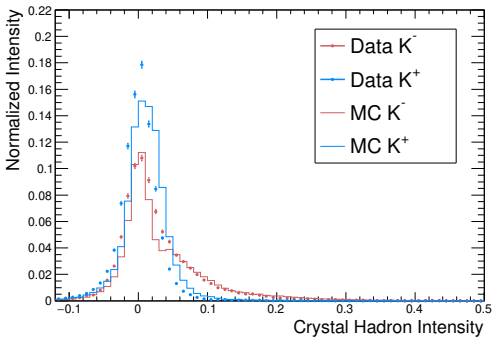

(a) $0.05 < \mathrm{E_{crystal}} < 0.15$ GeV

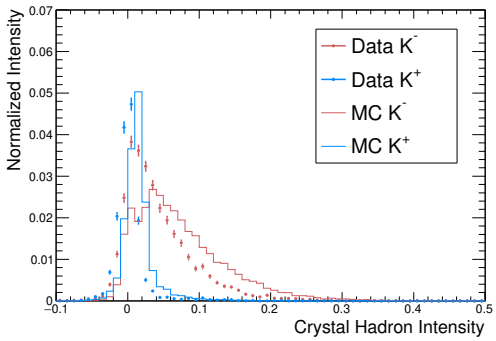

(b) $0.15 \leq \mathrm{E_{crystal}} < 0.25$ GeV

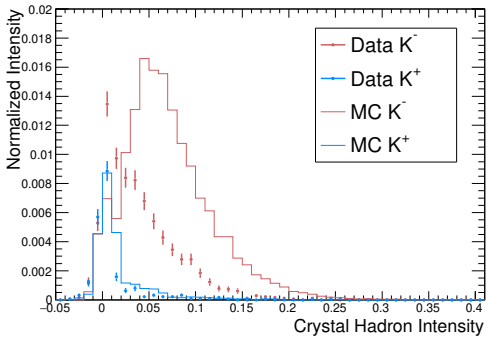

(c) $\mathrm{E_{crystal}} \geq 0.25$ GeV

Figure 7.31: Hadron intensity histograms of crystals in clusters from selected kaons with $p_{\mathrm{Lab}} < 0.5$ GeV/c

7.6 Protons and anti-protons

As protons are several times heavier than pions/muons, the ionization $d\mathrm{E}/dx$ of lower momentum protons is much larger than lower momentum pions/muon and the kinetic energy available for protons at an equivalent momentum is reduced. As a result the proton sample was divided in the momentum bins $p_{\mathrm{lab}} >$ 2 GeV/c, 1 $< p_{\mathrm{lab}} <$ 2 GeV/c and $p_{\mathrm{lab}} <$ 1 GeV/c.

7.6.1 $p_{\mathbf{lab}} > 2$ GeV/c Proton Hadronic Showers

Protons with $p_{\rm lab}>$ 2 GeV/c have low ionization dE/dx and thus produce either *ionization* or *shower* clusters, similar to pions and kaons. This is seen from Figure 7.32 showing the cluster energy distribution for the $p_{\rm lab}>$ 2 GeV/c protons where two distinct classes of clusters are observed. In this momentum range the protons will either ionizing through the calorimeter depositing $\sim$ 200 MeV or generate a hadronic shower producing a cluster with energy typically above the ionization cluster energy peak. From Figure 7.32 the impact of $\bar{p}$ annihilation is also observed as the $\bar{p}$ cluster energies extend much higher than the p clusters.

Comparing the data and MC distributions in Figure 7.32 for the p sample, the MC including the full CsI(Tl) scintillation response is observed to improve the MC agreement with the data. For the $\bar{p}$ clusters, including the full CsI(Tl) scintillation response in the MC does not have a significant impact on the cluster energy distribution and both MC distributions resemble the data distribution. This is consistent with the expectation from $\bar{p}$ annihilation which typically results in emission of multiples of charged and/or neutral pions [49]. After production from $\bar{p}$ annihilation, the charged pions ionize with a low enough dE/dx such that the scintillation efficiency is similar to an energy deposit from an electromagnetic shower and as a result, the Birks factor does not have a large impact in this case.

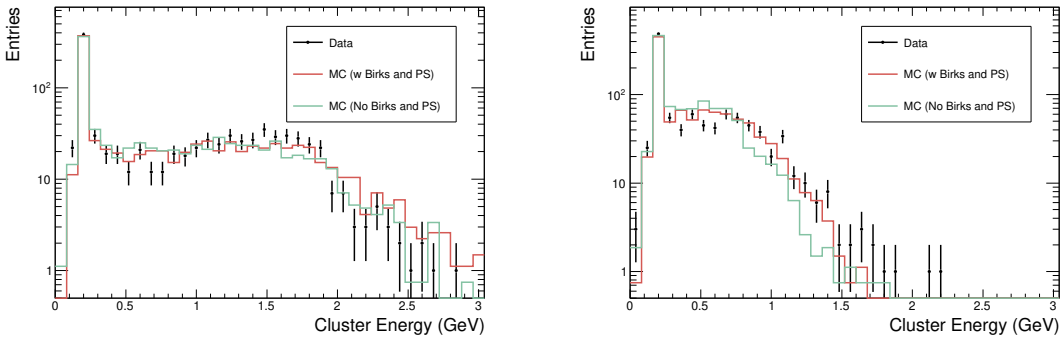

(a) $\bar{p}$ (b) p

Figure 7.32: Total cluster energy distribution for protons with $p_{\rm lab}>$ 2 GeV/c.

As the pulse shapes of crystals in *ionization* and *shower* clusters are expected to differ, the $p_{\rm lab}>$ 2 GeV/c proton sample is divided into *ionization* and *shower* samples where *ionization* clusters are defined as cluster in the cluster energy range of 0.15 $<$E$_{\rm ecl}<$ 0.25 GeV. In Figure 7.33 the crystal hadron intensity vs crystal energy

distributions are shown for the p_{lab}> 2 GeV/c proton clusters with cluster energy outside the *ionization* cluster energy window.

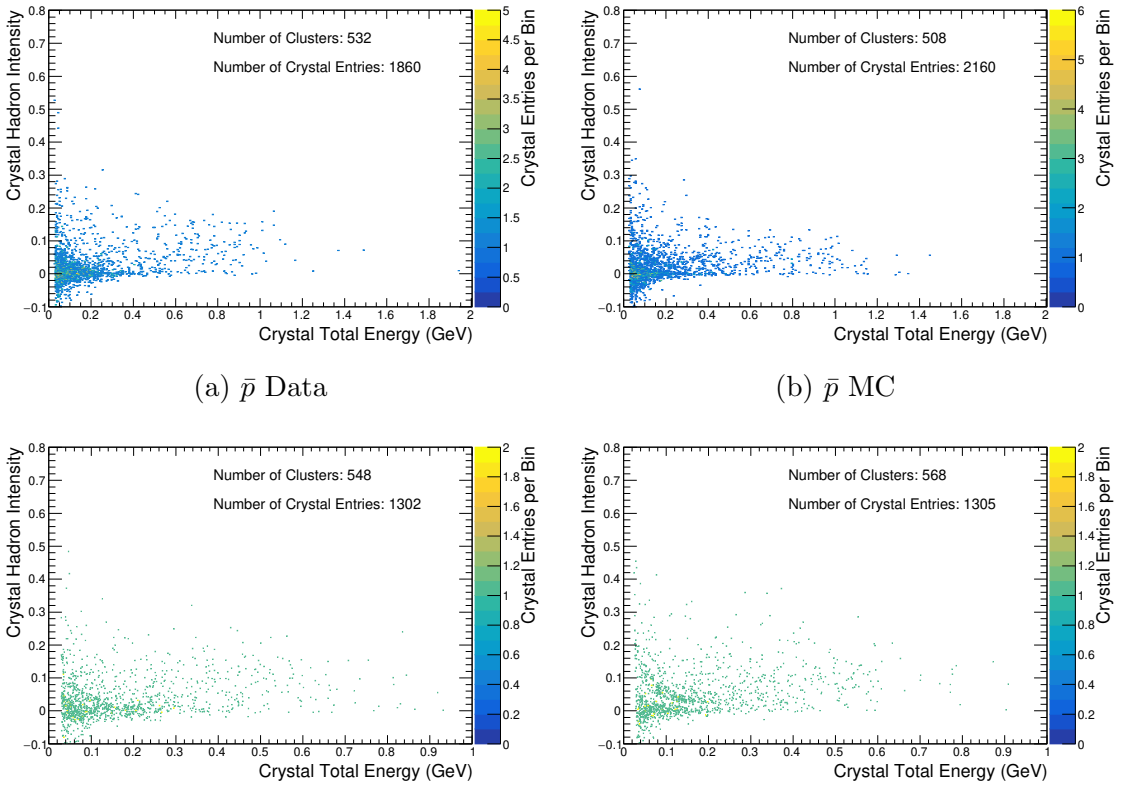

(a) $\bar{p}$ Data (b) $\bar{p}$ MC

(c) p Data (d) p MC

Figure 7.33: Crystal hadron intensity vs crystal total energy distribution for crystals in *shower* clusters from protons with p_{lab}> 2 GeV/c. Note crystal energy axis for $\bar{p}$ extends to 2 GeV. Histograms of hadron intensity for different crystal energy ranges are shown in Figure 7.34.

In Figure 7.33 many of the pulse shape features that were observed and discussed when studying the pion and kaon hadronic showers are also observed in hadronic showers produced by the p_{lab}> 2 GeV/c protons. Protons with p_{lab}> 2 GeV/c have a corresponding kinetic energy above 1.27 GeV and in this energy range p and $\bar{p}$ can interact with a nucleus by initiating spallation interactions [20, 50]. This interaction consists of an initial hard-scatter followed by a nuclear evaporation where the nucleus de-excites emitting many low energy particles, including hadrons [20, 50]. The initial hard-scatter that occurs can result in emission of high energy secondary neutrons, protons and/or pions [20, 50]. In addition, as the momentum increases above 2.3

GeV/c strange particles can also be produced [51]. Due to the large nuclear interaction length of CsI(Tl) relative to the calorimeter depth, the high energy neutrons emitted from these interaction are likely to escape the cluster and potentially re-scatter far from the primary interaction forming split-off clusters. The energetic protons and pions however, will ionize with a low $d\mathrm{E}/dx$ through the calorimeter crystals and potentially re-scatter in another crystal. The lower energy crystals (< 0.1 GeV) with photon-like pulse shapes observed in Figure 7.33 are mainly from energetic protons and pions ionizing through crystals after being emitted by these interactions. An interesting observation in Figure 7.33 is that in the data and MC the single proton band is observed in the p and $\bar{p}$ distributions. This is because only a p stopping in the crystal will produce an energy deposit with pulse shape in the region of the single proton band. If an $\bar{p}$ deposits most of its kinetic energy in the CsI(Tl) eventually the $\bar{p}$ will annihilate and produce additional secondary particles. It is thus interesting to observe the single proton band in both the p and $\bar{p}$ distributions, as this indicates these protons are likely secondary particles produced in the hadronic shower.

As mentioned above, after the primary proton scatter has occurred the nucleus is left in an excited state. Through nuclear evaporation the nucleus de-excites emitting high multiplicities of low energy neutrons, photons, protons, deuterons etc [20]. The charged hadrons emitted in this process will ionize with high $d\mathrm{E}/dx$ and stop in the crystal. The high multiplicity of the low energy charged hadrons produced in these events produces the energy deposits in the crystals in the multi-hadron pulse shape region (crystal energy above 0.2 GeV and hadron intensity above 0.02) in Figure 7.33.

In Figure 7.34 histograms of the hadron intensity for different crystal energy ranges are shown and allow for a detailed comparison of pulse shapes in the data and MC. Comparing the p and $\bar{p}$ distributions in the $0.05 < \mathrm{E_{crystal}} < 0.15$ GeV and $0.15 \leq \mathrm{E_{crystal}} < 0.25$ GeV energy ranges it is seen that the data and MC for the $\bar{p}$ clusters have a similar intensity of crystals in the tail to high hadron intensity, however, relative to the p clusters, the $\bar{p}$ clusters have a higher fraction of crystals with photon-like pulse shapes. This can be due to $\bar{p}$ annihilation frequently producing secondary charged pions that then ionize and produce crystal energy deposits below 0.25 GeV and photon-like pulse shape. Comparing the data and MC distributions for the $0.05 < \mathrm{E_{crystal}} < 0.15$ GeV and $0.15 \leq \mathrm{E_{crystal}} < 0.25$ GeV energy ranges there is agreement between the data and MC observed for the p and $\bar{p}$ samples. In the $\mathrm{E_{crystal}} \geq 0.25$ GeV crystal energy range, the p and $\bar{p}$ distributions have agreement between the data and MC at hadron intensity above 0.05, demonstrating the

CsI(Tl) scintillation response simulations developed in Chapter 5 [25] are modelling the CsI(Tl) scintillation emission for these interactions. At hadron intensity of zero the $\bar{p}$ data is found to have an excess of crystals relative to the MC. An excess of photon-like crystals in data relative to MC for crystals in the $E_{crystal} \geq 0.25$ GeV energy range was also observed in the pion and kaon hadronic shower samples studied previously. This excess could indicate that in the data there are a larger number of interactions that produce energetic secondary photons and/or π^0's as these secondary particles will produce photon-like pulse shapes in this crystal energy range.

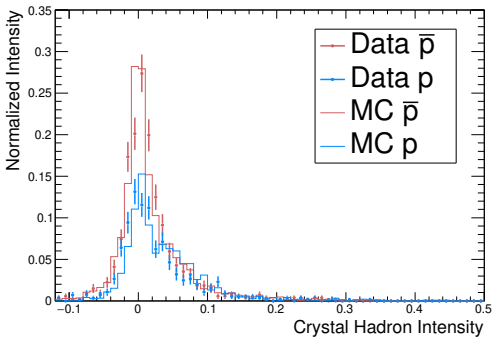

(a) $0.05 < E_{crystal} < 0.15$ GeV

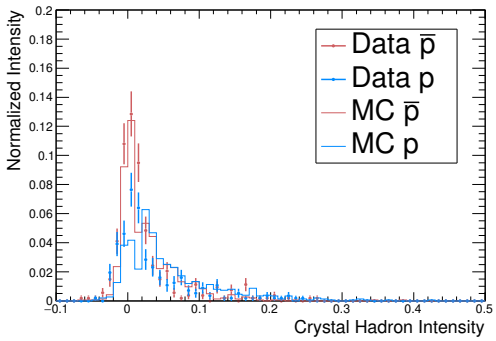

(b) $0.15 \leq E_{crystal} < 0.25$ GeV

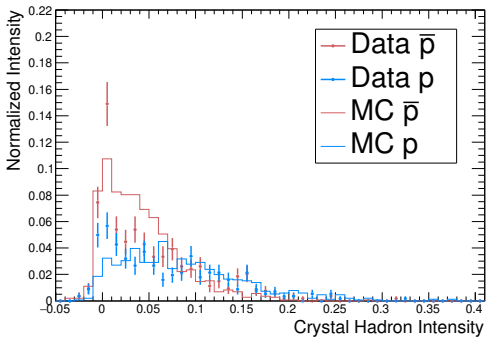

(c) $E_{crystal} \geq 0.25$ GeV

Figure 7.34: Hadron intensity histograms for crystals in *shower* clusters from protons with $p_{lab} > 2$ GeV/c.

7.6.2 $p_{lab} > 2$ GeV/c Proton Ionizing Clusters

Studying the clusters from $p_{lab} > 2$ GeV/c protons with cluster energy in the *ionization* cluster energy window of $0.15 < E_{ecl} < 0.25$ GeV, the distribution of the pulse shapes of the crystals in these clusters is shown in Figure 7.35. In this figure

the pulse shapes of the crystals in the $p_{\rm lab}>$ 2 GeV/c proton *ionization* clusters are observed to have very different characteristics compared to the *shower* proton clusters. The crystals in the *ionization* cluster have primarily photon-like pulse shapes demonstrating the proton ionization $d\mathrm{E}/dx$ in this momentum range is too low to produce hadron scintillation component emission. In general the pulse shapes in these cluster are found to be very similar to the high momentum muon cluster and pions and kaons *ionization* clusters studied in the above sections.

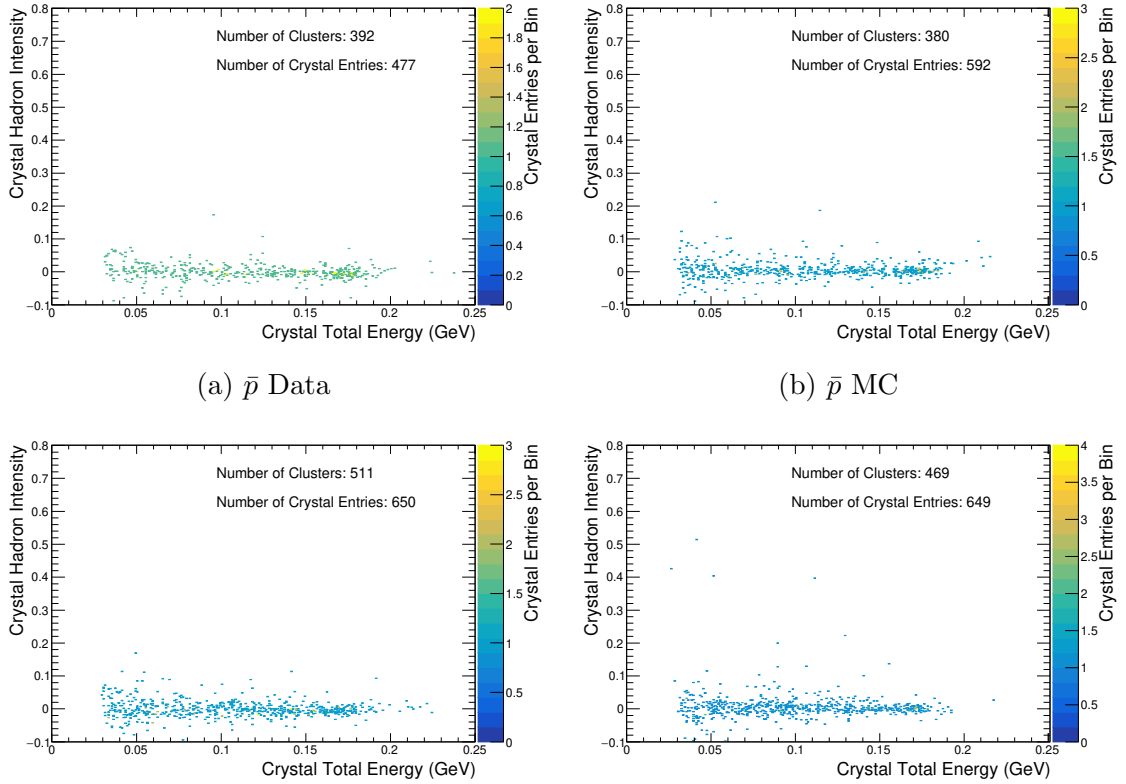

(a) $\bar{p}$ Data

(b) $\bar{p}$ MC

(c) p Data

(d) p MC

Figure 7.35: Crystal hadron intensity vs total crystal energy for crystals in clusters from protons with $p_{\rm lab}>$ 2 GeV/c and total cluster energy in the region of 0.15 $<\mathrm{E}_{\rm ecl}<$ 0.25 GeV.

7.6.3 $1 < p_{\rm lab} < 2$ GeV/c Momentum Protons

The corresponding decrease in kinetic energy from $p_{\rm lab}>$ 2 GeV/c to 1 $<p_{\rm lab}<$ 2 GeV/c has a significant impact on the interactions protons have in the calorimeter. This is demonstrated in Figure 7.36 showing the cluster energy distribution for the

selected protons in the $1 < p_{\text{lab}} < 2$ GeV/c momentum region. Compared to the clusters from protons with $p_{\text{lab}} > 2$ GeV, the clusters from $1 < p_{\text{lab}} < 2$ GeV/c protons are found to still have a distinct peak at 200 MeV however only the $\bar{p}$ clusters have a significant number of cluster with energy above 1 GeV.

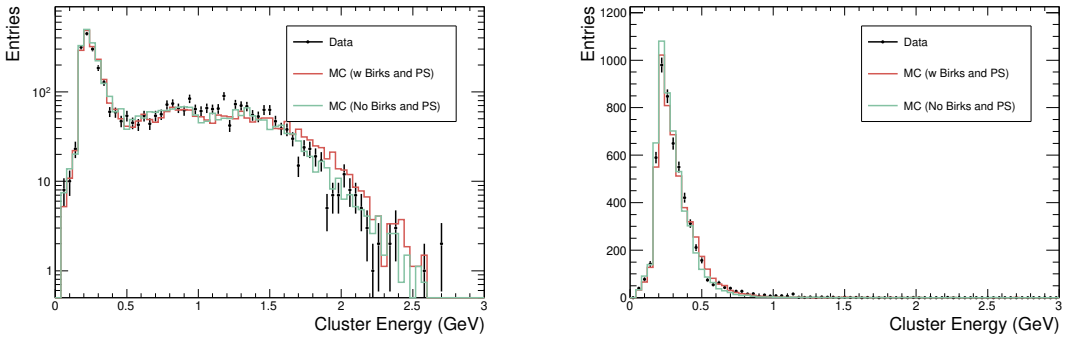

(a) $\bar{p}$ (b) p

Figure 7.36: Cluster energy distribution for protons with $1 < p_{\text{lab}} < 2$ GeV/c.

Comparing the data and MC distributions in Figure 7.36 there is reasonable agreement observed for both the p and $\bar{p}$ samples. In this proton momentum range it is observed that including the full CsI(Tl) scintillation response in simulation has a small impact in the MC modelling of the cluster energies. To gain more insight into the interactions occurring in these clusters the hadron intensity vs crystal energy for crystals in these clusters are shown in Figure 7.37. Note for Figure 7.37 a *ionization* cluster energy veto is not applied, thus all crystals in all proton clusters in this momentum region are shown.

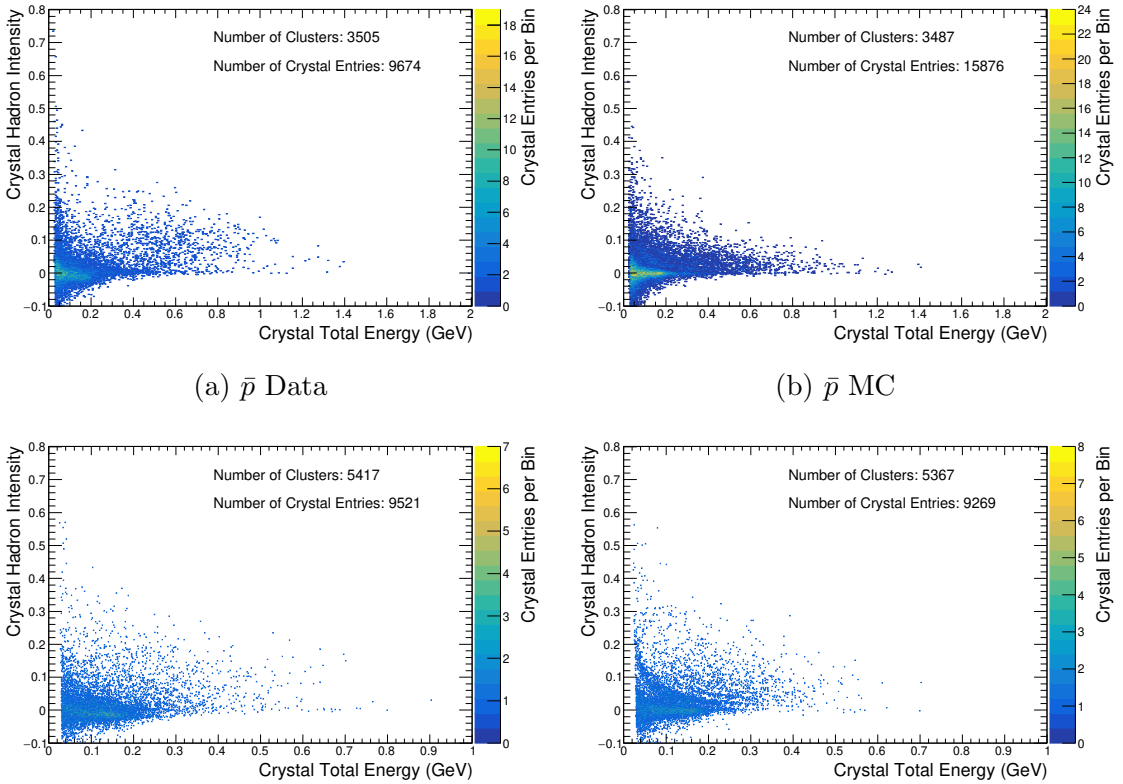

(a) $\bar{p}$ Data (b) $\bar{p}$ MC

(c) p Data (d) p MC

Figure 7.37: Crystal hadron intensity vs total crystal energy for crystals in clusters from protons with 1 $<p_{\text{lab}}<$ 2 GeV/c. Note $\bar{p}$ distribution extends to 2 GeV.

In the distributions shown in Figure 7.37 the p and $\bar{p}$ clusters have a significant number of photon-like crystals with energies up to 0.2 GeV. This is expected as no veto is applied to remove the *ionization* clusters in this sample and as a result many of these photon-like crystals are produced by the primary proton ionizing through the calorimeter and dividing the 0.2 GeV total cluster energy deposit across multiple crystals. For the p distributions, similar hadron pulse shape features are observed to be present in the data and MC with the multi-hadron pulse shapes spanning a similar crystal energy and hadron intensity range. For the $\bar{p}$ sample, the maximum hadron intensity values of the crystals with energy above 0.25 GeV are higher in the data compared to the MC. In addition from the crystal entry statistics in Figure 7.37, the $\bar{p}$ MC is found to have $\sim \times 1.6$ more crystal entries per cluster compared to the data.

A detailed comparison of the crystal hadron intensity distributions are shown in Figure 7.38 for the 1 $<p_{\text{lab}}<$ 2 GeV/c protons. In this figure the same trend that

was observed for the $p_{\rm lab}>$ 2 GeV/c proton sample is also found for the 1 $<p_{\rm lab}<$ 2 GeV/c protons where in the crystal energy ranges $0.05 < \mathrm{E_{crystal}} < 0.15$ GeV and $0.15 \leq \mathrm{E_{crystal}} < 0.25$ GeV, the $\bar{p}$ clusters have a larger number of photon-like crystals relative the p clusters. As mentioned this is expected as the $\bar{p}$ clusters will typically have multiple charged pions produced from the $\bar{p}$ annihilation. Comparing the p data and MC in the $0.05 < \mathrm{E_{crystal}} < 0.15$ GeV and $0.15 \leq \mathrm{E_{crystal}} < 0.25$ GeV crystal energy ranges, the distributions for the p data are observed to be shifted by 0.02 to negative hadron intensity values relative to the p MC. This systematic shift is due to a limitation of the pulse shape simulations as discussed in detail in Chapter 6 Section 6.8.1.

For the $\bar{p}$ sample, the data and MC distributions in Figure 7.38 for the $0.05 < \mathrm{E_{crystal}} < 0.15$ GeV and $0.15 \leq \mathrm{E_{crystal}} < 0.25$ GeV crystal energy ranges are found to have a similar fraction of crystals with hadron intensity above 0.05, however, for zero hadron intensity, the MC has an excess relative to the data. In the $\mathrm{E_{crystal}} \geq 0.25$ GeV crystal energy range, the maximum hadron intensity values of the crystals in the MC are observed to be lower than in the data. These two observations were also derived from the $\bar{p}$ distributions in Figure 7.37. It is challenging to identify the specific part of the $\bar{p}$ interaction that could produce these features in the MC. This is because the $\bar{p}$ hadronic shower modelling is sensitive to the modelling of the primary $\bar{p}$ interaction/annihilation and the modelling of the interactions of any secondary hadronic particles produced by the primary $\bar{p}$ interaction. The $\bar{p}$ results in Figures 7.37 and 7.38 however could suggest the MC modelling of the interactions in the $\bar{p}$ shower that produce the energy deposits result in the multi-hadron pulse shapes have an excess of secondary particles with low $d\mathrm{E}/dx$ produced. This could occur if the MC is overproducing secondary pions or photons with energy $<$ 0.05 GeV. This is because the additional energy from pion ionization or photon shower would increase the fraction of photon scintillation component emission in the crystals in the multi-hadron region and correspondingly cause these crystals to have smaller hadron intensity values in MC relative to the data.

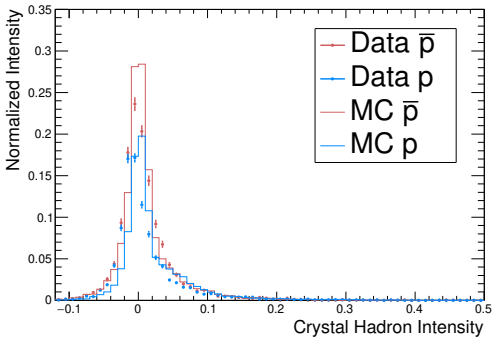

(a) $0.05 < \mathrm{E}_{\mathrm{crystal}} < 0.15$ GeV

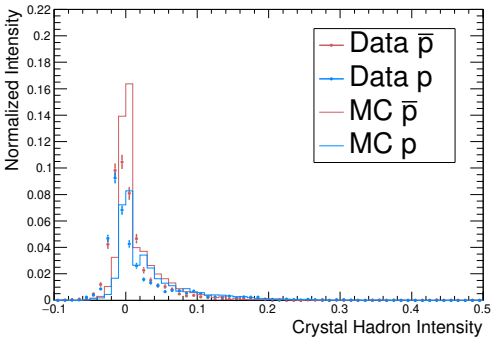

(b) $0.15 \leq \mathrm{E}_{\mathrm{crystal}} < 0.25$ GeV

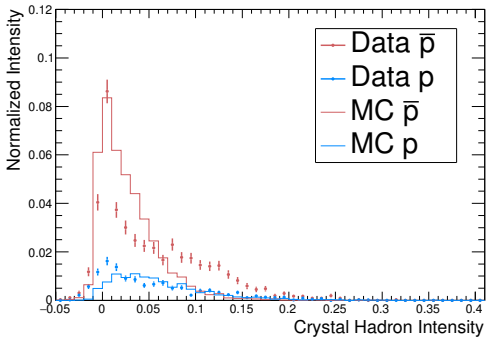

(c) $\mathrm{E}_{\mathrm{crystal}} \geq 0.25$ GeV

Figure 7.38: Hadron intensity histograms for selected protons with 1 $<p_{\mathrm{lab}}<$ 2 GeV/c.

7.6.4 $p_{\mathrm{lab}} < 1$ GeV/c Protons

As the proton momentum drops below 1 GeV/c the kinetic energy limit allowing the proton to ionize through the 30 cm thick CsI(Tl) calorimeter begins to be reached. For a p this means that if a hadronic scatter does not occur, the primary p will likely only ionize and eventually stop in the crystal after depositing its kinetic energy. This process produces significant amounts of hadron scintillation component emission do to the high $d\mathrm{E}/dx$ of the slow proton and results in a crystal energy deposit with hadron intensity in the region of the single proton band corresponding to the total ionization energy deposited by the p. This will be approximately equal to the kinetic energy of proton when it entered the crystal, due to the Birks scintillation efficiency. For $\bar{p}$'s however, the cross-section for $p\bar{p}$ annihilation increases as the proton momentum decreases [49, 52, 53] and when $p\bar{p}$ annihilation occurs, multiples of pions are typically emitted [49], forming an hadronic shower. The differences in the

calorimeter interactions that p and $\bar{p}$ in this momentum region undergo is seen in the cluster energy distributions shown in Figure 7.39. In this figure the p clusters show a sharp cut-off around 0.45 GeV. This is expected as the majority of p in this sample are ionizing and stopping in the calorimeter, depositing only their kinetic energy. The situation is very different for the $\bar{p}$ clusters where a significant fraction of the clusters have energies above the kinetic energy limit. This additional energy is from the $\bar{p}$ annihilation that occurs in the cluster.

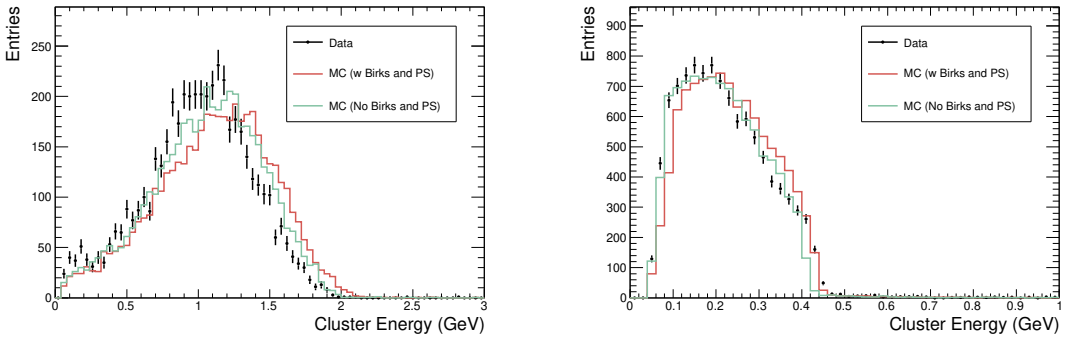

(a) $\bar{p}$ (b) p

Figure 7.39: Cluster energy distributions for selected protons with $p_{\text{lab}}<$ 1 GeV/c. Note Cluster Energy axis of distributions have different energy ranges.

Comparing the $\bar{p}$ data and MC in Figure 7.39 the data and MC distributions are observed to have similar shapes, however, the MC is found to extend to higher cluster energies relative to the data. This is found for both the MC with and without the full scintillation response included in the simulation. By including the full scintillation response however, the cluster energies extend to slightly higher values.

For the p distributions in Figure 7.39, the data and MC distributions have a similar shape however by including the full CsI(Tl) response to the simulation the p clusters with energy below 0.4 GeV extend to higher cluster energies in the MC relative to the data. Above 0.4 GeV however there is agreement between the data and MC when the full CsI(Tl) response in included. For the lower momentum p's, as the primary interaction is the p ionizing and stopping in the cluster, the cluster energy of for a p in this sample is determined by the kinetic energy of the p when it entered the calorimeter. Due to the higher ionization $d\text{E}/dx$ of the protons in this momentum region relative the the previous sections, the p cluster energies in the sample are highly sensitive to the material in the detector that is in front of the calorimeter, such as

the drift chamber wall and the TOP detector. If the detector geometry in simulation is missing material compared to the real detector then this would cause the trend that is observed in Figure 7.39 where at lower cluster energies the MC has higher cluster energies relative to the data. This is because the p clusters at lower energies in this sample correspond to the lower momentum p in the sample and the lower the proton momentum, the higher the ionization $d\mathrm{E}/dx$, and thus more sensitive the cluster energy is to the material modelling in the MC. The higher momentum p's in this sample, which correspond to the higher cluster energies, are less sensitive to the material modelling before the calorimeter because of their lower $d\mathrm{E}/dx$. For this reason only at the higher p cluster energies in Figure 7.39 there is agreement between the data and MC.

For the selected protons with $p_{\mathrm{lab}} <$ 1 GeV/c, the crystal hadron intensity vs crystal energy distributions are shown in Figure 7.40. From these distribution, the differences in the p and $\bar{p}$ calorimeter interactions are seen by the different types of pulse shapes present in the p vs $\bar{p}$ cluster crystals. In the $\bar{p}$ clusters, the crystals have pulse shape features that are similar to the higher momentum $\bar{p}$ hadronic shower clusters. This includes a large fraction of crystals with energy < 0.1 GeV and photon-like pulse shapes, expected from energy deposits by secondary pions ionizing and also a distribution of energetic crystals in the multi-hadron pulse shape region. In Figure 7.39 the same trends that were seen and discussed when studying the $1 < p_{\mathrm{lab}} < 2$ GeV/c sample, are also observed for the $p_{\mathrm{lab}} <$ 1 GeV/c $\bar{p}$ sample such that the maximum hadron intensity of the multi-hadron pulse shapes for the $\bar{p}$ cluster crystals is lower in the MC relative to the data. In addition the average number of crystals in the $\bar{p}$ clusters is found to now be $\sim \times 2.2$ higher in the MC relative to the data.

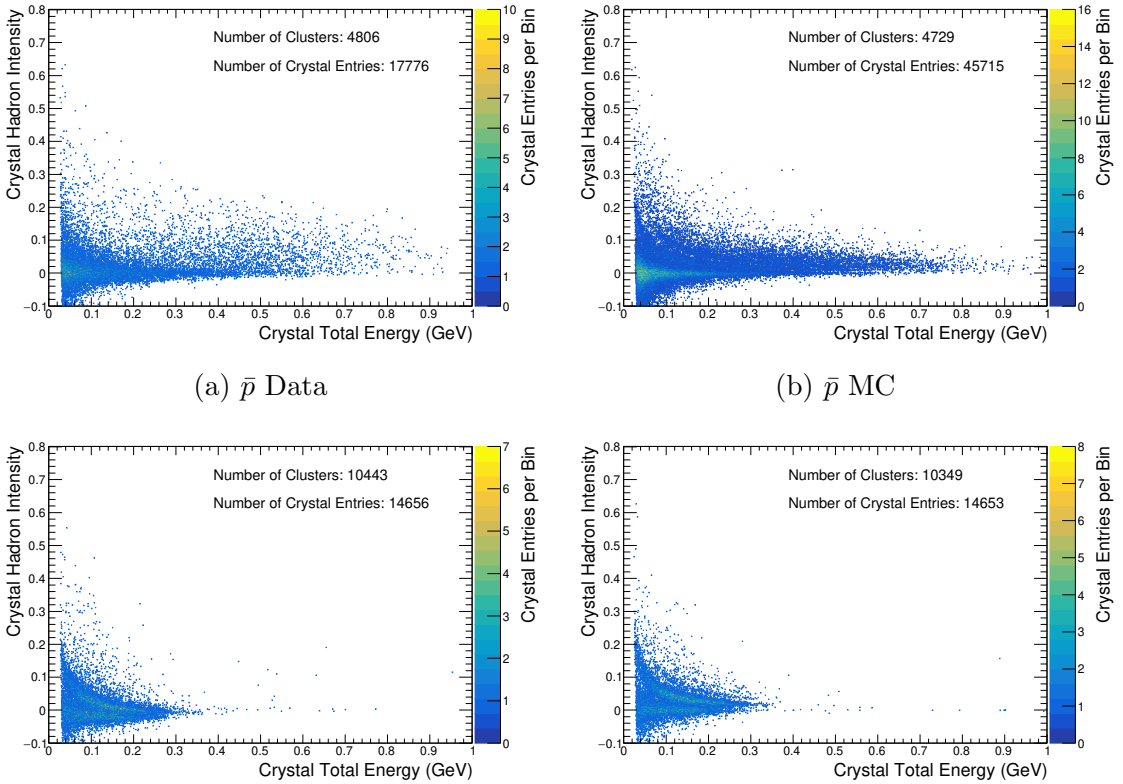

(a) $\bar{p}$ Data (b) $\bar{p}$ MC

(c) p Data (d) p MC

Figure 7.40: Crystal hadron intensity vs total crystal energy for crystals in clusters from selected protons with $p_{\rm lab} < 1$ GeV/c.

The crystals in the p clusters in Figure 7.40 show two prominent bands in the pulse shape distributions. These bands are from the primary proton ionizing in the cluster crystals. The band at higher hadron intensity values is the single proton band. As discussed, a crystal energy deposit will have an pulse shape with hadron intensity on this band if the proton stops in the crystal volume. Below this band at lower hadron intensity, a second pulse shape band is observed. This band is from the primary p initially ionizing through a crystal but not stopping in the crystal and thus not yet having a high enough dE/dx to generate hadron component scintillation emission.

In Figure 7.41 the hadron intensity histograms are shown for the $p_{\rm lab}<$ 1 GeV/c proton sample for different crystal energy regions. In this result the $\bar{p}$ distributions have the same trends that were discussed when studying the 1 $<p_{\rm lab}<$ 2 GeV/c $\bar{p}$ sample in the previous section. For the p sample both the data and MC in the $0.05 < {\rm E}_{\rm crystal} < 0.15$ GeV and $0.15 \leq {\rm E}_{\rm crystal} < 0.25$ GeV ranges show two peaks

corresponding to the two bands in Figure 7.40. In each energy range there agreement in the shape of the data and MC distributions however there is an offset that is observed such that the data distribution is offset by -0.02 relative to the MC. This offset was discussed in 6 Section 6.8.1 and is a limitation of the pulse shape simulations that derives from the observation in Figure 7.41 that the peak in the p data at lower hadron intensity in the $0.05 < \mathrm{E_{crystal}} < 0.15$ GeV and $0.15 \leq \mathrm{E_{crystal}} < 0.25$ GeV ranges has a mean of -0.02 as opposed to zero. At truth level the MC cannot produce a negative hadron intensity thus the MC model used to simulation the hadron component scintillation emission cannot reproduce the -0.02 offset in the data. With further improvements to the offline fitting template calibrations used to fit the waveforms in data, this small effect can be further investigated in future studies.

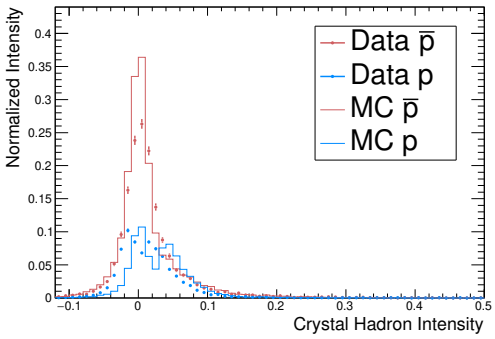

(a) $0.05 < \mathrm{E_{crystal}} < 0.15$ GeV

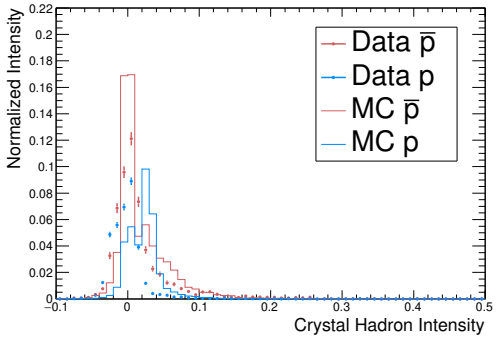

(b) $0.15 \leq \mathrm{E_{crystal}} < 0.25$ GeV

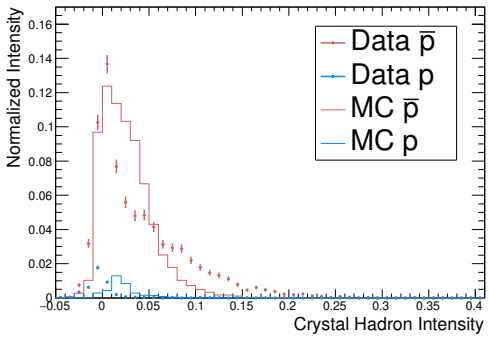

(c) $\mathrm{E_{crystal}} \geq 0.25$ GeV

Figure 7.41: Hadron intensity histograms for selected protons with $p_{\mathrm{lab}} < 1$ GeV/c.

7.7 Charged Particle Identification with PSD - Muon vs Pion Separation

In this section low momentum (p_{lab}< 1 GeV/c) muon vs pion separation through PSD is briefly studied. Demonstrated in Sections 7.3 and 7.4 where the crystal pulse shapes in clusters produced by muons and pions were studied, a muon or pion ionizing through the calorimeter has a low enough $d\text{E}/dx$ such that significant hadron scintillation component emission is not observed and thus the pulse shapes for energy deposits from ionizing muons and pions are photon-like. In pion hadronic showers however, secondary highly ionizing particles such as protons and alpha particles can produce significant amounts of hadron scintillation component emission resulting in these clusters to have crystals with hadron-like pulse shapes. The results presented in Sections 7.3 and 7.4 thus demonstrate clear potential to improve charged particle identification by using pulse shape discrimination.

To determine if a cluster is a hadronic shower or ionizing particle, the basic variable X_{Hadron} is used. X_{Hadron} is defined in equation 7.1 to be the weighted sum crystals in a cluster that have hadron intensity above a hadron intensity threshold. The hadron intensity threshold applied is a function of crystal energy in order to account for the crystal energy dependent hadron intensity resolution. A crystal above the hadron intensity threshold is referred to as a "Hadron Crystal" and is likely to be produced by energy deposits that contain highly ionizing particles such as protons and alpha particles. Ionizing muons or pions are expected to have clusters with X_{Hadron}< 0.5 and clusters from pion hadronic showers are expected to have X_{Hadron}> 0.5. Note because X_{Hadron} is a sum of weights, X_{Hadron} can have non-integer values.

$$X_{\text{Hadron}} = \sum_{i}^{\text{crystals in cluster}} \delta^{i}_{\text{Hadron}} \delta^{i}_{\chi^2} \tag{7.1}$$

where:

$$\delta^{i}_{\chi^2} = \begin{cases} 1, & \text{if } \chi^2 < 60 \\ 0, & \text{else} \end{cases}$$

$$\delta^{i}_{\text{Hadron}} = \begin{cases} W^{i}_{\text{crystal}}, & \text{if } E^{i}_{\text{Hadron}} > 3 \text{ MeV and } E^{i}{}_{\text{Total}} < 0.6 \text{ GeV} \\ W^{i}_{\text{crystal}}, & \text{if } E^{i}_{\text{Hadron}}/E^{i}_{\text{Total}} > 0.005 \text{ and } E^{i}_{\text{Total}} >= 0.6 \text{ GeV} \\ 0, & \text{else} \end{cases}$$

W^i_{crystal} = Weight of i^{th} crystal in cluster computed by calorimeter clustering algorithm to determine crystals relation to the cluster. Ranges from 0 to 1.
E^i_{Hadron} = Hadron component light output of i^{th} crystal in the cluster measured by multi-template offline fit.
E^i_{Total} = Total (photon component + hadron component) light output of i^{th} crystal in the cluster measured by multi-template offline fit.

7.7.1 Muon vs Pion: $0.5 \leq p_{\textbf{Lab}} < 1$ GeV/c

In Figure 7.42 the distributions of X_{Hadron} are shown for the selected muons and pions in the momentum range $0.5 \leq p_{\text{Lab}} < 1$ GeV/c. In each plot in this figure an additional sample for the pions with cluster energy in the range $0.15 < \text{E}_{\text{ecl}} < 0.25$ GeV is also shown. Discussed and shown in Section 7.4.3, although the *ionization* pion sample is dominated by pions ionizing through the calorimeter without a hadronic interaction occurring, there is a small sample of pions that did produced an hadronic shower present in the *ionization* pion sample. This is expected as the only requirement for an *ionization* cluster is for the cluster energy to be in the range $0.15 < \text{E}_{\text{ecl}} < 0.25$ GeV.

In Figure 7.42 the distributions from muons are observed to peak at $X_{\text{Hadron}} = 0$. This is expected given the studies shown in Section 7.3 as the pulse shapes of the crystals in the muon clusters were consistently observed to be photon-like and demonstrate that the muon ionization $d\text{E}/dx$ for this sample is not high enough to generate hadron scintillation component emission. For the pion distributions shown in Figure 7.42, it can be seen that there is discrimination achieved by using X_{Hadron}. Independent of charge, $\sim 50\%$ of the pions are observed to have $X_{\text{Hadron}} > 0.5$ whereas the muons only have $\sim 10\%$ of clusters with $X_{\text{Hadron}} > 0.5$. For the pion *ionization* clusters $\sim 25\%$ of the clusters have $X_{\text{Hadron}} > 0.5$ demonstrating with PSD the hadronic showers in this sample can be identified.

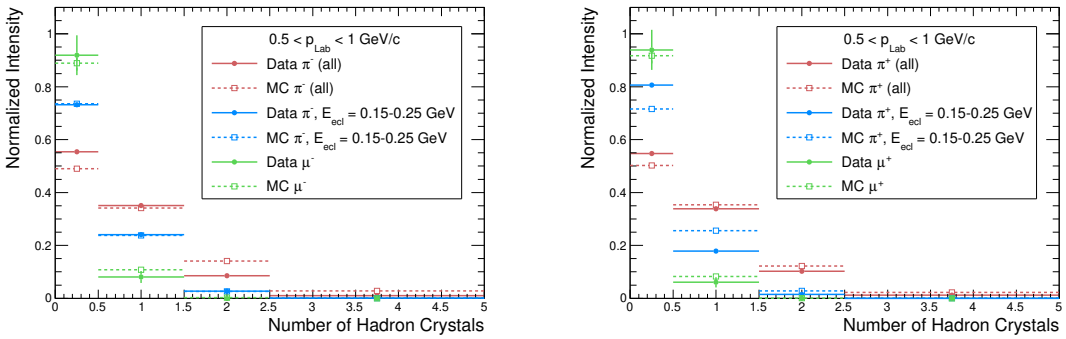

(a) (b)

Figure 7.42: X_{Hadron} distributions for pions and muons selected with $0.5 \leq p_{\text{Lab}} < 1$ GeV/c. a) Negative charge b) Positive charge. Errors are statistical only.

7.7.2 Muon vs Pion: $p_{\text{Lab}} < 0.5$ GeV/c

Figure 7.43 shows the X_{Hadron} distributions for the selected pions and muons with $p_{\text{Lab}} < 0.5$ GeV/c. The results shown in Figure 7.43 demonstrate that by applying PSD, discrimination can be achieved for muons vs pions with $p_{\text{Lab}} < 0.5$ GeV/c. Less than 10% of muons are observed to have $X_{\text{Hadron}} > 0.5$ whereas for the pions in data, 40% of the clusters have $X_{\text{Hadron}} > 0.5$. Comparing the pion data and MC in the plots in Figure 7.43 a larger fraction of pions have $X_{\text{Hadron}} > 0.5$ in the MC vs data. This difference in data and MC is consistent with the results in Section 7.4.4 where the pions in MC with $p_{\text{Lab}} < 0.5$ GeV/c were found to over-produce secondary protons relative to the data.

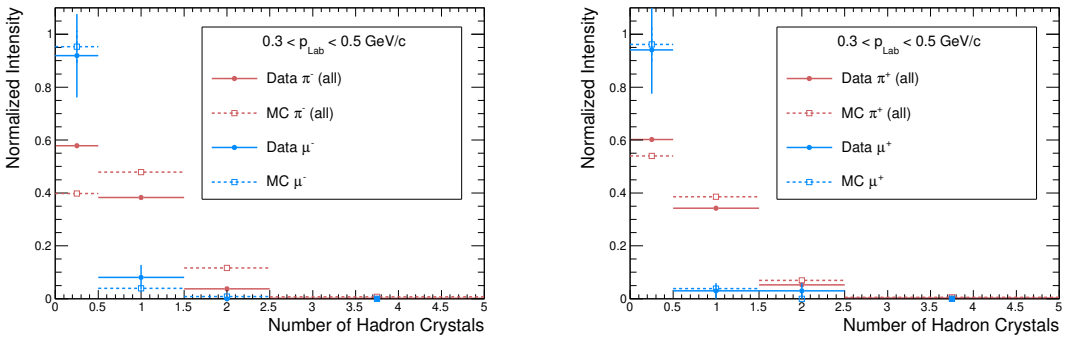

(a) (b)

Figure 7.43: X_{Hadron} distributions for pions and muons selected with $p_{\text{Lab}} < 0.5$ GeV/c. a) Negative charge b) Positive charge. Errors are statistical only.

7.8 Areas for Future Study

The results presented in this Chapter provide a first look at the types of CsI(Tl) pulse shapes produced in calorimeter clusters from the long-lived charged particles produced in SuperKEKB collisions. There are several areas of further study that can be pursued to improve the understanding of the interactions of these particles in the CsI(Tl) calorimeter. In particular, as a cluster will typically have several crystals, correlations in the types of pulse shapes produced in clusters can by studied and potentially be used to determined the inelastic interactions that occur in the specific cluster. This would answer questions such as: Does a cluster with a crystal on the single proton band always have a corresponding multi-hadron pulse shape? In addition studying the spatial locations of the different types of crystals in the cluster can potentially provide insights into the pulse shapes from the primary vs secondary scatters. By applying a machine learning approach utilizing the initial track momentum in addition to the crystal energies, pulse shapes and spatial coordinates relative to the track entrance it is likely that charge particle identification can be improved potentially allowing for improved electron/pion/kaon/proton identification. For example, at a given momentum particle A might be more likely to generate single protons or multi-hadron crystals or high energy photon crystals relative to particle B at the same momentum.

Another area of study that can be investigated is to see if split-off clusters from neutrons can be identified using the proximity of a cluster to crystals in the event with muti-hadron pulse shapes. As nuclear evaporation leads to high multiplicities of neutron emission [20], it might be beneficial to assign a split-off cluster likelihood based on the location of the multi-hadron pulse shape crystals in an event.

In this chapter detailed comparisons of GEANT4 hadronic simulation models were presented. Another interesting study could be to evaluate the impact of different GEANT4 physics lists, which can apply different hadronic interaction models [45], on the simulated pulse shape distributions.

7.9 Chapter Summary

This chapter studied the CsI(Tl) pulse shapes of crystals in calorimeter clusters produced by control samples of $e^{\pm}$, $\mu^{\pm}$, $\pi^{\pm}$, $K^{\pm}$ and $p/\bar{p}$ selected from Belle II Phase 2 data and Monte Carlo Simulations. This was the first time CsI(Tl) pulse shape

discrimination was applied in this energy regime to study the interactions of these particles in CsI(Tl). Crystals in $e^{\pm}$ and $\mu^{\pm}$ clusters were observed to have photon-like pulse shapes (hadron intensity of zero) independent of the crystal energy or the cluster energy, as expected. Crystals in ionizing clusters produced by $\pi^{\pm}$, $K^{\pm}$ and $p/\bar{p}$ were found to also have photon-like pulse shapes, as expected. Crystals in hadronic showers produced by $\pi^{\pm}$, $K^{\pm}$ and $p/\bar{p}$ were observed to have a variety of pulse shapes with hadron intensity values up to $\sim$ 0.6 and it was shown that from the pulse shape the types of secondary particles that deposited energy in the crystal could be identified. Detailed comparisons between data and MC were presented, evaluating the CsI(Tl) pulse shape simulation methods that were developed in Chapter 5 [25]. The pulse shape simulations were shown to reproduce the pulse shape features observed in the data such as the single proton band and multi-hadron pulse shapes. In addition GEANT4 hadronic interaction models were evaluated and with PSD potential sources of data vs. MC disagreement were identified. In particular for low momentum pions and kaons an over-abundance of crystals from energy deposits by highly ionizing secondary particles was observed in the simulation relative to the data suggesting the modelling of nuclear absorption can be improved. Low momentum muon vs. pion separation using pulse shape discrimination was also demonstrated.

Chapter 8

Neutral Particle Identification at Belle II with Pulse Shape Discrimination

The ability to distinguish calorimeter clusters initiated by K_L^0's vs photons with high efficiency and high purity is expected to have significant impact in improving a number of physics measurements planned to be conducted at Belle II as outlined initially in Chapter 2. This chapter studies the application of CsI(Tl) pulse shape discrimination for improving neutral particle identification at the Belle II experiment. Section 8.1 of this chapter details the training of a PSD-based multivariate classifier designed to classify calorimeter clusters as hadronic or electromagnetic showers using the pulse shape information provided by the CsI(Tl) cluster crystals that had a waveform saved offline during data taking. The remaining sections of this chapter apply the trained classifier to evaluate the photon, K_L^0 and π^0 identification performance that can be achieved. Section 8.2 evaluates the classifier performance using control samples of photons and K_L^0 selected from Belle II collision data. With these samples the K_L^0 identification efficiency and photon fake-rates of the classifier are measured and compared to existing methods for K_L^0 identification. In Section 8.3 the classifier is applied to improve π^0 identification and the photon-fake rate is independently measured with a $\pi^0 \to \gamma\gamma$ sample. In Section 8.4 "Areas of Future Study" are discussed and potential extensions to this work to further improve particle identification at Belle II through the use of PSD are outlined.

8.1 PSD-based Classifier for Hadronic vs Electromagnetic Shower Identification

A multivariate classifier is trained with the objective to classify neutral calorimeter clusters as electromagnetic or hadronic showers using the scintillation pulse shapes of the CsI(Tl) crystals in the cluster. Neutral clusters are calorimeter clusters that are not matched to a charged track and are typically produced by long-lived neutral particles such as photons, K_L^0's, neutrons or anti-neutrons. Photons incident on the calorimeter will interact by generating electromagnetic showers consisting only of secondary photons, electron and positrons. As a result, the crystals in photon clusters will consistently have photon-like scintillation pulse shapes. This is different from clusters produced by strongly interacting particles, such as K_L^0, as the hadronic showers produced by these particles will typically contain highly ionizing secondary particles, such as protons and alpha particles. The energy deposits by these secondary highly ionizing particles produces hadron scintillation component emission, resulting in crystals in the hadronic shower to have different scintillation pulse shapes than crystals in electromagnetic showers. The objective of the PSD-based classifier is to use the scintillation pulse shapes of cluster crystals to perform neutral particle identification. The classifier trained is a stochastic gradient boosted decision tree (BDT) [54]. This classifier was chosen as it was found to achieve good K_L^0 vs. photon separation performance while also having fast execution times for training and evaluation.

8.1.1 Classifier Inputs

A calorimeter cluster is a collection of calorimeter crystals that have been determined by the clustering algorithm to originate from the same primary particle. This grouping is determined by the spatial locations and energies of the crystals in the calorimeter. As a cluster typically consists of several crystals, a single cluster can have several waveforms recorded, one for each crystal with energy greater than 30 MeV. Each waveform provides information on the interactions that occur in the cluster. A function of the multivariate classifier is to condense the information of the numerous cluster crystals into a single cluster level quantity. To maximize the information available, the inputs to the classifier are crystal level quantities as opposed to higher level cluster variables. Only a subset of the crystals in a cluster are

used however, as not all crystals will have an waveform recorded, due to the 30 MeV crystal energy threshold for waveform readout that is applied online. In order for the crystal information to be used by the classifier, the crystal must satisfy the following criteria:

- Crystal has an offline waveform saved. This criteria restricts the input crystals to have an energy of > 30 MeV measured by the photon template fit done online in the FPGA fit.
- The offline multi-template waveform fit has to have $\chi^2 < 60$, for either the photon+hadron or photon+hadron+pile-up photon fit hypothesises.

The purpose of these criteria is to limit the input crystals to only the crystals where information on the CsI(Tl) scintillation emission shape is available. The classifier is limited to a maximum of 20 input crystals. This maximum is only rarely reached, even when a cluster has energy > 5 GeV. Each input crystal has eight crystal level quantities that are used to characterize the energy deposit. These eight quantities are listed below.

1. $\mathrm{R_{Crystal}}$: Distance from cluster centre to crystal centre.
2. $\cos(\theta_{\mathrm{Crystal}})$: Cosine of the polar angle between cluster centre to crystal centre.
3. $\cos(\phi_{\mathrm{Crystal}})$: Cosine of the azimuthal angle between cluster centre to crystal centre.
4. $\mathrm{W_{Crystal}}$: Crystal weight computed by clustering algorithm.
5. $\mathrm{E^{Crystal}_{FPGA}}$: Crystal energy computed by a photon template fit done online in FPGA.
6. $\mathrm{E^{Crystal}_{Two\ Component,\ Total}}$: Crystal energy computed by multi-template fit done offline during reconstruction.
7. $\mathrm{N_h^{Crystal}} = \mathrm{E^{Crystal}_{Two\ Component,\ Hadron}}/\mathrm{E^{Crystal}_{Two\ Componentm,\ Total}}$: Crystal hadron intensity computed by multi-template fit done offline during reconstruction.
8. $\mathrm{FT_{Crystal}}$: Crystal offline fit type (indicates if templates used the offline multi-template fit are: Photon+Hadron, Photon+Hadron+Pile-up Photon or Photon+Diode-Crossing).

The first three quantities define the spatial location of the crystal relative to the cluster centre. The variable W_{Crystal}, is computed by the cluster algorithm and on a scale of $0-1$ determines how related the crystal is to the cluster. $E_{\text{FPGA}}^{\text{Crystal}}$ is the energy of the crystal as determined by the photon template fit done online in the FPGA. The final three variables listed define the pulse shape of the scintillation emission produced by the crystal. Together $E_{\text{Two Component}}^{\text{Crystal}}$ and $N_{\text{h}}^{\text{Crystal}}$ define the pulse shape and FT_{Crystal} indicates if the fit is Photon+Hadron or Photon+Hadron+Pile-up Photon or Photon+Diode-Crossing (Note distributions of fit types is discussed in Chapter 6 Section 6.6.2).

8.1.2 Training Samples

The methodology behind the classifier is to identify hadronic vs electromagnetic showers, primarily using the pulse shape information provided by the inputs $E_{\text{Two Component}}^{\text{crystal}}$ and $N_{\text{h}}^{\text{crystal}}$. Demonstrated by the electron control samples studied in Chapter 7, the crystals in electromagnetic showers consistently have zero hadron scintillation component emission. This is because highly ionizing secondary particles are not generated in electromagnetic showers. This results in the limiting factor for the maximum hadron intensity values of crystals in a sample of electromagnetic showers to be the resolution of the hadron intensity, determined by the signal-to-noise level of the waveforms. Hadronic showers on the other hand frequently contain crystals with very significant hadron intensity values relative to the distribution of hadron intensity values produced in electromagnetic showers. This contrast in the pulse shapes present in hadronic vs electromagnetic showers is the primary information that the classifier should learn during training. It is thus important that the samples used to train the classifier have very high purities in terms of electromagnetic/hadronic interactions. To achieve this requirement the classifier is trained using MC samples because MC truth information can be used to enhance the purities of the training samples.

Training samples are generated using the particle-gun generator which allows events with a single primary, photon, K_L^0 or $\bar{n}$, to be generated originating from the interaction point. To ensure the waveform noise levels in the MC match the Phase 2 data conditions the pseudo-random beam background overlays are used to model the detector background conditions. Although the classifier is mainly intended for photon vs K_L^0 identification, $\bar{n}$ events are also used in the training as $\bar{n}$ can undergo annihilation leading to a sample of hadronic showers that extends to higher total

cluster energies. The particle-gun samples are generated with lab momentum, p_{GEN}, uniformly distributed in the ranges outlined in below. These momentum ranges are used as they represent the typical momentum range of these particles when produced in SuperKEKB collisions.

- Photons: $0.05 \leq p_{\mathrm{GEN}} \leq 5$ GeV/c
- K_L^0: $0.05 \leq p_{\mathrm{GEN}} \leq 3$ GeV/c
- $\bar{n}$: $0.05 \leq p_{\mathrm{GEN}} \leq 3$ GeV/c

From the particle-gun samples, all neutral clusters are selected with $\mathrm{E_{ecl}} > 0.05$ GeV and $0.55 < \theta^{ECL} < 2.2$ rad, restricting the cluster to the calorimeter barrel region.

Although the events are generated using the particle-gun, this pre-selection can still contain clusters from beam background. To remove these beam background clusters, MC truth information is used. In the photon sample, clusters are required to be MC truth matched to a photon. This requirement significantly increases the probability that the cluster was produced by the generated photon in the event and not a beam background cluster that could potentially be a hadronic shower from background neutrons. For the $K_L^0/\bar{n}$ samples, the MC matching sometimes will match to a secondary particle rather than the primary $K_L^0/\bar{n}$. As a result, the clusters in the K_L^0 and $\bar{n}$ samples are required to be truth matched to any particle that is not a photon, electron or muon. This requirement removes clusters from secondary photons/electrons and beam background clusters that will not match to any particles in MC.

By applying the above selections, idealized samples of electromagnetic and hadronic showers are produced for the classifier training. For the clusters in the respective training samples the distribution of the cluster energies and number of crystal inputs with waveforms that have $\chi^2 < 60$ are shown in Figure 8.1. These distributions provide a reference to the cluster energies and number of crystals present in the clusters with waveforms, for the samples used to train and test the classifier. Due to the truth matching requirements these are idealized samples where the selection was designed primarily for training the BDT. In Section 8.2 of this chapter, control samples of photons and K_L^0 are used to test the classifier.

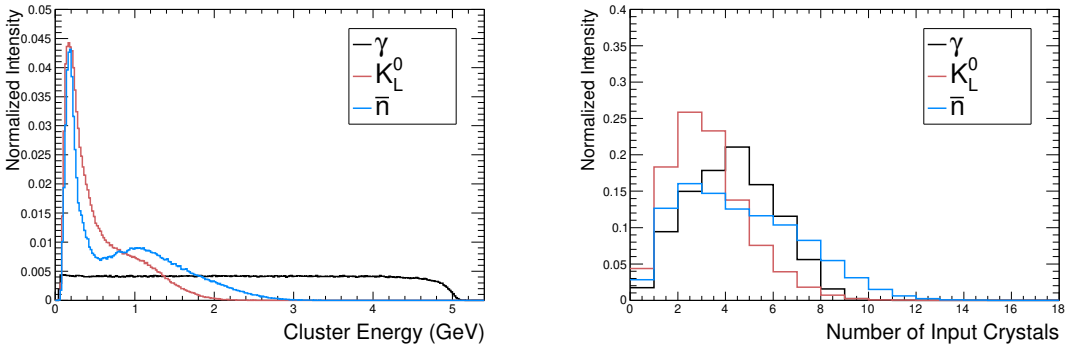

(a) (b)

Figure 8.1: Distributions of a)E_{ecl} b) Number of Input Crystals for particle gun MC samples used for classifier training and testing.

8.1.3 Training Results and Validation

To train the BDT 100 000 clusters from each of the photon, K_L^0 and $\bar{n}$ samples are used. Clusters from the photon sample are identified as the signal and the $K_L^0/\bar{n}$ clusters are identified as the background. This results in the expected BDT classifier output, Θ^{PSD}, to be Θ^{PSD}=1 for electromagnetic showers and Θ^{PSD}=0 for hadronic showers. The results of the training are shown in Figure 8.2 where Θ^{PSD}, computed using the trained BDT, is shown for clusters in the training and testing samples.

In Figure 8.2 agreement is observed between the distributions corresponding to the training and testing samples, verifying the classifier is not overtrained. From Figure 8.2 it is observed that the trained classifier is able to distinguish a significant fraction of the photon clusters from the K_L^0 and $\bar{n}$ clusters with a high degree of separation. This is evident from the distributions correctly peaking near Θ^{PSD}=0/1 for the respective samples of hadronic/electromagnetic showers, further demonstrating the classifier training was successful. As discussed, the single particle samples used for classifier training and testing were designed to provide the classifier with ideal samples of electromagnetic and hadronic showers. As a result, the detailed evaluation of the classifiers behaviour and performance will be done in the following sections of this chapter using control samples of photons and K_L^0's selected from Phase 2 data.

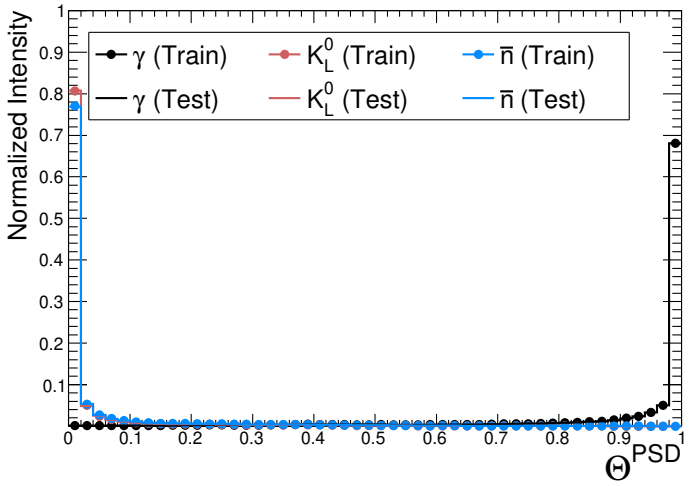

(a)

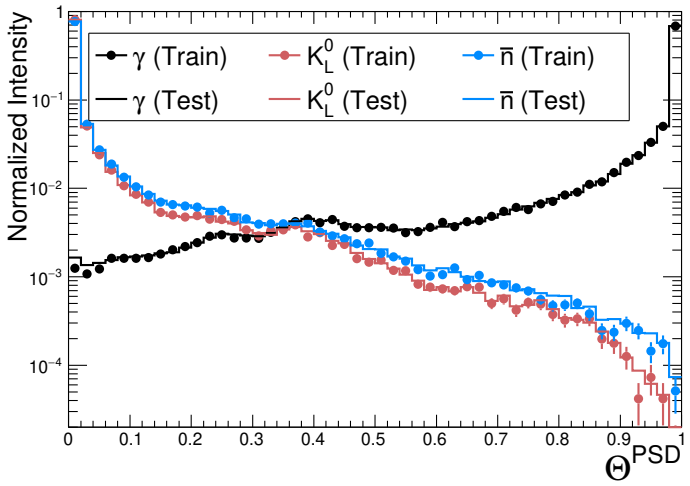

(b)

Figure 8.2: Distribution of trained classifier output, Θ^{PSD}, for photon, K_L^0 and $\bar{n}$ MC samples used for classifier training and testing. a) Linear scale. b) Log scale.

8.2 Kaon-Long vs Photon Identification with PSD

To evaluate the performance of the PSD classifier trained in the previous section, the following control samples are studied:

1. Photons in data and simulation selected from $e^+e^- \to \mu^+\mu^-(\gamma)$ events.

2. K_L^0 in data and simulation selected from $e^+e^- \to K_S^0 K_L^0 \gamma_{\rm ISR}$ events.

3. K_L^0 selected from B meson decay chains in $B^0\bar{B}^0$ simulation events.

4. K_L^0 selected from particle gun simulation events.

Sections 8.2.1 - 8.2.2 begin by studying the classifier response to each of these samples individually. In Section 8.2.4, the K_L^0 efficiencies and corresponding *photon as hadron* fake-rates for the classifier are presented and discussed.

8.2.1 Photons

A sample photons was isolated from Phase 2 data using the $e^+e^- \to \mu^+\mu^-(\gamma)$ selection detailed in Appendix A. Figure 8.3 shows the distribution of cluster energies for the selected photon sample, demonstrating this sample contains a range of photon energies extending from $0.05 - 7$ GeV.

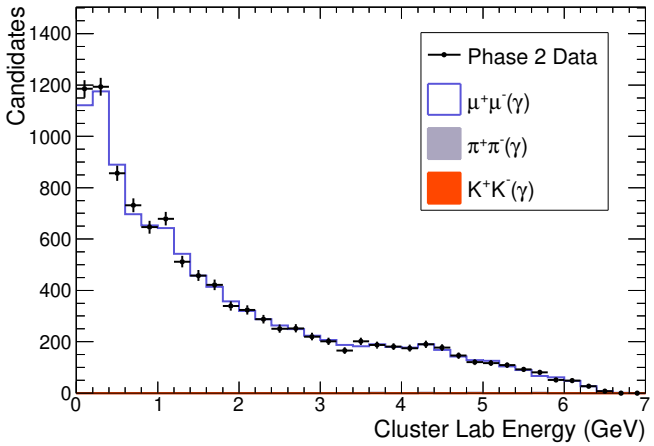

Figure 8.3: Cluster energy distribution of photons from $e^+e^- \to \mu^+\mu^-(\gamma)$ selection.

For this sample of photons the crystal energy vs crystal hadron intensity distribution is shown in Figure 8.4. In this figure the sample is divided into the photon momentum ranges of: $p_{\rm lab} > 1$ GeV/c, $0.5 < p_{\rm lab} \leq 1$ GeV/c and $p_{\rm lab} \leq 0.5$ GeV/c.

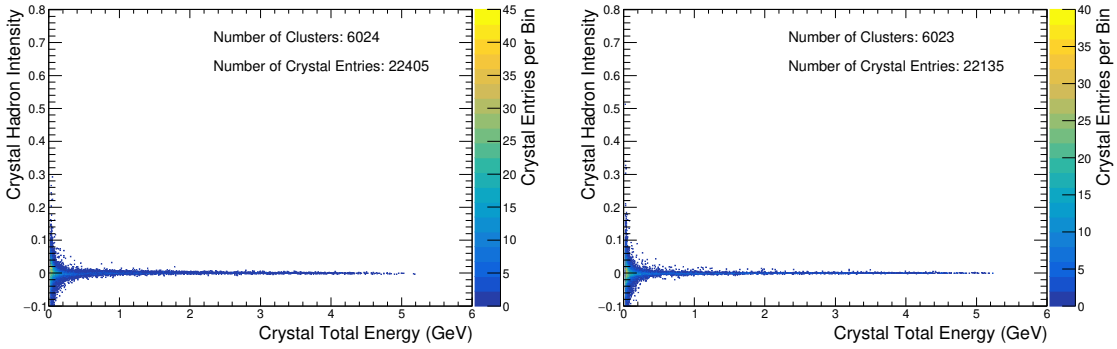

(a) Data

(b) MC

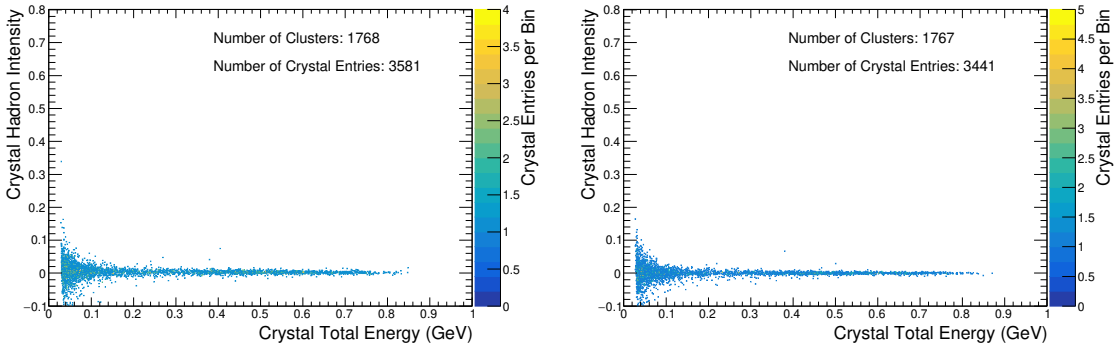

(c) Data

(d) MC

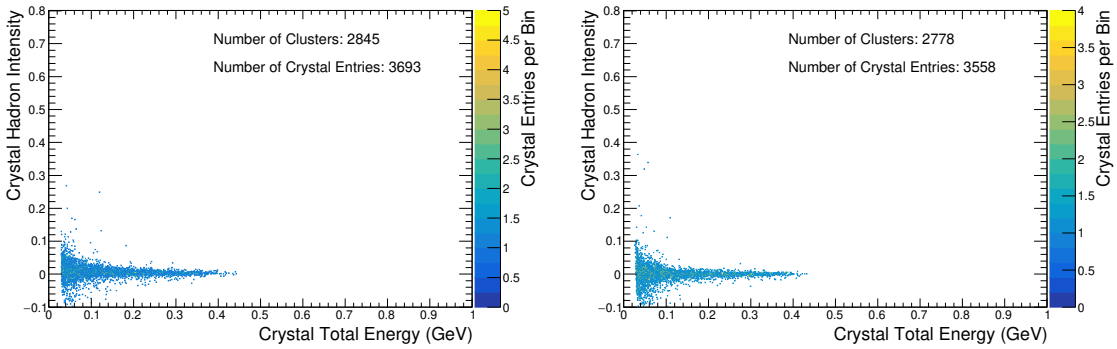

(e) Data

(f) MC

Figure 8.4: Crystal hadron intensity vs crystal energy distributions for crystals in photon clusters selected from $e^+e^- \rightarrow \mu^+\mu^-(\gamma)$. Figures a) and b) correspond to photons with $p_{\text{lab}} > 1.0$ GeV/c, b) and c) correspond to photons with $0.5 < p_{\text{lab}} \leq 1$ GeV/c ,and e) and f) correspond to photons with $p_{\text{lab}} \leq 0.5$ GeV/c.

The results in Figure 8.4 demonstrate that, independent of the cluster or crystal energy, the crystals in the selected photon cluster have hadron intensity values distributed near zero. This is consistent with the electron distributions studied in

Chapter 7 and is expected because highly ionizing secondary particles are not produced in electromagnetic showers. A detailed comparison of data and MC is presented in Figure 8.5 showing for all photons in the sample, histograms of the hadron intensity for different crystal energy ranges. In both data and MC these distributions are observed to peak at hadron intensity of zero. At crystal energies above 0.25 GeV, the hadron intensity resolution is shown to be sufficient such that crystals in the clusters from photons rarely will have hadron intensity above 0.02. Shown in the hadron control samples studied in Chapter 7 and in the K_L^0 samples studied later in this chapter, crystals in hadronic showers can frequently have crystals with energies above 0.25 GeV and hadron intensity values above 0.02.

Comparing the data and MC, small systematic shifts in the means are observed. Measurements of the mean and width of these distributions as a function of crystal energy were presented in Chapter 6 Section 6.7. Discussed in that section, the small difference in mean between data and MC are understood to be due to non-linearities in the electronics which are not modelled in the simulation. These systematic differences are small relative to the hadron intensity values of crystals from hadronic showers shown throughout Chapter 7 and in the K_L^0 sections of this chapter.

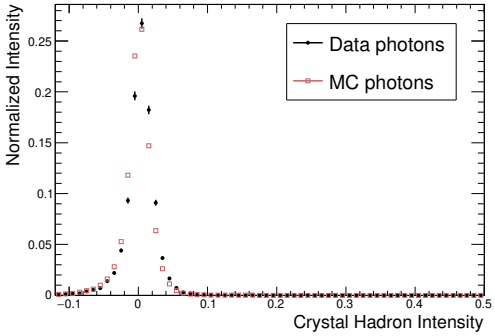

(a) $0.05 < \mathrm{E_{crystal}} < 0.15$ GeV

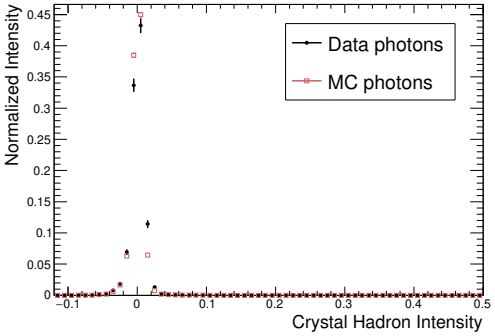

(b) $0.15 \leq \mathrm{E_{crystal}} < 0.25$ GeV

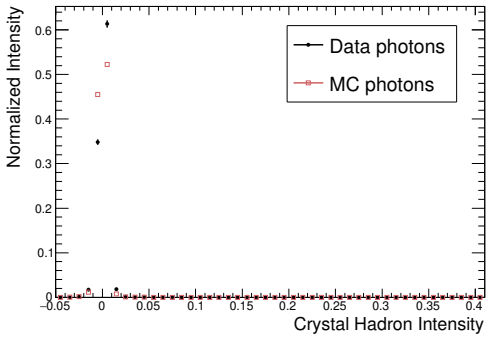

(c) $\mathrm{E_{crystal}} \geq 0.25$ GeV

Figure 8.5: Hadron intensity histograms for crystals in clusters from photons selected from $e^+e^- \to \mu^+\mu^-(\gamma)$.

For all photons in this sample, the distribution of the PSD classifier output, Θ^{PSD}, is shown in Figure 8.6. This figure includes several different views of the distribution to highlight different features. The first view in Figure 8.6a shows the full range of the distribution with a bin size of 0.02. From this view the classifier response to the photon sample is observed to peak near Θ^{PSD}=1, indicating that the classifier is correctly classifying a large fraction of the photons as electromagnetic-like showers. In Figure 8.6d a zoom in the region $\Theta^{\mathrm{PSD}} > 0.98$ is shown to further demonstrate that the distribution is highly peaking near Θ^{PSD}=1 and thus many of the photons are identified as electromagnetic showers with high likelihood. This behaviour is observed in the data and MC. Figure 8.6b shows the full range of the Θ^{PSD} distribution with a course binning allowing the tail of the distribution down to Θ^{PSD}=0 to be studied. With this binning it can be seen that over the full range the distribution, the classifier response is similar in the data and MC, with both distributions having

a small fraction of clusters extending down to Θ^{PSD}=0. In Figure 8.6c a zoom in the region $\Theta^{\mathrm{PSD}}<$ 0.02, is shown to demonstrate that for the photon sample there is no peaking in this region of the distribution. As will be shown in the following sections, K_L^0 clusters are observed to peak in the $\Theta^{\mathrm{PSD}}<$ 0.02 region similar to the photons peaking in the $\Theta^{\mathrm{PSD}}>$ 0.98 region.

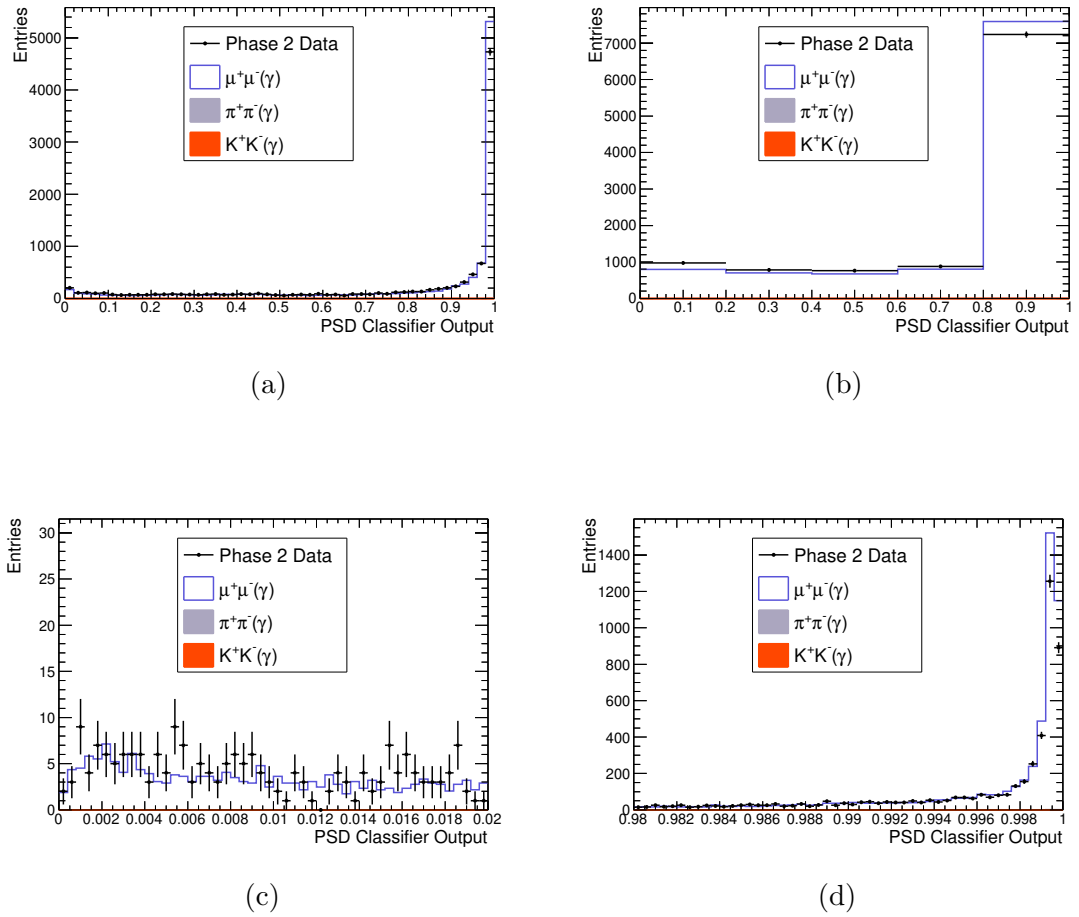

Figure 8.6: Response of the PSD classifier output to photons selected from $e^+e^- \rightarrow \mu^+\mu^-(\gamma)$. Several views of the distribution are shown: a) Full range. b) Full range with course binning. c) Zoom in region $\Theta^{\mathrm{PSD}}<$ 0.02. d) Zoom in region $\Theta^{\mathrm{PSD}}>$ 0.98.

Presented initially in Figure 8.3, the photon sample contains a range of cluster energies. To study the dependence of the classifier on photon energy, $\mathcal{E}_{\mathrm{Hadron}}$, defined in equation 8.1 as the fraction of clusters identified as hadronic showers for a $\Theta^{\mathrm{PSD}}_{\mathrm{cut}}$ threshold, is used.

$$\mathcal{E}_{\text{Hadron}}(\Theta^{\text{PSD}}_{\text{cut}}) = \frac{\sum_{i=0}^{n_{\text{candidates}}} H(\Theta^{\text{PSD}}_{\text{cut}} - \Theta^{\text{PSD}}_{i})}{n_{\text{candidates}}} \tag{8.1}$$

In equation 8.1, $H(x)$ is defined to be 0 if $x < 0$ and 1 if $x \geq 0$, $n_{\text{candidates}}$ is the total number of the candidates in the sample and $\Theta^{\text{PSD}}_{\text{cut}}$ is the classifier response threshold to determine if the classifier output is interpreted as a hadronic or electromagnetic shower.

When applied to a sample of photons, $\mathcal{E}_{\text{Hadron}}$ measures the *photon as hadron* fake-rate defined as the fraction of photon clusters mis-identified as hadronic showers. Note for the remainder of this chapter the *photon as hadron* fake-rate is referred to as the photon fake-rate. Conversely, $1-\mathcal{E}_{\text{Hadron}}$ is the photon identification efficiency, if the classifier were to be applied for photon identification. When applied to a photon sample, smaller values of $\mathcal{E}_{\text{Hadron}}$ indicate better classifier performance as the photon fake-rate of the hadron classifier is lower. Note to fully evaluate the classifier performance the photon fake-rate should be compared to the corresponding hadron identification efficiency. As measuring the hadron identification efficiency requires a sample of hadronic showers, a detailed discussion of the classifier K^0_L efficiency and corresponding photon fake-rate is presented later in this chapter in Section 8.2.4 after the K^0_L samples are discussed. In this section $\mathcal{E}_{\text{Hadron}}$ is used to study how the classifier response depends on the photon energy.

In Figure 8.7 $\mathcal{E}_{\text{Hadron}}$ is shown as a function of the photon momentum in the lab frame, for $\Theta^{\text{PSD}}_{\text{cut}}$ values of 0.02, 0.10 and 0.50. These thresholds are studied as they will be shown to cover a range of K^0_L efficiencies.

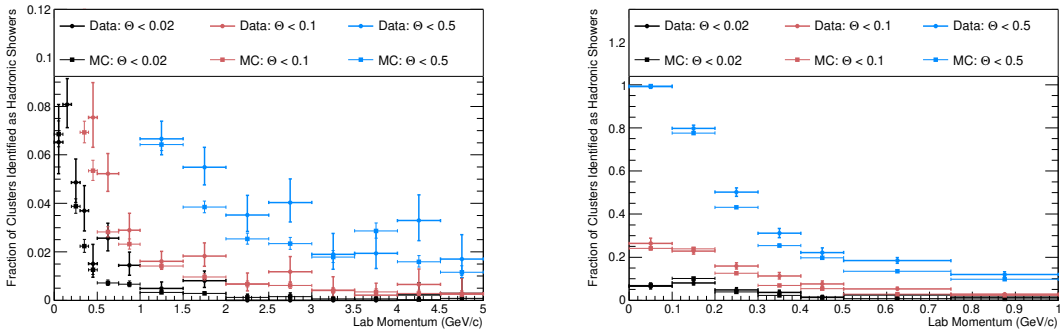

(a) (b)

Figure 8.7: $\mathcal{E}_{\text{Hadron}}$ as a function of the lab momentum for photons selected from $e^+e^- \to \mu^+\mu^-(\gamma)$, for data and simulation. a) Full momentum range b) Zoom in $p_{\text{lab}} < 1$ GeV/c region

From Figure 8.7 it is observed that in data and MC a lower Θ^{PSD} threshold produces a lower photon fake-rate. As shown by the zoom in Figure 8.7b, at photon energies below 1 GeV, an energy dependence in the classifier performance is observed to develop such that at a fixed $\Theta^{\text{PSD}}_{\text{cut}}$ threshold, the photon fake-rate increases as the cluster energy decreases. This is observed for each $\Theta^{\text{PSD}}_{\text{cut}}$ studied and is present in the data and MC. The photon energy dependence is most prominent for the $\Theta^{\text{PSD}}_{\text{cut}}$=0.10 and 0.50 thresholds and not as large for the $\Theta^{\text{PSD}}_{\text{cut}}$=0.02 threshold. This demonstrates that for photons below 0.5 GeV, the classifier begins to be limited in its ability to definitively classify some of the photons as electromagnetic showers. This behaviour is caused by a combination of factors that relate to the fact that as the photon energy decreases, the average energy of the crystals in the cluster decreases. Lower average crystal energies result in less crystals in the cluster that pass the 30 MeV online threshold required to save the CsI(Tl) waveform during data taking. Due to this practical limitation, lower energy photons at Belle II will have less PSD information available. An additional factor is that as the crystal energy decreases, the resolution of the hadron intensity also degrades due to the signal to noise level of the waveforms decreasing. This was demonstrated in Chapter 6 Section 6.7 where the crystal hadron intensity resolution was measured as a function of crystal energy. That result showed that above crystal energies of 1 GeV the crystal hadron intensity resolution is slowly changing. However as the crystal energy drops below 1 GeV the resolution of the hadron intensity degrades, increasing the difficultly to definitively classify an energy deposit as hadronic or electromagnetic.

To demonstrate the impact of these factors, the crystal hadron intensity vs crystal energy distributions for samples of photons corresponding to different Θ^{PSD} regions are shown in Figure 8.8. Note although the distributions in Figure 8.8 only show the classifier input information related to the photon+hadron fits, this information is expected to be driving the classifier performance. Surveying the distributions in Figure 8.8, it is seen that independent of the Θ^{PSD} value, the majority of the crystals in the photon sample have hadron intensity values near zero and thus have photon-like pulse shapes, as expected for electromagnetic showers. A primary difference that is observed between these distributions is the maximum energy of the crystals in the distributions. Almost all of the photon clusters with a crystal above 1 GeV have $\Theta^{\mathrm{PSD}} > 0.9$. For photon clusters in the regions $0.2 < \Theta^{\mathrm{PSD}} < 0.9$, $0.02 < \Theta^{\mathrm{PSD}} < 0.2$ and $\Theta^{\mathrm{PSD}} < 0.02$, although the pulse shapes of the energy deposits in the crystals are still primarily photon-like, the trend is observed that the maximum crystal energies in the photon clusters are lower for lower values of Θ^{PSD}. This can be explained by the decrease in hadron intensity resolution that begins to occur at crystal energies below 1 GeV. The entries statistics in Figure 8.8 also demonstrate a trend that photons with higher Θ^{PSD} values also have, on average, more crystal inputs to the classifier. Recall only crystals with energy greater than 30 MeV and an offline waveform fit with good χ^2 are used as classifier inputs. The photon clusters with $\Theta^{\mathrm{PSD}} > 0.9$ are observed to have an average 3-4 crystal inputs. This average is observed to decrease for the photon clusters with lower Θ^{PSD}. This is expected as the lower energy photons have less energy deposited in the calorimeter resulting in less crystals that reach the 30 MeV threshold to have an the CsI(Tl) waveform saved. In particular for photons with $\Theta^{\mathrm{PSD}} < 0.02$, it is observed that on average many of the clusters only have one input crystal with a photon+hadron fit and the energy of the crystal is below 0.5 GeV. This very limited input information restricts the classifier performance for these photons and demonstrates that a primary limitation for the classifier performance for photons is the number of input crystals and the energy of the input crystals. A secondary factor in the photon performance that can cause photons to produce a cluster in the $\Theta^{\mathrm{PSD}} < 0.02$ region is from photonuclear interaction which can produce secondary protons. The cross section for this interaction however is small [21] and thus to study this background in detail a higher statistics sample of photons is required.

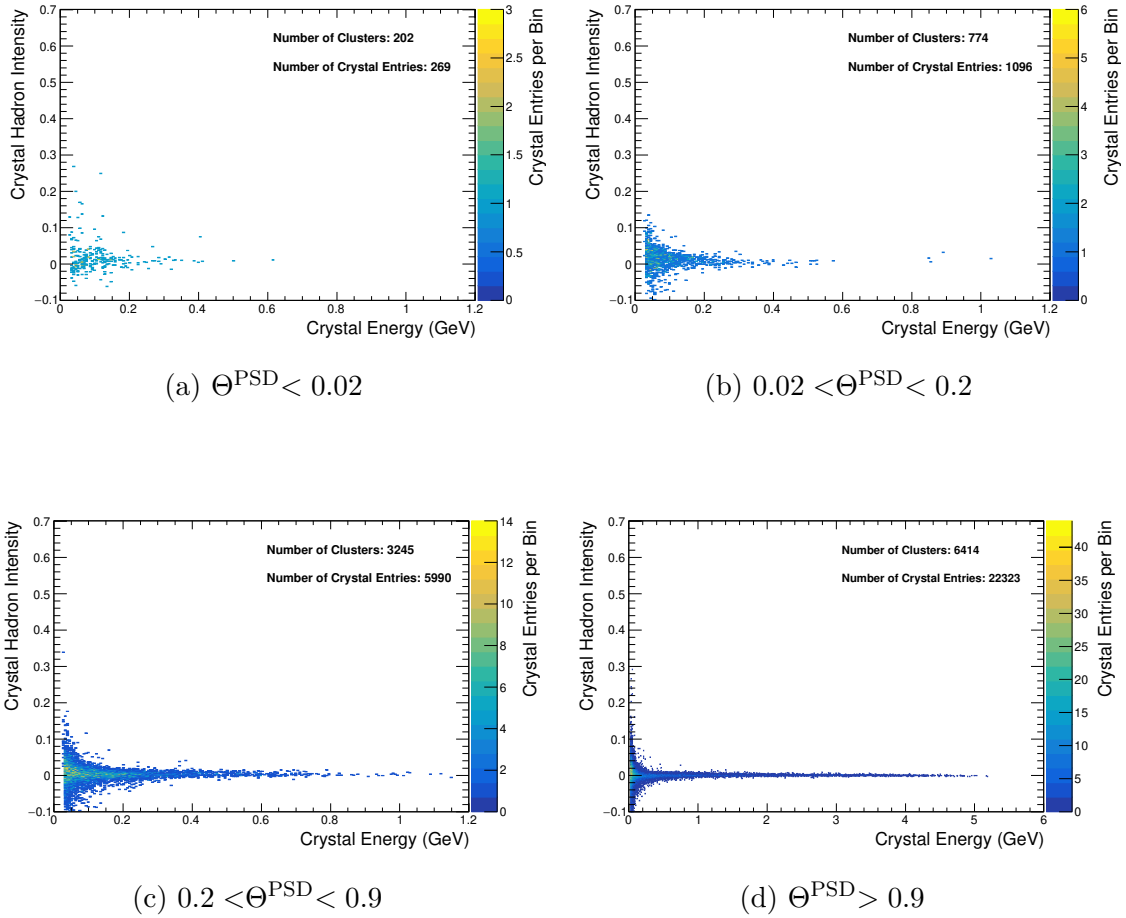

(a) $\Theta^{\mathrm{PSD}} < 0.02$

(b) $0.02 < \Theta^{\mathrm{PSD}} < 0.2$

(c) $0.2 < \Theta^{\mathrm{PSD}} < 0.9$

(d) $\Theta^{\mathrm{PSD}} > 0.9$

Figure 8.8: Crystal hadron intensity vs crystal energy distribution for crystals in photon clusters from data with different PSD classifier response (Θ^{PSD}).

8.2.2 K_L^0 from $e^+e^- \to K_S^0 K_L^0 \gamma_{\mathrm{ISR}}$

A sample of K_L^0 was isolated from the Belle II Phase 2 dataset using $e^+e^- \to K_S^0 K_L^0 \gamma_{\mathrm{ISR}}$ events by applying the selection criteria detailed in Appendix B. For this K_L^0 sample, the magnitude of the K_L^0 momentum in the lab frame, $p_{\mathrm{KL}}^{\mathrm{calc}}$, was computed by applying energy conservation, assuming the interaction proceeded as $e^+e^- \to K_S^0 K_L^0 \gamma_{\mathrm{ISR}}$. In Figure 8.9 the distribution of $p_{\mathrm{KL}}^{\mathrm{calc}}$ and $\mathrm{E_{ecl}}$ are shown for the selected K_L^0 candidates.

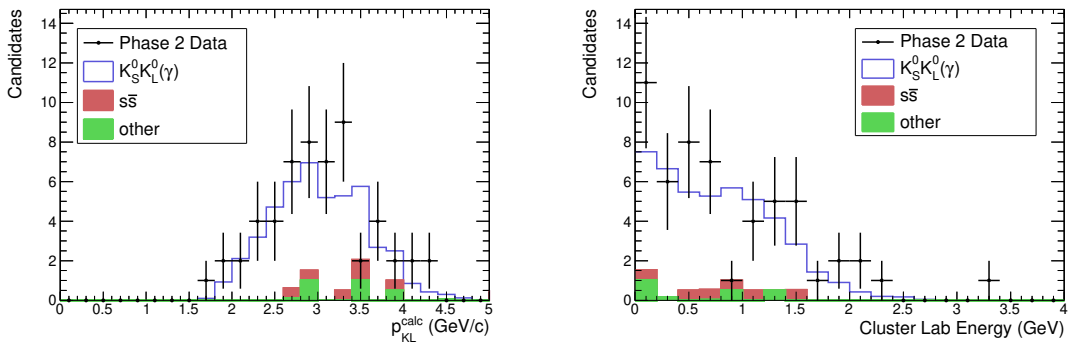

(a) (b)

Figure 8.9: Distributions of a) $p_{\mathrm{KL}}^{\mathrm{calc}}$ and b) $\mathrm{E_{ecl}}$ for K_L^0 candidates selected from $e^+e^- \to \phi\gamma_{\mathrm{ISR}} \to K_S^0K_L^0\gamma_{\mathrm{ISR}}$ events.

As can be seen in Figure 8.9, the K_L^0 candidates in this sample have momenta ranging from 1.5-5 GeV/c. For these K_L^0 candidates the distribution of the cluster energies is also shown in Figure 8.9 and observed to primarily be below 1.5 GeV. The lower cluster energies relative to the K_L^0 total energy are expected due to the energy losses in hadronic interactions and energy leakage due to the long nuclear interaction length relative to the depth of the calorimeter.

For the K_L^0 candidates in this sample, the PSD classifier response is shown in Figure 8.10. In this figure multiple views of the distribution are presented in order to study the various features of the distribution. Figure 8.10 presents one of the main results of this dissertation as it is observed that in the data and MC the PSD classifier response to the K_L^0 sample peaks near Θ^{PSD}=0, indicating a large fraction of the K_L^0 are correctly identified as hadronic showers using PSD. In addition, the zoom shown in Figure 8.10c in the region $\Theta^{\mathrm{PSD}} < 0.02$ demonstrates that several of the K_L^0, in data and MC, are classified as hadronic showers with high probability. This is a distinct difference from the classifier response to photons studied in the previous section and shown previously in Figure 8.6 where the response was observed to peak near Θ^{PSD}=1.0 and not peak in the region $\Theta^{\mathrm{PSD}} < 0.02$.

In Figure 8.10b the classifier response for the K_L^0 selected from $K_S^0K_L^0\gamma_{\mathrm{ISR}}$ is shown with a course binning to accommodate the low statistics in the data sample and demonstrate that across the classifier output range, the response in the data and MC are similar. In this figure it is also observed that in the highest bin, near Θ^{PSD}=1.0, the MC predicts that the data is dominated by background from $s\bar{s}$. By investigating the MC information of these events it was verified that the K_L^0 candidates from $s\bar{s}$

background in the region $\Theta^{\mathrm{PSD}} > 0.8$ are actually photons from π^0 or η decays. These $s\bar{s}$ events have the form such as $e^+e^- \to K^0\bar{K}^0\pi^0(\gamma)$ or $K^0\bar{K}^0\eta\ (\gamma)$ where, the $K^0_S \to \pi^+\pi^-$ and the radiated photon in the event satisfy the selection requirements applied for the $e^+e^- \to K^0_S K^0_L \gamma_{\mathrm{ISR}}$ sample. As the π^0 or η in the event decay to multiple photons, if the calorimeter cluster location of one of the photons is consistent with the expected location of a K^0_L from $e^+e^- \to K^0_S K^0_L \gamma_{\mathrm{ISR}}$, then the photon will be mis-identified as a K^0_L by the selection. Although the kinematic selection requirements were unable to reject these background events, as observed in Figure 8.10b, the PSD classifier is able to distinguish the photons and true K^0_L candidates with a high degree of separation. This is demonstrated by the significant peak in the data and MC for classifier response of $\Theta^{\mathrm{PSD}} < 0.02$.

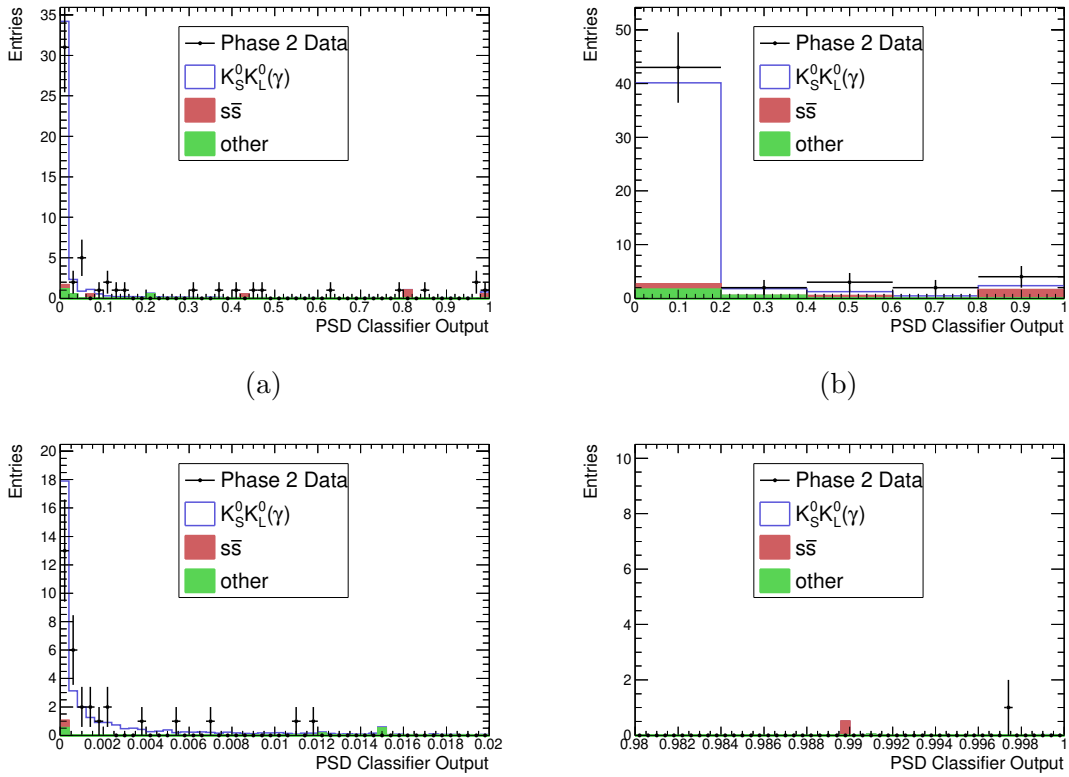

Figure 8.10: Θ^{PSD} distribution for K^0_L candidates selected from $e^+e^- \to K^0_S K^0_L \gamma_{\mathrm{ISR}}$. Several views of the distribution are shown: a) Full range. b) Full range with course binning. c) Zoom in region $\Theta^{\mathrm{PSD}} < 0.02$. d) Zoom in region $\Theta^{\mathrm{PSD}} > 0.98$.

In Figure 8.10 there is also a background remaining in the $\Theta^{\mathrm{PSD}} < 0.02$ region.

The primary source of this background is from $u\bar{u}$ and $d\bar{d}$ events where a K^0_S and K^* was produced and the K^* decay includes a true K^0_L. Thus, although this background is not from the signal process, $e^+e^- \to K^0_S K^0_L \gamma_{\rm ISR}$, these candidates are predicted by the MC to be true K^0_L's.

To proceed with studies of the K^0_L sample, a cut is applied requiring $\Theta^{\rm PSD} < 0.80$ in order to remove the fake K^0_L candidates from photons in the $s\bar{s}$ background. By applying this cut, it is assumed that a negligible fraction of true K^0_L candidates in the $e^+e^- \to K^0_S K^0_L \gamma_{\rm ISR}$ selection produce a cluster with $\Theta^{\rm PSD} > 0.80$. In Section 8.2.4 the approximation is validated by showing that this cut has a $\sim 3\%$ level impact on the K^0_L identification efficiency when compared to an independent K^0_L control sample that does no have this cut applied. This cut allows the accuracy of the K^0_L identification efficiencies to be improved as the known photon background is removed.

With this sample of K^0_L from data it is interesting to study the types of crystal pulse shapes present in the sample. In Figure 8.11 the crystal hadron intensity vs crystal energy distribution for the crystals in the clusters from the K^0_L sample are shown. In this figure the MC distribution corresponds to a high statistics sample of $e^+e^- \to K^0_S K^0_L \gamma_{\rm ISR}$ MC in order to allow the predicted pulse shape distribution features to be observed.

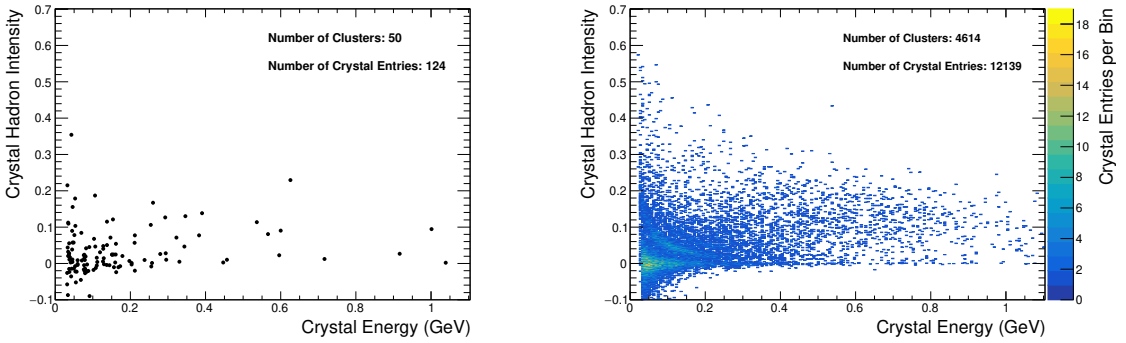

(a) Data

(b) $e^+e^- \to K^0_S K^0_L \gamma_{\rm ISR}$ MC

Figure 8.11: Crystal hadron intensity vs crystal energy distributions for crystals in K^0_L clusters with $\Theta^{\rm PSD} < 0.8$ from $e^+e^- \to K^0_S K^0_L \gamma_{\rm ISR}$ selection.

In Figure 8.11, the pulse shapes of the crystals in the low statistics data sample are observed to follow similar trends to the higher statistics MC distribution that is also shown. Despite the low statistics in the data sample, several crystals are observed to have total crystal energy above 0.1 GeV and crystal hadron intensity above 0.02,

indicating significant amounts of hadron scintillation component emission. Shown previously in Figure 8.5 crystals in clusters produced by photons rarely have energies above 0.25 GeV and hadron intensity above 0.02. Discussed throughout Chapter 7, when the crystal hadron intensity vs crystal energy distributions produced by charged hadron samples were studied, crystals with high energy and high hadron intensity crystals are produced when an nucleus in the CsI(Tl) is excited by an nuclear interaction and then de-excites. The nuclear de-excitation emits numerous low energy charged hadrons [20] that ionize and deposit a significant amount of energy in the crystal at a high ionization $d\mathrm{E}/dx$, leading to hadron scintillation component emission.

For a detailed comparison of the pulse shape of the crystals in these clusters, histograms of the crystal hadron intensity are shown in Figure 8.12 for the crystal energy ranges of $0.05 < \mathrm{E_{crystal}} < 0.15$ GeV, $0.15 \leq \mathrm{E_{crystal}} < 0.25$ GeV and $\mathrm{E_{crystal}} \geq 0.25$ GeV. This result further demonstrates that the pulse shapes observed in the K_L^0 clusters in data follow a similar distribution to the higher statistics MC sample. In the crystal energy ranges of $0.05 < \mathrm{E_{crystal}} < 0.15$ GeV and $0.15 \leq \mathrm{E_{crystal}} < 0.25$ GeV the distributions have a peak at hadron intensity values near zero, in addition to a large fraction of crystals with hadron intensity above 0.05. The crystals in the peak at hadron intensity of zero are consistent with energy deposits from energetic charged pions, produced as secondary particles in the K_L^0 hadronic shower that then ionizing through the cluster. The crystals in these energy ranges and with larger hadron intensity are consistent with energy deposits from multiples of protons stopping in the crystal volume. These secondary protons and pions are expected to arise from K_L^0 interactions that produce a hyperon such as, $K_L^0 p \rightarrow \pi^+ \Lambda$ [10], as the hyperon will typically decay in the cluster to pions and protons. In the crystal energy range $\mathrm{E_{crystal}} \geq 0.25$ GeV, the majority of the crystals in the K_L^0 clusters have hadron intensity values much larger than 0.02, and thus can readily be classified as a hadron energy deposit. Comparing the data and the MC, both distributions are observed to cover a similar hadron intensity range, providing further validation of the CsI(Tl) scintillation response simulation techniques that were developed in Chapter 5 [25].

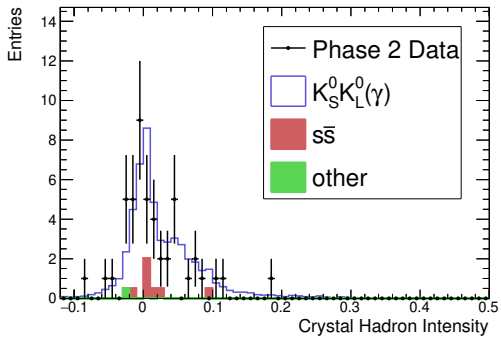

(a) $0.05 < \mathrm{E_{crystal}} < 0.15$ GeV

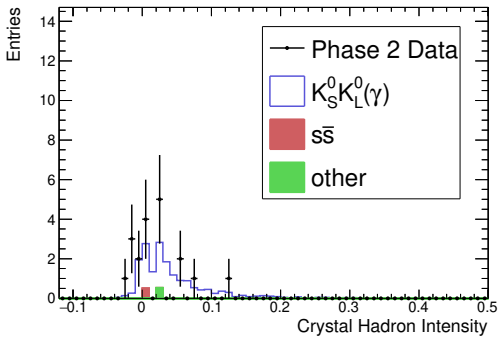

(b) $0.15 \leq \mathrm{E_{crystal}} < 0.25$ GeV

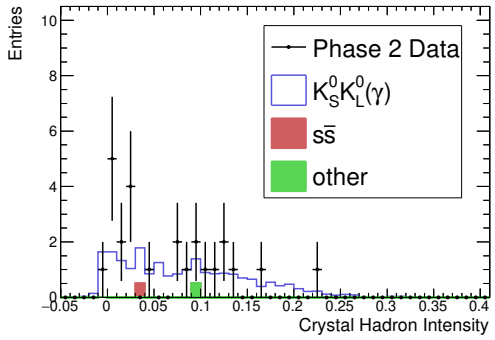

(c) $\mathrm{E_{crystal}} \geq 0.25$ GeV

Figure 8.12: Hadron intensity histograms for crystals in clusters from K^0_L clusters with $\Theta^{\mathrm{PSD}} < 0.8$ from $e^+e^- \to K^0_S K^0_L \gamma_{\mathrm{ISR}}$ selection.

8.2.3 K^0_L from $B^0\bar{B}^0$ MC

The selection criteria for this K^0_L sample is outlined in Appendix C. This selection used MC generator level information to verify the event included a K^0_L produced in an decay chain that was initiated by one of the generated B mesons in the event. The calorimeter cluster was then matched to the generated K^0_L by ensuring the cluster location was in the direction of the K^0_L generated momentum.

For the selected K^0_L in this sample, the distribution of p_{GEN} is shown in Figure 8.13. Seen from this distribution, the K^0_L produced in the neutral B meson decay chains typically have momentum below 1 GeV/c. Many of these K^0_L are produced from various decay chains involving D meson decays etc and only a small sample of these K^0_L candidates are from the process $B \to J/\phi K^0_L$. In Figure 8.13 the K^0_L candidates in this selection from $B \to J/\phi K^0_L$ decays are isolated and p_{GEN} is shown.

From this result it is seen that in $B \to J/\phi K_L^0$ decays the K_L^0 momentum is likely to be above 1 GeV/c, as expected from the low multiplicity of the decay. As this K_L^0 sample covers a wide range of K_L^0 momentum, it is complementary to the K_L^0 sample studied in the previous section where the candidates typically had momentum above 2 GeV/c. In Figure 8.13 the distribution of the cluster energies for all the selected clusters in this sample are shown demonstrating that the cluster energies peak around 0.4 GeV.

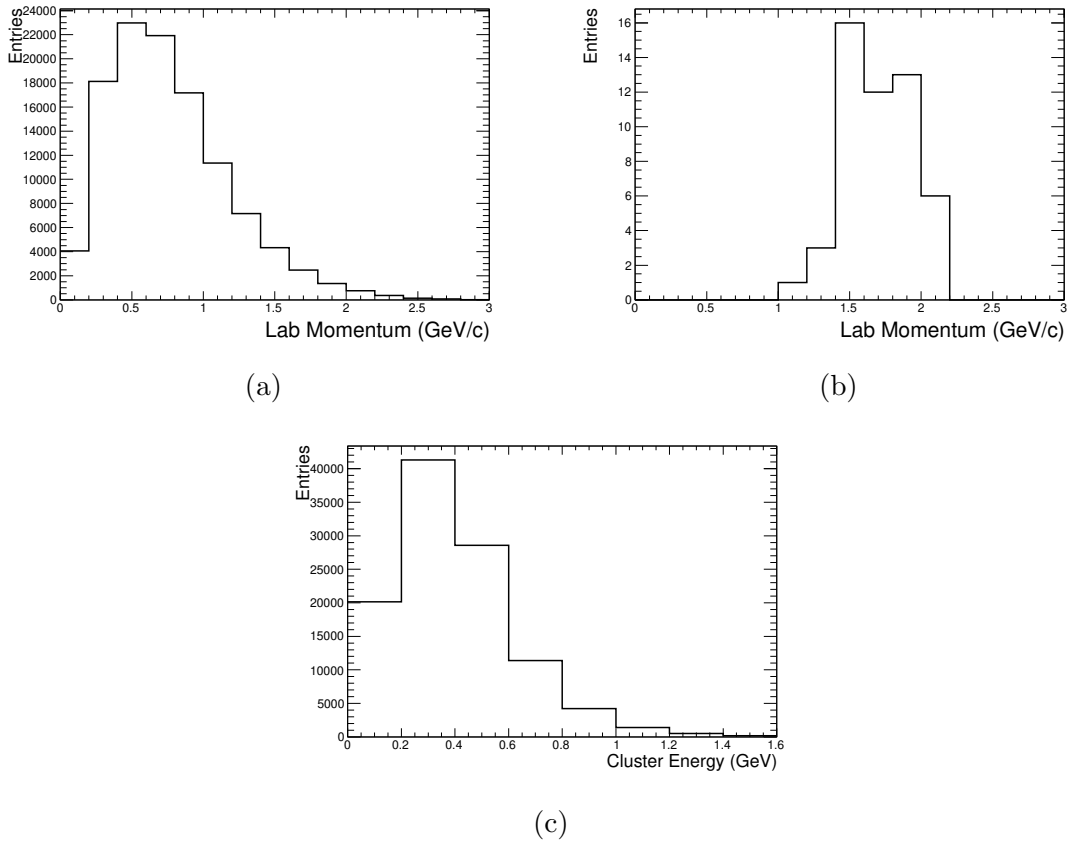

Figure 8.13: a) p_{GEN} of K_L^0 candidates selected from $B^0\bar{B}^0$ MC. b) p_{GEN} of candidates from the decay $B \to J/\phi K_L^0$. c) $\mathrm{E_{ecl}}$ of K_L^0 candidates selected from $B^0\bar{B}^0$ MC.

In Figure 8.14 the classifier response for the K_L^0 selected from $B^0\bar{B}^0$ MC is shown. Seen from this result, the classifier response peaks near Θ^{PSD}=0 and thus the classifier is correctly classifying many of the K_L^0 as hadronic showers with high probability.

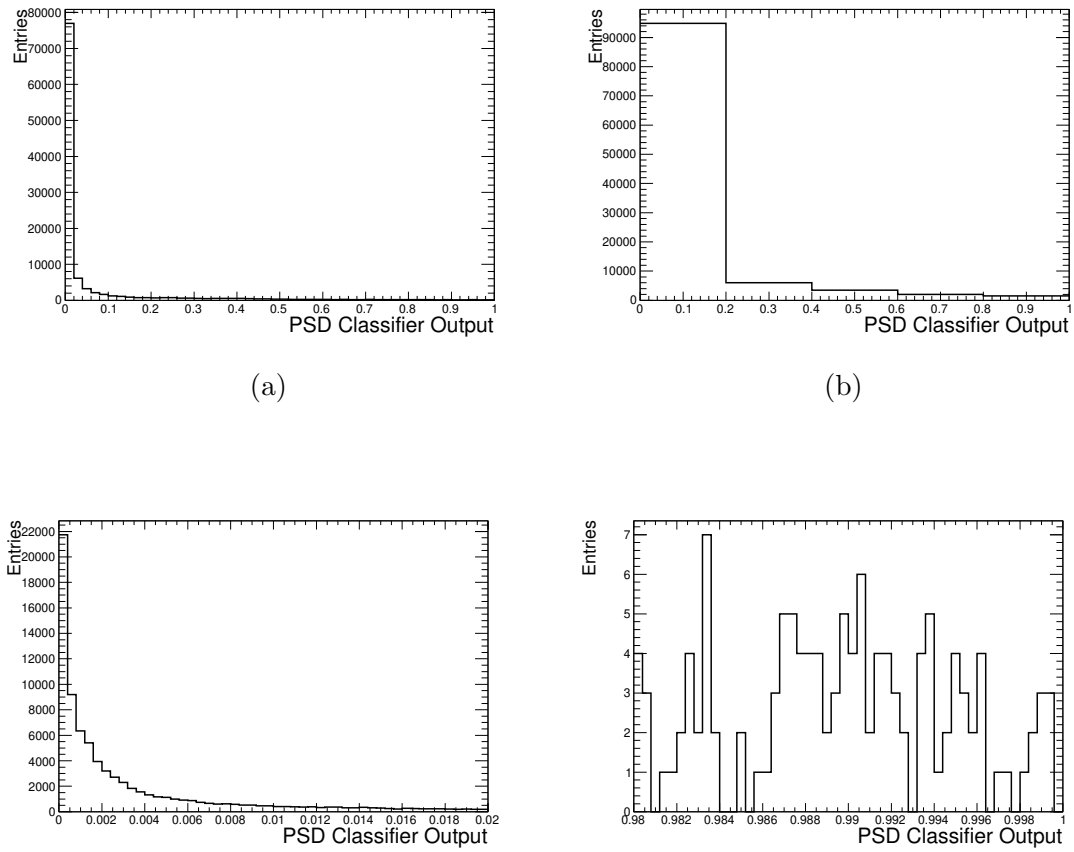

Figure 8.14: Θ^{PSD} distribution for K_L^0 candidates selected from $B^0\bar{B}^0$ MC. Several views of the distribution are shown including: a) Full range. b) Full range with course binning. c) Zoom in region $\Theta^{\mathrm{PSD}} < 0.02$. d) Zoom in region $\Theta^{\mathrm{PSD}} > 0.98$.

As shown in Figure 8.14, in addition to the candidates peaking at Θ^{PSD}=0, a small tail in the distribution is observed up to Θ^{PSD}=1. To further investigate the classifier behaviour to the K_L^0 in this sample, the crystal energy vs crystal hadron intensity distributions for crystals in the K_L^0 clusters in different Θ^{PSD} regions are shown in Figure 8.15. Comparing the different distributions it is seen that the classifier response is directly related to the types of pulse shapes present in the K_L^0 clusters. If a K_L^0 cluster has a crystal with energy above 1 GeV and hadron intensity above 0.05 it is found that the classifier response will be in the region $\Theta^{\mathrm{PSD}} < 0.02$. These high energy and high hadron intensity crystals are produced from the emission of numerous low energy charged hadrons during nucleus de-excitations following a hadronic interaction. This demonstrates the classifier is correctly interpreting the PSD information. For

the clusters with $0.02 \leq \Theta^{\mathrm{PSD}} < 0.2$, numerous crystals with hadron pulse shapes also present, as expected, however the maximum hadron intensity of these crystals is lower than the crystals in the K_L^0 clusters with $\Theta^{\mathrm{PSD}} < 0.02$ and thus the classification is not as strong. In the figures showing the crystals in clusters with $0.2 \leq \Theta^{\mathrm{PSD}} < 0.9$ and $\Theta^{\mathrm{PSD}} \geq 0.9$ it is interesting to observe that in these clusters almost all of the crystal pulse shapes are photon-like, closely resembling the crystals distributions observed for clusters produced by photons. Thus although the classifier is not classifying these clusters as hadronic showers, this behaviour is expected given the pulse shapes of the crystals as they are consistent with the pulse shapes expected for energy deposits from electromagnetic showers.

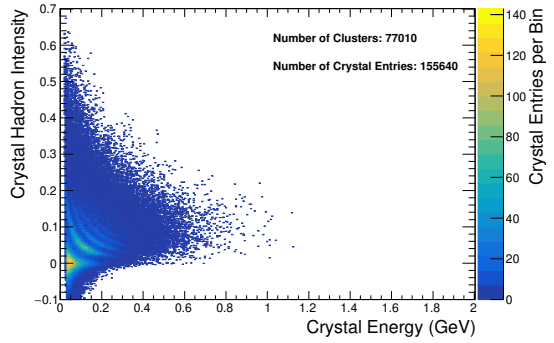

(a) $\Theta^{\mathrm{PSD}} < 0.02$

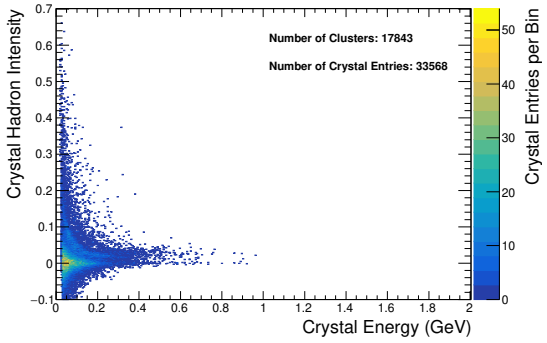

(b) $0.02 \leq \Theta^{\mathrm{PSD}} < 0.2$

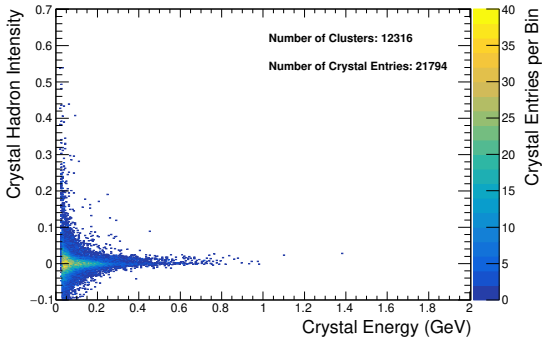

(c) $0.2 \leq \Theta^{\mathrm{PSD}} < 0.9$

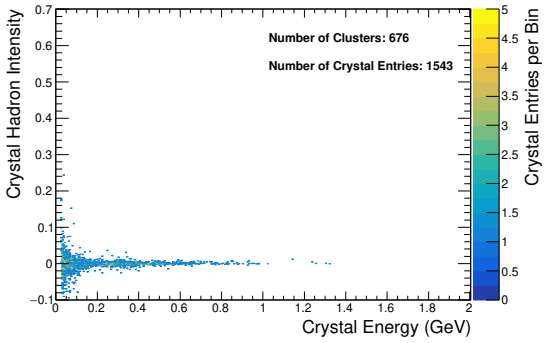

(d) $\Theta^{\mathrm{PSD}} \geq 0.9$

Figure 8.15: Crystal hadron intensity vs crystal energy distribution for crystals in K_L^0 clusters with different PSD classifier response. K_L^0 are selected from $B^0\bar{B}^0$ MC.

8.2.4 K_L^0 vs Photon Identification Efficiency and Fake-rates

In this section the K_L^0 identification efficiency and corresponding *photon as hadron* fake-rate, referred to as the photon fake-rate, of the PSD classifier are evaluated as a function of the lab momentum and cluster energy using the photon and K_L^0 samples studied individually in the previous three sections. The K_L^0 identification efficiency and photon fake-rates, $\mathcal{E}_{\text{Hadron}}$, are computed with equation 8.1 at the thresholds of $\Theta_{\text{cut}}^{\text{PSD}} = 0.02$, 0.10 and 0.50. Recall for a sample of K_L^0, $\mathcal{E}_{\text{Hadron}}$ gives the K_L^0 identification efficiency and for a sample of photons $\mathcal{E}_{\text{Hadron}}$ gives the *photon as hadron* fake-rate. These thresholds are chosen as they span a range of hadron identification efficiencies/photon fake-rates that can be achieved by the classifier.

Figure 8.16 shows $\mathcal{E}_{\text{Hadron}}(0.02)$, $\mathcal{E}_{\text{Hadron}}(0.10)$ and $\mathcal{E}_{\text{Hadron}}(0.50)$ as a function of the lab momentum for the photon and K_L^0 samples studied. For the K_L^0 from $e^+e^- \to K_S^0 K_L^0 \gamma_{\text{ISR}}$ sample, the lab momentum is given by $p_{\text{KL}}^{\text{calc}}$ defined in Appendix B and for the K_L^0 from $B^0\bar{B}^0$ sample the lab momentum is given by p_{GEN} defined in Appendix C.

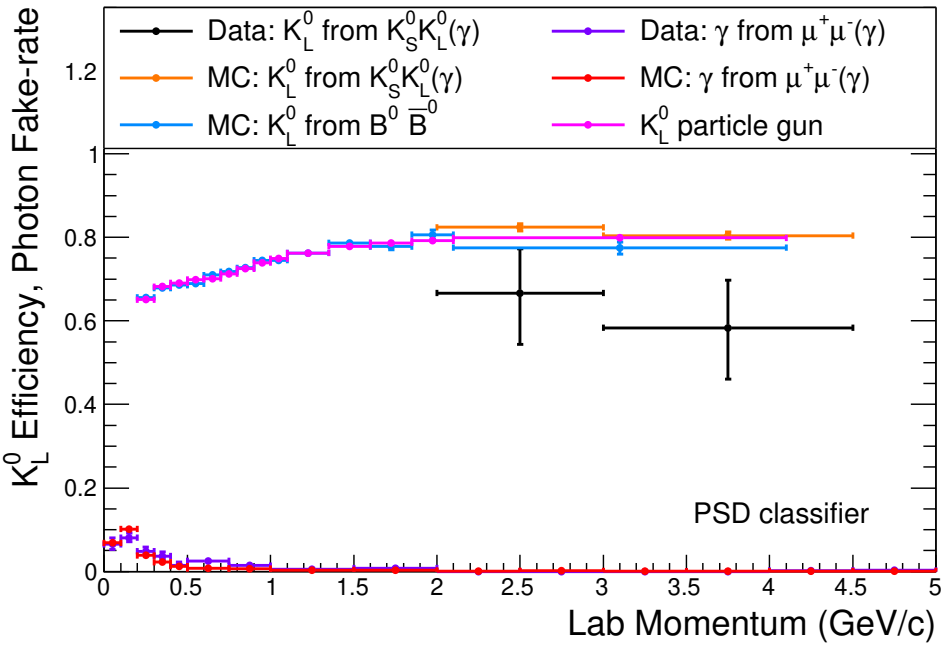

(a) $\Theta_{\text{cut}}^{\text{PSD}}$=0.02

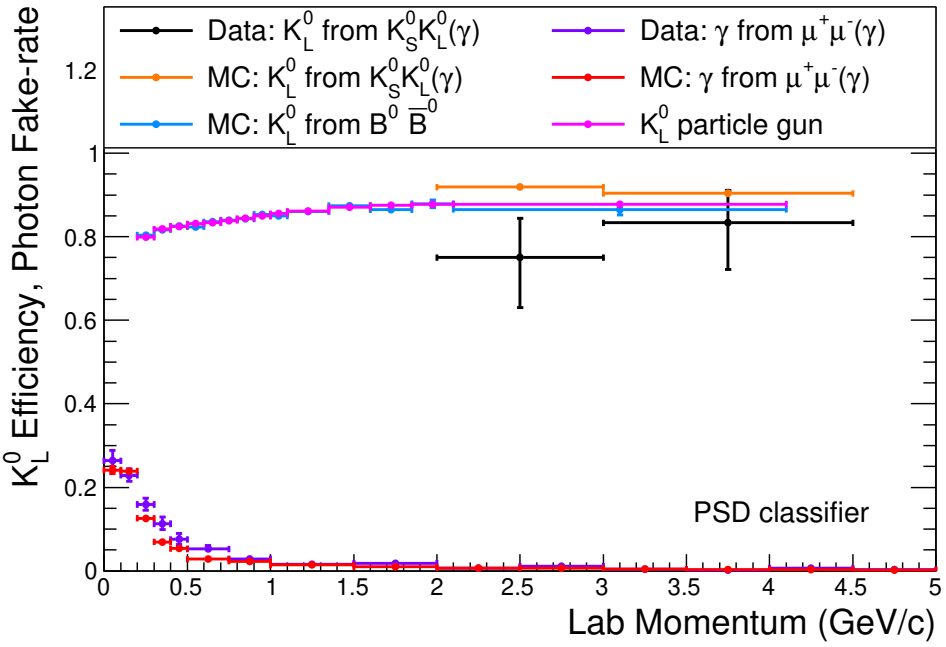

(b) $\Theta^{\mathrm{PSD}}_{\mathrm{cut}}$=0.10

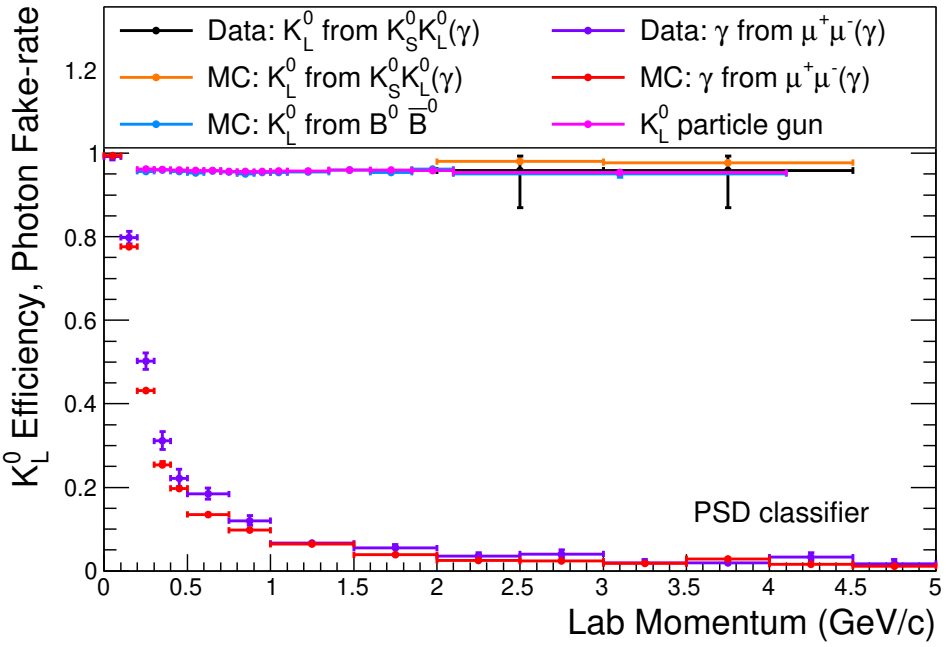

(c) $\Theta_{\rm cut}^{\rm PSD}$=0.50

Figure 8.16: a) $\mathcal{E}_{\rm Hadron}(0.02)$ b) $\mathcal{E}_{\rm Hadron}(0.1)$ and c) $\mathcal{E}_{\rm Hadron}(0.5)$ computed as a function of lab momentum for photon and K_L^0 control samples. Errors are statistical only.

In Figure 8.16, the K_L^0 efficiency is measured with three MC samples corresponding to K_L^0 from $B^0\bar{B}^0$, $K_S^0K_L^0\gamma_{\rm ISR}$ and particle gun events. As the $B^0\bar{B}^0$ and $K_S^0K_L^0\gamma_{\rm ISR}$ samples are selected using independent selection criteria, these samples can be compared to evaluate any biases potentially present. As discussed in Section 8.2.2, there is expected to be a small bias introduced in the K_L^0 selected from $K_S^0K_L^0\gamma_{\rm ISR}$ sample as candidates with $\Theta^{\rm PSD}>$ 0.8 in the K_L^0 from the $e^+e^- \rightarrow K_S^0K_L^0\gamma_{\rm ISR}$ sample are removed, for data and MC. This cut was applied to remove a residual photon background in the sample. By comparing the K_L^0 MC samples in Figure 8.16, it is found that for each $\Theta_{\rm cut}^{\rm PSD}$ threshold studied, the efficiency of the K_L^0 from $K_S^0K_L^0\gamma_{\rm ISR}$ MC is $\sim$ 3% larger relative to the K_L^0 selected from the $B^0\bar{B}^0$ MC sample. Relative to the statistical error present in the K_L^0 data sample and also relative to the separation achieved between the K_L^0 and photon samples, this bias is small. The overall impact of the cut on the $K_S^0K_L^0\gamma_{\rm ISR}$ samples is thus an improved accuracy for the K_L^0 efficiency measurements as a known photon background is removed with minimal impact on the K_L^0 efficiency.

Comparing the results across Figures 8.16a - 8.16c, as the classifier threshold increases, the K_L^0 efficiency also increases, in addition to the photon fake-rate, for all momenta. For the tighter threshold of $\Theta_{\text{cut}}^{\text{PSD}}$=0.02, the photon fake-rate above 1 GeV/c measured to be less than 1% and reaches a maximum fake-rate of 10% at 0.25 GeV/c. At this threshold the corresponding K_L^0 efficiency is as high as 80% at K_L^0 momenta above 1 GeV/c and down to 70% at 0.25 GeV/c. Increasing $\Theta_{\text{cut}}^{\text{PSD}}$ to a looser threshold of 0.50, the K_L^0 efficiency improves to be higher than 95% across all momenta studied. At this high efficiency the photon fake-rate only increases to about 5% above 1 GeV/c and up to 80% at 0.25 GeV/c.

In Figures 8.16a - 8.16c the photon fake-rate is observed to be in agreement in data and MC across the different $\Theta_{\text{cut}}^{\text{PSD}}$ thresholds and photon momenta studied. Both the data and MC show the same behaviour, such that as the classifier threshold decreases, the photon fake-rate increase faster at lower photon momentum. This behaviour was discussed in detail in Section 8.2.1 and is attributed to the lower energy photon clusters having lower energy crystals, resulting in less classifier input crystals and degraded hadron intensity resolution.

Comparing the K_L^0 from $K_S^0 K_L^0 \gamma_{\text{ISR}}$ data and MC samples, both samples have a high degree of separation from the photon samples. For the Θ^{PSD} thresholds of $\Theta_{\text{cut}}^{\text{PSD}}$=0.02 and 0.10, the efficiency measured in the data is 1-1.5 sigma lower than the efficiency measured in the MC. For the threshold of $\Theta_{\text{cut}}^{\text{PSD}}$=0.50, there is agreement between the data and MC. To have an improved understanding of the factors that impact the K_L^0 performance, the K_L^0 efficiency is also studied as a function of the cluster energy. Unlike photons, the K_L^0 cluster energy is only loosely correlated with the K_L^0 momentum due to energy losses that occur in hadronic showers [2]. In Figure 8.17 $\mathcal{E}_{\text{Hadron}}$ is shown as a function of the cluster energy for the samples studied.

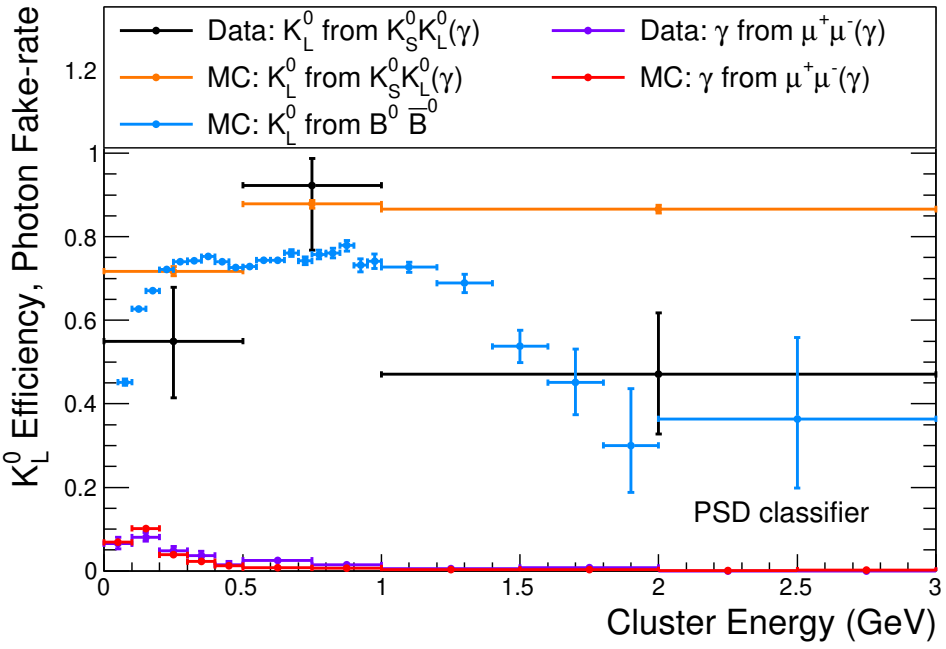

(a) $\Theta_{\rm cut}^{\rm PSD}$=0.02

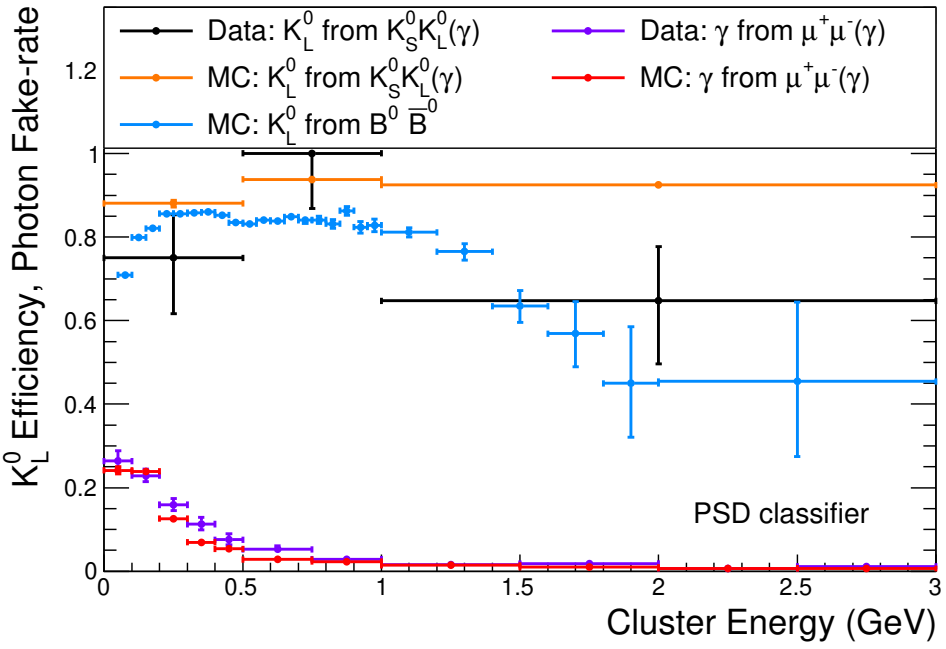

(b) $\Theta_{\rm cut}^{\rm PSD}$=0.10

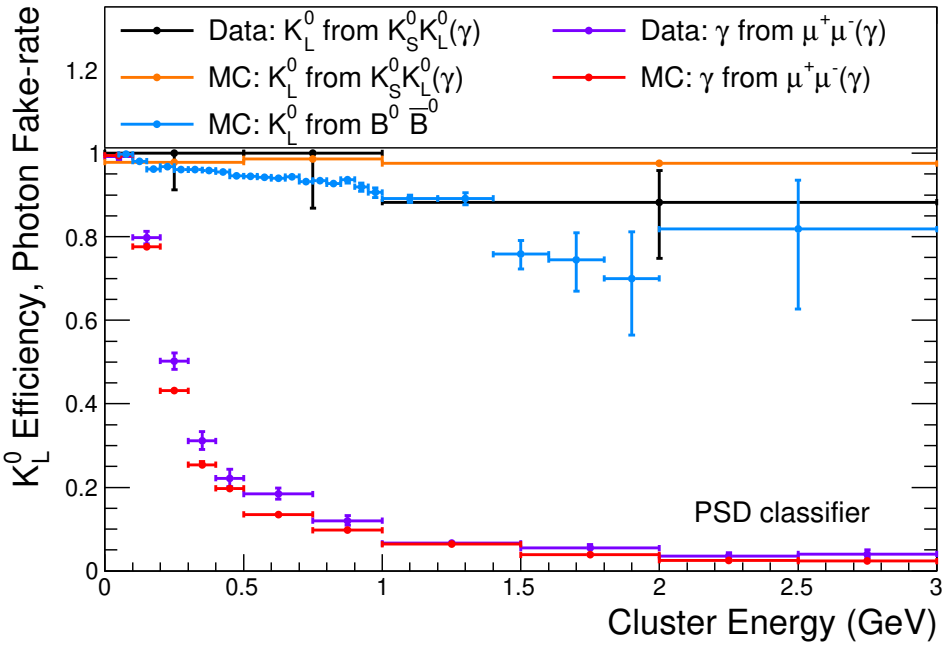

(c) $\Theta_{\text{cut}}^{\text{PSD}}$=0.50

Figure 8.17: a) $\mathcal{E}_{\text{Hadron}}(0.02)$ b) $\mathcal{E}_{\text{Hadron}}(0.1)$ and c) $\mathcal{E}_{\text{Hadron}}(0.5)$ computed as a function of calorimeter cluster energy for photon and K_L^0 control samples. Errors are statistical only.

For each K_L^0 sample studied, $\mathcal{E}_{\text{Hadron}}(0.02)$ and $\mathcal{E}_{\text{Hadron}}(0.1)$ peak at an intermediate cluster energy then decreases as the cluster energy drops below 0.25 GeV. The decrease in efficiency for K_L^0 with cluster energies below 0.25 GeV can be attributed to several factors. Similar to photons, due to the 30 MeV online threshold for a waveform to be saved, there will be less PSD information available offline for lower energy clusters. Another factor is the long K_L^0 interaction length in CsI(Tl) relative to the calorimeter depth. If the K_L^0 scatters deep in the calorimeter then the energetic secondary hadrons produced with momentum in the forward direction will only have a limited range of CsI(Tl) to interact before escaping the calorimeter. This large leakage would result in a lower cluster energy and less energy deposits from secondary particles that could potentially produce crystals with hadron pulse shapes. When the classifier threshold is set to $\Theta_{\text{cut}}^{\text{PSD}}$=0.50 the K_L^0 efficiency at cluster energies below 0.25 GeV increases to be the most efficient cluster energy region, however, the increased K_L^0 efficiency is also accompanied by a large increase in the photon fake-rate in this

cluster energy region.

In the K_L^0 from $B^0\bar{B}^0$ MC results shown in Figure 8.17, the K_L^0 efficiency decreases when the cluster energy increases above 1.5 GeV. This is also seen for the K_L^0 from $K_S^0K_L^0\gamma_{\rm ISR}$ data sample but not in the K_L^0 from $K_S^0K_L^0\gamma_{\rm ISR}$ MC sample. In particular, comparing the K_L^0 from $K_S^0K_L^0\gamma_{\rm ISR}$ in data and MC, there is good agreement in all cluster energy regions except for K_L^0 cluster energies above 1.5 GeV where the data has 1-2 sigma lower efficiency relative to the MC. In general the K_L^0 efficiency as a function of cluster energy is not expected to follow the same behaviour for the K_L^0 from $B^0\bar{B}^0$ vs $K_S^0K_L^0\gamma_{\rm ISR}$ samples. This is because the K_L^0 momentum in the $B^0\bar{B}^0$ sample peaks below 1 GeV/c whereas in the $K_S^0K_L^0\gamma_{\rm ISR}$ sample, the K_L^0 momentum ranges from 2-5 GeV/c. Due to the difference in momenta between the two samples, a cluster from each sample at the equivalent cluster energy will likely be produced from a very different type of K_L^0 interaction such that the secondary particle composition of the hadronic shower differs.

For a sample of K_L^0 at fixed momentum, the clusters at the higher end of the cluster energy distribution are expected be the clusters where the K_L^0 hadronic shower contains a larger electromagnetic fraction from secondary π^0's and/or photons. This is because after production, secondary π^0's and photon's are immediately and with minimal leakage, absorbed in the calorimeter through an electromagnetic shower, as opposed to if the K_L^0 energy is released by neutrons, or charged hadrons which can escape the cluster. As a result, for a fixed momentum K_L^0 sample, the higher energy clusters in the sample are more likely to have larger electromagnetic component to the hadronic shower. In terms of PSD, this results in the K_L^0 clusters with higher energies to be more likely to include energetic crystals with significant photon component scintillation emission. This effect causes the higher energy clusters in a K_L^0 sample to look more electromagnetic-like and thus are more difficult to classify as a hadronic shower by using PSD. This effect is demonstrated in Figure 8.17 where the K_L^0 efficiency as a function of cluster energy is shown for two K_L^0 samples selected from particle gun K_L^0's generated with uniformly distributed momentum between $0.05 - 3.0$ GeV/c. In Figure 8.17 the particle-gun sample is divided into low and high momentum samples of corresponding to $p_{\rm GEN} <$ 0.75 GeV/c and $p_{\rm GEN} >$ 2 GeV/c. In each sample, the K_L^0 efficiency peaks at an intermediate cluster energy then decreases at larger cluster energies. In Figure 8.18b the cluster energy distributions of the samples are shown to demonstrate the K_L^0 efficiency is highest where the cluster energy distributions peaks and the drop in efficiency for high cluster energies occurs in the tail of the

distributions. By examining the MC truth information of the secondary particles in the clusters, it was verified that the higher energy clusters in each sample frequently have at least one secondary π^0 produced. Returning to Figure 8.17, this can explain why the K_L^0 efficiency above cluster energies of 1.5 GeV is lower in the K_L^0 from $B^0\bar{B}^0$ sample relative to the K_L^0 from $K_S^0 K_L^0 \gamma_{\text{ISR}}$ MC sample.

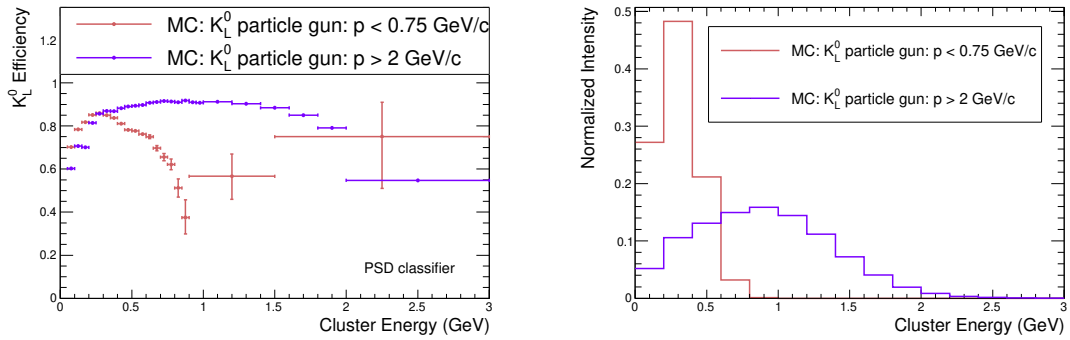

(a) (b)

Figure 8.18: a) $\mathcal{E}_{\text{Hadron}}(0.1)$ computed as a function of calorimeter cluster energy for high and low momentum K_L^0 control samples from MC particle gun. b) Cluster energy distributions of samples in Figure 8.18a. Errors are statistical only.

8.2.5 Comparison with Shower Shape based Classifier

At the past B-Factory experiments Belle and BaBar, K_L^0 identification was done using shower shape cluster variables, which characterize the spatial distribution of the energy in a cluster to determine if the cluster is photon-like or hadronic-like. Following this approach, a shower shape based multivariate classifier for K_L^0 vs photon identification was independently developed for Belle II and is described in detail in reference [55]. The classifier inputs in this case are shower shape quantities called Zernike moments [55]. The Zernike moments of a cluster are computed by using the Zernike polynomials as weights to derive an energy centroid-like quantity to characterize the cluster [55].

There are several key differences between the Zernike classifier and the PSD classifier, which is studied throughout this chapter. Although the Zernike classifier is restricted to information related to the crystal energy and crystal positions, unlike the PSD classifier, the Zernike classifier is not restricted to only cluster crystals with an offline waveform saved. For a single cluster the Zernike classifier uses information

from all crystals in the cluster.

Another significant difference between the PSD and Zernike classifier is that the Zernike classifier also uses information from any clusters that are in close proximity to the primary cluster. This is related to the Belle II calorimeter cluster finding algorithm which initially will construct large regions in the calorimeter called Connected Regions. Connected Regions are defined as regions of the calorimeter that are connected by crystals with significant energy deposits. After the Connected Regions are formed, each Connected Region is either classified as a single cluster or sub-divided into several independent clusters, depending on how many local energy maxima are in the Connected Region.

For a single cluster, the Zernike classifier has 22 inputs. The first eleven are a set Zernike moments computed using the crystals in the primary cluster. The remaining eleven inputs are a set of Zernike moments computed using the crystals in Connected Region that the primary cluster belongs to [55]. By using information from the Connected Region, the Zernike classifier can significantly extend the information available to the Zernike classifier over the PSD classifier, as the PSD classifier only uses information from the higher energy crystals in the primary cluster. For clusters from K_L^0 in particular, this is advantageous as with the current version of the clustering algorithm a single K_L^0 shower can sometimes be divided into multiple clusters.

It was found that because the inputs to the Zernike classifier include information from clusters in close proximity to the primary cluster, there is a bias in the K_L^0 from $K_S^0 K_L^0 \gamma_{\mathrm{ISR}}$ sample for the Zernike classifier output. This is due the Zernike classifier including information from calorimeter clusters produced by the pions in the event from the $K_S^0 \to \pi^+\pi^-$ decay. In the K_L^0 from $K_S^0 K_L^0 \gamma_{\mathrm{ISR}}$ selection the K_L^0 is required to be produced through an intermediate ϕ via $e^+e^- \to \phi\gamma_{\mathrm{ISR}} \to K_S^0 K_L^0 \gamma_{\mathrm{ISR}}$. As the radiated photon carries > 4 GeV in the CMS frame, the ϕ is highly boosted in this selection. As a result when the ϕ decays the opening angle of the K_L^0 and K_S^0 momentum is small. The kinematics of this interaction result in the pions from the $K_S^0 \to \pi^+\pi^-$ decay to typically be in close proximity to the K_L^0 cluster. This is demonstrated by Figure 8.19 showing the distribution of $d_{\mathrm{min}}^{\mathrm{track}}$, defined as the distance from the K_L^0 cluster to the nearest track entering the calorimeter. In this figure, $d_{\mathrm{min}}^{\mathrm{track}}$ is shown for the K_L^0 clusters selected from the K_L^0 from $K_S^0 K_L^0 \gamma_{\mathrm{ISR}}$ and $B^0\bar{B}^0$ samples. Note $d_{\mathrm{min}}^{\mathrm{track}}$ is computed during reconstruction and is truncated at 250 cm causing the spike at the end of the distribution. As seen from Figure 8.19, on average the K_L^0 from $K_S^0 K_L^0 \gamma_{\mathrm{ISR}}$ sample are less isolated then K_L^0 from $B^0\bar{B}^0$ sample.

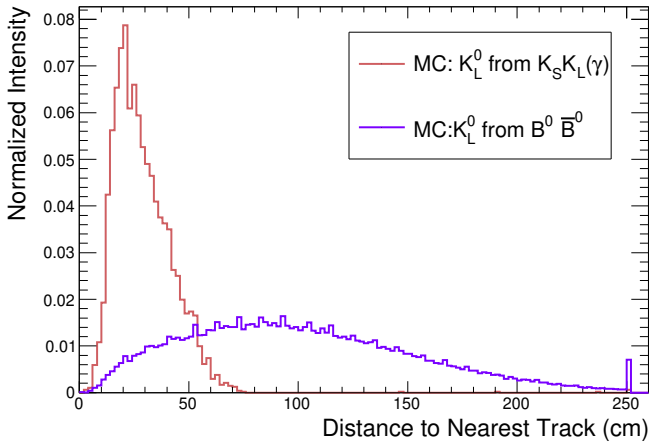

Figure 8.19: Distribution of $d_{\text{min}}^{\text{track}}$ used to measure the cluster isolation of the K_L^0 samples studied.

To study the impact the low isolation has on the K_L^0 from $K_S^0 K_L^0 \gamma_{\text{ISR}}$ sample efficiency, Figure 8.20 shows the K_L^0 efficiency as a function of momentum for several MC samples. In Figure 8.20a the PSD classifier is shown for the tighter threshold of $\Theta_{\text{cut}}^{\text{PSD}}$=0.02 and in Figure 8.20b the equivalent result for the Zernike classifier is shown for the $\Theta_{\text{cut}}^{\text{Zernike}}$=0.54, where $\Theta_{\text{cut}}^{\text{Zernike}}$ is analogous to $\Theta_{\text{cut}}^{\text{PSD}}$ and defines the Zernike classifier threshold used to classify a cluster as hadronic or electromagnetic. $\Theta_{\text{cut}}^{\text{Zernike}}$=0.54 is shown as this threshold for the Zernike classifier produces the equivalent K_L^0 efficiency at higher momentum as the PSD classifier with $\Theta_{\text{cut}}^{\text{PSD}}$=0.02, for the particle gun sample. The impact of cluster isolation is shown in Figure 8.20 by comparing the two K_L^0 from $K_S^0 K_L^0 \gamma_{\text{ISR}}$ samples overlaid. The "all events" sample refers to the standard selection and the "$d_{\text{min}}^{\text{track}}$> 0.4 m" sample is restricted to the K_L^0 clusters in the sample with good cluster isolation in terms of $d_{\text{min}}^{\text{track}}$. In Figure 8.20a the PSD classifier results show a small decrease in efficiency when the cluster isolation cut is applied however, independent of the isolation cut the efficiency remains in close agreement with the particle gun sample. For the Zernike classifier, before the cluster isolation cut is applied, the efficiency computed for the K_L^0 from $K_S^0 K_L^0 \gamma_{\text{ISR}}$ samples is $\sim$ 10% higher than the efficiency computed for the particle gun sample. After applying the isolation cut the $\sim$ 10% bias is reduced and the efficiency is in agreement with the particle gun sample. Also overlaid in the plots in Figure 8.20 is the K_L^0 efficiency computed from the $B^0 \bar{B}^0$ sample. For this sample K_L^0 efficiency of the PSD classifier agrees with the efficiency computed from the particle gun sample

for all momenta studied. For the Zernike classifier there are some deviations from the particle gun efficiency observed for the $B^0\bar{B}^0$ sample. These results demonstrate that the Zernike classifier will be biased from the low cluster isolation of the K_L^0 from $K_S^0 K_L^0 \gamma_{\rm ISR}$ sample. In addition this bias is not present for the PSD classifier. The reason the cluster isolation has a large impact on the Zernike classifier is because this classifier uses information from the primary cluster crystals as well as information from nearby clusters which in this case are likely to be from the pions from the K_S^0 decay. The PSD classifier however only uses information from the primary cluster thus the nearby clusters from the pions do not bias the result.

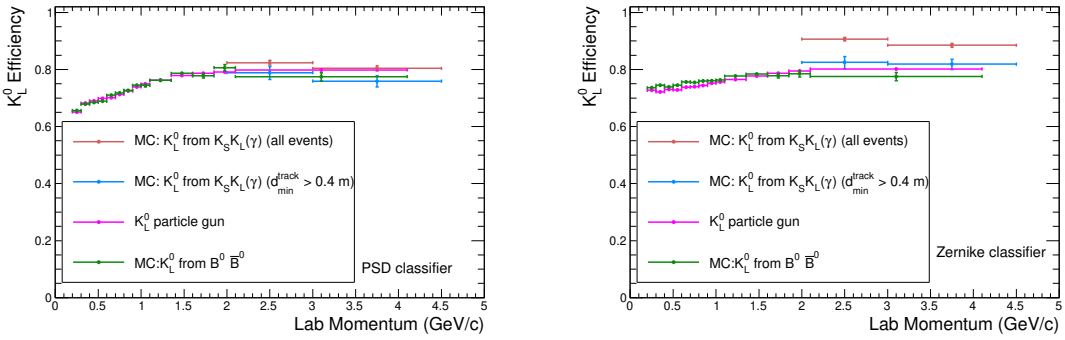

(a) $\Theta_{\rm cut}^{\rm PSD}$=0.02 (b) $\Theta_{\rm cut}^{\rm Zernike}$=0.54

Figure 8.20: K_L^0 efficiency as a function of lab momentum K_L^0 MC control samples studied. Errors are statistical only.

Similar the PSD classifier, the Zernike classifier response ranges continuously from 0 to 1, and thus by varying the $\Theta_{\rm cut}^{\rm Zernike}$ threshold any K_L^0 efficiency can be achieved. A higher $\Theta_{\rm cut}^{\rm Zernike}$ threshold however will also have a higher photon fake-rate. To compare the performance of the PSD and Zernike classifiers, the Zernike classifier thresholds were set such that the K_L^0 efficiency measured with the K_L^0 from particle gun sample, matches the PSD classifier efficiency in the higher momentum bins. With the K_L^0 efficiency fixed between the two classifiers, the performance of the two classifiers is compared using the corresponding photon fake-rates. In Figure 8.21 the K_L^0 efficiency and photon fake-rates are shown side-by-side for the PSD and Zernike classifier, allowing the photon fake-rates to be compared.

The results shown in Figure 8.21 demonstrate that for each threshold, ranging from lower to higher K_L^0 efficiencies, the photon fake-rate of the PSD classifier is lower than the Zernike classifier fake-rate. In particular at 1.5 GeV/c for the tighter threshold,

the PSD classifier has a photon fake-rate below 1% and the Zernike classifier fake-rate a 1.5 GeV/c is $\sim$ 10%. At the looser threshold the PSD classifier fake-rate is $\sim$ 6% at 1.5 GeV/c and the Zernike classifier fake-rate is 27%. This demonstrates improved performance achieved by applying pulse shape discrimination. An additional observation from Figure 8.21 is that for each threshold the photon fake-rate of the Zernike classifier follows a similar photon energy dependence as the PSD classifier such that at lower photon energies the photon fake-rate increases.

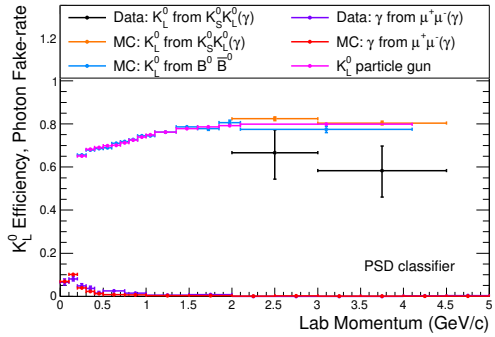

(a) $\Theta_{\text{cut}}^{\text{PSD}}$=0.02

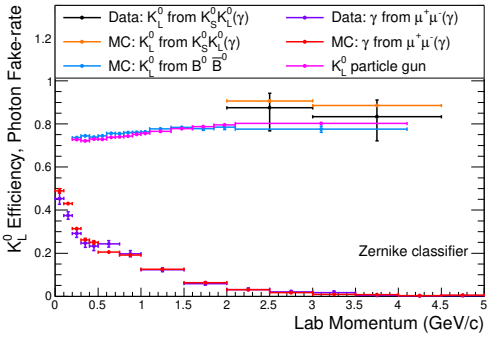

(b) $\Theta_{\text{cut}}^{\text{Zernike}}$=0.54

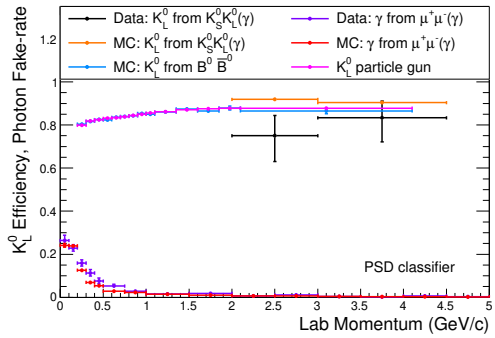

(c) $\Theta_{\text{cut}}^{\text{PSD}}$=0.1

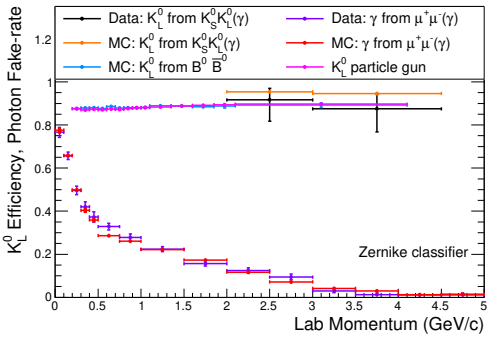

(d) $\Theta_{\text{cut}}^{\text{Zernike}}$=0.72

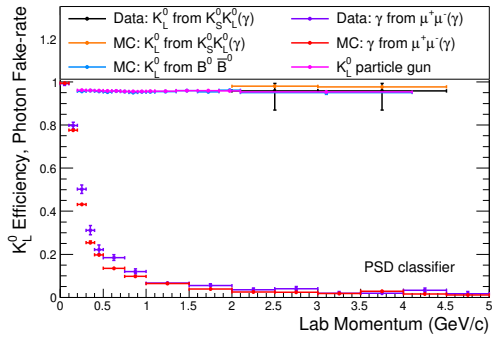

(e) $\Theta_{\text{cut}}^{\text{PSD}}$=0.5

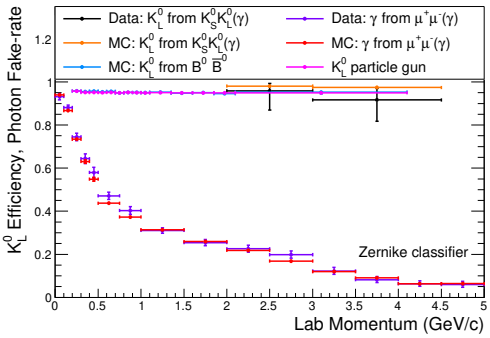

(f) $\Theta_{\text{cut}}^{\text{Zernike}}$=0.82

Figure 8.21: K_L^0 efficiency and photon fake-rate as a function of momentum of the PSD and Zernike classifiers computed with the photon and K_L^0 control samples studied. Errors are statistical only.

8.3 Improving π^0 Identification with Pulse Shape Discrimination

Neutral pions are produced frequently in decay chains initiated by B mesons produced in SuperKEKB collisions. π^0's decay with a 98.8% [2] branching fraction to two photons and thus one of the primary functions of the Belle II electromagnetic calorimeter is π^0 reconstruction [3]. The detector signature for $\pi^0 \to \gamma\gamma$ will typically be two neutral calorimeter clusters that together have an invariant mass consistent with the π^0 mass.

$\pi^0 \to \gamma\gamma$ candidates provide a useful photon control sample to evaluate the performance of the calorimeter. This is because the calorimeter is the only Belle II sub-detector used to reconstruct this decay. When constructing π^0 candidates, fake candidates arise when a hadronic shower, produced a neutron or K^0_L, is mis-identified as a photon, or when one of the photons used to reconstruct the decay is a true photon that did not originate from a π^0. This section uses the PSD classifier developed in Section 8.1 to improve π^0 identification by rejecting fake π^0 candidates produced when a neutral hadron is mis-identified as a photon. In addition, this section uses the $\pi^0 \to \gamma\gamma$ photon control sample to independently evaluate the photon fake-rate of the classifier.

8.3.1 Initial π^0 Selection

To establish a base sample of $\pi^0 \to \gamma\gamma$ candidates, the following photon selection is applied:

- Calorimeter cluster is in the calorimeter barrel ($32.2 < \theta < 128.7$ degrees).
- $E_{ecl} > 0.05$ GeV.
- $W_{\text{sum}} > 1.5$ where W_{sum} is the sum of the weights assigned to the crystals in the cluster that measure how associated the crystal is to a cluster.
- The calorimeter cluster must have at least one crystal with an offline waveform saved that passed the offline waveform fit χ^2 threshold applied in reconstruction. This requirement is applied to ensure the PSD classifier has at least one crystal input.

From this initial set of photon candidates, all $\pi^0 \to \gamma\gamma$ candidates in the invariant mass range 0.08 $< m_{\gamma\gamma} <$ 0.18 GeV/c^2 are reconstructed. To study π^0's likely to be from $B\bar{B}$ and $q\bar{q}$ events, a veto is applied on events with less than 4 tracks that pass the criteria:

- $\vec{p_T} > 0.15$ GeV/c
- $|d_0| < 1$ cm
- $|z_0| < 2$ cm

The energy distribution of the photon candidates that pass this section is shown in Figure 8.22. This figure shows that the majority of the photon candidates have energy below 200 MeV, however, the tail of the distribution also extends to several GeV. To study the photon energy dependence of the PSD classifier performance for π^0 identification, the π^0 sample is divided into three sub-samples defined by E_{min}= 50, 100 and 250 MeV where E_{min} is the lowest energy photon used to reconstruct the π^0 candidate.

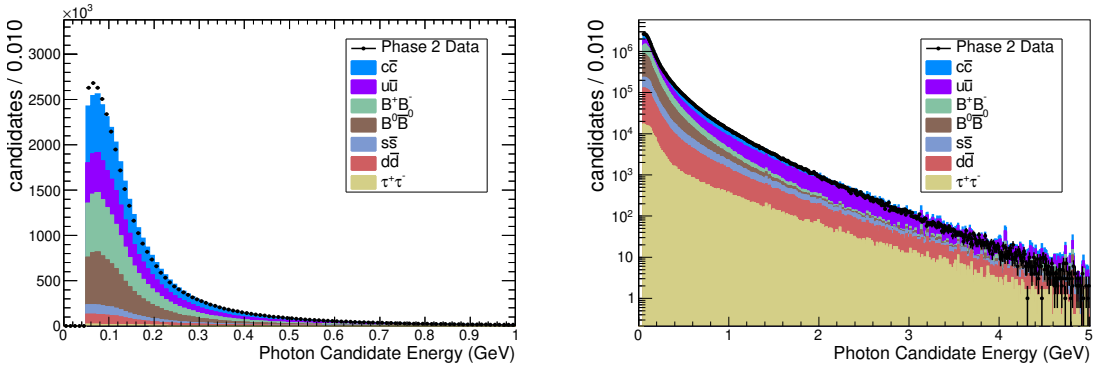

(a) (b)

Figure 8.22: Energy distribution of all photon candidates used in base π^0 selection. MC distribution is normalized to the number of entries in the data. a) Zoom into region below 1 GeV. b) Log scale, energy range extends to 5 GeV.

In Figure 8.23, the distribution of $m_{\gamma\gamma}$ is shown for all π^0 candidates in each E_{min} sample. In each plot in this figure, a peak is observed in the data and MC near the true π^0 mass ($m_{\pi^0} \approx 0.1349$ GeV/c^2 [2]), arising from true $\pi^0 \to \gamma\gamma$ candidates in the selection. This peak is accompanied by a slowly varying background from fake π^0 candidates. As mentioned above, the fake π^0 candidates can be from π^0 candidates

reconstructed from photons that did not originate from a true π^0, or from a neutral hadron mis-identified as a photon. As E_{min} increases, the signal-to-background is observed to increase in each sample. Comparing data and MC, the peak resolution is similar and a ~ 1 MeV/c^2 offset is observed in the peak mean. Given that the Phase 2 Belle II data corresponds to detector commissioning runs, this difference in data and MC is likely an indication that the ongoing calibrations related to the energy, position and simulation modelling of the material in front of the calorimeter, can be improved.

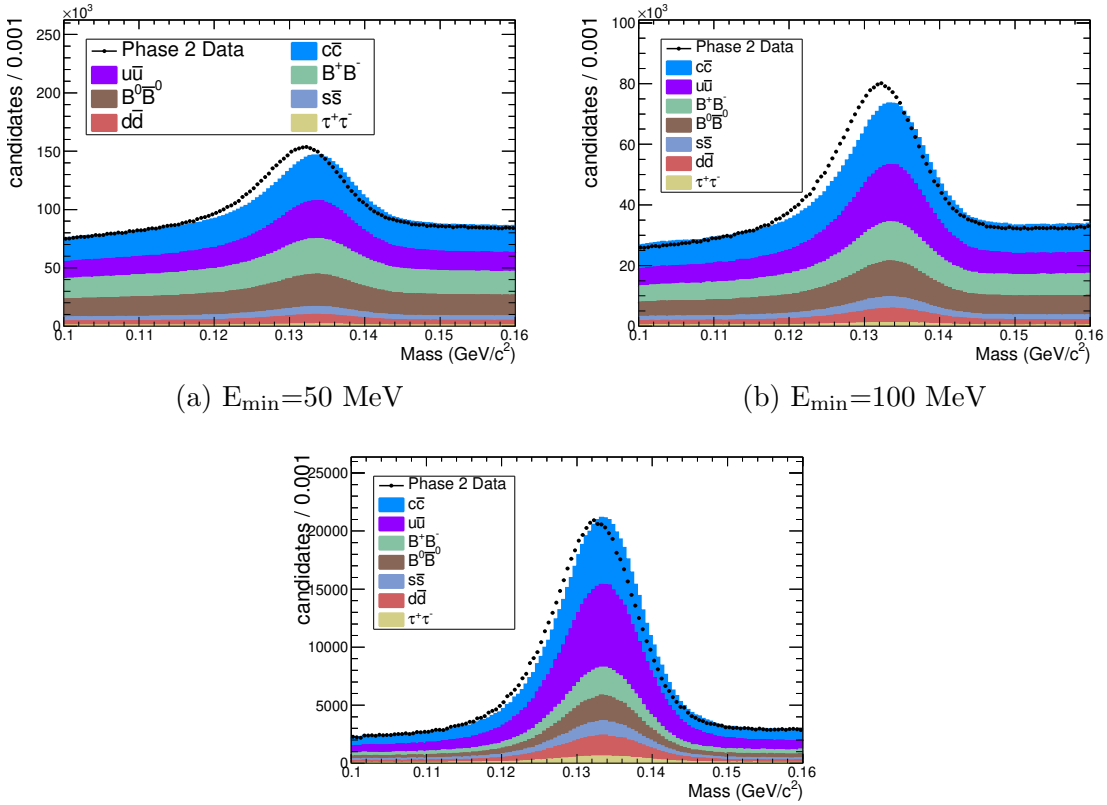

(a) E_{min}=50 MeV

(b) E_{min}=100 MeV

(c) E_{min}=250 MeV

Figure 8.23: Distributions of $m_{\gamma\gamma}$ candidates for each E_{min} sample selected with the base selection requirements. MC distribution is normalized to the number of entries in the data.

In Figure 8.24 the distribution of the classifier output, Θ^{PSD}, is shown for the photon candidates used to reconstruct the π^0 candidates in the mass range $0.12 < m_{\gamma\gamma} < 0.145$ GeV/c^2. Consistent with the studies in the previous sections of this chapter, the Θ^{PSD} distributions are peaking near Θ^{PSD}=0 or Θ^{PSD}=1, indi-

cating a number of the clusters are classified with high likelihoods as hadronic or electromagnetic showers. Comparing the different E_{min} samples, the relative number of hadronic-like vs electromagnetic-like clusters follows the same trend as the $m_{\gamma\gamma}$ distributions shown in Figure 8.23 such that as E_{min} increases, the fraction of clusters peaking near Θ^{PSD}=1 (photon-like) also increases. This trend is also expected as low energy photons are more difficult to classify due to the 30 MeV waveform readout threshold and lower signal to noise, as discussed in Section 8.2.1.

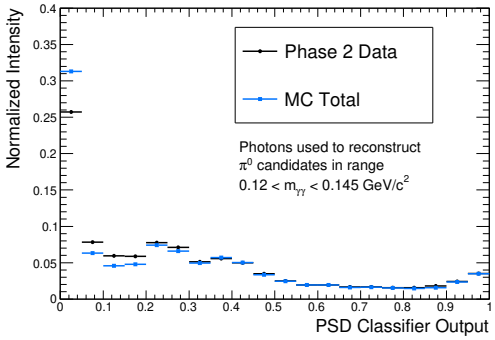

(a) E_{min}=50 MeV

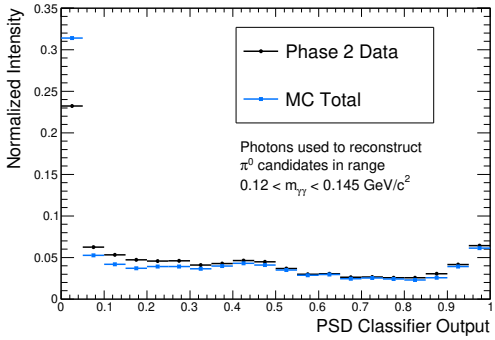

(b) E_{min}=100 MeV

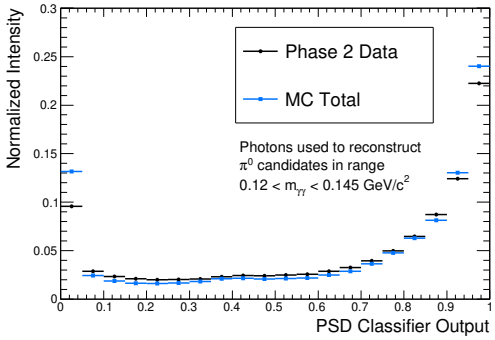

(c) E_{min}=250 MeV

Figure 8.24: Θ^{PSD} distribution for photons used to construct π^0 candidates for each E_{min} sample. MC distribution is normalized to the number of entries in the data.

8.3.2 Fits to π^0 Mass

The performance of a given sample of π^0 candidates is evaluated by the purity, $\mathcal{P}_{\pi^0}$, and efficiency, $\mathcal{E}_{\pi^0}$, of the sample. $\mathcal{P}_{\pi^0}$ and $\mathcal{E}_{\pi^0}$ are computed using equations 8.2 and 8.3, respectively.

$$\mathcal{P}_{\pi^0}(\Theta^{\rm PSD}_{\rm cut}) = \frac{n_{\pi^0}(\Theta^{\rm PSD}_{\rm cut})}{n_{\rm candidates}(\Theta^{\rm PSD}_{\rm cut})} \tag{8.2}$$

$$\mathcal{E}_{\pi^0}(\Theta^{\rm PSD}_{\rm cut}) = \frac{n_{\pi^0}(\Theta^{\rm PSD}_{\rm cut})}{n_{\pi^0}(\Theta^{\rm PSD}_{\rm cut} = 0)} \tag{8.3}$$

Where, $n_{\rm candidates}(\Theta^{\rm PSD}_{\rm cut})$ is the number of π^0 candidates in a sample where both photons used to reconstruct the candidate have $\Theta^{\rm PSD} > \Theta^{\rm PSD}_{\rm cut}$. Recall a larger value of $\Theta^{\rm PSD}$ indicates the cluster is more electromagnetic-like. $n_{\pi^0}(\Theta^{\rm PSD}_{\rm cut})$ is the number of π^0 candidates in a sample that are true $\pi^0 \to \gamma\gamma$ decays and both photons used to reconstruct the candidate have $\Theta^{\rm PSD} > \Theta^{\rm PSD}_{\rm cut}$.

To compute $n_{\rm candidates}$ and n_{π^0} at a given $\Theta^{\rm PSD}_{\rm cut}$ threshold, the $m_{\gamma\gamma}$ distribution of the sample is fit using a crystal ball function to model the π^0 peak and a second order Chebyshev polynomial to model the continuum background. $n_{\rm candidates}$ is computed by the fit result for the total number of candidates in the mass range $0.12 < m_{\gamma\gamma} < 0.145$ GeV/c^2. n_{π^0} is computed from the integral of the crystal ball function component of the fit result in the mass range of $0.12 < m_{\gamma\gamma} < 0.145$ GeV/c^2.

Figure 8.25 shows sample fits to $m_{\gamma\gamma}$ distributions in data and MC for the base $m_{\gamma\gamma}$ spectra of each $\rm E_{min}$ sample. In each plot the total fit results are reported as well as the signal and background components of the fit. For MC, the $m_{\gamma\gamma}$ distribution of the π^0 candidates in the sample that were truth-matched to a be true π^0's is also reported.

The results in this figure show the crystal ball + Chebyshev polynomial model used in the fit, models the $m_{\gamma\gamma}$ spectrum at a similar level of precision for the data and MC. The MC truth matched distributions shown in the MC results demonstrate the fit model is able to extract reasonably well the distribution of true π^0's in the mass range of $0.12 < m_{\gamma\gamma} < 0.145$ GeV/c^2, used to compute $\mathcal{P}_{\pi^0}$ and $\mathcal{E}_{\pi^0}$. The MC results also include the numerical value for n_{π^0} computed using the fit result and using the integral of the truth matched distribution. Recall using the fit result, n_{π^0} is computed by the integral of the signal component in the range $0.12 < m_{\gamma\gamma} < 0.145$ GeV/c^2. For the MC truth match result, n_{π^0} is computed from the integral of the MC truth matched $m_{\gamma\gamma}$ distribution in the same range. Comparing the two values in the MC plots, it is seen that the fit underestimates the number of true $\pi^0 \to \gamma\gamma$ candidates by $2-3\%$.

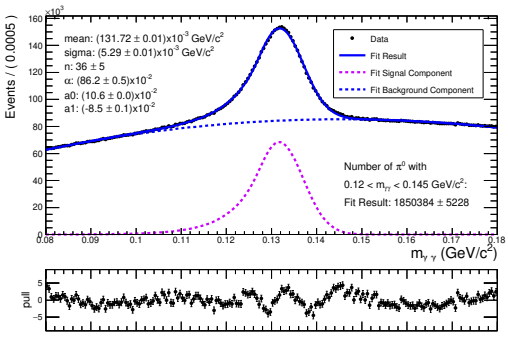

(a) E_{min}=0.05 GeV

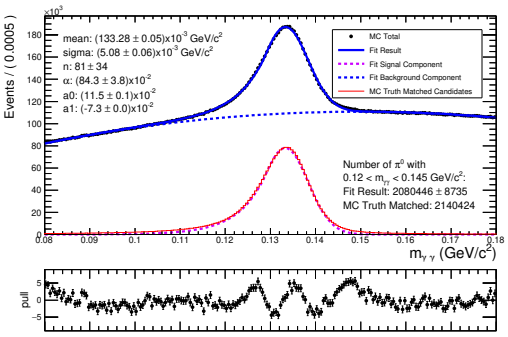

(b) E_{min}=0.05 GeV

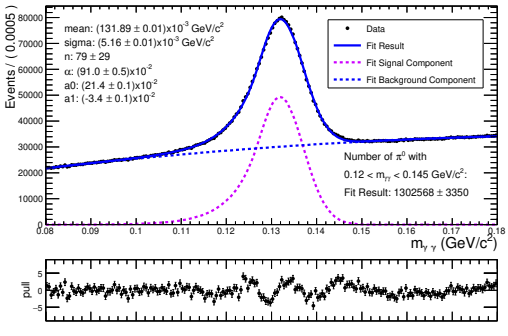

(c) E_{min}=0.1 GeV

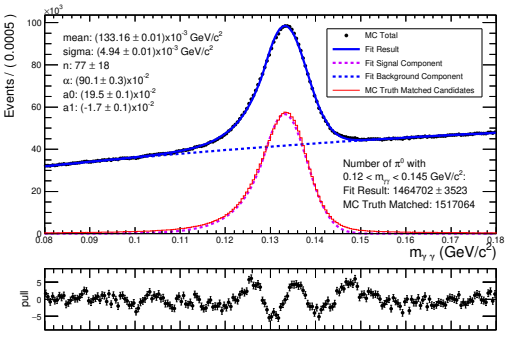

(d) E_{min}=0.1 GeV

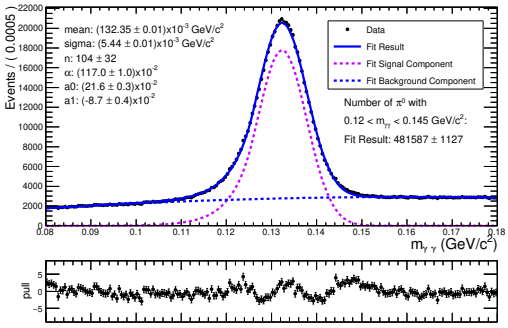

(e) E_{min}=0.25 GeV

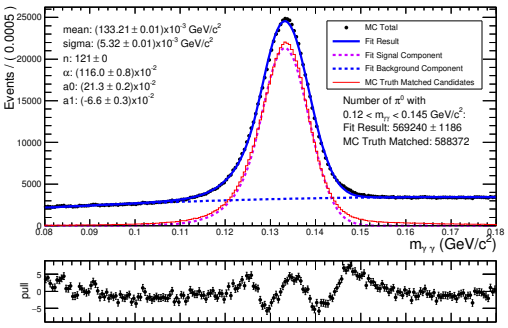

(f) E_{min}=0.25 GeV

Figure 8.25: Sample fits to to $\pi^0 \to \gamma\gamma$ spectra in data. Fit results are used to compute $n_{\text{candidates}}$ and n_{π^0}.

8.3.3 Improving π^0 Identification with PSD

To study the performance of the classifier for π^0 identification, $\mathcal{E}_{\pi^0}$ and $\mathcal{P}_{\pi^0}$ are computed for a set of $\Theta^{\text{PSD}}_{\text{cut}}$ values spanning the range of the classifier output ($0 < \Theta^{\text{PSD}} < 1$). For the PSD classifier $\mathcal{E}_{\pi^0}$ and $\mathcal{P}_{\pi^0}$ are evaluated for $\Theta^{\text{PSD}}_{\text{cut}}$=[0.01,

0.02, 0.03, 0.04, 0.05, 0.1, 0.15, 0.2, 0.25, 0.3, 0.4, 0.5, 0.6, 0.7, 0.8, 0.9]. To compare to the Zernike classifier described in Section 8.2.5, $\mathcal{E}_{\pi^0}$ and $\mathcal{P}_{\pi^0}$ are also evaluated by substituting $\Theta_{\text{cut}}^{\text{Zernike}}$ for $\Theta_{\text{cut}}^{\text{PSD}}$ in equations 8.2 and 8.3. For the Zernike classifier, $\mathcal{E}_{\pi^0}$ and $\mathcal{P}_{\pi^0}$ are evaluated for $\Theta_{\text{cut}}^{\text{Zernike}}$=[0.1, 0.2, 0.3, 0.4, 0.5, 0.6, 0.7, 0.8, 0.9]. The results are presented in Figures 8.26a - 8.26c which show $\mathcal{E}_{\pi^0}$ as a function of $\mathcal{P}_{\pi^0}$ for each E_{min} sample. In each result, the points labelled "Truth Matched" are the $\mathcal{E}_{\pi^0}$ vs $\mathcal{P}_{\pi^0}$ results for the MC, computed using by the integral of the $m_{\gamma\gamma}$ distribution of truth matched candidates. By comparing the "Truth Matched" to the MC results, the impact of biases from the fitting procedure are shown.

In Figure 8.26a, $\mathcal{E}_{\pi^0}$ vs $\mathcal{P}_{\pi^0}$ is shown for the E_{min}=0.05 GeV π^0 sample. This result shows the initial purity of the sample, corresponding to 100% π^0 efficiency, is measured to be 31% in data and 27% in MC. Applying the PSD classifier for hadronic shower rejection, the purity of the sample can be increased to 45% while maintaining a π^0 efficiency of 90%. For the Zernike classifier to achieve a purity of 45% the corresponding π^0 efficiency decreases to 80%. This demonstrates the PSD classifier is more effective in rejecting fake π^0 candidates. To achieve purities higher than $\sim$ 45%, both the PSD and Zernike classifiers result in an approximately linear drop in π^0 efficiency with increasing π^0 purity. This suggests that above a purity of $\sim$ 45% the remaining fake π^0 candidates are primarily from photons not originating from a π^0 decay and thus the hadronic shower rejection provided by the classifiers cannot suppress this remaining background.

Comparing the data and MC, the MC is found to have higher purities relative to the data by about $3-5\%$. This difference in data and MC can be caused by several factors. For this study a general selection was applied by selecting all events with more than 3 tracks originating from the interaction point and then reconstructing all π^0 candidates in those events. Although this allows a large sample of π^0 candidates to be studied over a wide energy range, the data and MC agreement will depend on the accuracy of the MC modelling for all the MC modes that contribute to the signal. In particular, the results will be dependent on the fraction of electromagnetic vs hadronic showers produced by the MC, and if this matches the rates in data. The conclusions of the study however demonstrate that π^0 identification can be improved by using the PSD classifier.

In Figures 8.26b and 8.26c, $\mathcal{E}_{\pi^0}$ vs $\mathcal{P}_{\pi^0}$ is shown for the E_{min}=100 MeV and E_{min}=250 MeV samples, respectively. These results show a similar behaviour to the E_{min}=50 MeV sample. Initially the PSD classifier can improve the π^0 purity by

5% for only a 10% drop in π^0 efficiency, however, after this initial improvement the π^0 efficiency drops approximately linearly with increasing π^0 purity. These results suggest that as E_{min} increases, the background present from neutral hadronic showers decreases.

In the E_{min}=250 MeV sample it is also seen that the π^0 purity is higher in MC relative to data. This is found for the PSD and Zernike classifiers, suggesting the data vs MC difference is due to MC modelling of the rates of hadronic vs electromagnetic showers in the events.

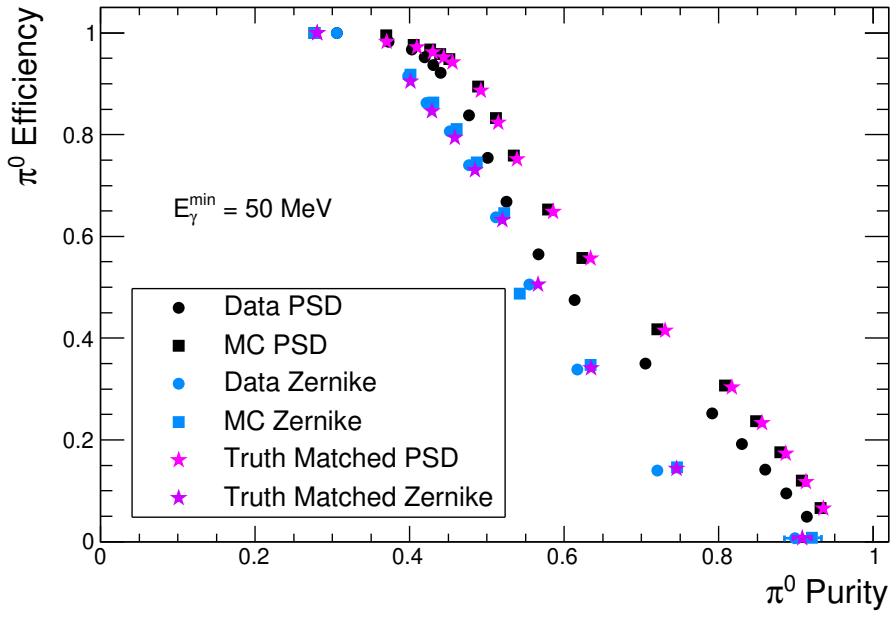

(a) E_{min}=0.05 GeV

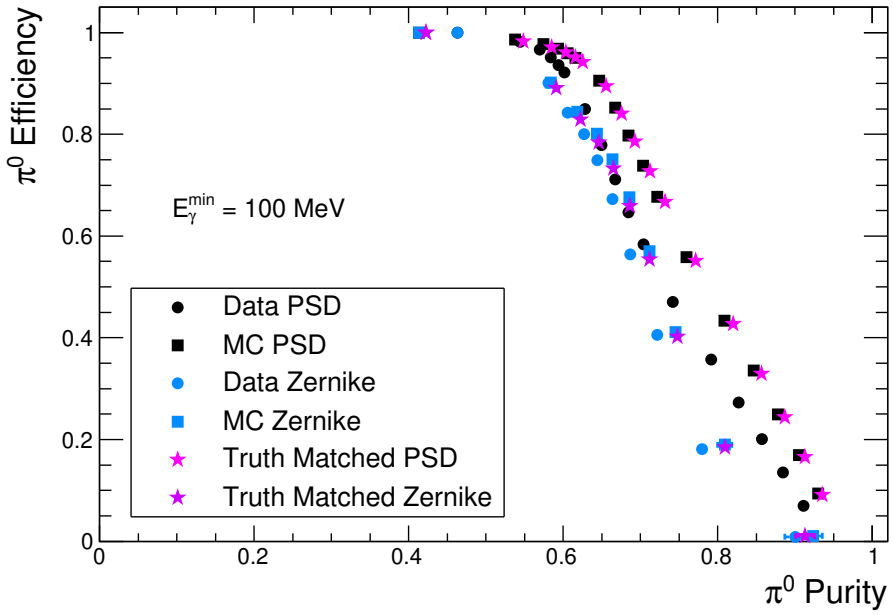
π^0 Efficiency
π^0 Purity
E_γ^{min} = 100 MeV
Data PSD
MC PSD
Data Zernike
MC Zernike
Truth Matched PSD
Truth Matched Zernike
0
0.2
0.4
0.6
0.8
1

(b) E_{min}=0.1 GeV

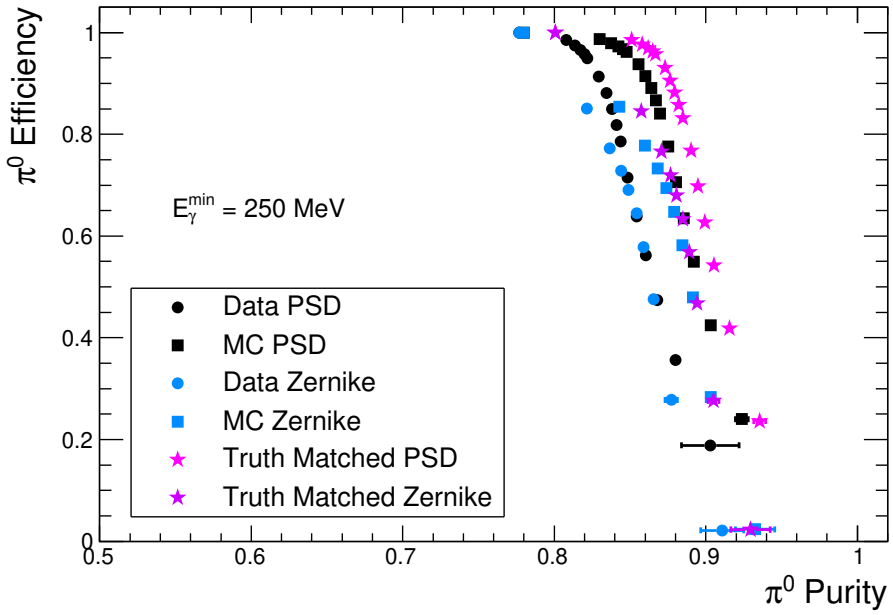

(c) E_{min}=0.25 GeV

Figure 8.26: $\mathcal{E}_{\pi^0}$ as a function of $\mathcal{P}_{\pi^0}$ computed for PSD and Zernike classifiers for corresponding E_{min} π^0 samples. Note in Figure 8.26c the $\mathcal{P}_{\pi^0}$ axis starts at 0.65. Errors are statistical only.

8.3.4 Measuring Photon as Hadron Fake-Rate with π^0's

The *photon as hadron* fake-rate, referred to as the photon fake-rate, is defined as the fraction of true photons that are incorrectly identified as a hadronic shower for a Θ^{PSD}_{cut} threshold ($\Theta^{PSD}<\Theta^{PSD}_{cut}$). In Section 8.2 the photon fake-rate was measured using photons selected in a $e^+e^- \rightarrow \mu^+\mu^-(\gamma)$ control sample. In this section the photon fake-rate of the PSD classifier is independently measured using photons from $\pi^0 \rightarrow \gamma\gamma$.

The methodology for this measurement is illustrated by Figures 8.27a and 8.27b. These figures show how the $m_{\gamma\gamma}$ spectrum changes once the photon candidates that are used to reconstruct the π^0 candidates are restricted to be hadronic shower-like, using the PSD classifier. In Figure 8.27a a loose requirement is applied such that at least one of the photon candidates used to reconstruct the π^0 is required to have $\Theta^{PSD}<\Theta^{PSD}_{cut}$. It is seen that when applying this criteria at the thresholds of Θ^{PSD}_{cut}=0.02 and Θ^{PSD}_{cut}=0.1, a significant decrease in the number of true π^0 candidates is observed. This occurs

because if one of the photon candidates used in the π^0 candidate reconstruction is a hadronic shower that was mis-identified as a photon, then true $\pi^0 \to \gamma\gamma$'s decays cannot be reconstructed. For the threshold of $\Theta^{\rm PSD}_{\rm cut}$=0.5, many of the initial π^0 candidates remain. This is consistent from the studies in Section 8.2 where at the threshold of $\Theta^{\rm PSD}_{\rm cut}$=0.5, the photon fake-rate was above 10% for lower energy photons. In Figure 8.27b a tighter criteria is applied where both of the photon candidates are required to be classified as hadronic showers. In this case, the $\Theta^{\rm PSD}_{\rm cut}$=0.02 and $\Theta^{\rm PSD}_{\rm cut}$=0.1 thresholds result in no peak in the $m_{\gamma\gamma}$ distribution from true π^0 candidates, again demonstrating that hadronic showers are being selected by the PSD classifier.

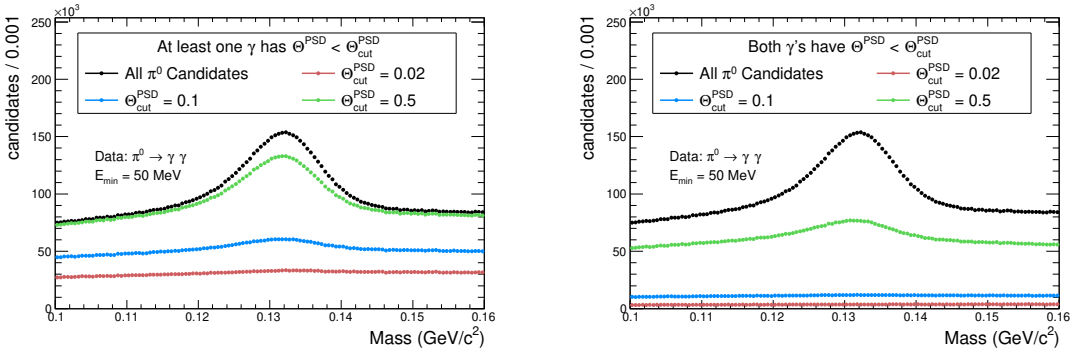

(a) (b)

Figure 8.27: $m_{\gamma\gamma}$ for π^0 candidates in $E_{\rm min}$=0.05 GeV data sample, where using PSD a) one b) both of the photons is required to have $\Theta^{\rm PSD} < \Theta^{\rm PSD}_{\rm cut}$. As expected for tighter $\Theta^{\rm PSD}_{\rm cut}$ thresholds, which have lower photon fake-rates, the peak from true π^0 candidates is reduced/cut away as true $\pi^0 \to \gamma\gamma$ candidates cannot be reconstructed from hadronic showers.

The procedure to compute the photon fake rate using the $\pi^0 \to \gamma\gamma$ sample is as follows. For a sample of $\pi^0 \to \gamma\gamma$ candidates, the total number of true π^0's in the sample, n_{π^0}, can be expressed as the sum of three types of true π^0's candidates as shown in equation 8.4,

$$n_{\pi^0} = n^{00}_{\pi^0} + n^{01}_{\pi^0} + n^{11}_{\pi^0} \tag{8.4}$$

where:

$n^{00}_{\pi^0}$ = Number of true π^0 candidates where both photons have $\Theta^{\rm PSD} > \Theta^{\rm PSD}_{\rm cut}$, thus both photons are correctly identified as a electromagnetic shower.

$n_{\pi^0}^{10}$ = Number of true π^0 candidates where only one of the photons has Θ^{PSD}>$\Theta_{\text{cut}}^{\text{PSD}}$, thus only one photon is correctly identified as an electromagnetic shower.

$n_{\pi^0}^{11}$ = Number of true π^0 candidates where neither of the photons have Θ^{PSD}>$\Theta_{\text{cut}}^{\text{PSD}}$, thus both photons are mis-identified as a hadronic shower.

Using $n_{\pi^0}^{00}$, $n_{\pi^0}^{10}$ and $n_{\pi^0}^{11}$ the photon fake-rate for a given $\Theta_{\text{cut}}^{\text{PSD}}$ is given by equation 8.5

$$\mathcal{E}_{\gamma}^{\text{fake-rate}} = \frac{2n_{\pi^0}^{11} + n_{\pi^0}^{10}}{2n_{\pi^0}^{\text{Total}}} \tag{8.5}$$

For computing $\mathcal{E}_{\gamma}^{\text{fake-rate}}$, equation 8.4 is substituted into equation 8.5 to give equation 8.6.

$$\mathcal{E}_{\gamma}^{\text{fake-rate}} = \frac{n_{\pi^0}^{11} + n_{\pi^0}^{\text{Total}} - n_{\pi^0}^{00}}{2n_{\pi^0}^{\text{Total}}} \tag{8.6}$$

To evaluate $n_{\pi^0}^{00}(\Theta_{\text{cut}}^{\text{PSD}})$ and $n_{\pi^0}^{11}(\Theta_{\text{cut}}^{\text{PSD}})$ in equation 8.6, after the corresponding classifier cuts are applied, the resulting $m_{\gamma\gamma}$ spectrum is fit using the same fitting procedure that was detailed in Section 8.3.2. The integral of the fit signal component is computed in the mass range $0.12 < m_{\gamma\gamma} < 0.145$ GeV/c^2 to give the total number of true π^0 candidates in the spectrum. To cross-check the fitting procedures, the same measurement is completed for the MC by computing the integral of the $m_{\gamma\gamma}$ distribution of the truth matched π^0 candidates.

The results are shown in Figure 8.28 where the photon fake-rate of the PSD classifier is measured as a function of $\Theta_{\text{cut}}^{\text{PSD}}$ for the three E_{min} samples of π^0's. Overlaid in these plots is the measurement done with data and MC using the fitting procedure, in addition to the MC measurement completed using the integral of the MC truth matched distributions. Comparing the MC fit results to the MC truth match results, there is agreement over the the range of classifier thresholds studied, demonstrating that the fitting procedure is accurately measuring the number true π^0 candidates in the $m_{\gamma\gamma}$ spectra.

Observed in the log scale plot in Figure 8.28a, at thresholds of $\Theta_{\text{cut}}^{\text{PSD}}< 0.1$ the photon fake-rates of the three E_{min} samples begin to converge. This demonstrated that for the range $\Theta_{\text{cut}}^{\text{PSD}}< 0.1$, the PSD classifier is unlikely to mis-identify photons as hadronic showers, independent of the photon energy. In the range of $\Theta_{\text{cut}}^{\text{PSD}}$=0.1-0.9,

the fake-rate of the E_{min}=250 MeV sample is significantly lower than the E_{min}=50 MeV and E_{min}=100 MeV samples. This independently demonstrates the trend that was observed previously in Section 8.2.1 where the PSD classifier performance improves as the photon energy increases. Discussed in Section 8.2.1, this is attributed to the cluster have a greater number of crystals with waveforms saved offline as well as the improved hadron intensity resolution for higher crystal energies.

Comparing the data and MC distributions in Figure 8.28, the fake-rate in MC is lower relative to the data, particularly for Θ_{cut}^{PSD} values that are in the range 0.2-0.9. This difference in data and MC is likely related to differences between the data and MC in terms of crystal energy resolution and hadron intensity resolution. A similar level of agreement as was found in the measurements made in Section 8.2.1 using the $e^+e^- \to \mu^+\mu^-(\gamma)$ control sample when the loose cut of Θ_{cut}^{PSD}=0.50 was applied. Improvements to the simulations which would allow the crystal-by-crystal variations in the scintillation response to be modelled will likely improve the agreement between data and MC.

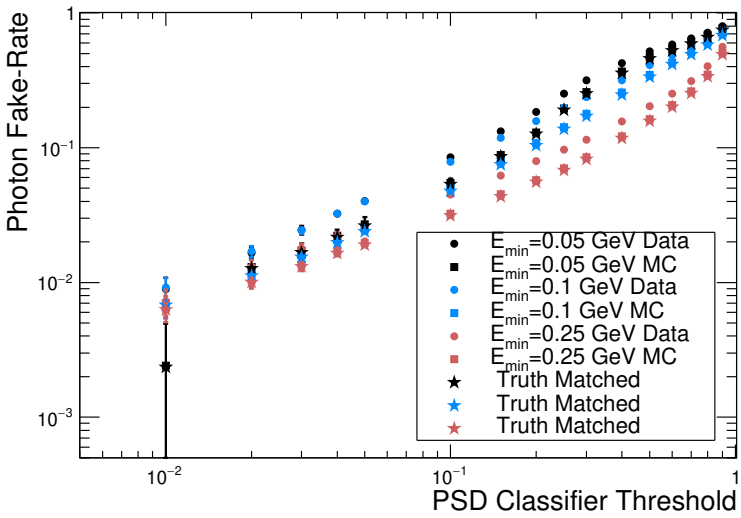

(a)

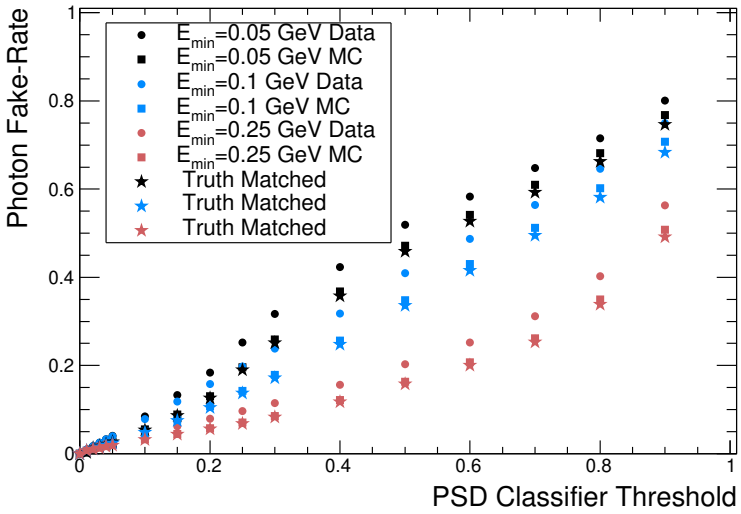

(b)

Figure 8.28: a) Log scale b) Linear scale. Photon fake-rate of PSD classifier measured using photons from $\pi^0 \to \gamma\gamma$ decays for different minimum photon energy thresholds. Energy distribution of all photons in sample is shown in Figure 8.22. Errors are statistical only.

8.4 Areas of Future Study

There a several ways the PSD-based classifier that was trained in this work can be improved in future studies. Currently the classifier inputs are limited to only crystals with waveforms saved offline and with good fit χ^2. This was done to study the performance achieved by using primarily the PSD information available in the cluster. This limitation however was also shown to restrict the performance of the classifier at lower cluster energies, due to the 30 MeV energy limit to record waveforms resulting in less information available to the classifier. To improve the classifier, the inputs can be extended to all crystals in the cluster, independent whether the crystal has a waveform. This would fully exploit the spatial and pulse shape information contained in a cluster. In addition, extending the crystal input information to include variables such as the fit χ^2 and crystal time can also likely lead to improvements.

The primary application of the classifier as discussed was for neutral particle identification and as a result, the classifier was trained using samples of K_L^0 and photons. For charged particle identification this classifier will likely have applications in improving $e^\pm$ vs $\pi^\pm$ and $\mu^\pm$ vs $\pi^\pm$ separation where the pion hadronically showers. A more optimal approach however for charged particle identification is expected to be achieved by implementing an independent classifier that uses track momentum in addition to the crystal level input variables and is trained for $e^\pm$ vs $\mu^\pm$ vs $\pi^\pm$ vs $K^\pm$ vs $p/\bar{p}$ classification.

8.5 Chapter Summary

A multivariate classifier was trained using particle gun MC samples to distinguish electromagnetic and hadronic showers using pulse shape discrimination. The performance of the classifier was evaluated with control samples of photons, K_L^0 and π^0 selected from Belle II Phase 2 data and simulation. By studying the trained classifier output to these control samples, the PSD-based classifier was measured to be highly effective for separating electromagnetic and hadronic showers with a significant degree of separation. These results completed several of the research objectives which were outlined in Chapter 3 Section 3.1. The primary limitation of the classifier was shown to be due to the 30 MeV online threshold for waveform readout, which limits the PSD information available in lower energy clusters. Compared to an independently trained classifier which applied shower-shape information for cluster classification, the

PSD-based classifier achieved over a factor of two lower *photon-as-hadron* fake-rate at the equivalent K_L^0 efficiency, for most momenta.

Chapter 9

Conclusions

The results presented in this dissertation demonstrate that CsI(Tl) pulse shape discrimination is a new and effective method to improve calorimeter-based particle identification at high energy physics experiments. The testbeam studies in Chapter 5, demonstrated that energy deposits by highly ionizing particles in CsI(Tl) produce a CsI(Tl) scintillation component with decay time of 630 ± 10 ns. This scintillation component was defined as the "hadron scintillation component" and was not present for energy deposits from photons and low $d\mathrm{E}/dx$ particles. By measuring the fraction of hadron scintillation component emission relative to the total scintillation emission, a new method for CsI(Tl) scintillation pulse characterization was developed and used for pulse shape discrimination. A theoretical model was formulated to compute the magnitude of hadron scintillation component emission produced in an energy deposit by using the instantaneous ionization $d\mathrm{E}/dx$ of the particle depositing the energy. Through incorporating this model in GEANT4 particle interactions in matter simulation libraries, simulations of the CsI(Tl) scintillation response to highly ionizing particles were achieved such that the particle dependent scintillation pulse shapes observed in the testbeam data could be reproduced by the simulations.

In Chapter 6, the data analysis and simulation techniques that were developed in Chapter 5 were applied to implement pulse shape discrimination at the Belle II experiment using the CsI(Tl) electromagnetic calorimeter. This allowed Belle II to be the first B-Factory experiment to use CsI(Tl) pulse shape discrimination for improving particle identification. In Chapter 7 pulse shape discrimination was used to study the interactions of charged particles in CsI(Tl) using control samples of $e^{\pm}$, $\mu^{\pm}$, $\pi^{\pm}$, $K^{\pm}$ and $p/\bar{p}$ selected from Belle II collision data. By studying the scintillation pulse shapes of crystals in calorimeter clusters produced by these particles, the

types of hadronic interactions that occurred in the calorimeter crystals were studied and detailed evaluations of GEANT4 hadronic interaction modelling were made. In Chapter 8 a multivariate classifier was trained to use pulse shape discrimination to distinguish electromagnetic vs. hadronic showers in the Belle II calorimeter. Using control samples of K_L^0, photons and π^0 selected from Belle II collision data, pulse shape discrimination was shown to be an effective method for neutral particle identification and provide improvements over shower-shape based methods.

This work extended the capabilities of the Belle II experiment in areas of particle identification using the unique information provided by pulse shape discrimination. The pulse shape characterization methods and simulation techniques that were developed are expected to have extended applications by benefiting areas of medical physics, space physics and nuclear security, which commonly use CsI(Tl) scintillators. In addition, pulse shape discrimination is not unique to CsI(Tl) and many commonly used scintillators such as, NaI(Tl) [56], CsI(Na)[57], pure CsI [58], $PbWO_4$ (doped) [59], BaF_2[57] (list is non-exhaustive) have been shown to have pulse shape discrimination capabilities. The techniques developed in this dissertation can potentially be extended to apply and simulate pulse shape discrimination with other scintillators. From the physics performance advancements that were achieved through the implementation of pulse shape discrimination at Belle II through this work, considerations should be given to extend the design criteria for calorimeters at future collider experiments to employ scintillators based on energy resolution, timing resolution, radiation hardness *and pulse shape discrimination capabilities.*

Appendix A

Selection of Charged Particle and Photon Control Samples in Phase 2 Data

This Appendix details the selection cuts used to isolate high purity control samples of electrons, muons, pions, kaons and protons from the Phase 2 Belle II dataset.

A.1 $e^+e^- \to e^+e^-(\gamma)$ Selection

Bhabha scattering events, $e^+e^- \to e^+e^-(\gamma)$, are selected to provide a low background and high statistics sample of high momentum electrons ($p_{\text{lab}} > 4$ GeV/c) allowing for the calorimeter response to high energy electromagnetic showers to be studied. This sample is also used for evaluating the waveform fitting templates in Chapter 6.

A Bhabha track was defined with the following criteria.

- $p_T > 0.15$ GeV/c where p_T is the magnitude of the transverse momentum in the lab frame.
- $|d_0| < 0.5$ cm
- $|z_0| < 1$ cm
- $E_{\text{ecl}} > 2$ GeV
- Calorimeter cluster is in the calorimeter barrel ($32.2 < \theta < 128.7$ degrees).

- $0.8 \leq E/p \leq 1.1$
- Track has no hits in SVD and PXD detectors. During Phase 2 a segment of the SVD and PXD detectors was installed, covering a small azimuthal angle of the detector acceptance. At the time of this analysis, the data calibration and simulation validation for these detectors was ongoing. This veto ensures during reconstruction the track quantities such as p_{Lab}, z_0 and d_0 were not computed using unreliable information from these detectors.
- Tracks selected in the MC samples are required to be MC truth matched to a particle. This is done as in simulation beam backgrounds are modelled using a beam background overlay approach. This approach uses data events collected from a pseudo-random trigger in order to collect a data sample of the detector readout with the noise characteristics of the Belle II detector during SuperKEKB collision operation but without the presence of a scattering event. For processes such as $e^+e^- \to e^+e^-$ that have relatively high cross sections, a small fraction of the pseudo-random trigger data will contain an event where an $e^+e^- \to e^+e^-$ scatter occurred. As the beam background overlays are reused when generating MC, this means when an $e^+e^- \to e^+e^-$ selection is applied these outlier events can be selected multiple times if the beam background satisfies the selection cuts and the generated MC particles where not in the analysis acceptance. By applying this veto, multiple counting of these backgrounds events is removed.

This criteria ensures the track originated near the interaction point and has a large energy deposit in the calorimeter, as expected from Bhabha electrons.

A selection of Bhabha events was performed by selecting events with two tracks with opposite charge and invariant mass, m_{ee}, between 10 and 10.7 GeV/c^2. In Figure A.1 the m_{ee} distribution of events passing the pre-selection is shown with data and MC overlaid. Backgrounds processes labelled "Other" include $e^+e^- \to e^+e^-e^+e^-$, $e^+e^-\mu^+\mu^-$, $\tau^+\tau^-$, $\mu^+\mu^-(\gamma)$, $\pi^+\pi^-\gamma_{\text{ISR}}$ and $K^+K^-\gamma_{\text{ISR}}$. In this figure a peak at the total CMS energy of SuperKEKB is observed. A tail in the m_{ee} distribution to lower masses is also seen due to radiative Bhabha events. The MC distributions overlaid in this figure show good agreement with the data and demonstrate the low backgrounds present after the selection requirements are applied.

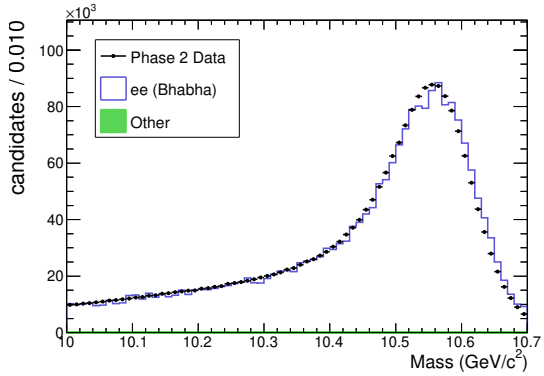

Figure A.1: m_{ee} distribution of events passing Bhabha selection. MC is scaled to data.

In Figure A.2 the distributions of p_{lab} are shown for the selected Bhabha tracks with a cluster in the barrel region of the calorimeter. As expected, the tracks in this selection have very high momentum.

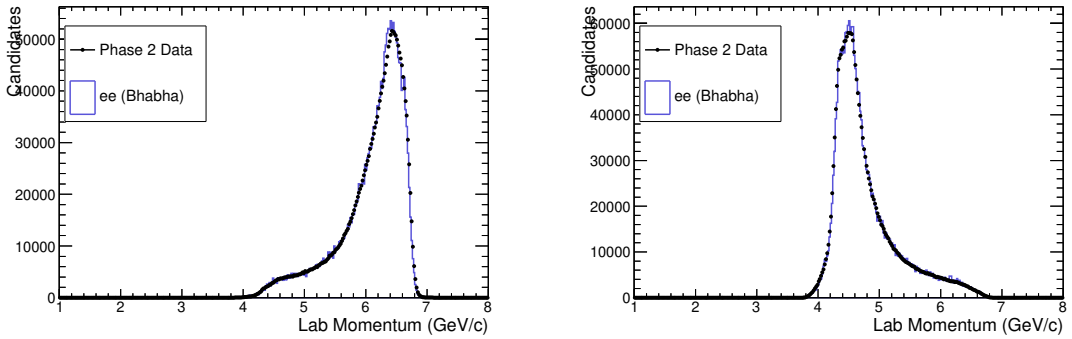

(a) e^- (b) e^+

Figure A.2: p_{lab} distribution of tracks passing Bhabha selection and with cluster in calorimeter barrel. MC is scaled to data.

A.2 $e^+e^- \to e^+e^-e^+e^-$ Selection

To study lower momentum electrons, $e^+e^- \to e^+e^-e^+e^-$ two-photon events are selected with a requirement that one of the $e^\pm$ pairs is scattered at small angles relative to the beams and escape the detector. In this case the event topology consists of two lower momentum tracks in the detector.

To select these events, a pre-selection is initially applied requiring two oppositely

charged tracks that pass the following selection cuts.

- $p_T > 0.15$ GeV/c where p_T is the magnitude of the transverse momentum.
- $|d_0| < 0.5$ cm
- $|z_0| < 1$ cm where z_0 is the z coordinate of the point of closest approach to the interaction point.
- $\mathrm{E_{ecl}} > 0$ GeV
- Calorimeter cluster is in the calorimeter barrel ($32.2 < \theta < 128.7$ degrees).
- Track has no hits in SVD and PXD detectors. During Phase 2 a segment of the SVD and PXD detectors was installed, covering a small azimuthal angle of the detector acceptance. At the time of this analysis, the data calibration and simulation validation for these detectors was ongoing. This veto ensures during reconstruction the track quantities such as p_{Lab}, z_0 and d_0 were not computed using unreliable information from these detectors.
- Tracks selected in the MC samples are required to be MC truth matched to a particle. This is done as in simulation beam backgrounds are modelled using a beam background overlay approach. This approach uses data events collected from a pseudo-random trigger in order to collect a data sample of the detector readout with the noise characteristics of the Belle II detector during SuperKEKB collision operation but without the presence of a scattering event. For processes such as $e^+e^- \to e^+e^-e^+e^-$ that have relatively high cross sections, a small fraction of the pseudo-random trigger data will contain an event where an $e^+e^- \to e^+e^-e^+e^-$ scatter occurred. As the beam background overlays are reused when generating MC, this means when an $e^+e^- \to e^+e^-e^+e^-$ selection is applied these outlier events can be selected multiple times if the beam background satisfies the selection cuts and the generated MC particles where not in the analysis acceptance. By applying this veto, multiple counting of these backgrounds events is removed.

These criteria ensure the track originated near the interaction point and has an associated calorimeter cluster. To suppress backgrounds from Bhabhas and pair conversions, the invariant mass of the two tracks in the event, m_{ee}, is required to be in

the range $0.5 < m_{ee} < 2$ GeV/c^2. A low invariant mass is expected in these events as two high momentum tracks are not detected.

To suppress $e^+e^- \rightarrow \tau^+\tau^-$ and other backgrounds, the total 3-momentum of the two tracks in the centre-of-mass frame is computed using equation A.1 and the transverse component of $\vec{p}^{\,\mathrm{CMS}}_{\mathrm{Total}}$ is required to be less than 0.25 GeV/c.

$$\vec{p}^{\,\mathrm{CMS}}_{\mathrm{Total}} = \vec{p}^{\,\mathrm{CMS}}_{+} + \vec{p}^{\,\mathrm{CMS}}_{-} \tag{A.1}$$

After the cuts detailed above are applied, the primary remaining backgrounds are from other two-photon processes such as, $e^+e^- \rightarrow e^+e^-\mu^+\mu^-$ and $e^+e^-\pi^+\pi^-$. To reduce backgrounds from these processes the variable E/p is used. The E/p distribution of the tracks passing the pre-selection are shown in Figure A.3 with data and MC overlaid. Background processes included are $e^+e^- \rightarrow e^+e^-\mu^+\mu^-$, $\tau^+\tau^-$, $\pi^+\pi^-\gamma_{\mathrm{ISR}}$ and $K^+K^-\gamma_{\mathrm{ISR}}$ [1]. As seen from Figure A.3 the E/p distribution for the electrons will peak near one as electrons deposit their full energy in the calorimeter and the mass of the electron is small relative to its momentum in this sample. For muons the E/p distribution is typically much less than one as the majority of muons will ionize through the cluster consistently depositing $\sim$ 200 MeV independent of its momentum. To suppress the muon backgrounds both tracks in the selection are required to have 0.8 <E/p< 1.02. After applying this cut the invariant mass distribution of the remaining candidates is shown in Figure A.3.

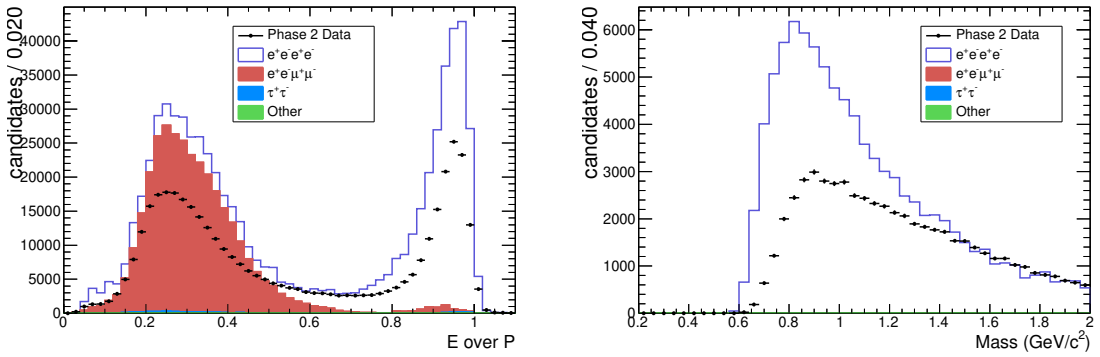

(a) (b)

Figure A.3: a) E/p of selected tracks before E/p cut is applied. b) m_{ee} distribution of events after E/p cut is applied. MC is scaled to 507.0 pb^{-1}. Trigger requirements and tracking/trigger efficiencies have not been applied to MC.

[1] MC samples for $e^+e^- \rightarrow e^+e^-\pi^+\pi^-$ could not be produced as there is no generator available in the Belle II software framework.

From the MC composition of the m_{ee} distribution in Figure A.3 it is found that low backgrounds remain after full selection requirements are applied. Comparing the data and MC distributions, an excess of MC events in the low mass region is observed. This excess is present as Level 1 trigger conditions and trigger/tracking efficiencies have not been applied to the MC. As it has been found in other studies of Phase 2 data that the drift chamber trigger efficiency was low during Phase 2 [60] it is expected that without applying these efficiencies in the MC there will be an excess of lower mass events in the MC. For the higher mass events, the MC excess is not as large, as these tracks would have produced a large enough calorimeter energy deposit for the calorimeter trigger to have fired. The drift chamber trigger inefficiency is further illustrated by the momentum distribution of the tracks passing the selection shown in Figure A.4. To account for these inefficiencies, the overall data inefficiency is computed as a function of the track momentum using equation A.2.

$$\mathcal{E}(p_{\mathrm{Lab}}) = \frac{n_{Data}(p_{\mathrm{Lab}})}{n_{Mc}(p_{\mathrm{Lab}})} \tag{A.2}$$

where $n_{\mathrm{Data}}(p_{\mathrm{Lab}})/n_{\mathrm{MC}}(p_{\mathrm{Lab}})$ is the number of tracks selected in the data/MC for a given momentum bin in Figure A.4. The computed efficiency, $\mathcal{E}(p_{\mathrm{Lab}})$, for the electrons is shown in Figure A.4. Using $\mathcal{E}(p_{\mathrm{Lab}})$ the tracks passing the final selection are rescaled. The resulting p_{lab} distributions are overlaid in Figure A.4 and as expected, the rescaled MC is in agreement with the data distribution. In addition compared to the Bhabha sample in the previous selection, Figure A.4 demonstrates this selection provides a low background sample of lower momentum electrons.

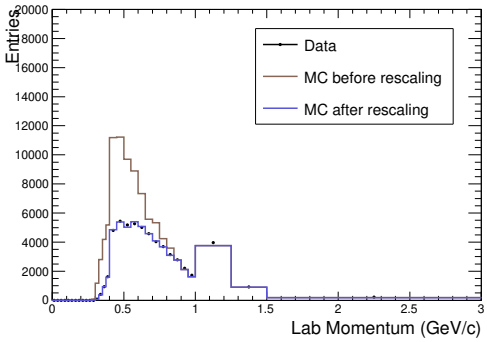

(a) e^-

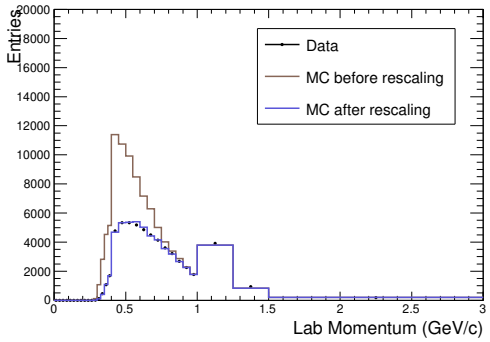

(b) e^+

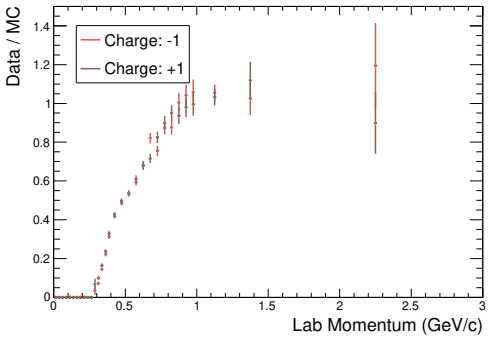

(c) $\mathcal{E}(P_{Lab})$

Figure A.4: a) and b) p_{lab} distributions of electrons passing $e^+e^- \to e^+e^-e^+e^-$ selection. c) $\mathcal{E}(p_{\text{Lab}})$ used to rescale MC to account for the drift chamber trigger and tracking in-efficiencies in the data.

A.3 $e^+e^- \to \mu^+\mu^-(\gamma)$ Selection

Samples of muons and photons are selected using radiative muon scattering, $e^+e^- \to \mu^+\mu^-(\gamma)$, events. The pre-selection requires the event to have exactly two oppositely charged tracks that pass the following criteria:

- $p_T > 0.15$ GeV/c where p_T is the magnitude of the transverse momentum.
- $|d_r| < 0.5$ cm, where d_r is the transverse distance to the interaction point
- $|z_0| < 4$ cm, where z_0 is the z coordinate of the point of closest approach to the interaction point.
- Number of hits in the drift chamber > 0.

- $E_{ecl} < 1$ GeV.
- Calorimeter cluster is in the calorimeter barrel ($32.2 < \theta < 128.7$ degrees).
- $E/p \leq 0.6$.
- Track has no hits in SVD and PXD detectors. During Phase 2 a segment of the SVD and PXD detectors was installed, covering a small azimuthal angle of the detector acceptance. At the time of this analysis, the data calibration and simulation validation for these detectors was ongoing. This veto ensures during reconstruction the track quantities such as $p_{\rm Lab}$, z_0 and d_0 were not computed using unreliable information from these detectors.

These cuts ensure the muon candidate tracks originate near the interaction point and have an associated calorimeter cluster. By requiring $E_{ecl} < 1$ GeV, Bhabha backgrounds are suppressed. In addition to the two charged tracks, the event is required to have at least one neutral calorimeter cluster passing the following criteria.

- $E_{ecl} \geq 0.05$ GeV.
- $W_{\rm sum} > 1.5$, where $W_{\rm sum}$ is the sum of the weights, ranging from 0 to 1, assigned to the crystals in the cluster and measure the relation of the crystal to the cluster. Typically crystals are assigned a weight of 1.0.
- Calorimeter cluster is in the calorimeter barrel ($32.2 < \theta < 128.7$ degrees).

With these particles, all $e^+e^- \to \mu^+\mu^-(\gamma)$ candidates with total invariant mass, $m_{\mu\mu\gamma}$, in the range $10 < m_{\mu\mu\gamma} < 11$ GeV/c^2 are reconstructed. In Figure A.5 the invariant mass of the two muon candidates, $m_{\mu\mu}$, is shown for all candidates passing the above pre-selection criteria. In this figure, peaks in the low mass region are observed from background processes $e^+e^- \to \pi^+\pi^-\gamma_{\rm ISR}$ and $e^+e^- \to K^+K^-\gamma_{\rm ISR}$. In these events the muons are mis-identified as pions/kaons from ρ/ϕ decays. Other backgrounds from $e^+e^- \to\ e^+e^-e^+e^-$, $e^+e^-\mu^+\mu^-$ and $\tau^+\tau^-$ are found to be negligible.

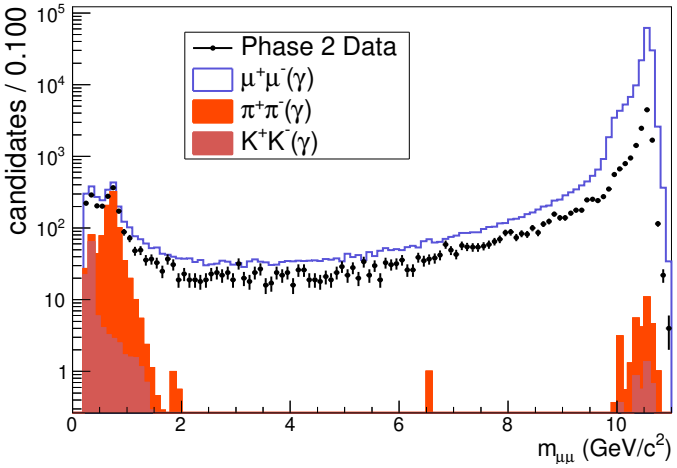

Figure A.5: $m_{\mu\mu}$ distribution of candidates passing pre-selection. MC is scaled to 507.0 pb^{-1}. Trigger requirements and trigger/tracking efficiencies have not been applied to MC.

To suppress the backgrounds from the $e^+e^- \to \pi^+\pi^-\gamma_{\rm ISR}$ and $e^+e^- \to K^+K^-\gamma_{\rm ISR}$, a cut is applied requiring $m_{\mu\mu} > 1.5$ GeV/c^2.

After applying the above requirements, a single event can potentially have multiple photon candidates if there are additional neutral clusters produced by beam backgrounds. This frequently occurs at photon energies below 0.5 GeV. To ensure the photon candidate selected is consistent with the process $e^+e^- \to \mu^+\mu^-(\gamma)$, the recoil 4-momentum of the muons, $\mathbf{P}^{\rm Lab}_{\rm recoil}$, is computed using equation A.3.

$$\mathbf{P}^{\rm Lab}_{\rm recoil} = \mathbf{P}^{\rm Lab}_{\rm beams} - \mathbf{P}^{\rm Lab}_{\mu\mu} \tag{A.3}$$

where $\mathbf{P}^{\rm Lab}_{\mu\mu}$ is the sum of the 4-momenta of the two tracks in the event. Using $\mathbf{P}^{\rm Lab}_{\rm recoil}$, $\alpha_{\rm recoil,\gamma}$ defined as the angle between the $\mathbf{P}^{\rm Lab}_{\rm recoil}$ 3-momentum vector and the measured photon candidates 3-momentum is computed and required to be less than 0.2 rad. In addition the ratio of the magnitudes of the $\mathbf{P}^{\rm Lab}_{\rm recoil}$ 3-momentum and the measured photon candidates 3-momentum is required to be less than 2.0. If two photon candidates pass this full selection criteria, the higher energy candidate is used.

After applying the full selection requirements the momentum distributions of the selected muon and photon candidates are shown in Figure A.6. In these figures the *MC before rescaling* distribution shows the results of the selection without any efficiency corrections applied and as expected these distributions show an excess of candidates in the MC relative to the data. This excess is expected as the trigger

requirements and trigger/tracking efficiencies have not been applied to the MC. As discussed in the previous section, the drift chamber trigger had low efficiency during Phase 2 data taking and thus it is expected that events with high $m_{\mu\mu}$ that rely on the drift chamber trigger to have lower efficiency. This means that the events with higher momentum muons, corresponding to the lower momentum photons, are expected to have lower efficiency than the events with lower momentum muons and higher momentum photons, as in this case the calorimeter trigger would be activated by the photon. Using the momentum distributions in Figure A.6 labelled *MC before rescaling*, the momentum dependent efficiency corrections are computed using equation A.2 defined in the previous section. The computed efficiency is shown in Figure A.6 and from this figure the transition from the drift chamber trigger to the calorimeter trigger can be seen as when the photon energy drops below 1 GeV there is a drop in efficiency observed. Following the same procedures as outlined in the $e^+e^- \to e^+e^-e^+e^-$ section, the MC is rescaled to account for the detector inefficiencies in the data. The rescaled momentum distribution is overlaid in Figure A.6 and as expected agrees well with the data.

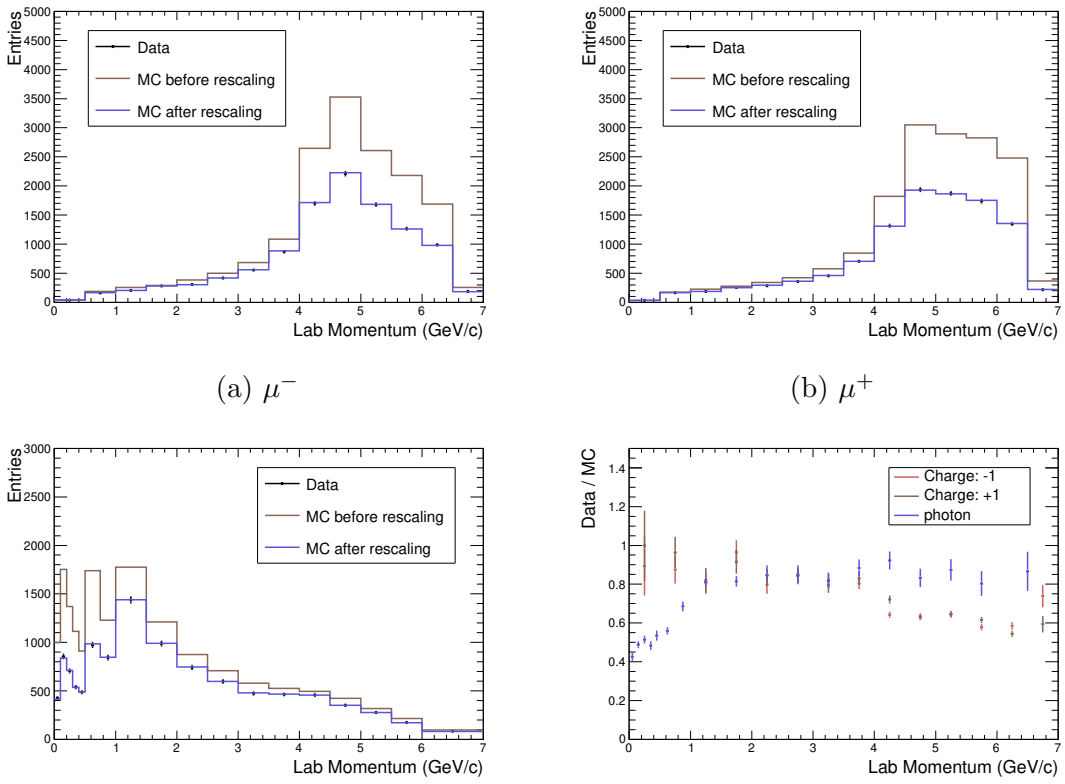

(a) μ^- (b) μ^+

(c) γ (d) μ^+

Figure A.6: a), b) and c) Lab momentum distribution of muon and photon candidates passing full $e^+e^- \to \mu^+\mu^-(\gamma)$ selection. d) $\mathcal{E}(p_{\text{Lab}})$ computed for the selected muon and photon samples.

A.4 $K^0_S \to \pi^+\pi^-$ Selection

K^0_S's are produced frequently in the Belle II detector and decay to two charged pions with a branching fraction of 69.2 % [2]. The K^0_S lifetime is long enough such that numerous K^0_S decays occur several centimetres from the interaction point, forming displaced vertices in the Belle II detector. This topology allows $K^0_S \to \pi^+\pi^-$ decays to be selected based only on kinematic requirements, providing a sample of $\pi^\pm$'s for studying calorimeter interactions.

Displaced vertices in the Belle II detector are reconstructed during offline data reconstruction and potential $K^0_S \to \pi^+\pi^-$ candidates are saved in a particle list called stdKshorts. This particle list contains displaced vertex candidates where a vertex constrained fit was applied and the invariant mass of the two tracks, $m_{\pi\pi}$, was

in the range $0.45 < m_{\pi\pi} < 0.55$ GeV [61].

For this study a pre-selection of $K^0_S \to \pi^+\pi^-$ candidates are selected from the stdKshorts particle list and requiring the event to have three or more tracks satisfying the conditions:

- $|\vec{p}_T| > 0.15$ GeV/c
- $|d_0| < 4$ cm
- $|z_0| < 6$ cm

Note these tracks do not need to be associated with the K^0_S candidate.

To improve the purity of the candidates in the stdKshorts particle list, a momentum dependent cut on the angle between the K^0_S candidates momentum vector and the decay vertex vector, ϕ_{KS}, is applied. The cut values used are from reference [62] and are as follows:

$$|p^{Lab}_{KS}| < 0.5 \text{ GeV/c and } \phi_{Ks} < 0.3 \text{ rad}$$
$$\text{OR}$$
$$|p^{Lab}_{KS}| < 1.5 \text{ GeV/c and } \phi_{Ks} < 0.1 \text{ rad}$$
$$\text{OR}$$
$$\phi_{KS} < 0.03 \text{ rad}$$

After applying these requirements the $m_{\pi\pi}$ distribution of the remaining K^0_S candidates is shown in Figure A.7. In addition the decay vertex displacement of the K^0_S candidates are also shown in Figure A.7. The $m_{\pi\pi}$ distribution shown in Figure A.7 has a peak from true K^0_S decays over a small background. A final mass window cut of $0.493 < m_{\pi\pi} < 0.502$ GeV/c^2 is applied.

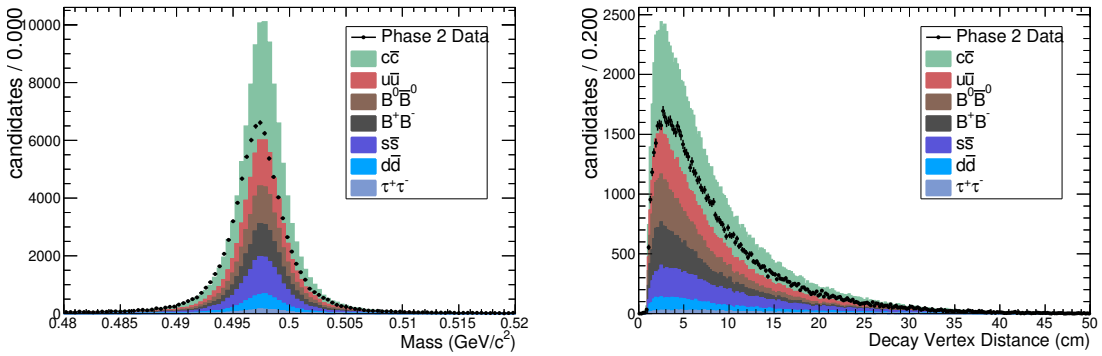

(a) (b)

Figure A.7: Selection plots for $K^0_S \to \pi^+\pi^-$. MC is scaled to 507.0 pb^{-1}. Trigger requirements and trigger/tracking efficiencies have not been applied to MC.

In Figure A.8 the momentum distribution of the selected $\pi^\pm$ tracks with a calorimeter cluster with energy below 2 GeV and in the barrel region is shown. In this figure the *MC before rescaling* is the total MC normalized to 507.0 pb^{-1}. To account for inefficiencies in the MC $\mathcal{E}(p_{\text{Lab}})$ is computed for the selected pion tracks and is also shown in Figure A.8. Using $\mathcal{E}(p_{\text{Lab}})$, the MC is rescaled to produce the *MC after rescaling* MC distribution in Figure A.8.

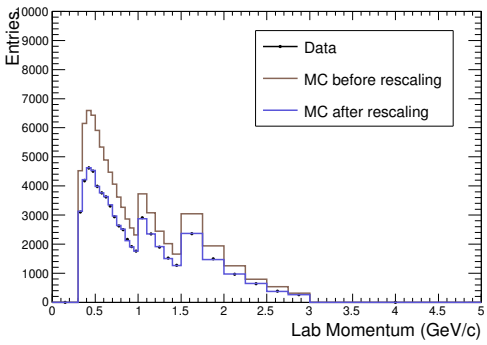

(a) π^-

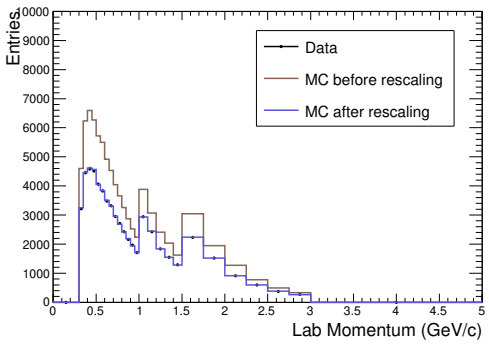

(b) π^+

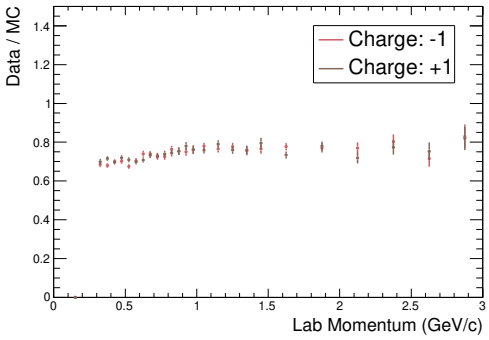

(c)

Figure A.8: a) and b) Lab momentum of pion samples selected. c) $\mathcal{E}(p_{\text{Lab}})$ computed for pion selection and used for MC re-scaling to account for in-efficiencies during data-taking.

The sample purity is evaluated with MC by computing as a function of the track lab momentum the fraction of selected tracks in MC that are matched to be a true pion. This is shown in Figure A.9. Below 1 GeV/c the sample selected has very high purity with $> 99\%$ of tracks matched to true pions. Above 1 GeV/c the decrease in purity is from proton and anti-proton contamination in the sample.

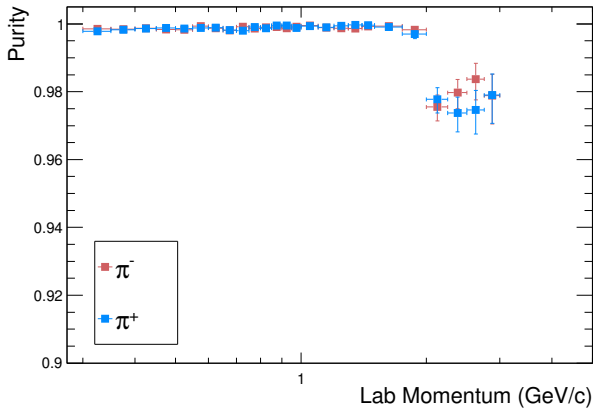

Figure A.9: Purity of pion sample as a function of pion lab momentum estimated with MC.

A.5 Charged kaon and proton Selections

The Phase 2 dataset was not large enough to kinematically select control samples of $K^{\pm}$ or $p^{\pm}$ that provided high statistics and high purity. As a result $K^{\pm}$ and $p^{\pm}$ samples are selected by a track level selection using the CDC and TOP detectors.

A pre-selection is performed selecting all tracks passing the criteria listed below. In addition the event is required to have > 4 good tracks and only data runs outside the run range of 2824-3548 are used as during these runs the TOP detector was not available. The track requirements for the pre-selection are:

- $0.3 < p_{\text{Lab}} < 3$ GeV/c
- $\text{E}_{\text{ecl}} > 0.05$ GeV
- Calorimeter cluster is in the calorimeter barrel ($32.2 < \theta < 128.7$ degrees).
- $|z_0| < 1$ cm
- $|d_0| < 0.5$ cm
- Track has no hits in SVD and PXD detectors. During Phase 2 a segment of the SVD and PXD detectors was installed, covering a small azimuthal angle of the detector acceptance. At the time of this analysis, the data calibration and simulation validation for these detectors was ongoing. This veto ensures during

reconstruction the track quantities such as p_{Lab}, z_0 and d_0 were not computed using unreliable information from these detectors.

- For MC, the track must be truth matched to a generated particle. This requirement removes tracks from beam backgrounds and is applied to avoid double counting tracks from beam background. As the beam overlays used in simulation are re-used, if the background overlay included a track that passed the above requirements then the same track can be selected multiple times if this veto is not applied.

After applying this pre-section, $K^{\pm}$ and $p^{\pm}$ candidates are identified using the CDC and TOP detectors by applying the following criteria.

A.5.1 $K^{\pm}$ Selection

The $K^{\pm}$ selection is optimized in momentum bins of $p_{\text{Lab}} < 0.5$ GeV/c, $0.5 \leq p_{\text{Lab}} < 1$ GeV/c and $p_{\text{Lab}} \geq 1$ GeV/c. Charged kaons are selected based on the CDC kaon log-likelihood, LL_K^{CDC}, computed during reconstruction from the CDC dE/dx measurements and using the variable P_K^{TOP} defined as,

$$P_K^{TOP} = \frac{LL_K^{TOP}}{LL_K^{TOP} + LL_\pi^{TOP} + LL_p^{TOP} + LL_e^{TOP} + LL_\mu^{TOP}} \tag{A.4}$$

where LL_X^{TOP} is the TOP log-likelihood for the particle X.

In Figure A.10 the distribution of LL_K^{CDC} for the $p_{\text{Lab}} < 0.5$ GeV/c tracks passing the pre-selection are shown including a zoom in range $-3 < LL_K^{CDC} < 0$ to highlight the kaons in the sample. Figure A.10 demonstrates that $p_{\text{Lab}} < 0.5$ GeV/c kaons can efficiently be selected by requiring the track has $LL_K^{CDC} > -1$.

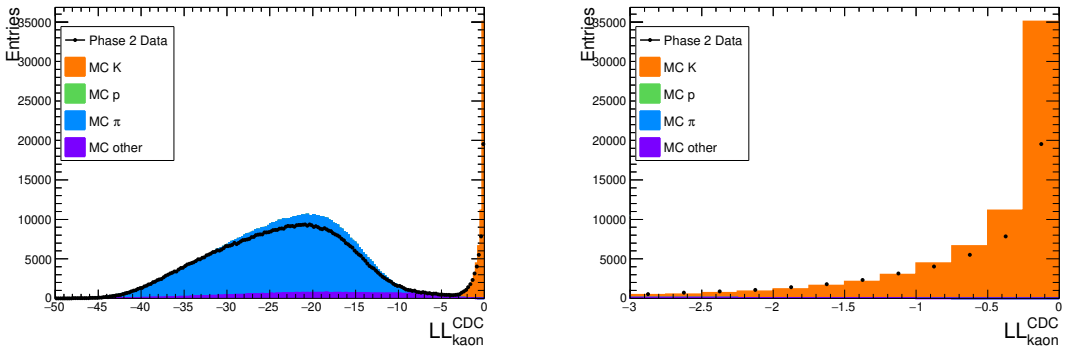

(a) (b)

Figure A.10: Distribution of LL_K^{CDC} for the $p_{\text{Lab}} < 0.5$ GeV/c tracks passing the pre-selection. MC is scaled to 372.0 pb^{-1}. Efficiencies have not been applied to MC.

Kaons in the momentum range $0.5 \leq p_{\text{Lab}} < 1$ GeV/c are identified using the CDC and TOP detectors. In Figure A.11 the distribution of LL_K^{CDC} is shown for the $0.5 \leq p_{\text{Lab}} < 1$ GeV/c tracks passing the pre-selection. From this figure kaons can efficiency be selected by requiring $LL_K^{CDC} > -1$ however a large background from pions remains. After requiring $LL_K^{CDC} > -1$, P_K^{TOP} is shown in Figure A.11. Figure A.11 shows that the remaining backgrounds can be suppressed by requiring $P_K^{TOP} < 0.17$.

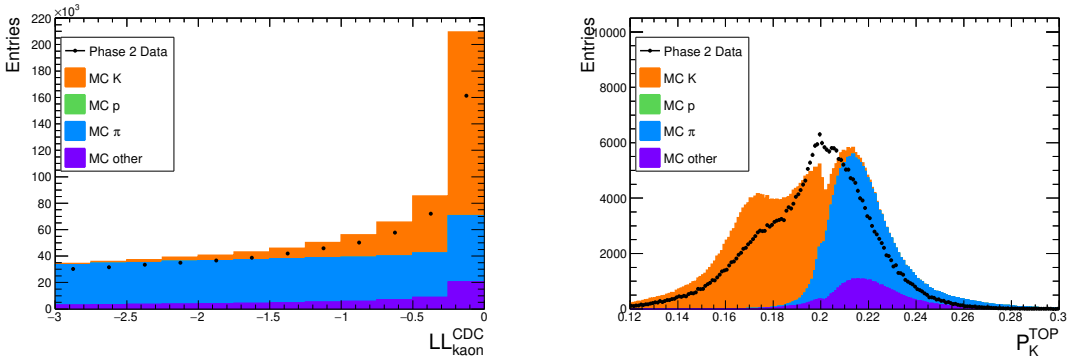

(a) (b)

Figure A.11: Kaon selection with a) CDC and b) TOP. MC is scaled to 372.0 pb^{-1}. Efficiencies have not been applied to MC.

Kaons in the momentum range $p_{\text{Lab}} \geq 1$ GeV/c are identified using only the TOP detector. The distribution of P_K^{TOP} for tracks in the momentum range $p_{\text{Lab}} \geq 1$

GeV/c is shown in Figure A.12. From this figure, a high purity sample of kaons can be isolated by requiring $P_K^{TOP} < 0.18$.

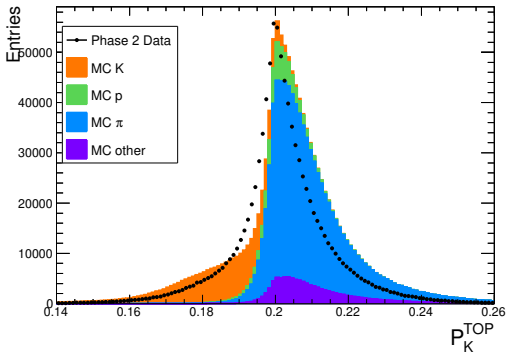

Figure A.12: Kaon selection with a) CDC and b) TOP. MC is scaled to 372.0 pb^{-1}. No tracking or trigger efficiencies have been applied to MC.

After applying the above selections the momentum distributions of the remaining candidates is shown in Figure A.13. As expected discontinuities are observed at the boundaries of the different momentum regions due to the momentum dependent cut optimizations. In Figure A.13 the MC before rescaling shows the total MC is scaled to 372.0 pb^{-1} with no efficiencies (tracking, trigger etc.) applied. In order to account for these inefficiencies, $\mathcal{E}(p_{\text{Lab}})$ as defined above, is computed and is also shown in Figure A.13. Using $\mathcal{E}(p_{\text{Lab}})$, the MC is rescaled producing the rescaled MC distribution in Figure A.13. As expected the MC rescaled in Figure A.13 agrees well with the data.

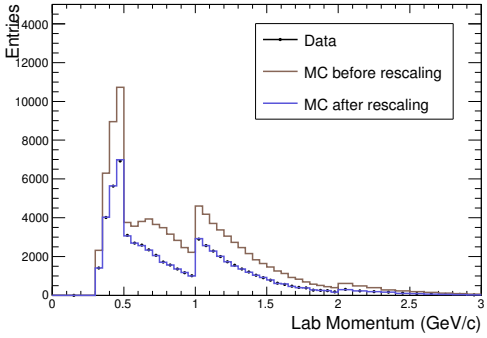

(a) K^-

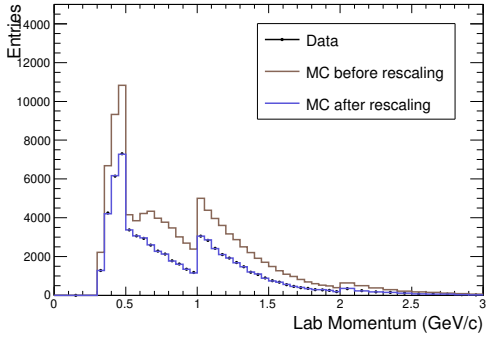

(b) K^+

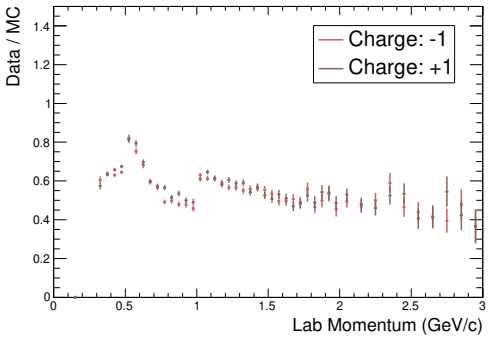

(c) $\mathcal{E}(P_{Lab})$

Figure A.13: a) and b) Lab momentum of charged kaon samples selected. c) $\mathcal{E}(p_{\text{Lab}})$ for the pion selection and used for MC re-scaling.

A.5.2 $p/\bar{p}$ Selection

The TOP and CDC requirements for identifying protons were optimized in momentum bins of $p_{\text{Lab}} < 1.0$ GeV/c, $1 < p_{\text{Lab}} < 2$ GeV/c and $p_{\text{Lab}} > 2$ GeV/c. Analogous to the charged kaon selection, protons are identified using the CDC proton log-likelihood LL_p^{CDC} and the variable P_p^{TOP} defined in equation A.5.

$$P_p^{TOP} = \frac{LL_p^{TOP}}{LL_K^{TOP} + LL_\pi^{TOP} + LL_p^{TOP} + LL_e^{TOP} + LL_K\mu^{TOP}} \tag{A.5}$$

The LL_p^{CDC} distribution for the pre-selected tracks with $p_{\text{Lab}} < 1.0$ GeV/c is shown in Figure A.14. As seen in Figure A.14, protons can efficiently be selected by requiring $LL_p^{CDC} > -1$.

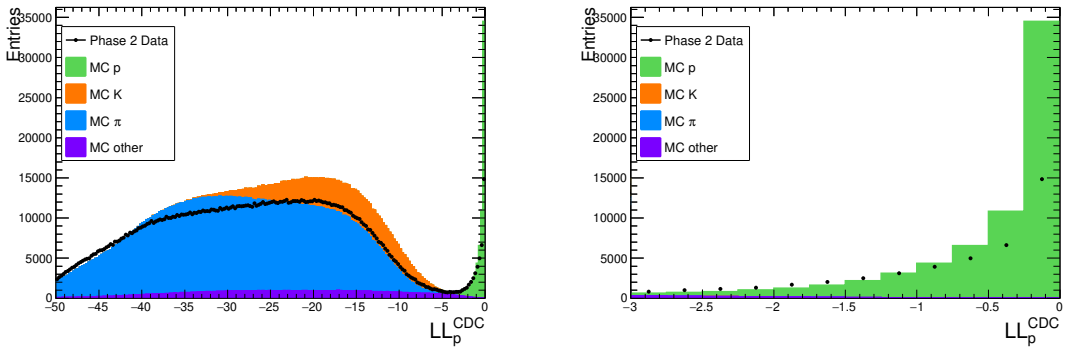

(a) LL_p^{CDC}

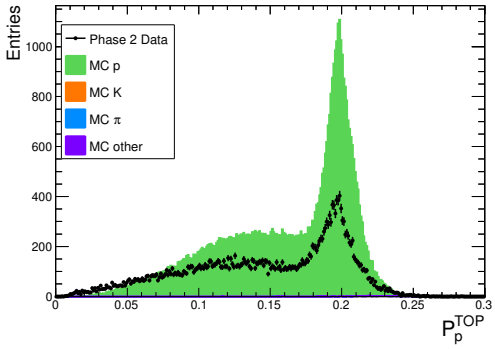

(b) P_p^{TOP}

Figure A.14: Proton selection plots. MC is scaled to 372.0 pb^{-1}. Efficiencies have not been applied to MC.

After requiring $LL_p^{CDC} > -1$ the distribution of P_p^{TOP} for the remaining tracks is shown in Figure A.14. From this distribution the remaining background, mainly from electrons, are suppressed by requiring $P_p^{TOP} < 0.18$.

For the momentum range $1 < p_{\text{Lab}} < 2$ GeV/c the proton selection adds a veto on tracks with $0.9 \leq \text{E}/p \leq 1.05$. This veto is applied to remove electrons from the sample. After this veto is applied, tracks in the momentum range $1 < p_{\text{Lab}} < 2$ GeV/c are identified as protons using the CDC and TOP detectors. In Figure A.15 LL_p^{CDC} is shown for all $1 < p_{\text{Lab}} < 2$ GeV/c tracks passing the pre-selection. From this figure protons can efficiently be selected by requiring $LL_p^{CDC} > -1$. To reduce the significant backgrounds remaining from pions and kaons, the TOP detector is used. After requiring $LL_p^{CDC} > -1$ the distribution for P_{TOP}^p is shown in Figure A.11. From Figure A.11 the remaining background can be suppressed by requiring $P_{TOP}^p < 0.17$.

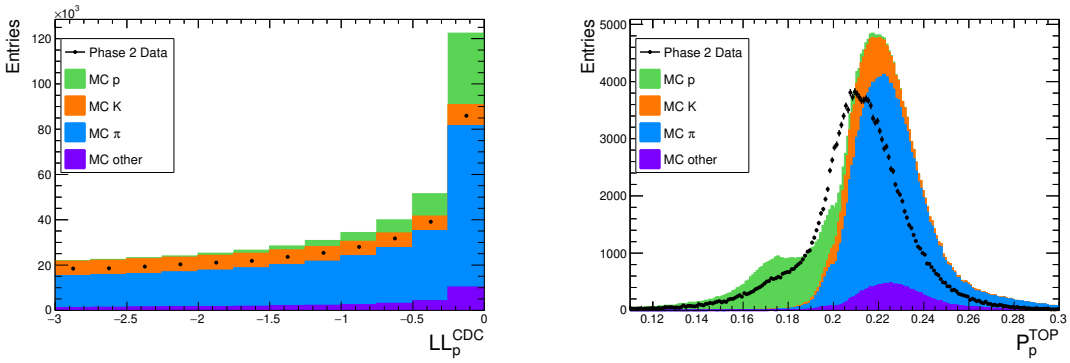

(a) (b)

Figure A.15: Proton selection with a) CDC and b) TOP. MC is scaled to 372.0 pb^{-1}. Efficiencies have not been applied to MC.

For the momentum range $p_{\text{Lab}} > 2$ GeV/c the proton selection also includes a veto on tracks with $0.9 \leq \text{E}/p \leq 1.05$ to remove electrons from the sample. Protons in the momentum range $p_{\text{Lab}} > 2$ GeV/c are identified by requiring $LL_p^{CDC} > -1$ followed by a cut on using the P_{TOP}^{proton}. The distribution of P_{TOP}^{proton} for tracks in the pre-selection with $p_{\text{Lab}} > 2$ GeV/c are shown in Figure A.16. Demonstrated by this figure, a high purity sample of protons can be isolated by requiring $P_{TOP}^{proton} < 0.18$.

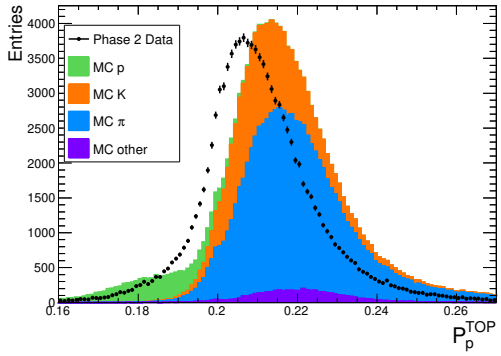

Figure A.16: Proton selection with a) CDC and b) TOP. MC is scaled to 372.0 pb^{-1}. Efficiencies have not been applied to MC.

After applying the above selections the momentum distributions of the selected proton tracks is shown in Figure A.17. As expected due to the momentum dependent cut optimizations, discontinuities are observed at the boundaries of the different momentum regions. Following the same procedures in the kaon selection, $\mathcal{E}(p_{\text{Lab}})$ is

computed for the tracks passing the proton selection and is shown in Figure A.17. Using $\mathcal{E}(p_{\text{Lab}})$ the momentum distribution of the MC tracks is rescaled.

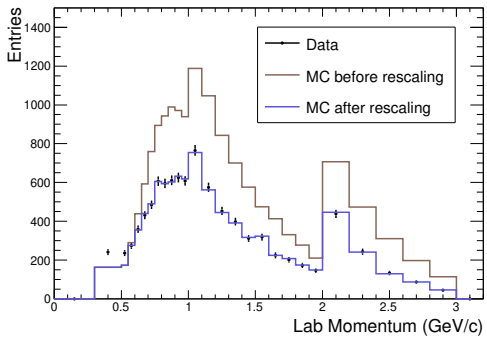

(a) p^-

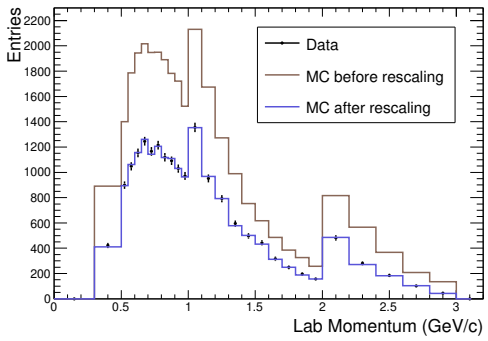

(b) p^+

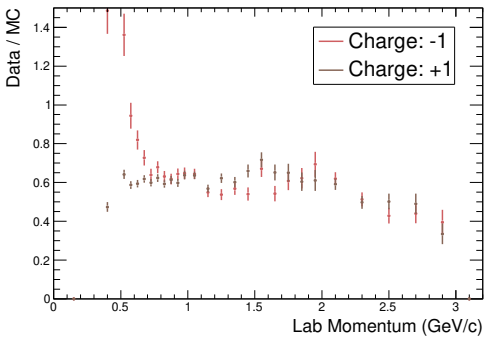

(c) $\mathcal{E}(P_{Lab})$

Figure A.17: a) and b) Lab momentum of selected tracks identified as protons. c) $\mathcal{E}(p_{\text{Lab}})$ for the proton selection and used for MC re-scaling.

Appendix B

Selection of a K_L^0 Control Sample in Belle II Phase 2 Data

This appendix details the selection criteria used to isolate a K_L^0 control sample from the Belle II Phase 2 dataset using $e^+e^- \to \phi\gamma_{\rm ISR} \to K_S^0 K_L^0 \gamma_{\rm ISR}$ events. First an initial pre-selection is defined to establish a sample based on a set of minimal selection requirements. With the pre-selection the full selection methodology is then developed. After the selection methodology is discussed, the additional cuts applied to define the full selection requirements are detailed.

B.1 Candidate Pre-Selection

The $e^+e^- \to K_S^0 K_L^0 \gamma_{\rm ISR}$ candidate selection requires the K_S^0 to be reconstructed as $K_S^0 \to \pi^+\pi^-$ and the K_L^0 and $\gamma_{\rm ISR}$ to be detected as neutral calorimeter clusters. To suppress backgrounds from $B\bar{B}$ and $q\bar{q}$, the event is required to have less than three tracks, each of which passes the following requirements:

- $p_T > 0.15$ GeV/c
- $|d_0| < 4$ cm
- $|z_0| < 6$ cm

$K_S^0 \to \pi^+\pi^-$ candidates are reconstructed as displaced vertices and from tracks originating from the interaction point. Initially all $K_S^0 \to \pi^+\pi^-$ candidates in the invariant mass range $0.3 < m_{\pi\pi} < 0.7$ GeV/c^2 are reconstructed. A vertex constrained fit is

then applied and an updated invariant mass, $m_{\pi\pi}^{\text{fit}}$, is computed. For this pre-selection the K_S^0 candidates are required to have $0.45 < m_{\pi\pi}^{\text{fit}} < 0.55$ GeV/c^2. In addition, the γ_{ISR} candidate is required to have:

- $E^{\text{CMS}} > 3$ GeV
- Calorimeter cluster is in the calorimeter barrel ($32.2 < \theta < 128.7$ degrees).

The K_L^0 candidate is required to have:

- $\text{E}_{\text{ecl}} > 0.05$ GeV
- Calorimeter cluster is in the calorimeter barrel ($32.2 < \theta < 128.7$ degrees).

B.2 Selection Methodology

An advantage of studying K_L^0's with $e^+e^- \to K_S^0 K_L^0 \gamma_{\text{ISR}}$ events is that the momentum of the K_L^0 can be computed using the detected K_S^0 and γ_{ISR} by applying total energy conservation. This is required as the K_L^0 momentum cannot directly measured by the Belle II detector as K_L^0's do not leave a track in the drift chamber and energy losses in hadronic showers prevent the K_L^0 energy from being precisely measured by the calorimeter.

For the process $e^+e^- \to K_S^0 K_L^0 \gamma_{\text{ISR}}$, the K_L^0 total energy in the lab frame can be computed using equation B.1.

$$\text{E}_{\text{KL}}^{\text{calc}} = \text{E}_{\text{Total}}^{\text{Lab}} - \text{E}_{\text{KS}}^{\text{Lab}} - \text{E}_{\gamma ISR}^{\text{Lab}} \tag{B.1}$$

Equation B.1 applies total energy conservation and takes advantage of the property of electron-positron colliders that the initial collision 4-momentum is known. In equation B.1, $\text{E}_{\text{Total}}^{\text{Lab}} = \text{E}_{\text{e+}}^{\text{Lab}} + \text{E}_{\text{e-}}^{\text{Lab}}$ is the total collision energy in the lab frame, $\text{E}_{\text{KS}}^{\text{Lab}}$ is the measured total energy of the reconstructed K_S^0 and $\text{E}_{\gamma ISR}$ is the measured energy of the γ_{ISR} candidate. With $\text{E}_{\text{KL}}^{\text{calc}}$, the magnitude of the K_L^0 momentum in the lab frame, $p_{\text{KL}}^{\text{calc}}$, can be computed using equation B.2, where m_{KL} is the mass of the K_L^0. The precision of $p_{\text{KL}}^{\text{calc}}$ is evaluated at the end of this appendix, after all selection cuts have been outlined.

$$p_{\text{KL}}^{\text{calc}} = \sqrt{\text{E}_{\text{KL}}^{\text{calc}\,2} - {m_{\text{KL}}}^2} \tag{B.2}$$

In the ideal case an $e^+e^- \to K^0_S K^0_L \gamma_{\rm ISR}$ event will contain only two neutral calorimeter clusters corresponding to the $\gamma_{\rm ISR}$ and K^0_L. This is rarely the case however as events typically contain additional neutral clusters produced by hadronic split-offs from the K^0_L or pion hadronic showers and/or clusters from beam background photons or neutrons. In addition the Belle II calorimeter clustering algorithm is optimized for photon clusters that typically have symmetry about the cluster centre compared to hadronic showers. This results in a single K^0_L hadronic shower to sometimes be classified as two nearby clusters. As the $\gamma_{\rm ISR}$ is required to have $E^{\rm CMS} > 3$ GeV (in the full selection, detailed below, this is increased to 4 GeV), there is generally only one $\gamma_{\rm ISR}$ candidate in the event. The lower energy requirement on the K^0_L cluster however can result in a single event to have multiple K^0_L candidates. In addition, background processes such as $e^+e^- \to K^0_L K^0_S \gamma_{\rm ISR} \pi^0$, can potentially also have similar detector signatures to $e^+e^- \to K^0_S K^0_L \gamma_{\rm ISR}$ events. A method for determining the K^0_L candidate most consistent with the process $e^+e^- \to K^0_S K^0_L \gamma_{\rm ISR}$ thus was developed. This is done by ensuring the $K^0_S K^0_L \gamma_{\rm ISR}$ candidate is consistent with the K^0_S and K^0_L originating from an intermediate ϕ through the process $e^+e^- \to \phi\gamma_{\rm ISR} \to K^0_S K^0_L \gamma_{\rm ISR}$. By enforcing this constraint, the location of the calorimeter cluster associated with the K^0_L can be used to evaluate if the K^0_L candidate is likely a true K^0_L.

As K^0_L's have straight trajectories to the calorimeter, the angular location of the K^0_L calorimeter cluster defined by, $\theta_{\rm ECL}$ and $\phi_{\rm ECL}$, can be used with $p^{\rm calc}_{\rm KL}$ to compute the 3-momentum of the K^0_L candidate, $\vec{p}^{\,\rm calc}_{\rm KL}$, using equation B.3.

$$\vec{p}^{\,\rm calc}_{\rm KL} = \begin{bmatrix} p^{\rm calc}_{\rm KL} \sin(\theta_{\rm ECL}) \cos(\phi_{\rm ECL}) \\ \\ p^{\rm calc}_{\rm KL} \sin(\theta_{\rm ECL}) \sin(\phi_{\rm ECL}) \\ \\ p^{\rm calc}_{\rm KL} \cos(\theta_{\rm ECL}) \end{bmatrix} \tag{B.3}$$

Together $\mathrm{E}^{\rm calc}_{\rm KL}$ and $\vec{p}^{\,\rm calc}_{\rm KL}$, define the 4-momentum of the K^0_L candidate, $\mathbf{P}^{\rm Lab}_{\rm KL}$. With $\mathbf{P}^{\rm Lab}_{\rm KL}$ and the measured K^0_S 4-momentum, $\mathbf{P}^{\rm Lab}_{\rm KS}$, the invariant mass of the $K^0_S K^0_L$ system, m^{calc}_{ϕ}, can be computed using equation B.4.

$$m^{\rm calc}_{\phi} = (\mathbf{P}^{\rm Lab}_{\rm KS} + \mathbf{P}^{\rm Lab}_{\rm KL})^2 \tag{B.4}$$

It is expected that if the K^0_L candidate is correctly associated with a K^0_L produced from the process $e^+e^- \to \phi\gamma_{\rm ISR} \to K^0_S K^0_L \gamma_{\rm ISR}$ then $m^{calc}_{\phi} = \mathrm{m}_{\phi} \approx 1019$ MeV/c^2 [2] will

be true.

To test the methodology above, $K^0_S K^0_L \gamma_{\rm ISR}$ candidates are selected from MC samples of $e^+e^- \to K^0_S K^0_L \gamma_{\rm ISR}$ using the pre-selection defined initially in Section B.1. In Figure B.1 the distribution of m_ϕ^{calc} is shown for all candidates selected. This distribution is normalized to the integrated Phase 2 luminosity. Outlined at the end of this Appendix, the final cut applied in this selection is to require $m_\phi^{calc} < 1.12$ GeV/c^2 and thus in Figure B.1 the candidates are highlighted depending if they are in the region $m_\phi^{calc} < 1.12$ GeV/c^2. This colour coding will be used in the remainder of this Appendix when distributions from signal MC are shown in order to highlight events in the $m_\phi^{calc} < 1.12$ GeV/c^2 region.

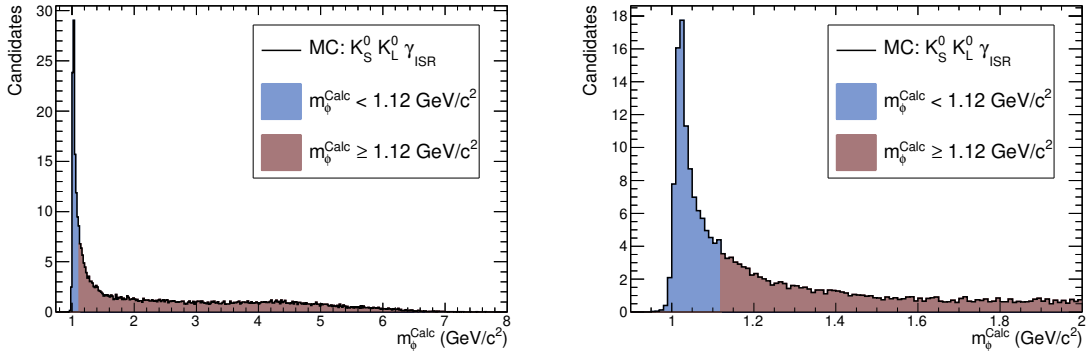

(a) Full Scale (b) ϕ Region Zoom

Figure B.1: Distribution of m_ϕ^{calc} computed for all candidates in $e^+e^- \to K^0_S K^0_L \gamma_{\rm ISR}$ MC sample passing pre-selection requirements defined in Section B.1. Distribution is normalized to Phase 2 integrated luminosity.

The distribution of m_ϕ^{calc} in Figure B.1 has a peak at m_ϕ^{calc}= m_ϕ followed by a tail of candidates to higher values of m_ϕ^{calc}. Many of the candidates in the tail of this distribution are from events that had an additional radiated photon (eg: $e^+e^- \to K^0_S K^0_L \gamma\gamma$) and thus equation B.1 cannot be used to compute the K^0_L energy. In addition the candidates in the tail can also be from when the cluster assigned to the K^0_L was produced by a beam background photon. The candidates in the peak region are identified as the candidates where the K^0_S and $\gamma_{\rm ISR}$ kinematics, in addition to the K^0_L cluster location, are consistent with the process $e^+e^- \to \phi\gamma_{\rm ISR} \to K^0_S K^0_L \gamma_{\rm ISR}$. For these candidates it is expected that the K^0_L candidate is correctly assigned to the K^0_L generated in the event. This is demonstrated by computing $\alpha_{\rm KL,ecl}$ defined as the angle between the momentum vector of the K^0_L generated in the event and

the K_L^0 candidate calorimeter cluster location vector. The distribution of $\alpha_{\mathrm{KL,ecl}}$ for all candidates in the pre-selection is shown in Figure B.2. In this distribution the same colour scheme as Figure B.1 is used to highlight the candidates that pass the $m_\phi^{calc} < 1.12$ GeV/c^2 requirement.

In Figure B.2 the distribution has a peak in the region $\alpha_{\mathrm{KL,ecl}} < 0.05$ rad demonstrating there is an excess of candidates where momentum vector of the K_L^0 generated in the event is pointing towards the K_L^0 candidate calorimeter cluster location. A tail to high values of $\alpha_{\mathrm{KL,ecl}}$ is also observed corresponding to K_L^0 candidates from calorimeter clusters that do not match the momentum direction of the generated K_L^0. This result demonstrates that requiring $m_\phi^{calc} < 1.12$ GeV/c^2 will ensure the K_L^0 candidate calorimeter cluster is in the direction of the true K_L^0 in the event.

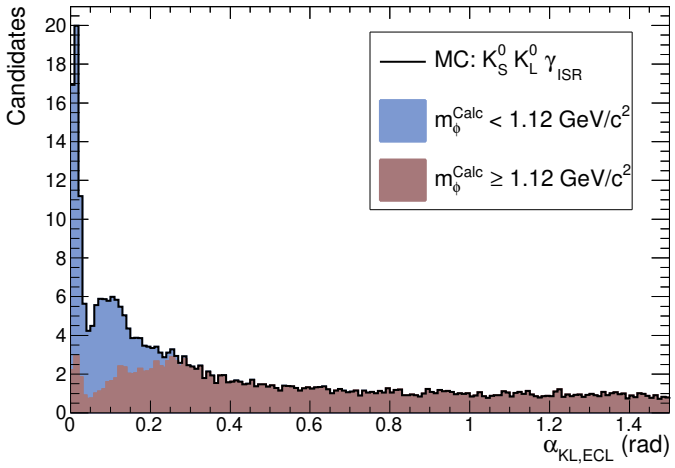

Figure B.2: Distribution of $\alpha_{\mathrm{KL,ecl}}$ computed from $e^+e^- \to K_S^0 K_L^0 \gamma_{\mathrm{ISR}}$ MC for all candidates passing pre-selection requirements defined in Section B.1. Distribution is normalized to Phase 2 integrated luminosity.

B.3 Selection Cuts

Section B.1 of this appendix outlined a pre-selection used to test the selection methodology with signal MC samples. Applying only the pre-selection requirements to data however is not sufficient to suppress a number of background processes and thus additional selection requirements are needed. The additional cuts applied are listed below, followed by a discussion of the motivations for the cuts.

In addition to the pre-selection in Section B.1, the $K_S^0 K_L^0 \gamma_{\mathrm{ISR}}$ candidate is required

to have:

1. $0.49 < m_{\pi\pi}^{\rm fit} < 0.505$ GeV/c^2, where $\rm m_{\pi\pi}^{fit}$ is the invariant mass of the K_S^0 candidate after the vertex constrained fit is applied.

2. $\rm E_{ECL}^{\pi} < 2$ GeV, where $\rm E_{ECL}^{\pi}$ is the calorimeter cluster energy of the $\pi^{\pm}$ used to reconstruct the K_S^0.

3. $1.9 < p_{\rm KS}^{\rm CMS} < 3.2$ GeV/c, where $p_{\rm KS}^{\rm CMS}$ is the magnitude of the K_S^0 momentum in the centre-of-mass frame.

4. $d_{\rm KS} > 1$ cm, where $d_{\rm KS}$ is the distance between the IP and the K_S^0 decay vertex.

5. $\phi_{\rm KS} < 0.1$ rad, where $\phi_{\rm KS}$ is the angle between the K_S^0 momentum vector and decay vertex vector.

6. $E_{\rm ISR}^{\rm CMS} > 4$ GeV.

7. $m_{\phi}^{calc} < 1.12$ GeV/c^2.

8. If a single event has multiple K_L^0 candidates passing the above requirements the candidate with the highest cluster energy is used.

Items 1-5 in the list above place tight requirements on the K_S^0 candidate. This begins by a mass window cut on the K_S^0 invariant mass distribution. Item 2 restricts the calorimeter cluster energy of the pions used to reconstruct the K_S^0 to be less than 2 GeV in order to remove fake K_S^0 candidates reconstructed with an e^+/e^- track. Item 3 applies a window cut on the K_S^0 momentum in the centre-of-mass frame. This cut was determined from Figure B.3a showing the distribution of $p_{\rm KS}^{\rm CMS}$ for the signal MC with the candidates in the $m_{\phi}^{calc} < 1.12$ GeV/c^2 region highlighted. As seen in this figure, the cut applied ensures the momentum of the K_S^0 candidate is consistent with the process $e^+e^- \to \phi\gamma_{\rm ISR} \to K_S^0 K_L^0 \gamma_{\rm ISR}$. The fifth and sixth cuts applied require the K_S^0 candidate is a displaced vertex and the momentum direction of the K_S^0 candidate is consistent with the K_S^0 originating from the interaction point. This cut suppresses backgrounds from process such as $(n\pi^0)\pi^+\pi^-\gamma_{\rm ISR}$ where n is an integer.

After applying the requirements on the K_S^0 candidate, item 7 in the cut list increases the threshold of the CMS energy for $\gamma_{\rm ISR}$ to be above 4 GeV. As discussed above, this selection is restricted to selecting $e^+e^- \to \phi\gamma_{\rm ISR} \to K_S^0 K_L^0 \gamma_{\rm ISR}$ events where an intermediate ϕ is produced. In this special case, $\gamma_{\rm ISR}$ has large fraction of the total

collision energy and thus the $\gamma_{\rm ISR}$ energy threshold can be increased with minimal impact on the selection efficiency. This is demonstrated by Figure B.3b showing the distribution of the reconstructed energy of $\gamma_{\rm ISR}$ for signal MC events with candidates with $m_\phi^{calc} < 1.12$ GeV/c^2 highlighted. The large energy deposit by $\gamma_{\rm ISR}$ also ensures Level 1 calorimeter trigger is activated.

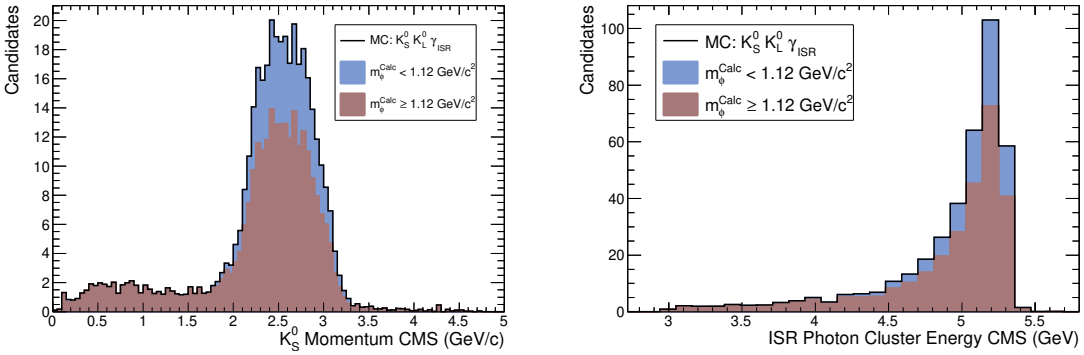

(a) a (b) b

Figure B.3: a) $p_{\rm KS}^{\rm CMS}$ b) $E_{\rm ISR}^{\rm CMS}$ distributions computed from $e^+e^- \to K_S^0 K_L^0 \gamma_{\rm ISR}$ MC for all candidates passing pre-selection requirements defined in Section B.1. Distribution is normalized to Phase 2 integrated luminosity.

After applying selection cuts 1-6 the distribution of m_ϕ^{calc} is shown in Figure B.4 for all remaining candidates with data and MC overlaid. Backgrounds labelled "Other" account for contributions from $e^+e^- \to d\bar{d}$, $u\bar{u}$, $\pi^0\pi^+\pi^-(\gamma)$, $\pi^0\pi^0\pi^+\pi^-(\gamma)$, $\eta^0\pi^+\pi^-(\gamma)$, $\mu^+\mu^-(\gamma)$, $\pi^+\pi^-\gamma_{\rm ISR}$, $B\bar{B}$ and $\tau^+\tau^-$. Observed in Figure B.4 is a peak in the data and MC at m_ϕ^{calc}= m$_\phi$ corresponding to candidates consistent with $e^+e^- \to \phi\gamma_{\rm ISR} \to K_S^0 K_L^0 \gamma_{\rm ISR}$. From the MC modes shown in this figure it is observed that in the region $m_\phi^{calc} < 1.12$ GeV/c^2 the majority of candidates are signal events. In order to avoid double counting signal events, a generator level veto is applied to the $s\bar{s}$ MC samples to remove events of the form $e^+e^- \to K^0\bar{K}^0(n\gamma)$ where n is an integer.

Up to the $m_\phi^{calc} < 1.12$ GeV/c^2 cut, a best candidate selection has not yet been applied and thus a single event can potentially have multiple K_L^0 candidates. Even after applying the $m_\phi^{calc} < 1.12$ GeV/c^2 requirement it is found that there are still several events with multiple K_L^0 candidates. This is an artefact of the calorimeter clustering algorithm which is not optimized for hadronic showers and thus the K_L^0 clusters are sometimes divided into two nearby clusters forming two K_L^0 candidates. As these K_L^0 candidates are nearby they will both be within the resolution of being

consistent the $m_{\phi}^{calc} < 1.12$ GeV/c^2 requirement. The final requirement applied is to select the K_L^0 candidate with the highest cluster energy.

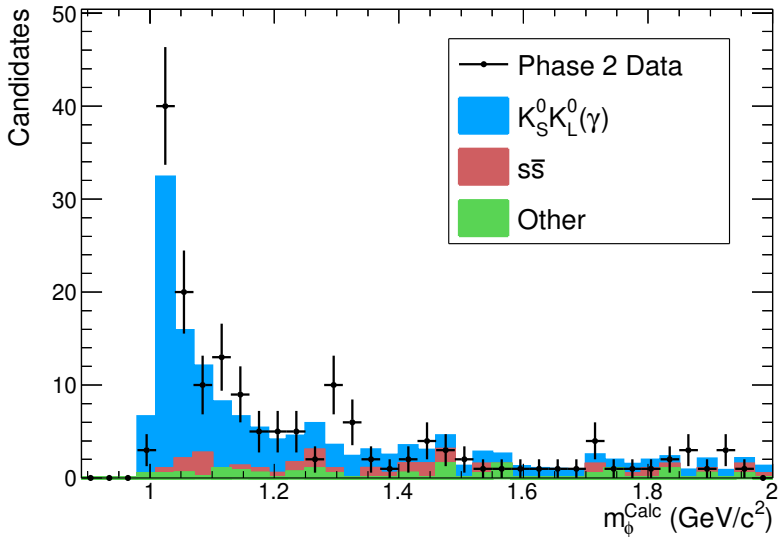

Figure B.4: Distribution of distribution of m_{ϕ}^{calc} for data and MC after applying all selection requirements up to item 7 in the cut list. MC is normalized to 507.0 pb^{-1}. Errors are statistical only.

B.4 Selection Results

After applying the full selection requirements the distributions of $p_{\mathrm{KL}}^{\mathrm{calc}}$ and $\mathrm{E_{ecl}}$ are shown in Figure B.5 with data and MC overlaid.

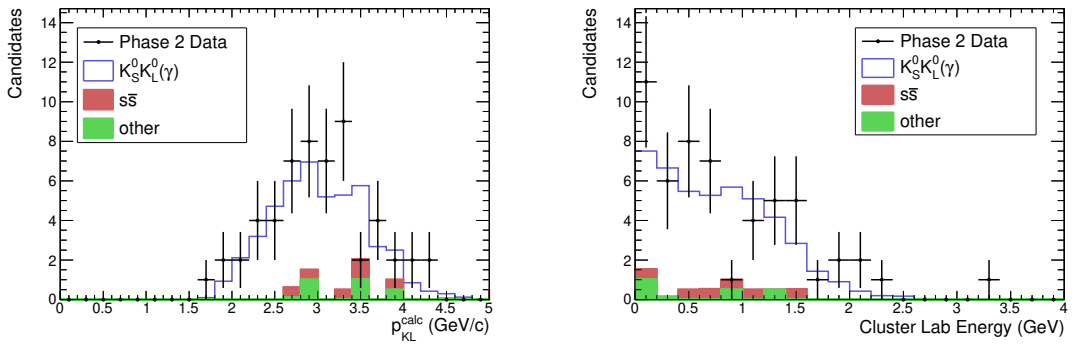

(a) (b)

Figure B.5: a) $p_{\mathrm{KL}}^{\mathrm{calc}}$ b) $\mathrm{E_{KL}^{ecl}}$ distributions for the K_L^0 candidates passing all selection requirements.

A final step of this selection is to evaluate the precision of $p_{\mathrm{KL}}^{\mathrm{calc}}$. As discussed above, $p_{\mathrm{KL}}^{\mathrm{calc}}$ is computed with equation B.1 that applied total energy conservation using the measured total energy of the K_S^0 and γ_{ISR} candidate to compute the expected K_L^0 momentum. A limitation of computing the K_L^0 momentum using this approach is that if the event has a second radiated photon, then this will cause equation B.1 to over estimate the true K_L^0 momentum. To evaluate the impact of this effect $\delta_{\mathrm{p}}^{\mathrm{KL}}$ defined in equation B.5 is used.

$$\delta_{\mathrm{p}}^{\mathrm{KL}} = \frac{p_{\mathrm{KL}}^{\mathrm{calc}} - p_{\mathrm{KL}}^{\mathrm{GEN}}}{p_{\mathrm{KL}}^{\mathrm{GEN}}} \tag{B.5}$$

In equation B.5 $p_{\mathrm{KL}}^{\mathrm{GEN}}$ is the magnitude of the lab momentum of the K_L^0 when it was generated in the MC event. For all candidates in the $K_S^0 K_L^0 \gamma_{\mathrm{ISR}}$ MC that pass the full selection requirements, the distribution of $\delta_{\mathrm{p}}^{\mathrm{KL}}$ is shown in Figure B.6. In this distribution the K_L^0 candidates are highlighted depending if the MC event contained one or two radiated photons at generator level with energy above 0.1 GeV.

The distribution in Figure B.6 has a peak at $\delta_{\mathrm{p}}^{\mathrm{KL}} = 0$ followed by a tail to higher values. The candidates in the tail are observed to primarily be from events with two photons. As expected this tail extends to higher positive values as when $p_{\mathrm{KL}}^{\mathrm{calc}}$ is computed without including the energy of the second photon, $p_{\mathrm{KL}}^{\mathrm{calc}}$ will over estimate the true momentum of the K_L^0. Overall however the majority of the candidates are predicted to have $p_{\mathrm{KL}}^{\mathrm{calc}}$ computed to within $\pm 10\%$ of the true K_L^0 momentum.

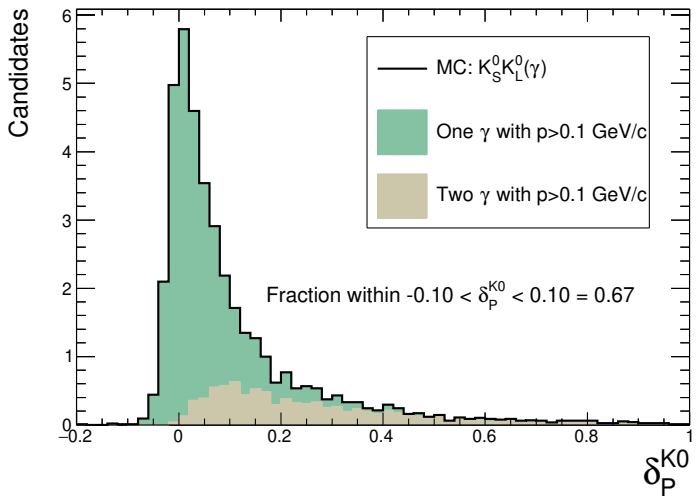

Figure B.6: Distribution of $\delta_{\mathrm{p}}^{\mathrm{KL}}$ for candidates selected from signal MC and passing full selection requirements. Distribution is normalized to phase 2 integrated luminosity.

Appendix C

Selection of a K_L^0 Control Sample from $B^0\bar{B}^0$ MC

To select K_L^0 from $B^0\bar{B}^0$ MC, a pre-selection is initially applied requiring the event contained B-meson decay chain that included a K_L^0. From these events all neutral calorimeter clusters are selected that pass the following criteria:

- $E_{ecl} > 0.05$ GeV.
- Calorimeter cluster is in the calorimeter barrel ($32.2 < \theta < 128.7$ degrees).
- $W_{sum} > 1.5$, where W_{sum} is the sum of the weights, ranging from 0 to 1, assigned to the crystals in the cluster and measure the relation of the crystal to the cluster. Typically crystals are assigned a weight of 1.0.

In this efficient pre-selection, the majority of the clusters are expected to not be produced by the generated K_L^0. To match the clusters that are most likely to be from the generated K_L^0 in the event, the angle between the generated K_L^0 momentum vector and the candidate calorimeter cluster position vector, $\alpha_{KL,ecl}$, is used. In Figure C.1 the distribution of $\alpha_{KL,ecl}$ is shown for all clusters in the pre-selection. As expected many of the clusters are at large angle to the K_L^0 momentum vector. In the zoom shown in Figure C.1 a peak in the distribution is observed corresponding to an excess of clusters located in the direction of the generated K_L^0 momentum vector. The K_L^0 cluster candidates are selected by requiring $\alpha_{KL,ecl} < 0.05$ rad. If there are two candidates in the same event that pass this criteria then the higher energy cluster is used.

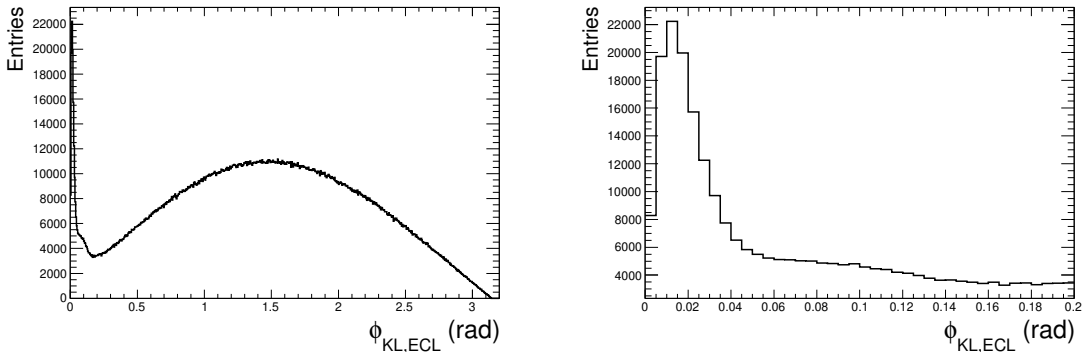

(a) Full Range (b) Zoom

Figure C.1: Distribution of $\alpha_{\mathrm{KL,ecl}}$ for clusters passing K_L^0 from $B^0\bar{B}^0$ pre-selection criteria.

Appendix D

Data and Monte-Carlo Samples

The Belle II Phase 2 data used is corresponds to `Proc8` processed by the Belle II Data Production group with release-03-00-03. The MC samples are produced by the Belle II Data Production Group using release-03-00-03. Table D.1 details the cross-sections used for normalization.

MC Sample	σ_{MC} (nb)	Events Generated	Luminosity Generated
$e^+e^-(\gamma)$	-	4 million	
$e^+e^-e^+e^-$	40.5	4 million	
$e^+e^-\mu^+\mu^-$	18.8	4 million	
$\mu^+\mu^-(\gamma)$	1.147	4 million	
$\tau^+\tau^-$	0.919	-	$1fb^{-1}$
$B^0\bar{B}^0$	0.5654	-	$1fb^{-1}$
B^+B^-	0.5346	-	$1fb^{-1}$
$u\bar{u}$	1.605	-	$1fb^{-1}$
$d\bar{d}$	0.401	-	$1fb^{-1}$
$s\bar{s}$	0.383	-	$1fb^{-1}$
$c\bar{c}$	1.329	-	$1fb^{-1}$
$K^+K^-\gamma_{\mathrm{ISR}}$	1.56×10^{-2}	0.5 million	
$K^0_SK^0_L\gamma_{\mathrm{ISR}}$	8.58×10^{-2}	0.5 million	
$\pi^+\pi^-\gamma_{\mathrm{ISR}}$	0.117	0.5 million	
$\pi^0\pi^+\pi^-\gamma$	2.52×10^{-2}	0.5 million	
$\pi^0\pi^0\pi^+\pi^-\gamma$	3.7×10^{-2}	0.5 million	
$\eta^0\pi^+\pi^-\gamma$	2.51×10^{-3}	0.5 million	

Table D.1: Monte Carlo samples used and cross-sections used for normalization.

Bibliography

[1] D. Griffiths. *Introduction to Elementary Particles*. WILEY-VCH Verlag GmbH & Co., Weinheim, Germany, 2nd edition, 8 2008. ISBN 9783527406012.

[2] C. Patrignani et al. Review of Particle Physics. *Chin. Phys.*, C40(10):100001, 2016. doi: 10.1088/1674-1137/40/10/100001.

[3] T. Abe et al. Belle II Technical Design Report. 2010.

[4] E. Kou et al. The Belle II Physics Book. 2018.

[5] S. Agostinelli et al. GEANT4-a simulation toolkit. *Nucl. Instrum. Meth.*, A506: 250–303, 2003. doi: 10.1016/S0168-9002(03)01368-8.

[6] B. R. Martin and G. Shaw. *Particle Physics*. John Wiley & Sons, Ltd, The Atrium, Southern Gate, Chichester, West Sussex, United Kingdom, 4th edition, 1 2017. ISBN 9781118912164.

[7] I. Aitchison and A. Hey. *Gauge Theories in Paritcle Physics A Pratical Introduction*, volume 1. Taylor & Francis Group, LLC, 600 Broken Sound Parkway NW, Suite 300, 4th edition, 2013. ISBN 9781466512993.

[8] I. Aitchison and A. Hey. *Gauge Theories in Paritcle Physics A Pratical Introduction*, volume 2. Taylor & Francis Group, LLC, 600 Broken Sound Parkway NW, Suite 300, 4th edition, 2013. ISBN 9781466513075.

[9] C. Amsler. *Nuclear and Particle Particles*. IOP Publishing Ltd 2015, IOP Publishing, Temple Circus, Temple Way, Bristol, UK, 2015. ISBN 9780750311410.

[10] K. M. Eisenberg and D.S. Kolton. *Theory of meson interactions with nuclei*. United States John Wiley & Sons Inc, 1980. ISBN 0471039152.

[11] A. Di Domenico. *HANDBOOK ON NEUTRAL KAON INTERFEROMETRY AT A ϕ-FACTORY*, volume XLIII of *Frascati Physics Series*. Istituto Nazionale di Fisica Nucleare, Frascati, Italy, 2007.

[12] Super KEKB and Belle II. `https://www.belle2.org/project/super_kekb_and_belle_ii`. Accessed: 2019-06-06.

[13] B. Aubert et al. Observation of CP violation in the B^0 meson system. *Phys. Rev. Lett.*, 87:091801, 2001. doi: 10.1103/PhysRevLett.87.091801.

[14] K. Abe et al. Observation of mixing induced CP violation in the neutral B meson system. *Phys. Rev.*, D66:032007, 2002. doi: 10.1103/PhysRevD.66.032007.

[15] B. Aubert et al. Measurement of Time-Dependent CP Asymmetry in $B^0 \to c\bar{c}K^{(*)0}$ Decays. *Phys. Rev.*, D79:072009, 2009. doi: 10.1103/PhysRevD.79.072009.

[16] I. Adachi et al. Precise measurement of the CP violation parameter $\sin 2\phi_1$ in $B^0 \to (c\bar{c})K^0$ decays. *Phys. Rev. Lett.*, 108:171802, 2012. doi: 10.1103/PhysRevLett.108.171802.

[17] B. Aubert et al. A study of time dependent CP-violating asymmetries and flavor oscillations in neutral B decays at the $\Upsilon(4S)$. *Phys. Rev.*, D66:032003, 2002. doi: 10.1103/PhysRevD.66.032003.

[18] I. Adachi et al. Evidence for $B^- \to \tau^- \bar{\nu}_\tau$ with a Hadronic Tagging Method Using the Full Data Sample of Belle. *Phys. Rev. Lett.*, 110(13):131801, 2013. doi: 10.1103/PhysRevLett.110.131801.

[19] R. M. Sternheimer, J. M. Berger, and S. M. Seltzer. Density Effect for the Ionization Loss of Charged Particles in Various Substances. *Atom. Data Nucl. Data Tabl.*, 30:261–271, 1984. doi: 10.1016/0092-640X(84)90002-0.

[20] N. Watanabe. Neutronics of pulsed spallation neutron sources. *Reports on Progress in Physics*, 66(3):339, 2003.

[21] W. O. Lock and D. F. Measday. *Intermediate Energy Nuclear Physics*. Methuen, 1970.

[22] G. F. Knoll. *Radiation Detection and Measurement*. John Wiley & Sons, Inc, New York, NY, United States, 3rd edition, 2000.

[23] G. Bizarri. Scintillation mechanisms of inorganic materials: From crystal characteristics to scintillation properties. *Journal of Crystal Growth*, 312:1213–1215, 2010. doi: 10.1016/j.jcrysgro.2009.12.063.

[24] R. S. Storey, W. Jack, and A. Ward. The Fluorescent Decay of CsI(Tl) for Particles of Different Ionization Density. *Proceedings of the Physical Society*, 72 (1):1– 8, July 1958. doi: 10.1088/0370-1328/72/1/302.

[25] S. Longo and J. M. Roney. Hadronic vs. electromagnetic pulse shape discrimination in CsI(Tl) for high energy physics experiments. *Journal of Instrumentation*, 13(03):P03018, March 2018. doi: 10.1088/1748-0221/13/03/p03018.

[26] Y. Koba et al. Scintillation Efficiency of Inorganic Scintillators for Intermediate-Energy Charged Particles. *Progress in Nuclear Science and Technology*, 1:219–221, 2011.

[27] X. Lu et al. Coupled rate and transport equations modeling proportionality of light yield in high-energy electron tracks: CsI at 295 K and 100 K; CsI:Tl at 295 K. *Phys. Rev. B*, 92:115207, Sep 2015. doi: 10.1103/PhysRevB.92.115207.

[28] Z. Wang et al. Kinetic Monte Carlo simulations of excitation density dependent scintillation in CsI and CsI(Tl). *Phys. Status Solidi B*, 250(8):1532–1540, 2013.

[29] Y. Ohnishi. Highlights from SuperKEKB Phase 2 Commissioning. In *Proceedings, 62nd ICFA Advanced Beam Dynamics Workshop on High Luminosity Circular e^+e^- Colliders (eeFACT2018): Hong Kong, China, September 24-27, 2018*, page MOXAA02, 2019. doi: 10.18429/JACoW-eeFACT2018-MOXAA02.

[30] K. Akai, K. Furukawa, and H. Koiso. SuperKEKB Collider. *Nucl. Instrum. Meth.*, A907:188–199, 2018. doi: 10.1016/j.nima.2018.08.017.

[31] P. M. Lewis et al. First Measurements of Beam Backgrounds at SuperKEKB. *Nucl. Instrum. Meth.*, A914:69–144, 2019. doi: 10.1016/j.nima.2018.05.071.

[32] H. Moser. The Belle II DEPFET pixel detector. *Nucl. Instrum. Meth.*, A831: 85–87, 2016. doi: 10.1016/j.nima.2016.02.078.

[33] U. Tamponi. The TOP counter of Belle II: status and first results. In *10th Workshop on Ring Imaging Cherenkov Detectors (RICH2018) Moscow, Russia, July 29-August 4, 2018*, volume A, 2019. doi: 10.1016/j.nima.2019.05.049.

[34] M. Mrvar et al. First experience with Belle II Aerogel RICH detector. *Nucl. Instrum. Meth.*, A936:552–553, 2019. doi: 10.1016/j.nima.2018.10.197.

[35] V. Aulchenko et al. Electromagnetic calorimeter for Belle II. *Journal of Physics: Conference Series*, 587(1):012045, 2015.

[36] T. Aushev et al. A scintillator based endcap K_L and muon detector for the Belle II experiment. *Nucl. Instrum. Meth.*, A789:134–142, 2015. doi: 10.1016/j.nima.2015.03.060.

[37] A. Sibidanov. Belle II readiness for Phase II collisions. Lake Louise Winter Institute 2018, 2018.

[38] S. Longo and J. M. Roney. Proposal to use CsI(Tl) Pulse Shape Analysis for Neutral Hadron Identification. 25th Belle II General Meeting, 2016.

[39] C. Hearty. L1 trigger menu for low-luminosity running. 28th Belle II General Meeting, 2017.

[40] V. Vorobyev et al. Testbench of shaper-digitizer modules for Belle II calorimeter. *Journal of Instrumentation*, 9(08):C08016, 2014.

[41] *Hamamatsu R580 photomultiplier*. Hamamatsu Photonics, June 2014.

[42] *Si PIN photondiodes S2744/S3588-08,-09*. Hamamatsu Photonics, October 2011.

[43] T. S. Lee and R. P. Redwine. PION-NUCLEUS INTERACTIONS. *Annual Review of Nuclear and Particle Science*, 52(1):23–63, 2002. doi: 10.1146/annurev.nucl.52.050102.090713.

[44] D. Ashery and J. P. Schiffer. Pion Absorption in Nuclei. *Annual Review of Nuclear and Particle Science*, 36(1):207–252, 1986. doi: 10.1146/annurev.ns.36.120186.001231.

[45] Geant4 Collaboration. Physics Reference Manual. `http://geant4-userdoc.web.cern.ch/geant4-userdoc/UsersGuides/PhysicsReferenceManual/fo/PhysicsReferenceManual.pdf`, 2018.

[46] C. B. Dover and G. E. Walker. The interaction of kaons with nucleons and nuclei. *Physics Reports*, 89(1):1 – 177, 1982. ISSN 0370-1573. doi: 10.1016/0370-1573(82)90043-6.

[47] A. Gal et al. Strangeness in nuclear physics. *Rev. Mod. Phys.*, 88:035004, Aug 2016. doi: 10.1103/RevModPhys.88.035004.

[48] D.H. Wright and M.H. Kelsey. The Geant4 Bertini Cascade. *Nuclear Instruments and Methods in Physics Research Section A: Accelerators, Spectrometers, Detectors and Associated Equipment*, 804:175 – 188, 2015. ISSN 0168-9002. doi: 10.1016/j.nima.2015.09.058.

[49] E. Klempt et al. Antinucleon-nucleon interaction at low energy: Annihilation dynamics. *Physics Reports*, 413:197 – 317, 2005.

[50] J. Cugnon. Proton-nucleus interaction at high energy. *Nuclear Physics A*, 462 (4):751 – 780, 1987. ISSN 0375-9474. doi: 10.1016/0375-9474(87)90575-6.

[51] H. Machner and J. Haidenbauer. Meson production close to threshold. *Journal of Physics G: Nuclear and Particle Physics*, 25(10):R231, 1999.

[52] E. Klempt et al. Antinucleon-nucleon interaction at low energy: scattering and protonium. *Physics Reports*, 368(2):119 – 316, 2002. ISSN 0370-1573. doi: 10.1016/S0370-1573(02)00144-8.

[53] H. Aghai-Khozani et al. Measurement of the antiproton nucleus annihilation cross-section at low energy. *Nuclear Physics A*, 970:366 – 378, 2018. ISSN 0375-9474. doi: 10.1016/j.nuclphysa.2018.01.001.

[54] T. Keck. FastBDT: A Speed-Optimized Multivariate Classification Algorithm for the Belle II Experiment. *Computing and Software for Big Science*, 1(1):2, Sep 2017. ISSN 2510-2044. doi: 10.1007/s41781-017-0002-8.

[55] A. Hershenhorn et al. ECL shower shape variables based on Zernike moments. BELLE2-NOTE-TE-2017-001, 2017.

[56] C.M. Bartle and R.C. Haight. Small inorganic scintillators as neutron detectors. *Nucl. Instrum. Meth.*, A422(1):54 – 58, 1999. ISSN 0168-9002. doi: 10.1016/S0168-9002(98)01062-6.

[57] L. E. Dinca et al. Alpha-gamma pulse shape discrimination in CsI:Tl, CsI:Na and BaF2 scintillators. *Nucl. Instrum. Meth.*, A486(1):141 – 145, 2002. ISSN 0168-9002. doi: 10.1016/S0168-9002(02)00691-5.

[58] J. Woo et al. A Pulse Shape Discrimination Method with CsI Using the Ratio of Areas for Identifying Neutrons and Gamma Rays. 62(5):839 – 844, 2013.

[59] L. Bardelli et al. Pulse-shape discrimination with PbWO4 crystal scintillators. *Nucl. Instrum. Meth.*, A584(1):129 – 134, 2008. ISSN 0168-9002. doi: 10.1016/j.nima.2007.10.021.

[60] I. Komarov and G. Inguglia. Performance of the CDC trigger for very low multiplicity studies in Phase 2 data. BELLE2-NOTE-TE-2018-017, 2018.

[61] Belle II Collaboration. Standard particles. `https://confluence.desy.de/display/BI/Physics+StandardParticles`.

[62] K. Prasanth et al. K0S reconstruction using phase 2 data. BELLE2-NOTE-PH-2018-017, 2018.